3-2-2021

Improving Flat Plate Heat Transfer Using Flexible Rectangular Strips

Yang Yang
University of Windsor

Improving Flat Plate Heat Transfer Using Flexible Rectangular Strips

By

Yang Yang

A Dissertation
Submitted to the Faculty of Graduate Studies
through the Department of Mechanical, Automotive & Materials Engineering
in Partial Fulfillment of the Requirements for
the Degree of Doctor of Philosophy
at the University of Windsor

Windsor, Ontario, Canada

2020

Improving Flat Plate Heat Transfer Using Flexible Rectangular Strips

by

Yang Yang

APPROVED BY:

Y. S. Muzychka, External Examinar
Memorial University of Newfoundland

R. Carriveau
Department of Civil and Environmental Engineering

G. Rankin
Department of Mechanical, Automotive, & Materials Engineering

---

V. Stoilov
Department of Mechanical, Automotive, & Materials Engineering

---

S. Ray
Essex Energy Corporation

D. S-K. Ting, Advisor
Department of Mechanical, Automotive, & Materials Engineering

November 6, 2020

DECLARATION OF CO-AUTHORSHIP/PREVIOUS PUBLICATION

I. Co-Authorship

I hereby declare that this thesis incorporates material that is result of joint research, as follows:

Chapter 2~7, and Appendix B of the thesis was co-authored with S. Ray under the supervision of professor D. S-K. Ting. Appendix C. of the thesis was co-authored with A. Ahmed and S. Ray under the supervision of professor D. S-K. Ting. In all cases, the key ideas, primary contributions, experimental designs, data analysis, interpretation, and writing were performed by the author. S. Ray and A. Ahmed provided feedback on refinement of editing of the manuscript.

I am aware of the University of Windsor Senate Policy on Authorship and I certify that I have properly acknowledged the contribution of other researchers to my thesis, and have obtained written permission from each of the co-author(s) to include the above material(s) in my thesis.

I certify that, with the above qualification, this thesis, and the research to which it refers, is the product of my own work.

II. Previous Publication

This thesis includes eight original papers that have been previously published/submitted for publication in peer reviewed journals/conferences/book chapters, as follows:

Thesis Chapter	Publication title/full citation	Publication status
Chapter 2	*Y. Yang, D. S-K. Ting, S. Ray, "Improving heat transfer efficiency with innovative turbulence generators," for Climate Change and Pragmatic Engineering Mitigation, Jenny Stanford, 2021.*	*Accepted*
Chapter 3	*Y. Yang, D. S-K. Ting, S. Ray, "Convective heat transfer enhancement downstream of a flexible strip normal to the freestream," International Journal of Thermal Sciences 145 (2019) 106059*	*Published*

Chapter 4	*Y. Yang, D. S-K. Ting, S. Ray, "On flexible rectangular strip height on flat plate heat convection," International Journal of Heat and Mass Transfer 150 (2020) 119269*	*Published*
Chapter 5	*Y. Yang, D. S-K. Ting, S. Ray, "Heat transfer enhancement of a heated flat surface via a flexible strip pair," International Journal of Heat and Mass Transfer 159 (2020) 120139*	*Published*
Chapter 6	*Y. Yang, D. S-K. Ting, S. Ray, "The effect of freestream turbulence on convection enhancement by a flexible strip," Experimental Thermal and Fluid Science*	*Under review*
Chapter 7	*Y. Yang, D. S-K. Ting, S. Ray, "Mechanisms Underlying Flat Surface Forced Convection Enhancement by Rectangular Flexible Strips," Thermal Science and Engineering Progress*	*Under review*
Appendix B	*Y. Yang, D. S-K. Ting, S. Ray, "Perforated-plate turbulence: orifice versus converging nozzle," Proceedings of the 5th Joint US-European Fluids Engineering Summer Conference, 2018*	*Presented & Published*
Appendix C	*Y. Yang, A. Ahmed, D. S-K. Ting, S. Ray, "The influence of square wire attack angle on the heat convection from a surrogate PV panel," The Energy Mix for Sustaining Our Future, Springer, 2018, pp. 103-128*	*Published*

I certify that I have obtained a written permission from the copyright owner(s) to include the above published material(s) in my thesis. I certify that the above material describes work completed during my registration as a graduate student at the University of Windsor.

III. General

I declare that, to the best of my knowledge, my thesis does not infringe upon anyone's copyright nor violate any proprietary rights and that any ideas, techniques, quotations, or any other material from the work of other people included in my thesis, published or otherwise, are fully acknowledged in accordance with the standard referencing practices. Furthermore, to the extent that I have included copyrighted material that surpasses the bounds of fair dealing within the meaning of the Canada Copyright Act, I certify that I have obtained a written permission from the copyright owner(s) to include such material(s) in my thesis.

I declare that this is a true copy of my thesis, including any final revisions, as approved by my thesis committee and the Graduate Studies office, and that this thesis has not been submitted for a higher degree to any other University or Institution.

ABSTRACT

Many engineering systems involve proper transfer of heat to operate. As such, augmenting the heat transfer rate can lead to performance improvement of systems such as heat exchangers and solar photovoltaics panels. Among the many existing and studied heat transfer enhancement techniques, a well-designed passive turbulence generator is a simple and potent approach to augmenting convective heat transfer. Two of the most recognized passive convective heat enhancers are wings and winglets. Their potency is attributed to the long-lasting induced longitudinal vortices which are effective in scooping and mixing hot and cold fluids. Somewhat less studied are flexible turbulence generators, which could further the heat transfer enhancement compared to their rigid counterpart. In the current study, the flexible rectangular strips are proposed, marrying the long-lasting vortex streets with the periodic oscillation, to maximize heat convection.

This study was conducted in a closed-looped wind tunnel with 76 cm square cross-section. The effects of flexible strips on the turbulent flow characteristics and the resulting convective heat transfer enhancement from a heated flat surface are detailed in four papers which are presented as Chapters 3, 4, 5 and 6. In Chapter 3, the effect of the thickness of the strip is detailed. The 12.7 mm wide and 38.1 mm tall rectangular strip was cut from an aluminum sheet with thickness of 0.1, 0.2 and 0.25 mm. The incoming wind velocity was maintained at around 10 m/s, giving a Reynolds number based on the strip width of 8500. It is observed that the thinnest 0.1 mm strip could induce a larger downwash velocity and a stronger Strouhal fluctuation at 3H (strip height) downstream, leading to a better heat transfer enhancement. The peak of the normalized Nusselt number (Nu/Nu_0) at 3H downstream of the 0.1 mm strip was around 1.67, approximately 0.1 larger than that of the 0.25 mm strip.

In Chapter 4, the height effect of the strip is disclosed. The strip was 12.7 mm wide and 0.1 mm thick, with a height of 25.4 mm, 38.1 mm and 50.8 mm. The Reynolds number in this chapter was also fixed at around 8500, based on the strip width and the freestream velocity. It was found that the shortest, 25.4 mm strip could induce the closest-to-wall swirling vortices, and the largest near-surface downwash velocity toward the heated surface. Thus, the largest heat transfer augmentation was observed. At 9W (strip width) downstream, the 25.4 mm-strip provided the Nu/Nu_0 peak of around 1.76, 0.26 larger than that associated with the tallest, 50.8 mm-strip.

In Chapter 5, the effect of the transversal space of a pair of strips is expounded. A pair of 0.1 mm thick, 12.7 mm wide, and 25.4 mm tall aluminum rectangular flexible strips was placed side-by-side with a spacing of 1W (strip width), 2W and 3W. The Reynolds number based on the strip width was around 8500. The results showed that the 1W-spaced strip pair induced the strongest vortex-vortex interaction, the largest downwash velocity, and the most intense turbulence fluctuation. These resulted in the most effective heat convection. At Y=0 (middle of the strip pair) and X=9W, the largest Nu/Nu_0 value of around 1.50 was identified when using the 1W-spaced strip pair. This was approximately 0.24 and 0.33 larger than that of the 2W- and 3W-spaced strip pairs.

Chapter 6 presents the effect of freestream turbulence on the flat plate heat convection enhancement with a 12.7 mm wide, 25.4 mm tall and 0.1 mm thick flexible strip. A 6 mm thick sharp-edged orificed perforated plate (OPP) with holes of 38.1 mm diameter (D) was placed at 10D, 13D and 16D upstream of the strip to generate the desirable levels of freestream turbulence. The corresponding streamwise freestream turbulence intensity at the strip was around 11%, 9% and 7%. The Reynolds number based on the strip width and freestream velocity was approximately 6000. The freestream turbulence was found to diminish the effect of flexible strip in terms of the relative heat transfer enhancement (Nu/Nu_0). This is due to the significant increase of Nu_0 with the increasing freestream turbulence. In other words, the flexible strip could always improve the heat transfer, and the relative improvement is greatest for the largely laminar freestream case in the absence of the OPP.

Chapter 7 summarizes the effect of all the parameters in previous chapters on the convective heat transfer enhancement. The results show that the freestream turbulence intensity (Tu) had the most significant effect in augmenting the averaged Nu/Nu_0, and the local Nu/Nu_0 correlated best with the local ke. The maximal averaged Nu/Nu_0 over 23W downstream, within ±1 and ±4 strip widths cross-stream was found for Tu=7% case and Tu=11% case, respectively.

Conclusions are drawn and recommendations are provided in Chapter 8.

DEDICATION

To my family

ACKNOWLEDGEMENTS

First, I sincerely thank my supervisor Dr. David S-K. Ting for his precious advice and inspiration. His words, “Keep striving upstream,” always encourage me to move forward and finally finishing this dissertation. I would like to thank Mr. Steve Ray for scrutinizing through every manuscript. A big Thank You goes to my committee members, Dr. Gary Rankin, Dr. Vesselin Stoilov and Dr. Rupp Carriveau for their time and invaluable suggestions. I am grateful to Dr. Yuri S. Muzychka of Memorial University of Newfoundland, for his willingness to serve as the external examiner which demands much of his precious time. As well, my sincere thanks go to Mr. Andy Jenner and Mr. Ramadan Barakat for their technical support.

This work was made possible by Natural Sciences and Engineering Research Council of Canada and Ontario Centres of Excellence.

TABLE OF CONTENTS

LIST OF TABLES

LIST OF FIGURES

LIST OF ABBREVIATIONS/SYMBOLS

A	Area of the *PTFE* (Polytetrafluoroethylene) plate
f	Frequency
H	Height of the strip
h	Convective heat transfer coefficient
K_{air}	Thermal conductivity of air
K_{PTFE}	Thermal conductivity of *PTFE* plate
ke	Non-dimensional turbulent kinetic energy
Nu	Nusselt number
$PTFE$	Polytetrafluoroethylene
$\dot{Q}_{convection}$	Rate of convective heat transfer
$\dot{Q}_{radiation}$	Rate of radiation heat transfer
$\dot{Q}_{total}$	Rate of total heat transfer
Re	Reynolds number
St	Strouhal Number
T_{air}	Temperature of air
T_{bottom}	Bottom surface temperature of the *PTFE* plate
T_{top}	Local top surface temperature of the *PTFE* plate
T_{wall}	Wind tunnel wall temperature
t_{PTFE}	Thickness of the *PTFE* plate
Tu	Streamwise turbulence intensity
U_i, V_i, W_i	Instantaneous velocities in the *X*, *Y*, and *Z* direction, respectively
$\overline{U}, \overline{V}, \overline{W}$	Time-averaged velocities in the *X*, *Y*, and *Z* direction, respectively
U_∞	Streamwise freestream velocity
u, v, w	Instantaneous fluctuating velocities in *X*, *Y*, and *Z* direction
$u_{rms}, v_{rms}, w_{rms}$	Root-mean-square velocities in the *X*, *Y*, and *Z* direction
W	Strip width
X	Streamwise direction
Y	Widthwise direction
Z	Vertical direction
β_j	Regression coefficient of each individual parameter
β_j^{std}	Standardized regression coefficient of each individual parameter
ε	Emissivity

Λ	Integral length scale
λ	Taylor microscale
ν	Kinematic viscosity
σ	Boltzmann's constant
τ	Temporal distance
τ_{Λ}	Integral time scale
τ_{λ}	Taylor time scale
Ω	Normalized *X*-vorticity of the vortex
ω	*X*-vorticity of the vortex

CHAPTER 1
INTRODUCTION

1.1 Motivation and Background

Augmenting heat transfer could improve the efficiency of many engineering systems and thus, help in alleviating the rising energy demand, around 1.3% each year to 2040 [1], and more importantly, mitigating the energy related emissions. Thus, much effort has been continuously invested in furthering the heat transfer rate. Numerous innovative techniques have been proposed, including the active and the passive approaches. Among others, employing the passive turbulence generators is one of the simple but effective methods to enhance heat transfer. This passive method is widely explored in engineering applications, such as heat exchangers and solar air heaters [2][3][4]. Placing the turbulence generators could disturb the flow structure, increase the turbulence intensity, and even induce the swirling vortices. Therefore, the fluid mixing is improved, and the heat transfer is effectively enhanced.

Due to the booming development of solar photovoltaics (PV) panel, it is predicted to be the largest component of global installed electricity capacity in 2040 [1]. Thus, the cooling of PV panel has started to draw great attention recently. For this specific application, the turbulence generators should be only placed at the leading edge of the panel, so that the heat transfer rate could be improved without blocking the solar radiation. Therefore, a long-lasting heat transfer augmentation is specifically desired. Among others, winglets and wings could produce the long-lasting longitudinal vortices [5], outlasting the turbulence induced from the conventional turbulence generators, such as ribs, more effectively improving the heat transfer from the entire heated surface. Further, it is found that the flexible type turbulence generators could strengthen the vortex, creating a better flow condition for thermal transporting, and thus, further boosting the heat transfer augmentation compared to their rigid counterpart [6].

To marry the longitudinal vortices with the vibration, a flexible rectangular wing type turbulence generator, named flexible strip, was proposed and explored in the current study for its effectiveness in enhancing the convective cooling from a heated flat surface. Different from most of the previous studies, which were developed in the internal channel, the flexible strip was placed in front of a flat surface under the open-flow condition in this study.

1.2 Objective and Organization

The objective of the current study is to investigate the effect of flexible strips on the heat transfer enhancement from a heated surface. The study was conducted in a closed-loop wind tunnel with a 76 cm by 76 cm cross-section. The turbulent flow was characterized by a triple sensor hotwire probe with a constant-temperature anemometer. The temperature was obtained from a thermal camera, from which the convective heat transfer augmentation was deduced. For the accomplishment of this research, different steps are detailed in the chapters of this thesis as follows:

<u>Chapter 2</u>

This chapter presents a brief review of passive turbulence generators for heat transfer augmentation, including grids, ribs, winglets, wings, and flexible turbulence generators. It is found that winglets and wings could produce long-lasting longitudinal vortices, which disrupt the boundary layer and increase the turbulence intensity over the involved heat transfer surface, effectively enhancing the heat transfer rate. Furthermore, flexible turbulence generators also provide a significant potential in furthering the heat transfer augmentation by oscillating one or more turbulent vortex streets between the surface and the freestream. In other words, marrying long-lasting vortex street with periodic fluttering seems promising in maximizing heat convection.

<u>Chapter 3</u>

In this chapter, a flexible 12.7 mm wide by 38.1 mm tall rectangular strip positioned normal to the freestream is explored for its effectiveness in enhancing the convective cooling of a heated plate. The effect of the flexibility of the strip is of particular interest. Thus, strip thicknesses of 0.1, 0.2 and 0.25 mm are investigated at a wind velocity of 10 m/s, a Reynolds number based on the strip width and freestream velocity of 8500. The resulting Nusselt number augmentation with respect to the unperturbed reference case is explained in terms of the turbulent flow characteristics detailed via a triple-sensor hotwire. A higher velocity toward the heated plate is detected behind the 0.1 mm-thick strip, contributing to the most effective heat transfer performance, approximately 0.1 higher than that associated with the 0.25 mm-thick strip in terms of the normalized Nusselt number.

<u>Chapter 4</u>

A 0.1 mm thick and 12.7 mm wide (W) rectangular flexible strip is experimentally investigated. According to the study in Chapter 3, the vortices behind the strip are surmised to be strongly correlated with the mixing between the cooler freestream air and the hotter air near the surface. Thus, the location of the vortices, presumably affected the strip height, is supposed to have a significant influence on the heat transfer enhancement. Therefore, three strip height, 25.4 mm, 38.1 mm and 50.8 mm, were explored at a 10 m/s wind, and a Reynolds number of 8500, based on the strip width. The 25.4 mm-high strip was observed to generate closest-to-surface vortex structures, and the largest near-surface-downwash velocity. These attributes result in a better mixing, and thus, heat removal. The 25.4 mm-high strip provides the highest normalized Nusselt number (Nu/Nu_0), with a peak value of approximately 1.76 at 9W downstream, 0.26 larger than that of the 50.8 mm-high strip.

Chapter 5

To further enhance the heat transfer rate, the strip pairs are explored in this chapter, investigating the effect of vortex interaction on the heat transfer enhancement. A pair of 12.7 mm wide (W) and 25.4 mm tall rectangular flexible strips made of 0.1 mm thick aluminum sheet was employed in this study, and was placed side-by-side with a spacing of 1W, 2W and 3W. The incoming wind velocity was fixed at 10 m/s, resulting in a Reynolds number based on the strip width of 8500. Particularly strong vortex-vortex interactions, a large downwash velocity and intense flow fluctuations were obtained behind the 1W-spaced strip pair. These contributed to better mixing and transport of the thermal energy. The 1W-spaced strip pair generated the highest Nu/Nu_0 values. Nu/Nu_0 of approximately 1.50 was achieved at the middle of the strip pair at X=9W. At this location, the pairs separated by 2W and 3W resulted in Nu/Nu_0 value of around 1.26 and 1.17, respectively. The 1W-spaced strip pair also produced the largest span-averaged Nu/Nu_0.

Chapter 6

To simulate a more realistic nature wind with higher fluctuating velocity [7], the orificed perforated plate, from which a high turbulence intensity could be induced [8][9], was installed at the upstream of the flexible strip. This chapter aims at furthering the research of the flexible strip, uncovering the effect of freestream turbulence on the flat plate heat convection by the flexible strip. The freestream turbulence was furnished by a 6 mm thick sharp-edged orificed perforated plate (OPP) with holes of 38.1 mm diameter (D) which spanned the entire 76 cm by 76 cm wind tunnel cross section. To achieve 11%, 9% and 7% turbulence at the flexible strip, the OPP was installed at 10D, 13D and 16D upstream of the strip. The investigation was conducted at a Reynolds number based on the strip width of 6000. The freestream turbulence is found to diminish the flexible-strip induced Nu/Nu_0 significantly. This is principally because Nu_0 increases considerably with increasing freestream turbulence. Of most practical significance is that the flexible strip always further *Nu*, and this improvement is largest with respect to an otherwise 'laminar' freestream

Chapter 7

In the current chapter, the relationships between the averaged Nu/Nu_0 and the strip thickness, height, spacing, Re and Tu were determined using multiple linear regression. The correlations between the local Nu/Nu_0 and turbulent flow parameters, including turbulent kinetic energy, downwash velocity and near surface streamwise velocity were also illustrated. The freestream turbulence intensity (Tu) had the most significant effect in augmenting the averaged Nu/Nu_0, and the local Nu/Nu_0 correlated best with the local ke. The maximal averaged Nu/Nu_0 over 23W downstream, within ±1 and ±4 strip widths cross-stream was found for Tu=7% case and Tu=11% case, respectively.

Chapter 8

The final chapter summarizes the studies in the previous chapters and concludes the heat transfer enhancement by the flexible strip. Some strategies for next steps are also included.

Appendix A.

This section includes the uncertainty of the studied parameters in the previous chapters.

Appendix B.

The turbulent flow characteristics induced by the sharp-edged orificed perforated plate (OPP), employed in Chapter 6, is detailed in this appendix.

Appendix C.

A more conventional turbulence generator, a square wire, was investigated in the initial exploration. This appendix presents this piece of work. The 4 mm square wire, placed at 6 mm from the flat surface, with 15° to 75° attack angle was scrutinized in a wind tunnel at 5 m/s wind velocity, a Reynolds number of around 1300 based on the 4 mm width. The square wire with an attack angle of 60° promoted the highest heat transfer enhancement in the current study, with a maximum Nu/Nu_0 value of around 1.8.

Appendix D.

The distribution of reference Nusselt number in the absence of the strips at an incoming flow velocity of around 10 m/s is presented in this section.

References

[1] International Energy Agency, "World Energy Outlook 2019: Executive summary," 2019.

[2] T. Alam, R. P. Saini, and J. S. Saini, "Use of turbulators for heat transfer augmentation in an air duct - A review," Renew. Energy, vol. 62, pp. 689–715, 2014, doi: 10.1016/j.renene.2013.08.024.

[3] S. Liu and M. Sakr, "A comprehensive review on passive heat transfer enhancements in pipe exchangers," Renew. Sustain. Energy Rev., vol. 19, pp. 64–81, 2013, doi: 10.1016/j.rser.2012.11.021.

[4] A. R. S. Suri, A. Kumar, and R. Maithani, "Convective heat transfer enhancement techniques of heat exchanger tubes: a review," Int. J. Ambient Energy, vol. 39, no. 7, pp. 649–670, 2018, doi: 10.1080/01430750.2017.1324816.

[5] G. Biswas, H. Chattopadhyay, and A. Sinha, "Augmentation of heat transfer by creation of streamwise longitudinal vortices using vortex generators," Heat Transf. Eng., vol. 33, no. 4–5, pp. 406–424, 2012, doi: 10.1080/01457632.2012.614150.

[6] R. K. B. Gallegos and R. N. Sharma, "Flags as vortex generators for heat transfer enhancement: Gaps and challenges," Renew. Sustain. Energy Rev., vol. 76, pp. 950–962, 2017, doi: 10.1016/j.rser.2017.03.115.

[7] M. C. H. Hui, A. Larsen, and H. F. Xiang, "Wind turbulence characteristics study at the Stonecutters Bridge site: Part I-Mean wind and turbulence intensities," J. Wind Eng. Ind. Aerodyn., vol. 97, no. 1, pp. 22–36, 2009, doi: 10.1016/j.jweia.2008.11.002.

[8] R. Liu and D. S.-K. Ting, "Turbulent flow downstream of a perforated plate: Sharp-edged orifice versus finite-thickness holes," J. Fluids Eng. Trans. ASME, vol. 129, no. 9, pp. 1164–1171, 2007, doi: 10.1115/1.2754314.

[9] R. Liu, D. S.-K. Ting, and M. D. Checkel, “Constant Reynolds number turbulence downstream of an orificed perforated plate,” Exp. Therm. Fluid Sci., vol. 31, no. 8, pp. 897–908, 2007, doi: 10.1016/j.expthermflusci.2006.09.007.

CHAPTER 2

IMPROVING HEAT TRANSFER EFFICIENCY WITH INNOVATIVE TURBULENCE GENERATORS

Y. Yang, D. S-K. Ting, S. Ray, "Improving heat transfer efficiency with innovative turbulence generators," in Climate Change and Pragmatic Engineering Mitigation, Jenny Stanford, accepted for publication.

2.1 Introduction

A straightforward way to mitigate climate change is to improve the efficiency of engineering systems. Every bit of the performance improvement is translated into less resources usage, reduced entropy generation, decreased emissions, and ultimately less adverse effect on our environment. Many engineered systems involve effective heat transfer to function. They typically involve heat exchangers in one form or another. Renewable energy systems such as a solar photovoltaic (PV) and solar thermal system are no exception. Currently, the prevailing commercial silicon PV modules have an energy conversion efficiency of around 16% [1], and this decreases under abundant solar energy exposure as the cell temperature increases. On average, the energy conversion efficiency of a silicon module decreases by 0.2% per degree Celsius increase in cell temperature [2]. This implies cooling PV panels offers a significant potential for improving their performance. By the end of 2013, PV systems generated 160TWh/yr of clean electricity, resulting in a 140 million metric tons of CO_2 reduction per year [1]. Even a 1% increase in power output, around 5°C decrease induced by augmented heat transfer, could contribute to more than one million metric tons of CO_2 reduction per year. This can definitely play an important role in mitigating climate change.

2.2 Techniques of Heat Transfer Enhancement

2.2.1 Active Methods

Heat transfer enhancement can be categorized into two groups: active and passive cooling methods. The active approaches require external power input to realize the heat transfer enhancement. Some examples include fluid stream [3], jet impingement, vibration, etc. [4].

An innovative technique using water spray was proposed by Nizetic et al. [5]. The solar PV panel was studied on a clear summer day with surrounding temperature ranging from 27°C to

30°C. Without any cooling, the average panel temperature was 56°C, and the maximum power output was 35 W. When they simultaneously sprayed water on the front and back sides of the PV panel, Fig. 2.1, the average panel temperature was reduced to 24°C. The corresponding maximal power output increased by 16%, to 41 W.

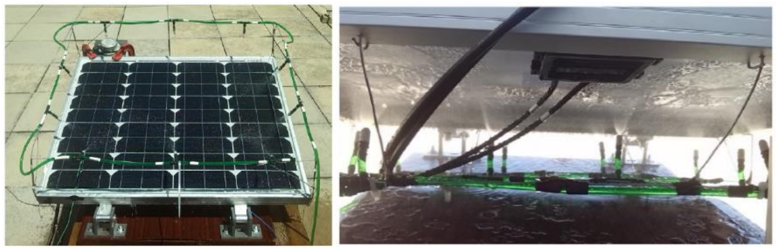

Figure 2. 1. The front and backside of the PV panel with water spray system [5].

Kianifard et al. [6] conducted an investigation on a novel design of a water-cooled PV panel, see Fig. 2.2. A serpentine half pipe was employed on the backside of the panel instead of the full circle pipe. According to their study, the new design provided a 13% increase in the thermal efficiency and a 0.6% increase in the electrical efficiency, compared to the conventional circular design.

Figure 2. 2. Experimental PV panel and the back of the panel [6].

Chen et al. [7] investigated the thermal performance of a building-integrated photovoltaic-thermal (BIPV/T) system. Via a variable speed fan, the outdoor air was drawn and transferred beneath the PV panels. It was found that the air flow had a significant effect on the PV. The temperature of the PV was around 50 to 60°C, while the roof without BIPV arrays, i.e. no air flow underneath, was higher than 70°C. In addition, the heated air from the PV arrays could also be utilized for the domestic hot water, improving the overall thermal performance.

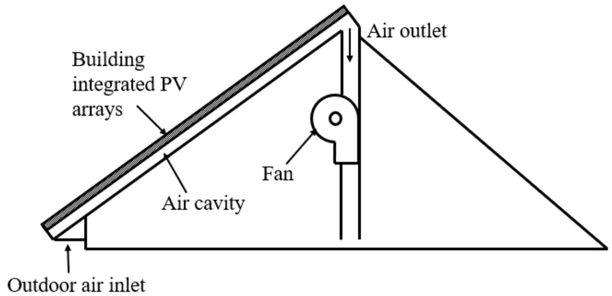

Figure 2. 3. Schematic of building-integrated photovoltaic-thermal system; redrawn based on Ref [7]

Rajaseenivasan et al. [8] developed an experimental study, examining the performance of an impinging jet solar air heater. In this study, the nozzle diameter of the jet was varied from 3 to 7 mm, and the mass flow rate was altered from 0.012 to 0.016 kg/s. Also, attack angles of 0°, 10°, 20°, 30°, 60° and 90° were considered. A maximum thermal enhancement factor of around 2.2 was obtained for the 5 mm diameter and 30° attack angle nozzle with a mass flow rate of 0.016 kg/s.

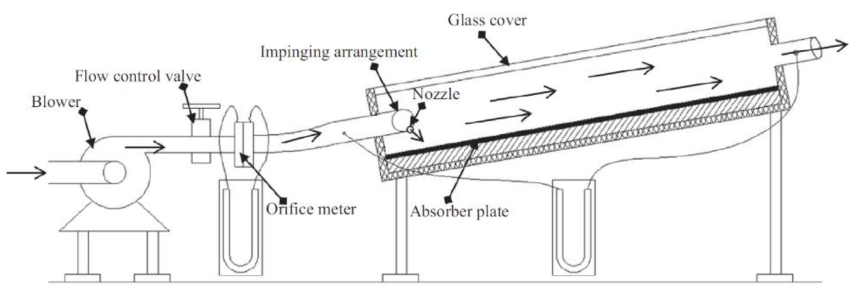

Figure 2. 4. Schematic of an impinging jet solar air heater [8]

Hsu et al. [9] explored the heat transfer characteristics of a pulsed jet impinging on a flat plate; see Fig. 2.5. They found that the convective heat transfer increases with increasing convective velocity of the vortex ring and also the fluctuation intensity. The average Nusselt number enhancement was up to 100% over the range of studied conditions.

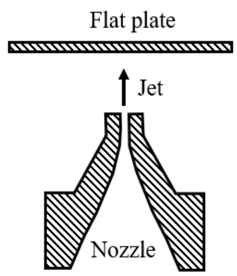

Figure 2. 5. Experimental schematic of a pulsed jet impinging on a flat plate; redrawn based on Ref [9].

An experimental and numerical study on heat transfer augmentation via ultrasonic vibration in a double-pipe heat exchanger was developed by Setareh et al. [10]; see Fig. 2.6. The effect of the transmitted acoustic power on the overall heat transfer coefficient was investigated. Under the condition of Q_h=0.5L/min and Q_c=1L/min, where Q_h and Q_c are the volume flow rate of hot and cold fluid, respectively, the 120W-transmitted acoustic power could induce approximately 57% overall heat transfer coefficient augmentation.

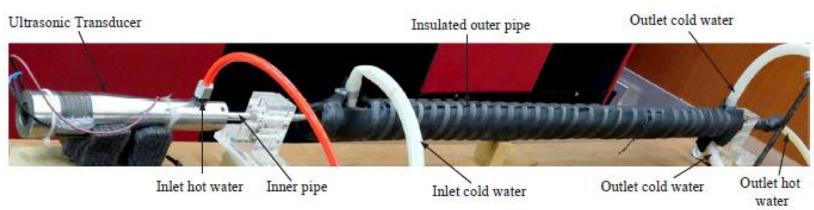

Figure 2. 6. Experimental setup of double-pipe heat exchanger with ultrasonic transducer [10].

An innovative design of active vacuum system was proposed by Roesle et al. [11] to minimize the heat loss from a parabolic trough absorber tube, and thus, enhance the overall thermal efficiency. They found that the heat loss was approximately 400Wm^{-2} at a temperature of 400°C, less than 10% of the energy gain. In a similar study, Daniel et al. [12] conducted a numerical study, comparing the thermal performance between the evacuated parabolic trough receiver and the non-evacuated receiver. And they found that the heat loss for the evacuated receiver was around 100Wm^{-2}, much less than that associated with the non-evacuated receiver, which was approximately 500Wm^{-2}.

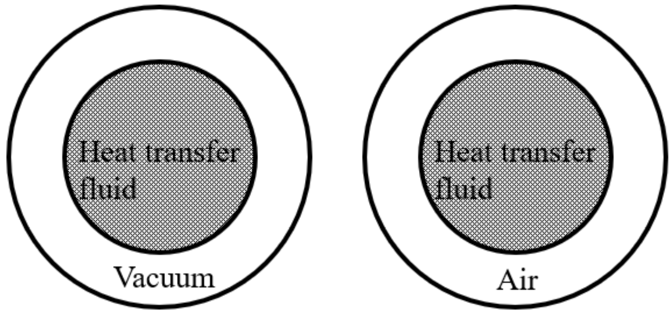

(a) Evacuated receiver (b) Non-evacuated receiver

Figure 2. 7. Schematic of (a) evacuated receiver and (b) non-evacuated receiver; redrawn based on Ref [12]

Park and Gharib [13] experimentally investigated the heat convection from a cylinder. With an oscillating mechanism, the cylinder was forced to vibrate in a sinusoidal motion with frequency of 0 to 14Hz, corresponding to a Strouhal number ranged from 0 to 1 based on the cylinder diameter and freestream velocity. According to their results, a peak value of heat convection was observed near a Strouhal number of around 0.21, corresponding to the synchronization of mechanical oscillations with the vortex shedding.

2.2.2 Passive Methods

As mentioned above, a significant drawback of the active cooling approach is the necessity of external power. Other than higher initial costs, more maintenance is also required because of the added complexity. For this reason, the simple passive approach is often preferred. Among others, employing an appropriate turbulence generator is a promising and simple approach for improving heat convection. Accordingly, it has drawn significant attention in recent years. We will focus on the passive methods for the remaining of the chapter.

2.3 Turbulence Generators

2.3.1 Rigid Type Turbulence Generator

Turbulence generators including grid, rib, cylinder, winglet and wing have been proposed and studied in an effort to boost the heat transfer rate. In this section, the rigid type is introduced first, and the flexible ones follow thereafter.

2.3.1.1 Grid

Grids are widely employed in many engineering applications, for reducing low frequency noise [14], improving the turbulent combustion rate [15], and augmenting the heat transfer. An experimental study of heat transfer enhancement of a cylinder via different types of grids was developed by Melina et al. [16]. In this study, a regular square-mesh bi-planar grid, a fractal-square grid and a single-square grid were examined, the blockage ratio of the grids were 32%, 25%, and 20% respectively. According to their results, the fractal square grid showed superior performance, which provided a higher heat transfer rate from the cylinder in the turbulence production region than that of the single square grid, despite the turbulence intensity being lower. At a larger downstream distance in the decay region, the heat transfer is similar for the fractal square grid and the single square grid, and both are higher than that of the regular square-mesh bi-planar grid. In their other study [17], eleven different grids, including the regular grid, the fractal square grid and the single-square grid used in the previous study, were investigated for their effectiveness in heat transfer enhancement of a flat plate. A new type of grid, multi-scale inhomogeneous grids, were also considered, noting that all the grids have the same blockage ratio of 28%. Their results demonstrated that the multi-scale inhomogeneous grid led to the most effective overall heat transfer rate, furthering the heat transfer performance by around 20% in the near-grid region, compared to the no-grid case. However, due to the dissipative nature of turbulence, the heat transfer augmentation dropped to only 10% farther downstream. Based on curve-fittings, the effect of the turbulence intensity on the flat plate heat transfer was identified, and a relation of $St/St_{\infty}=0.02u'/U$ was concluded, where St/St_{∞} denotes the convective heat transfer enhancement and u'/U is the streamwise turbulence intensity.

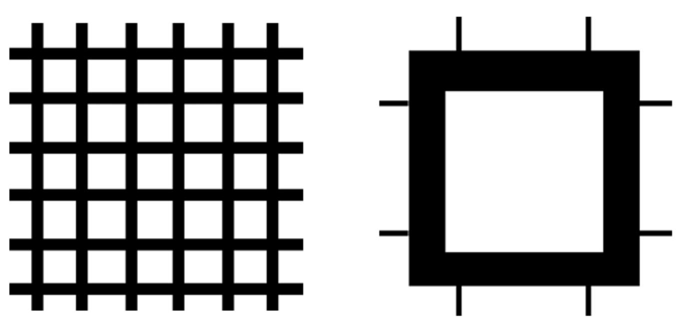

(a) regular grid (b) single square grid

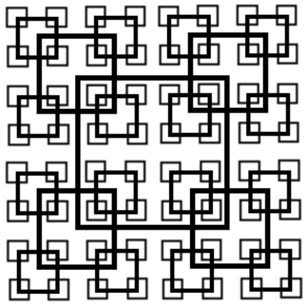

(c) fractal-square grid

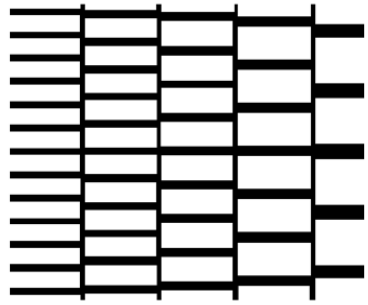

(d) multi-scale inhomogeneous grid

Figure 2. 8. Sketches of turbulence-generating grids (a) regular grid (b) single-square grid (c) fractal-square grid (d) multi-scale inhomogeneous grid; redrawn based on Ref [16] [17].

2.3.1.2 Rib and Cylinder

To further heat transfer rate, larger organized vortical flow structures are considered in addition to the rapidly dissipating turbulence. As these secondary swirling structures move across the heated surface, they enhance the mixing of the cooler freestream with the hotter fluid near the heated surface, further enhancing the heat convection. These vortices could be divided into two main categories: transverse and longitudinal vortex, where the rotation axis is closely perpendicular to and aligned with, respectively, the freestream direction. Among others, ribs and cylinders are common transverse vortex generators that are widely developed and utilized in many engineering applications due to their structural simplicity. A summary of studies using ribs are presented in Table 2.1. The studies of grid are also included in the table for comparison. It is interesting to note that the introduction of organized vortical flow structures seems to have a significant impact on the heat transfer, boosting the maximum relative heat transfer enhancement from 20%, induced by an inhomogeneous grid [17], to as high as 120%, provided by the crescent rib [21].

Table 2. 1. Summary of grids and ribs

Authors	Classification			Remarks		
	Flexibility	Type	Advantages	Studied case	Best condition for heat transfer	Relative maximal heat transfer enhancement (compared to the reference case)
Melina et al. [16][17]	Rigid	Grid	Turbulence is induced, enhancing heat and mass transporting	Regular square-mesh bi-planar grid, fractal-square grid, a single-square grid and multi-scale inhomogeneous grids	Multi-scale inhomogeneous grids	20%
Yang et al. [18]	Rigid	Rib	Transverse vortex structures are induced in addition to the dissipative turbulence, furthering heat transfer enhancement	Attack angle from 15° to 75°	60°	80%
Changcharoen and Eiamsa-ard [19]	Rigid	Rib		Detached-clearance ratio from 0 to 0.4	0.1	75%
Tanda [20]	Rigid	Rib		Pitch-to-height ratios, 6.66, 10, 13.33 and 20	13.33	45%
Xie et al. [21]	Rigid	Rib		Straight rib and the crescent rib	The crescent rib concave to the streamwise direction (longitudinal vortex occurs)	120%

Yang et al. [18] investigated the influence of a square cylinder attack angle on heat transfer enhancement from a surrogate PV panel; see Fig. 2.9. The attack angle from 15° to 75° with 15° increment was scrutinized at a wind velocity of 5 m/s, a Reynolds number, based on the width of the square wire, of around 1300. They found that the cylinder with a 60° attack angle provided the highest heat transfer augmentation, with a maximum normalized Nusselt number of around 1.8, due to it generating the strongest turbulence intensity. This equates a 2.8% gain in the harnessed power output.

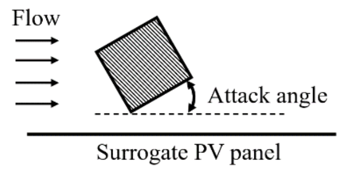

Figure 2. 9. Attack angle of square cylinder; redrawn based on Ref [18].

Changcharoen and Eiamsa-ard [19] conducted a numerical investigation of heat transfer in a channel with attached/detached rib arrays; see Fig. 2.10. They found that the detached-clearance ratio of 0 (attached rib), 0.1, 0.2, 0.3, and 0.4 were able to improve the average heat transfer rates by around 60%, 75%, 71%, 64%, and 56%, respectively. In addition to the turbulence intensity, a significant correlation between the flow recirculation (transverse vortex) and the heat transfer was found. With the detached-clearance ratio increased from 0.1 to 0.4, a decreasing trend of the heat transfer enhancement was clear, which was observed to be directly related to the reduction of the recirculation size.

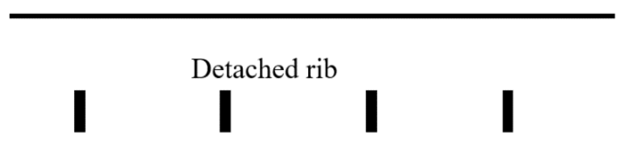

Figure 2. 10. Detached rib in the channel; redrawn based on Ref [19].

Tanda [20] experimentally explored heat convection in a rectangular channel with an angled rib turbulator; see Fig. 2.11. Four different pitch-to-height ratios, 6.66, 10, 13.33 and 20, were investigated. Among the studied conditions, the best heat transfer performance was obtained at a pitch-to-height ratio of 13.33 for the one-ribbed wall channel, providing a heat transfer augmentation as high as 1.45. For the two-ribbed wall channel, the optimal pitch-to-height ratio was found to be 10, which induced a maximal heat transfer enhancement of around 1.2.

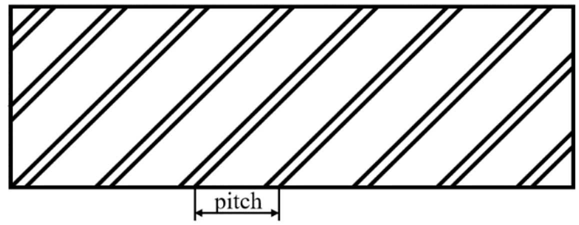

Figure 2. 11. Ribbed surface; redrawn based on Ref [20].

In addition to the conventional straight square rib, some new types of ribs have also been proposed for furthering the heat transfer rate. Xie et al. [21] explored the turbulent flow characteristics and the heat transfer enhancement in a channel with crescent ribs; see Fig. 2.12. The straight rib, the crescent rib concave to the streamwise direction, and the crescent rib convex to the streamwise direction were investigated. The crescent rib was able to generate longitudinal vortices, intensifying the flow mixing, increasing the turbulent kinetic energy, and reducing the boundary layer thickness. In summary, the crescent rib concave to the streamwise direction provided the best thermal performance, providing a normalized Nusselt number as high as 2.2, around 21-40% higher than that of the straight ribbed channel, along with an inevitably higher pressure drop of around 15-80%.

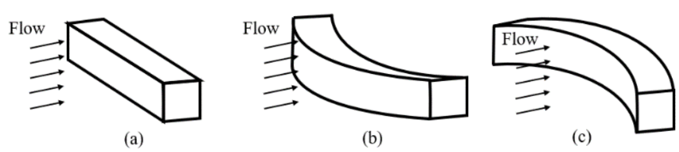

Figure 2. 12. Schematic of (a) straight rib (b) crescent rib concave to the streamwise direction (c) crescent rib convex to the streamwise direction; redrawn based on Ref [21].

2.3.1.3 Winglet and Wing

As mention in Ref [21], longitudinal vortices tend to enhance heat transfer more effectively. These longitudinal vortical streets can drastically outlast the turbulence created by the more conventional turbulence generators such as grids and ribs. Among many others, winglets and wings, such as those shown in Fig. 2.13, are commonly used as longitudinal vortex promoters for the heat transfer enhancement [22]. Table 2.2 presents a brief summary of winglets and wings. Discussion of each of these studies will follow accordingly.

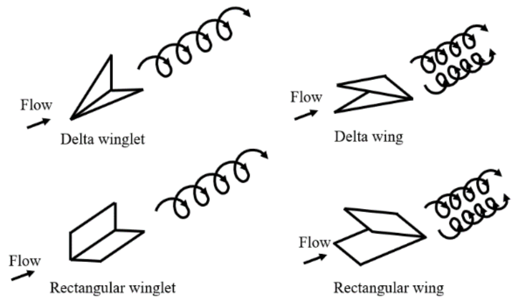

Figure 2. 13. Winglets and wings; redrawn based on Ref [22].

Table 2. 2. Summary of winglets and wings

Authors	Classification			Remarks		
	Flexibility	Type	Advantages	Studied case	Best condition for heat transfer	Relative maximal heat transfer enhancement (compared to the reference case if there is no specific mention)
Wu et al. [23]	Rigid	Winglet	More effective and long-lasting longitudinal vortices are generated, which can drastically outlast the turbulence over the whole heated surface	Attack angle from 30° to 60°	60°	100%
Abdollahi and Shams [24]	Rigid	Winglet		Attack angle from 15° to 90°	45°	8% higher than that at 15°
Khanjian et al. [25]	Rigid	Winglet		Roll angle from 20° to 90°	90°	60%
Li et al. [26]	Rigid	Winglet		Arrangements	Common-flow-up arrangement with vertical edge being the trailing edge	22%
Promvonge et al. [27]	Rigid	Winglet		Relative heights RB from 0.1 to 0.2 Relative pitches RP from 0.5 to 2	RB=0.2 and RP=0.5	380%
Pourhedayat et al. [28]	Rigid	Winglet		Transversal distance from 0 to 40 mm, tube diameter=47 mm	20 mm	140%

Table 2.2. Summary of winglets and wings (continued)

Authors	Classification			Remarks		
	Flexibility	Type	Advantages	Studied case	Best condition for heat transfer	Relative maximal heat transfer enhancement (compared to the reference case if there is no specific mention)
Gholami et al. [29]	Rigid	Winglet	More effective and long-lasting longitudinal vortices are generated, which can drastically outlast the turbulence over the whole heated surface	Wavy and flat winglet	Wavy winglet	58%
Oneissi et al. [30][31]	Rigid	Winglet		Inclined projected winglet with protrusion and conventional delta winglet	Inclined projected winglet with protrusion	7.1% compared to the conventional delta winglet
Haik et al. [32]	Rigid	Winglet		Curved and flat winglets	Concave-curved winglet with 75° arc angle	22%
Biswas et al. [33]	Rigid	Winglet & Wing		Winglet & Wing	Wing	34%
Sheikhzadeh et al. [34]	Rigid	Wing		The rectangular, triangle and trapezoid wing	Rectangular wing	13% and 30% higher than those of trapezoidal and triangular wings

Wu et al. [23] experimentally investigated the effect of delta winglet attack angle on the heat transfer from a flat surface as depicted in Fig. 2.14. The single delta winglet was positioned on a heated surface, under a Reynolds number based on winglet height of 6000. The attack angle of winglet was 30°, 45°, and 60° with respect to the streamwise direction. According to their results, a heat transfer augmentation region was obtained downstream of the winglet, due to the scooping motions of the longitudinal vortices, turbulence fluctuation and the thinning of boundary layer. With attack angle increases from 30° to 60°, the maximum heat transfer enhancement increases from around 1.5 to 2.0. They pointed out that, in addition to the turbulent kinetic energy, the secondary flow motion also significantly influences the heat transfer enhancement -- the larger velocity toward the heated surface, the better heat transfer performance. The near-surface streamwise velocity was found to have a moderate effect, while the influence of the boundary layer thickness was marginal.

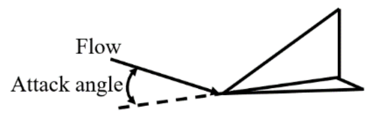

Figure 2. 14. Attack angle of delta winglet; redrawn based on Ref [23].

The optimization of shape and attack angle of the winglet was developed by Abdollahi and Shams [24]. Rectangular, trapezoidal and delta winglets were employed in this research, with attack angle of 15°, 30°, 45°, 60° and 90°. The Reynolds number based on the hydraulic diameter of the channel was varied from 117 to 467. Their results showed that the rectangular winglet provided the best heat transfer augmentation, followed by the trapezoidal winglet and then, delta winglet. Further, when the Reynolds is low, the heat transfer was observed to be insensitive to the attack angle. But at a higher Reynolds number of 467, the attack angle showed a significant effect, with average Nusselt number of around 13.5 at 45°, approximately 8% higher than that at 15°. It was also mentioned in the study that, the longitudinal vortical motions induced by the winglets resulted in a higher fluid mixing between the cold freestream fluid and the hot fluid near the heated surface, and thus, significantly increased the heat transfer rate.

The effect of roll angles of rectangular winglets, ranging from 20° to 90°, was investigated by Khanjian et al. [25]. The attack angle in this study was maintained at 30°, and the Reynolds number based on the channel hydraulic diameter of 456 and 911 were selected. They concluded that the heat transfer improved with the increase of the roll angle, but so does the pressure drop. The global Nusselt number of around 11 was obtained at 20° roll angle and a Reynolds number of 911. The Nusselt number increased to approximately 16 when the roll angle increased to 90°, due to the stronger vortices, with a 12 times higher helicity peak value than that of 20° roll-angle winglet. If the pressure drop was also considered, the overall thermal enhancement factor reached a maximum value of 1.32 for a 70° roll angle.

Also worth mentioning is a numerical investigation by Li et al. [26]. Four different arrangements of the delta winglet pairs in a jacket were explored, including common-flow-down with vertical edge being the trailing edge (CFD-V), common-flow-up with vertical edge being the trailing edge (CFU-V), common-flow-down with inclined edge being the trailing edge (CFD-I) and common-flow-up with inclined edge being the trailing edge (CFU-I); see Fig. 2.15. According to their results, the common-flow-up configuration provided better heat transfer than that of the common-flow-down arrangement for Reynolds number based on pipe diameter from 4000 to 18000. Overall, the CFU-V had the superior heat transfer performance due to the stronger, larger-scale and slower-dissipative vortices, providing an average Nusselt number enhancement up to approximately 22%, compared to the smooth jacket in the absence of winglets.

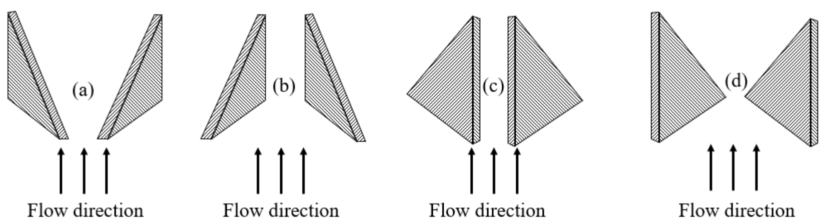

Figure 2. 15. The arrangement of the delta winglet pair (a) Common-flow-down with vertical edge being the trailing edge (b) Common-flow-up with vertical edge being the trailing edge (c) Common-flow-down with inclined edge being the trailing edge (d) Common-flow-up with inclined edge being the trailing edge; redrawn based on Ref [26].

Promvonge et al. [27] conducted an experimental and numerical investigation on heat transfer enhancement in a tube with rectangular winglet, as portrayed in Fig. 2.16, aiming at optimizing the height, pitch and arrangement of the winglet. The Reynolds number was varied from 4200 to 25800. Two arrangements of winglets are introduced, i.e., V-tip pointing upstream and downstream, with three relative heights RB (winglet height / tube diameter = 0.1, 0.15 and 0.2) and four different relative pitches RP (longitudinal pitch of winglets / tube diameter = 0.5, 1.0, 1.5 and 2.0). They concluded that the larger height and smaller pitch resulted in a higher Nusselt number as well as friction factor. The winglet with RB=0.2 and RP=0.5 increased the maximum Nusselt number and friction factor by about 3.8 times and 18.8 times, respectively. The best overall thermal performance enhancement factor was obtained at RB=0.15 and RP=1.0, up to 1.99 and 2.02 for the V-tip pointing upstream and downstream, respectively. They also postulated that the key reason for the heat transfer enhancement was the impinging jets on the heated surface induced by the secondary flow motion.

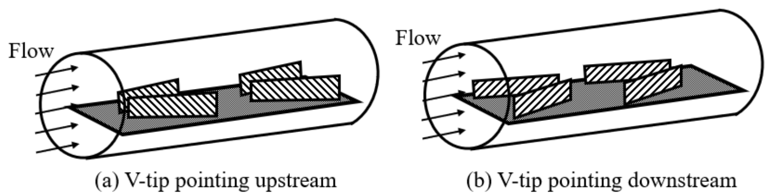

Figure 2. 16. Winglet arrangement (a) V-tip pointing upstream (b) V-tip pointing downstream; redrawn based on Ref [27].

In another numerical study, a novel arrangement of the delta winglet was proposed by Pourhedayat et al. [28]. In this study, the winglets were placed on both sides of the plate, Fig. 2.17, furthering the heat transfer augmentation through a 47-mm-diameter tube. The backward and forward configurations were analyzed in this study. In addition, the transversal distance of the winglets were also investigated. Their results pointed out that the forward configuration resulted in a higher heat transfer rate than that of the backward configuration. Moreover, smaller longitudinal pitch provided a stronger heat transfer rate, which is in agreement with Ref [27]. Concerning the effect of transversal pitch, it is found that the winglet should not be placed very close to the wall or the center of the tube. The winglet with a transversal distance of 20 mm induced the best heat transfer performance. This was attributed to the best fluid mixing condition in the cross-section of the tube, providing a heat transfer enhancement of around 2.4, compared to the reference case without the winglet at a Reynolds number of 12000.

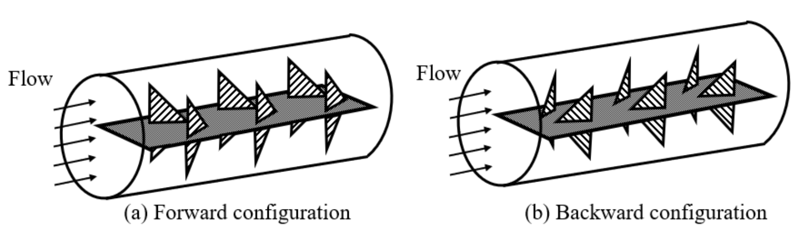

Figure 2. 17. Partial view of the delta winglet in the tube (a) forward configuration (b) backward configuration; redrawn based on Ref [28].

Besides the conventional delta and rectangular winglet, some additional innovative winglet designs were also developed to further enhance the heat convection. For example, Gholami et al. [29] explored the effect of wavy rectangular winglet on the heat transfer of a fin-and-tube compact heat exchanger. The winglets were positioned behind the tube, with an attack angle of 30°, see Fig. 2.18, for a Reynolds number ranging from 400 to 800. The wavy-down winglet, wavy-up winglet, convectional flat rectangular winglet, and the reference case without any winglet were investigated. They concluded that the wavy-down winglet and the wavy-up winglet could further decrease the stationary wake region behind the tube compared to the flat winglet, and thus, a better Nusselt number could be obtained. Among their studied cases, the wavy-up winglet provided the most effective heat transfer, with Nusselt number of around 15.0. And the Nusselt number for wavy-down winglet, flat winglet and the reference case are around, 14.5, 13.5 and 9.5 respectively.

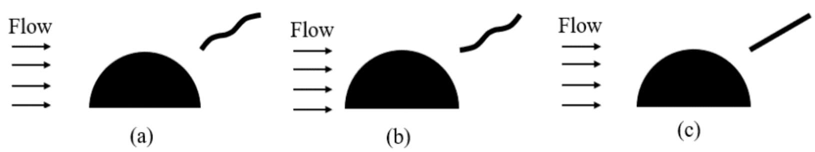

Figure 2. 18. Winglets in the heat exchanger (a) wavy-down winglet (b) wavy-up winglet (c) convectional flat winglet; redrawn based on Ref [29].

Oneissi et al. [30] proposed a different winglet, calling it an inclined projected winglet. The inclined angle, shown in Fig. 2.19, was varied from 25° to 60° to investigate its effect on the heat transfer enhancement and the pressure drop in a channel. The Reynolds number was varied from 270 to 30000. It was found that the delta winglet with 30°~35° inclined angle had a superior overall heat transfer performance, providing a small increase of 3.1% in average Nusselt number and a significant decrease of 55% in friction factor, compared to the conventional delta winglet. This has been attributed to the 35.5% higher intensification of vortex. In their other study [31], the inclined projected winglet with protrusions was explored, Fig. 2.20, aiming at furthering the heat transfer enhancement. The 30° inclined projected winglet was employed in this study, and the semi-sphere protrusion was located downstream of the winglet. According to their results, the inclined projected winglet could provide an overall thermal enhancement of around 4.8% and the protrusion could further boost the heat transfer improvement to 7.1%, compared to the conventional delta winglet. The further enhancement was because the protrusions were able to generate two additional small vortex structures near the wall.

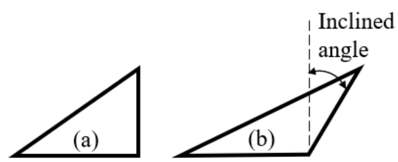

Figure 2. 19. Schematic of winglet (a) conventional delta winglet (b) inclined delta winglet; redrawn based on Ref [30].

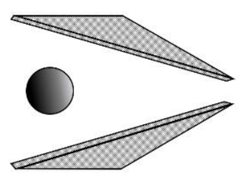

Figure 2. 20. Schematic of winglet with protrusion; redrawn based on Ref [31].

Haik et al. [32] conducted a numerical study, demonstrating the heat transfer enhancement in a channel with the curved rectangular winglet. The concavely and convexly curved winglets, see Fig. 2.21, with arc angle ranging from 15° to 75°, were investigated at a Reynolds number, based on the height of the channel, of 3000. Their results showed that the concave-curved winglet induced more disruption in boundary layer growth and fluid mixing, due to the wider horseshoe vortices and the higher strength of longitudinal vortices. These resulted in higher heat transfer rate as well as higher pressure loss. In summary, the maximum heat transfer rate was obtained when using the concave-curved winglet with a 75° arc angle, about 3% and 22% higher than those of the flat winglet case and the reference case in absence of the winglet, respectively.

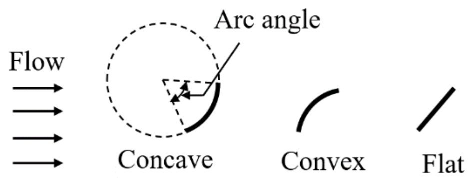

Figure 2. 21. Schematic of the curve winglet; redrawn based on Ref [32].

Compared to the winglet type turbulence generators, the wing type seemed to provide a larger heat transfer enhancement, together with a higher pressure drop penalty. Biswas et al. [33] studied the flow and heat transfer characteristics in a rectangular channel with a delta wing and a pair of delta winglets. They found that, both wing and winglet could induce long-lasting longitudinal vortices. The fluid was swirling as it moved downstream, promoting the mixing of the cooler stream of the vortex core with the hotter fluid near the channel wall, and thus, augmenting the heat transfer rate. In addition, the delta wing generated stronger vortices and therefore provided a better heat transfer improvement compared to the winglet pair. The Nusselt number and friction coefficient at the exit of the channel with the delta wing was around 34% and 79% more than that of the reference clean channel, respectively. The corresponding values for the winglet pair were around 14% and 65%, respectively.

In another numerical study, the effects of the shape of the wings on heat transfer and friction factor were investigated at a Reynolds number of 200 to 1600 by Sheikhzadeh et al. [34]. Three types of wings, rectangular, triangular and trapezoidal wings as sketched in Fig. 2.22, were studied. From the perspective of heat transfer enhancement, the rectangular wings seemed to have a better effect compared to the triangle and the trapezoid wing. The average Nusselt number induced by the rectangular wings was around 130 at a Reynolds number of 1600, approximately 13% and 30% higher than those of trapezoidal and triangular wings. The rectangular wings also induced a higher friction factor of around 0.8 at a Reynolds number of 1600, followed by the trapezoidal and the triangular wings, which was 0.5 and 0.3, respectively.

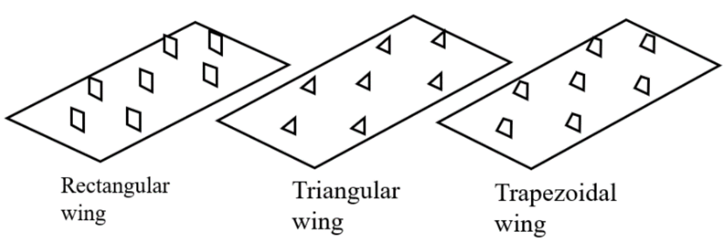

Figure 2. 22. Schematic of rectangular, triangular, and trapezoidal wing; redrawn based on Ref [34].

2.3.2 Flexible Type Turbulence Generator

Allowing the turbulence generators to vibrate when induced by the incoming flow adds another dimension, i.e., the possibility of harmonizing a portion of the swirling vortex street into furthering heat transfer augmentation. From the selected studies [35-40], listed in Table 2.3, it is clear that flexible turbulence generators could provide better heat transfer performance, compared to their rigid counterpart. Discussion of these studies will follow.

Table 2. 3. Summary of flexible turbulence generators

Authors	Classification			Remarks		
	Flexibility	Type	Advantages	Studied case	Best condition for heat transfer	Relative maximal heat transfer enhancement (compared to the reference case if there is no specific mention)
Ali et al. [35][36]	Flexible	2D-plate	Flow induced vibration occurs, enhancing the mixing process, and thus, further improving the heat transfer augmentation	Number of flexible vortex generators (two, three, four)	Four flexible vortex generators	275%
Ali et al. [37]	Flexible	Wing		Flexible and rigid wing	Flexible wing	118%
Shi et al. [38]	Flexible	2D-plate		The cylinder with the flexible/rigid plate	The cylinder with the flexible plate	90%
Shi et al. [39]	Flexible	2D-cylinder		Flexible/rigid cylinder	Flexible cylinder	235%
Sun et al. [40]	Flexible	2D-plate		The cylinder with the flexible/rigid plate	The cylinder with the flexible plate	11% higher than that of the cylinder with a rigid plate

A numerical investigation of the heat transfer enhancement induced by a few flexible turbulence generators was conducted by Ali et al. [35]. These flexible vortex generators fixed at the channel wall, as shown in Fig. 2.23, were free to vibrate when induced by the incoming flow at a Reynolds number of 1000 and 1850. It was found that the flexible vortex generator provided a better mixture quality, a function of local concentration value, indicating the fraction of fluid from the lower part of the domain mixed in the upper part, or vice versa. As high as 98% increase of mixture quality and 134% increase of overall heat transfer rate was observed compared to their rigid counterparts. Subsequently, they conducted another numerical study, investigating the flow pattern and the heat transfer with different numbers of flexible vortex generators in a channel [36]. They found that an increase in the number of flexible vortex generators could produce a lock-in state between the flow and the vortex generators, inducing a larger motion amplitude and greatly improving fluid mixing and heat transfer. Compared to the reference empty channel, the two, three, and four flexible vortex generators could improve the overall heat transfer by 174%, 250% and 275%, respectively.

In another study by Ali et al. [37], a three-dimensional numerical investigation was executed. The flexible trapezoidal vortex generators and their rigid counterparts were employed in a circular pipe at a Reynolds number of 1500; see Fig. 2.24. They found that the vortex generator which was free to oscillate could enhance the overall heat transfer by approximately 118% compared to the reference empty pipe, while the rigid type only produced a 97% heat transfer augmentation. For the rigid case, an overheated area could be observed behind the turbulence generator, as the heat stayed trapped in the stagnant wake region and could only be transported by diffusion. The presence of the oscillation was observed to have a significant impact on the wake, eliminating the overheated region behind the turbulence generators. Instead of being trapped like that in the rigid case, the vortices in the wake region of the flexible type were convected downstream, which played an important role in the thermal energy transporting.

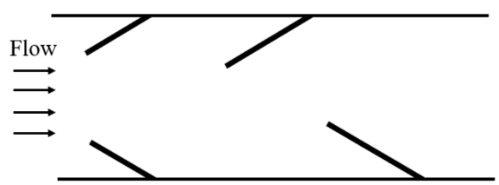

Figure 2. 23. Schematic of flexible turbulence generators in the channel; redrawn based on Ref [35].

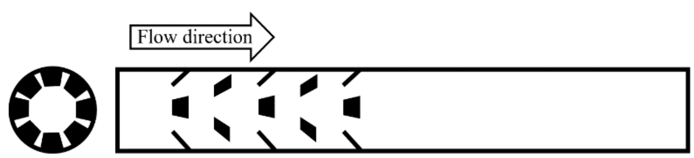

Figure 2. 24. Schematic of flexible trapezoidal turbulence generators in a circular pipe; redrawn based on Ref [37].

Shi et al. [38] numerical investigated the heat transfer augmentation of a channel with vortex induced vibration. A stationary cylinder with a flexible plate was studied, compared to a cylinder with a rigid plate and a cylinder without the plate, as depicted in Fig. 2.25. The studied Reynolds number based on the diameter of the cylinder ranged from 204 to 327. Their results showed that the flow structure interaction induced by the cylinder with flexible plate could provide the stronger and closer-to-wall vortices, and thus, further disrupt the thermal boundary layer and improve the mixing process. The cylinder without the plate, and the cylinder with the rigid plate could enhance the Nusselt number by around 57% and 24%, respectively, with respect to the reference empty channel. The cylinder with the flexible plate further improved the heat transfer rate, boosting the enhancement up to 90%. In their other study, a flexible cylinder was developed for Reynolds number between 84 and 168 [39]. The vortex shedding from the cylinder induced the cylinder to vibrate periodically. This vibration caused the vortex cores to move closer to the wall and strengthened the vortex intensity. Thus, a better heat transfer augmentation was observed. Based on their study, the channel with the flexible cylinder provided an enhancement of around 235% and 51% in Nusselt number with respect to the reference clean channel and the channel with a stationary cylinder, respectively.

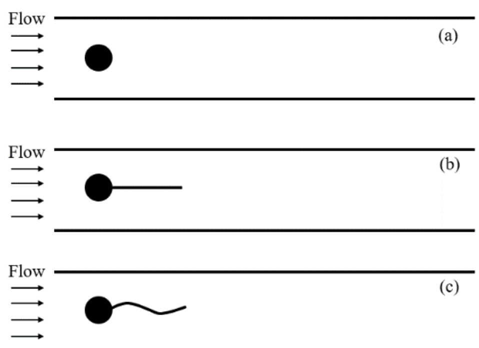

Figure 2. 25. Schematic of a channel with (a) cylinder without the plate (b) cylinder with a rigid plate (c) cylinder with a flexible plate; redrawn based on Ref [38].

Sun et al. [40] conducted a numerical study on the effect of a flexible plate on the heat transfer from a circular cylinder; see Fig. 2.26. The Reynolds number was maintained at 200. The elastic modulus of the flexible plate ranged from 104 to 5×10^5. Their results showed that a large-amplitude vibration occurred when the vortex shedding frequency approached the natural frequency of the flexible plate. Thus, the ‘dead water’ region behind the cylinder was reduced, leading to a 11% heat transfer enhancement compared to the cylinder with a rigid plate.

Figure 2. 26. ‘Dead water’ region behind the (a) cylinder with rigid plate and (b) cylinder with flexible plate; redrawn based on Ref [40].

2.4 Conclusions

Augmenting heat transfer rate can improve the performance of many engineering systems and thus facilitate climate change mitigation. For example, heightening the heat transfer of a heat exchanger ultimately boosts the efficiency of the system invoking the heat exchanger. More solar energy can be harnessed by a PV panel by lowering its temperature via augmented heat convection. Among plethora of approaches for boosting heat transfer, a turbulence generator that appropriately disturbs the flow is appealing due to its simplicity. Different types of turbulence generators and their effectiveness on the heat transfer enhancement were reviewed. The following conclusions can be drawn:

1. Turbulence intensity appears to be the most important parameter in convection heat transfer enhancement.

2. Swirling flow motions that promote mixing of freestream fluid with the near-surface fluid are effective in augmenting heat transfer.

3. Vibrations of the passive turbulence generators can lead to additional heat transfer augmentation.

4. Appropriate geometrical design can be implemented to reduce stagnant fluid, such as that in the wake region behind a heat exchanger tube, and hence, augment heat transfer.

5. Marrying the long-lasting swirling flow with the fluid-induced vibration seems to provide a significant potential in maximizing the heat convection augmentation.

References

[1] International Energy Agency, “Technology Roadmap: Solar Photovoltaic Energy,” 2014.

[2] S. Kalogirou, Solar Energy Engineering: Processes and Systems, Second Edition. Academic Press, UK, 2014.

[3] M. Hemmat Esfe, M. H. Kamyab, and M. Valadkhani, “Application of nanofluids and fluids in photovoltaic thermal system: An updated review,” Sol. Energy, vol. 199, pp. 796–818, 2020.

[4] S. Liu and M. Sakr, “A comprehensive review on passive heat transfer enhancements in pipe exchangers,” Renew. Sustain. Energy Rev., vol. 19, pp. 64–81, 2013.

[5] S. Nižetić, D. Čoko, A. Yadav, and F. Grubišić-Čabo, “Water spray cooling technique applied on a photovoltaic panel: The performance response,” Energy Convers. Manag., vol. 108, pp. 287–296, 2016.

[6] S. Kianifard, M. Zamen, and A. A. Nejad, “Modeling, designing and fabrication of a novel PV/T cooling system using half pipe,” J. Clean. Prod., vol. 253, p. 119972, 2020.

[7] Y. Chen, A.K. Athienitis, K. Galal, “Modeling, design and thermal performance of a BIPV/T system thermally coupled with a ventilated concrete slab in a low energy solar house: Part 1, BIPV/T system and house energy concept,” Solar Energy, vol. 84, pp. 1892-1907, 2010.

[8] T. Rajaseenivasan, S.R. Prasanth, M.S. Antony, K. Srithar, “Experimental investigation on the performance of an impinging jet solar heater,” Alexandria Engineering Journal, vol. 56, pp. 63-69, 2017

[9] C. M. Hsu, W. C. Jhan, and Y. Y. Chang, “Flow and heat transfer characteristics of a pulsed jet impinging on a flat plate,” Heat Mass Transf. und Stoffuebertragung, vol. 56, no. 1, pp. 143–160, 2020

[10] M. Setareh, M. Saffar-Avval, and A. Abdullah, “Experimental and numerical study on heat transfer enhancement using ultrasonic vibration in a double-pipe heat exchanger,” Appl. Therm. Eng., vol. 159, pp. 113867, 2019.

[11] M. Roesle, V. Coskun, A. Steinfeld, “Numerical analysis of heat loss from a parabolic trough absorber tube with active vacuum system,” Journal of Solar Energy Engineering, vol. 133, pp. 031015, 2011.

[12] P. Daniel, Y. Joshi, A.K. Das, “Numerical investigation of parabolic trough receiver performance with outer vacuum shell,” Solar Energy, vol. 85, pp. 1910-1914, 2011.

[13] H.G. Park, M. Gharib, “Experimental study of heat convection from stationary and oscillating circular cylinder in cross flow,” Journal of Heat Transfer, vol, 123, pp. 51-62, 2001

[14] J. Nedić, B. Ganapathisubramani, J. C. Vassilicos, J. Borée, L. E. Brizzi, and A. Spohn, “Aeroacoustic performance of fractal spoilers,” AIAA J., vol. 50, no. 12, pp. 2695–2710, 2012.

[15] D. S.-K. Ting and M. D. Checkel, “The importance of turbulence intensity, eddy size and flame size in spark ignited, premixed flame growth,” Proc. Inst. Mech. Eng. Part D J. Automob. Eng., vol. 211, no. 1, pp. 83–86, 1997.

[16] G. Melina, P. J. K. Bruce, G. F. Hewitt, and J. C. Vassilicos, “Heat transfer in production and decay regions of grid-generated turbulence,” Int. J. Heat Mass Transf., vol. 109, pp. 537–554, 2017.

[17] G. Melina, P. J. K. Bruce, J. Nedić, S. Tavoularis, and J. C. Vassilicos, “Heat transfer from a flat plate in inhomogeneous regions of grid-generated turbulence,” Int. J. Heat Mass Transf., vol. 123, pp. 1068–1086, 2018.

[18] Y. Yang, A. Ahmed, D. S.-K. Ting, and S. Ray, “The Influence of Square Wire Attack Angle on the Heat Convection from a Surrogate PV Panel,” in The Energy Mix for Sustaining Our Future, Springer, pp. 103–128, 2018.

[19] W. Changcharoen and S. Eiamsa-ard, “Numerical investigation of turbulent heat transfer in channels with detached rib-arrays,” Heat Transf. - Asian Res., vol. 40, no. 5, pp. 431–447, 2011.

[20] G. Tanda, “Effect of rib spacing on heat transfer and friction in a rectangular channel with 45° angled rib turbulators on one/two walls,” Int. J. Heat Mass Transf., vol. 54, no. 5–6, pp. 1081–1090, 2011.

[21] G. Xie, X. Liu, H. Yan, and J. Qin, “Turbulent flow characteristics and heat transfer enhancement in a square channel with various crescent ribs on one wall,” Int. J. Heat Mass Transf., vol. 115, pp. 283–295, 2017.

[22] L. Chai and S. A. Tassou, “A review of airside heat transfer augmentation with vortex generators on heat transfer surface,” Energies, vol. 11, p. 2737, 2018.

[23] H. Wu, D. S.-K. Ting, and S. Ray, "The effect of delta winglet attack angle on the heat transfer performance of a flat surface," Int. J. Heat Mass Transf., vol. 120, pp. 117–126, 2018.

[24] A. Abdollahi and M. Shams, "Optimization of shape and angle of attack of winglet vortex generator in a rectangular channel for heat transfer enhancement," Appl. Therm. Eng., vol. 81, pp. 376–387, 2015.

[25] A. Khanjian, C. Habchi, S. Russeil, D. Bougeard, and T. Lemenand, "Effect of rectangular winglet pair roll angle on the heat transfer enhancement in laminar channel flow," Int. J. Therm. Sci., vol. 114, pp. 1–14, 2017.

[26] Y. X. Li, X. Wang, J. Zhang, L. Zhang, and J. H. Wu, "Comparison and analysis of the arrangement of delta winglet pair vortex generators in a half coiled jacket for heat transfer enhancement," Int. J. Heat Mass Transf., vol. 129, pp. 287–298, 2019.

[27] P. Promvonge, P. Promthaisong, and S. Skullong, "Experimental and numerical heat transfer study of turbulent tube flow through discrete V-winglets," Int. J. Heat Mass Transf., vol. 151, p. 119351, 2020.

[28] S. Pourhedayat, S. M. Pesteei, H. E. Ghalinghie, M. Hashemian, and M. A. Ashraf, "Thermal-exergetic behavior of triangular vortex generators through the cylindrical tubes," Int. J. Heat Mass Transf., vol. 151, 2020.

[29] A. A. Gholami, M. A. Wahid, and H. A. Mohammed, "Heat transfer enhancement and pressure drop for fin-and-tube compact heat exchangers with wavy rectangular winglet-type vortex generators," Int. Commun. Heat Mass Transf., vol. 54, pp. 132–140, 2014.

[30] M. Oneissi, C. Habchi, S. Russeil, D. Bougeard, and T. Lemenand, "Inclination angle optimization for 'inclined projected winglet pair' vortex generator," J. Therm. Sci. Eng. Appl., vol. 11, no. 1, pp. 1–10, 2019.

[31] M. Oneissi, C. Habchi, S. Russeil, T. Lemenand, and D. Bougeard, "Heat transfer enhancement of inclined projected winglet pair vortex generators with protrusions," Int. J. Therm. Sci., vol. 134, pp. 541–551, 2018.

[32] H. Naik, S. Harikrishnan, and S. Tiwari, “Numerical investigations on heat transfer characteristics of curved rectangular winglet placed in a channel,” Int. J. Therm. Sci., vol. 129, 2017, pp. 489–503, 2018.

[33] G. Biswas, P. Deb, and S. Biswas, “Generation of longitudinal streamwise vortices—a device for improving heat exchanger design,” J. Heat Transfer, vol. 116, no. 3, pp. 588–597, 1994.

[34] G. A. Sheikhzadeh, F. N. Barzoki, A. A. A. Arani, and F. Pourfattah, “Wings shape effect on behavior of hybrid nanofluid inside a channel having vortex generator,” Heat Mass Transf. und Stoffuebertragung, vol. 55, no. 7, pp. 1969–1983, 2019.

[35] S. Ali, C. Habchi, S. Menanteau, T. Lemenand, and J.-L. Harion, “Heat transfer and mixing enhancement by free elastic flaps oscillation,” Int. J. Heat Mass Transf., vol. 85, pp. 250–264, 2015.

[36] S. Ali, S. Menanteau, C. Habchi, T. Lemenand, and J. L. Harion, “Heat transfer and mixing enhancement by using multiple freely oscillating flexible vortex generators,” Appl. Therm. Eng., vol. 105, pp. 276–289, 2016.

[37] S. Ali, C. Habchi, S. Menanteau, T. Lemenand, and J. L. Harion, “Three-dimensional numerical study of heat transfer and mixing enhancement in a circular pipe using self-sustained oscillating flexible vorticity generators,” Chem. Eng. Sci., vol. 162, pp. 152–174, 2017.

[38] J. Shi, J. Hu, S. R. Schafer, and C. L. Chen, “Numerical study of heat transfer enhancement of channel via vortex-induced vibration,” Appl. Therm. Eng., vol. 70, no. 1, pp. 838–845, 2014.

[39] J. Shi, J. Hu, S. R. Schafer, and C. C. L. Chen, “Heat transfer enhancement of channel flow via vortex-induced vibration of flexible cylinder,” Proceedings of the ASME 2014 4th Joint US-European Fluids Engineering Division Summer Meeting, pp. 1–8, 2014.

[40] X. Sun, Z. Ye, J. Li, K. Wen, and H. Tian, “Forced convection heat transfer from a circular cylinder with a flexible fin,” Int. J. Heat Mass Transf., vol. 128, pp. 319–334, 2019.

CHAPTER 3

CONVECTIVE HEAT TRANSFER ENHANCEMENT DOWNSTREAM OF A FLEXIBLE STRIP NORMAL TO THE FREESTREAM

Y. Yang, D. S-K. Ting, S. Ray, "Convective heat transfer enhancement downstream of a flexible strip normal to the freestream," International Journal of Thermal Sciences 145 (2019) 106059

3.1 Introduction

Augmenting heat transfer rate can improve the performance of many engineering systems – the most application being the heat exchanger. Traditionally, cylinders and ribs have been explored and utilized to enhance heat convection due to their structural simplicity. For example, Marumo et al. [1] placed a cylinder parallel to and near a heated plate to promote the heat convection rate. They found that leaving a small gap between the cylinder and the plate had a positive effect on the heat transfer performance. In another study, the end effect of truncated ribs was explored by Wang and Sundén [2]. They pointed out that the vortices induced by the end effect were able to sweep more cooling fluid to the hot wall, and thus, enhanced the heat transfer rate. Kamali and Binesh [3] investigated effects based on rib shape and concluded that trapezoidal shaped ribs could more effectively promote heat transfer rate. Ravi et al. [4] numerically investigated the heat transfer in a two-pass ribbed channel and found that V-shaped ribs provide maximum heat transfer enhancement in the first and second pass, while the M-shaped ribs resulted in the best thermal performance in the bend area(s).

In recent years, rectangular and delta winglets have become attractive because they have shown great promise for heat transfer augmentation by inducing a swirling motion in the downstream of the winglets, and disrupting the thermal boundary layer [5]. Qian et al. [6] studied the heat transfer in a fin-tube exchanger using rectangular winglets. They illustrated that the heat transfer in the wake region behind the tube was improved, resulting in a better overall thermal performance. In addition, different length winglets were compared in this study, which showed that longer length was beneficial to heat transfer performance, but at a larger cost of energy loss. Khanjian et al. [7] numerically studied the effect of rectangular winglet pair roll angle on heat transfer improvement and found that the heat transfer would be enhanced by increasing the roll angle value. Wijayanta et al. [8] experimentally examined the role of winglet attack angle and found that both Nusselt number and friction factor increased with its increase. Besides the more conventional rectangular and delta winglet, novel types of winglets were also developed to further promote the heat convection. For instance, Zhou and Feng [9] conducted an experimental study on curved winglets with perforation. They concluded that the curved type vortex generator had a better heat transfer enhancement than the corresponding plane winglet. In another study, the curved rectangular winglets were investigated in the fin-tube heat exchanger by Gong et al. [10]. Their results showed a significant heat transfer improvement in the wake region with curved rectangular winglets. Another novel design, named "inclined projected winglet", was explored by Oneissi et al. [11]. They found that the inclined projected winglet pair exhibited similar heat transfer performance as the delta winglet pair, but with lower pressure drop penalty.

In addition to the stationary turbulence generators, passive vibrating enhancers also have potential to further enhance the thermal performance [12]. Go et al. [13] conducted an experimental study on heat transfer using a vibrating microfin array. They found that as the vibrating deflection increased with freestream velocity, the heat transfer rate enhancement improved. In a different study, Shi et al. [14] detailed the effect of a vibrating cylinder on heat transfer enhancement. They concluded that the vibrating cylinder reinforces the interaction between the vortex structures and wall shear layers, resulting in over 50% increase in the average Nusselt number compared with a stationary cylinder. Besides, Mohammadshahi et al. [15] numerically illustrated that a flexible plate attached behind a stationary cylinder marginally increased (2.3%) the Nusselt number while lowering the pressure loss significantly (31%). Moreover, Ali et al. [16] investigated the heat transfer performance of the channel using the flexible vortex generators fixed at the walls. They found that the vortex shedding induced by the flexible vortex generators was intense, which plays a significant role in mixing and heat transfer processes, and results in a 134% overall heat transfer enhancement compared to their rigid counterparts. Subsequently, they numerically explored the oscillations of multiple flexible vortex generators and their effect on the heat transfer [17][18]. Their results showed that, the increase in the number of flaps produced a larger amplitude oscillations in the channel, which has a positive impact on the heat transfer augmentation. Within their study cases, the overall heat transfer enhancement compared to the empty channel is around 174%, 250% and 275% for the cases of two, three, and four flexible vortex generators, respectively. In their other research, a 3D numerical simulation was conducted to study the heat transfer in a circular pipe with trapezoidal vortex generators [19]. And they concluded that the flexible vortex generator can increase the overall heat transfer of around 118%, while the rigid vortex generator only provided about 97% enhancement, compared to the empty pipe.

It is clear from the literature that a properly designed turbulence generator can substantially improve the thermal performance of the system of concern. Much advancement has been achieved in recent years, and much more remains to be accomplished. Most of the aforementioned studies were developed in the internal channel or the fin-tube heat exchangers, where the vortex development and the resulting heat transfer performance might be influenced by the tube and the channel walls. The current study aims at furthering the development of state-of-the-art convection heat transfer enhancers by focusing on the simple flexible strip placed normal to the freestream. This rectangular strip is designed to vibrate under a prevailing wind, resulting in highly-transient turbulent vortical flow downstream which is expected to be beneficial in furthering heat transfer augmentation. To unambiguously study the effect of flexible strip on the heat transfer enhancement, excluding the influence of the tube and the channel walls, the studied models were placed in front of an unconfined flat surface. This study was under an open-flow condition, which is also potential for the corresponding engineering system, such as the solar photovoltaic panel.

3.2 Experimentation

The experiment was conducted in a 76 cm × 76 cm cross-section wind tunnel with a 3 mm thick, 295 mm wide and 380 mm long PTFE (polytetrafluoroethylene) plate inlaid in the center of fiberglass test section base. The thermal conductivity of the PTFE plate was 0.25 $Wm^{-1}K^{-1}$, and its emissivity was 0.92 [20][21]. As depicted in Figure 3.1, water in the tank was boiled, generating steam which continuously condensed on the bottom surface of the PTFE plate. As such, a uniform and constant temperature of 100℃ was maintained. The most important parameter, convective heat transfer enhancement, was deduced from the top surface temperature of the PTFE plate, measured by a FLIR C2 thermal camera with resolution of 60 × 80 pixels. The 12.7 mm wide and 38.1 mm tall flexible strips were cut from 0.1, 0.2 and 0.25 mm thick aluminum sheets. The strip was placed at the front edge of the PTFE plate to perturb the flow with respect to the reference (empty wind tunnel); see Figure 3.2. The wind speed was fixed at approximately 10 m/s, resulting in a Reynolds number based on the width and wind speed of 8.5×10^3. The orthogonal streamwise, widthwise and vertical directions were denoted as X, Y and Z; see Figures 3.1 and 3.2. The strip-induced turbulent flow was measured by a triple sensor hot wire probe (type 55P95) with a constant-temperature anemometer. The measure plane was 120 mm by 55 mm with a resolution of 5 mm. To avoid aliasing, the 10^6 measurements were sampled at 80 kHz and low passed at 30 kHz. Based on our previous experience, the flow is more-or-less 'developed' at 3H, beyond which it slowly decays. Therefore, 3H is a representative of the stretch of cooling enhancement, especially when dealing with a long stretch of solar PV panels. And thus, the hot wire probe was placed at 3H downstream in this study. Future studies will also examine the complex and rapidly changing flow right behind the strip and how the flow structures develop as they move downstream. Moreover, a Hotshot CC high speed camera with 500 frames per second was used to capture the vibration induced by the incoming flow.

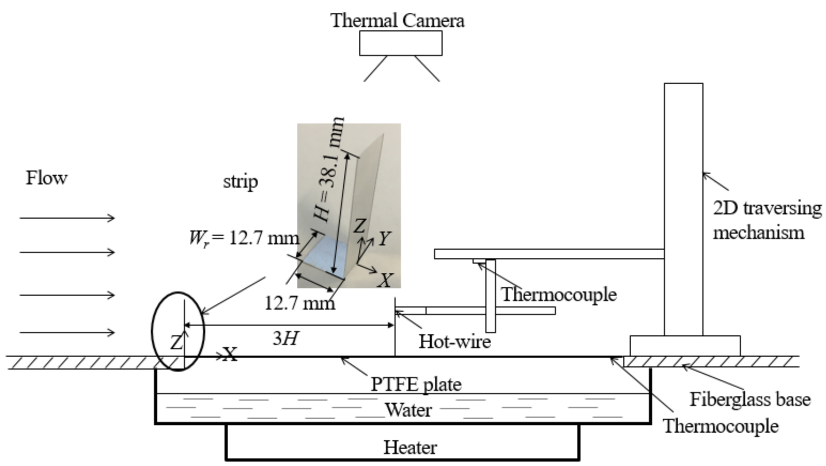

Figure 3. 1 The experimental setup

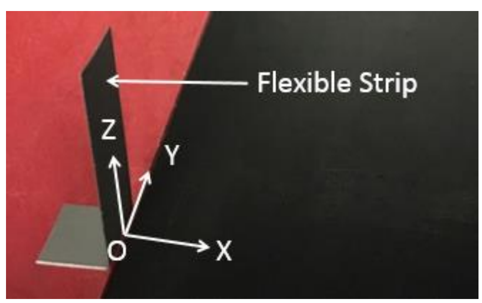

Figure 3. 2 Photo of a flexible strip

3.3 Data Processing

The rate of total heat through the PTFE surface,

$$\dot{Q}_{total} = K_{PTFE} A \left(\frac{T_{bottom} - T_{top}}{t_{PTFE}}\right) \tag{3.1}$$

The thermal conductivity of the PTFE, K_{PTFE} was 0.25W m^{-1}K^{-1}, the area of the PTFE surface, A was 295 mm by 380 mm, the thickness of the PTFE plate t_{PTFE} was 3mm, the bottom surface temperature of the PTFE plate, T_{bottom} was fixed at 100°C, and the local top surface temperature T_{top} was measured by the thermal camera. The total heat transferred away from the PTFE plate through the convection and the radiation, due to the negligible conduction loss to the rest of the wind tunnel base. Therefore, the rate of the convective heat transfer can be deduced,

$$\dot{Q}_{convection} = \dot{Q}_{total} - \dot{Q}_{radiation} \tag{3.2}$$

Here, $\dot{Q}_{radiation}$ is the rate of radiation heat transfer,

$$\dot{Q}_{radiation} = \varepsilon\sigma A(T_{top}^4 - T_{wall}^4) \tag{3.3}$$

where σ is Boltzmann's constant, which is $5.67\times 10^{-8}\,\mathrm{Wm^{-2}K^{-4}}$[22], ε is emissivity, and T_{wall} is the wind tunnel wall temperature. Here, T_{wall} is assumed to be equal to the air temperature T_{air}, which was measured by a thermocouple.

The convective heat transfer coefficient is defined as

$$h = \frac{\dot{Q}_{convection}}{A(T_{top} - T_{air})} \tag{3.4}$$

And the corresponding non-dimensional Nusselt number is,

$$Nu = \frac{hL}{K_{air}} \tag{3.5}$$

where L and K_{air} are the characteristic length and the thermal conductivity of air, respectively. To evaluate the enhancement of the convective heat transfer, Nu is normalized with respect to the corresponding Nusselt number without the strip perturbing the flow over the flat plate, i.e.,

$$\frac{Nu}{Nu_0} = \frac{h}{h_0} \tag{3.6}$$

where Nu_0 and h_0 are the Nusselt number and the convective heat transfer coefficient for the unperturbed reference case in the absence of the strip.

The instantaneous velocities in streamwise, widthwise and vertical direction, measured by the 3D hotwire, can be shown as,

$$U = \bar{U} + u\ ;\ V = \bar{V} + v\ ;\ W = \bar{W} + w \tag{3.7}$$

where $\bar{U}, \bar{V}, \bar{W}$ are the corresponding time-averaged velocities, which can be deduced from,

$$\bar{U} = \frac{1}{N}\sum_{i=1}^{N} U_i \; ; \bar{V} = \frac{1}{N}\sum_{i=1}^{N} V_i \; ; \bar{W} = \frac{1}{N}\sum_{i=1}^{N} W_i \tag{3.8}$$

where the sample size, N=10^6. And the u, v, and w are the respective instantaneous fluctuating velocities, from which the root-mean-square velocities can be deduced.

$$u_{rms} = \sqrt{\sum_{i=1}^{N} \frac{{u_i}^2}{N-1}} \; ; v_{rms} = \sqrt{\sum_{i=1}^{N} \frac{{v_i}^2}{N-1}} \; ; w_{rms} = \sqrt{\sum_{i=1}^{N} \frac{{w_i}^2}{N-1}} \tag{3.9}$$

The relative turbulence intensity can be obtained by this root-mean-square velocity normalized by the freestream velocity, i.e.,

$$Tu = \frac{u_{rms}}{U_\infty} \tag{3.10}$$

As turbulence is three dimensional [23], in order to describe the total turbulence level, the turbulent kinetic energy is introduced. The turbulent kinetic energy is composed of the contributions from X, Y and Z directions, i.e.,

$$ke = \frac{1}{2}\frac{(u_{rms}^2 + v_{rms}^2 + w_{rms}^2)}{U_\infty^2} \tag{3.11}$$

The studied model, flexible strip, can be considered as a bluff body, resulting in some regular vortex shedding of certain frequency. This frequency can be normalized by the width of the strip and the freestream velocity to give the Strouhal number,

$$St = \frac{fW_r}{U_\infty} \tag{3.12}$$

Turbulent flow is rich in scales of eddies motion [23], in order to better characterize the turbulent flow generated by the strip, the turbulence length scale was also analyzed in this study. The integral scale represents the large eddies that associated with the fluctuating energy. And its temporal scale can be deduced from the autocorrelation function,

$$f(\tau) = \frac{\overline{u(t)u(t+\tau)}}{\overline{u^2(t)}} \tag{3.13}$$

From this, the integral time scale can be derived via integration, which was terminated at the first zero crossing point,

$$\tau_\Lambda = \int_0^\infty f(\tau)d\tau \tag{3.14}$$

According to the Taylor frozen hypothesis [24], the corresponding integral length scale can be obtained,

$$\Lambda = \bar{U}\tau_{\Lambda} \tag{3.15}$$

The Taylor microscale is at the other end of the turbulence energy cascade, which represents the dissipation. The Taylor time scale can be expressed as:

$$\tau_{\lambda} = \sqrt{\frac{\overline{2u^2(t)}}{[\frac{du(t)}{dt}]^2}} \tag{3.16}$$

Applying the Taylor frozen hypothesis [24], the Taylor microscale can be obtained from,

$$\lambda = \bar{U}\tau_{\lambda} \tag{3.17}$$

To better illustrate the comparison results, the span-averaged values are introduced,

$$\bar{P} = \frac{1}{n}\sum_{i=1}^{n} P_i \tag{3.18}$$

Here P is the parameters, such as normalized Nusselt number, velocity toward the heated surface, and the non-dimensional turbulence kinetic energy. And *n* is the number of values in the range of averaging, for example, *n* = 19 if averaging the results across the ±1H in the Y direction.

3.4 Results and Discussion

3.4.1 Flow-induced Vibration

The incoming flow induced the flexible strip to vibrate. To investigate the motion of flexible strips, the oscillation amplitudes of the strips with different thickness and the resulting power spectrum density are shown in Figure 3.3. As expected, with increasing strip thickness, and thus, the rigidity, the frequency of the vibration increases. The most distinct peak of the power spectrum density took place at around 62Hz, 100Hz and 120Hz, for the 0.1, 0.2 and 0.25 mm-thick strips, respectively. It should be noted that the vortex shedding frequencies of strips with different thickness are approximately 68Hz, which are detailed in Section 3.4.2.3. And thus, the ratio of vortex shedding frequency to the structural vibration frequency for 0.1 mm-thick strip is close to 1, reaching lock-in state [25]. This lock-in state shed vortex forces 0.1 mm-thick strip to vibrate with much larger displacement than the other two, which presumably can lead to a higher heat and mass transfer performances [16].

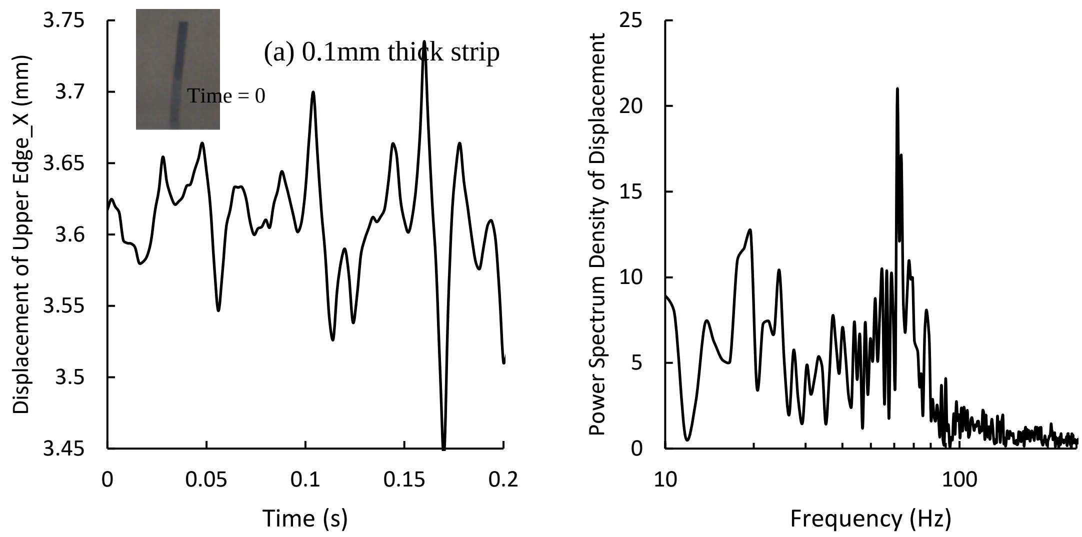
(a) 0.1mm thick strip
Time = 0
Displacement of Upper Edge_X (mm)
3.75
3.7
3.65
3.6
3.55
3.5
3.45
0
0.05
0.1
0.15
0.2
Time (s)
Power Spectrum Density of Displacement
25
20
15
10
5
0
10
100
Frequency (Hz)

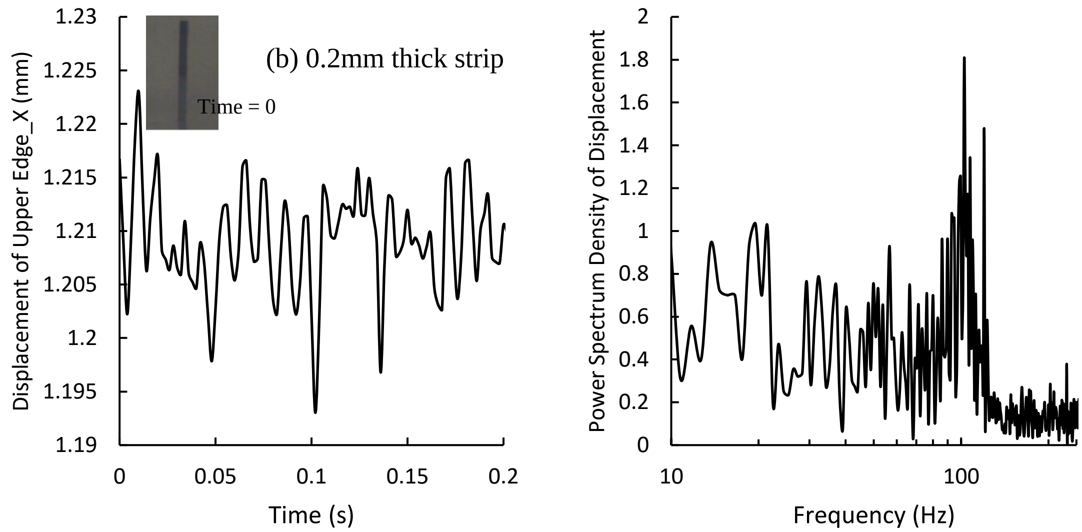
(b) 0.2mm thick strip
Time = 0
Displacement of Upper Edge_X (mm)
1.23
1.225
1.22
1.215
1.21
1.205
1.2
1.195
1.19
0
0.05
0.1
0.15
0.2
Time (s)
Power Spectrum Density of Displacement
2
1.8
1.6
1.4
1.2
1
0.8
0.6
0.4
0.2
0
10
100
Frequency (Hz)

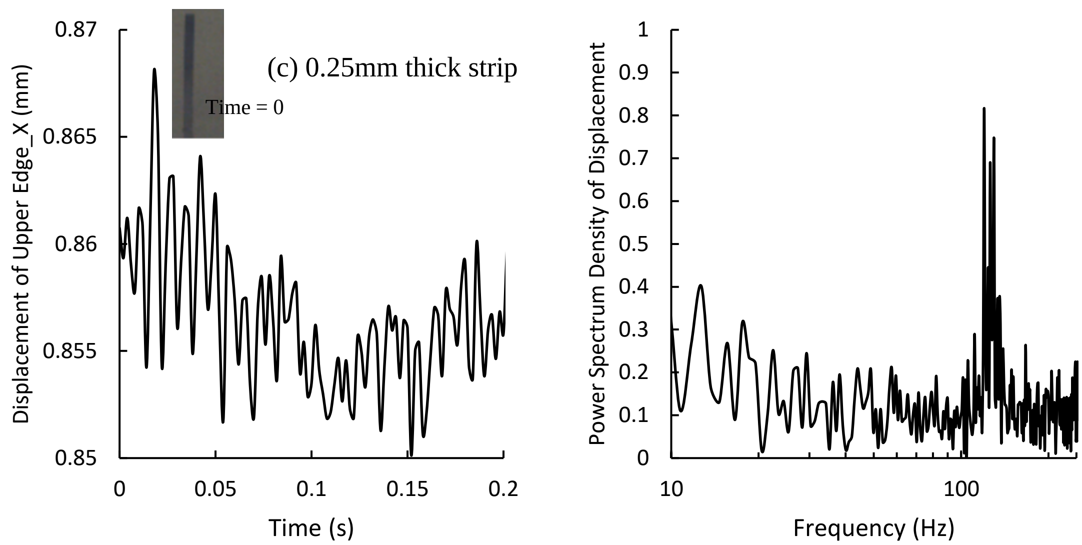

Figure 3. 3. Displacement of upper edge and power spectrum density of strip displacement for cases (a) 0.1 mm thick strip, (b) 0.2 mm thick strip, (c) 0.25 mm thick strip.

3.4.2 Flow Characteristics

3.4.2.1 Velocity Profile

The contours of streamwise velocity normalized by the freestream velocity ($U_\infty \approx 10$ m/s) at 3H downstream are depicted in Figure 3.4. Velocity vectors, in the YZ plane, are also included to complementarily elucidate the flow behavior. The swirling motions at around Z/H=0.7, Y/H=-0.5 and Z/H=0.7, Y/H=0.5 are clear. These flow motions cause a notable downwash movement, especially at Y≈0. It should be underlined that as far as the heat transfer is concerned, the wind velocity toward the hot plate surface is important. In other words, a larger downwash velocity would more effectively bring the cooler freestream air toward the heated surface, increasing the mixing of fluid with the hotter air, resulting in a larger heat transfer augmentation near Y/H=0, as shown and detailed in Section 3.4.3

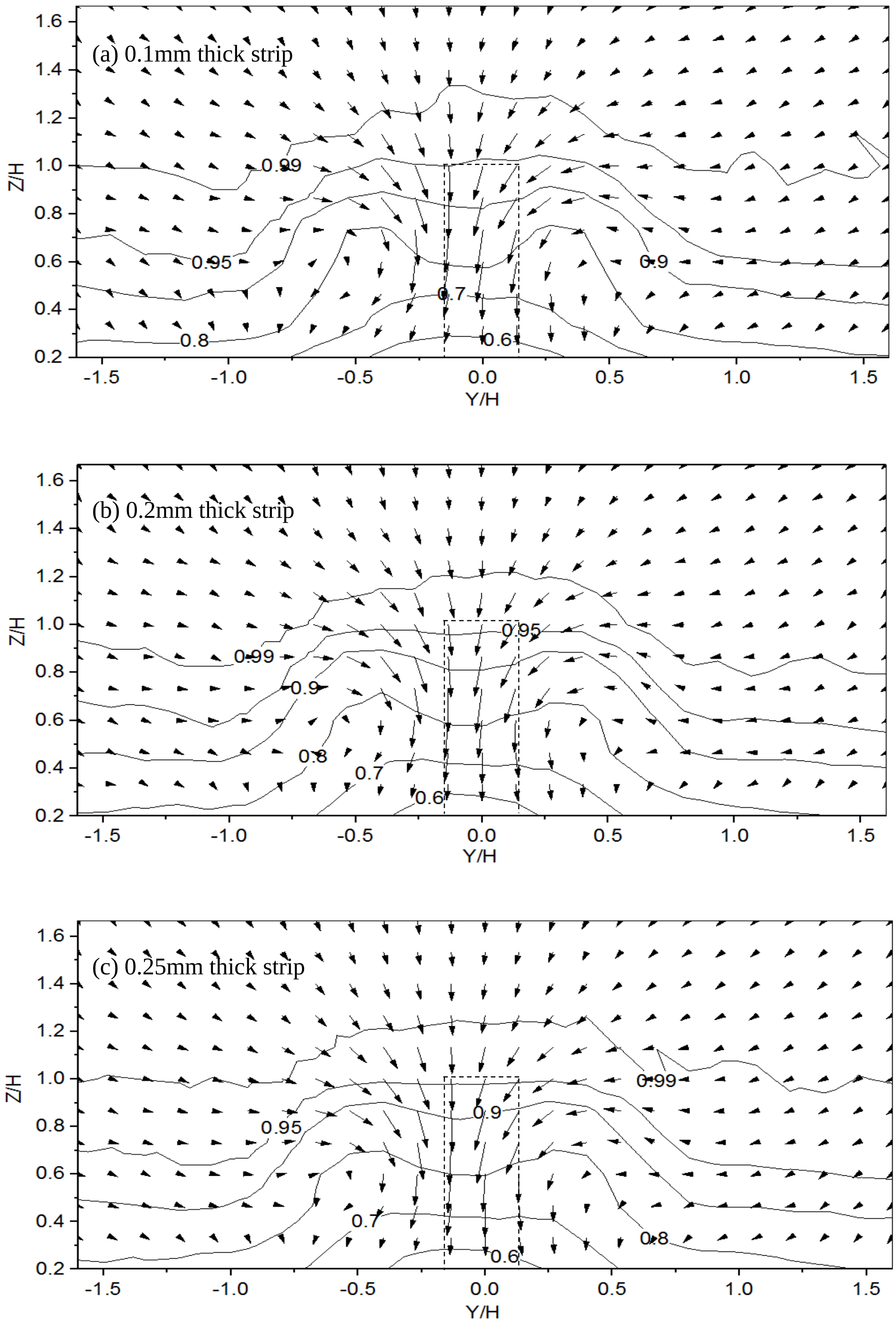

Figure 3. 4. Normalized Streamwise Velocity Profile and Velocity Vector in the YZ Plane at X = 3H downstream of (a) 0.1 mm, (b) 0.2 mm, and (c) 0.25 mm thick flexible strip.

The prevailing downwash is of interest. Thus, the span-averaged normalized $\overline{W}$ velocity at 3H downstream was introduced to better illustrate the secondary flow induced by the studied strips with different thickness; see Figure 3.5. A negative peak value can be identified at Z ≈ H, indicating a consequential amount of flow circulates downward from the upper edge of the strip. The two side recirculating flow motions presumably solidified this negative $\overline{W}$ flow onto the plate. Also, the more negative $\overline{W}/U_\infty$ values, between Z=0.2H to 1H, generated by the 0.1 mm-thick strip are clearly distinguishable. As this transpires just above the hot surface, the resulting surplus cooling is pervasive.

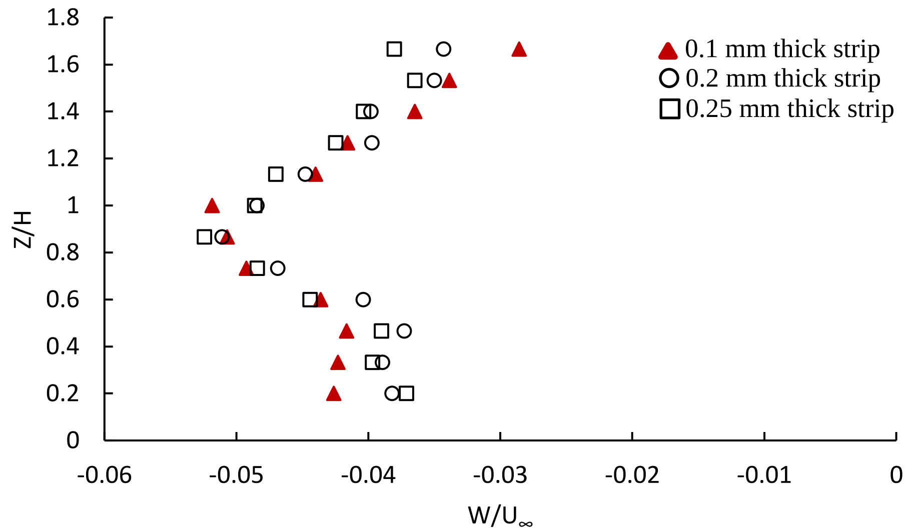

Figure 3. 5. $\overline{W}/U_\infty$ Profile at X = 3H downstream of the flexible strip (span-averaged from Y = -1H to 1H)

3.4.2.2 Turbulence Intensity

It is essential to scrutinize the underlying turbulence intensity when it comes to thermal energy transport enhancement such as that disseminated in this study. Figure 3.6 depicts the streamwise turbulence intensity (*Tu*) contour at 3H downstream of the flexible strip. Two peak *Tu* regions are highly distinguishable around Y/H=-0.5, Z/H=0.7 and Y/H=0.5, Z/H=0.7. These presumably correspond to the highest shear stress areas from the edges of the strip and the core of vortex swirling motion shown in Figure 3.4. The maximum *Tu* value generated by the 0.1 mm strip is around 0.178, at the same level of the 0.2 mm and 0.25 mm thick strips, with maximum *Tu* value of 0.176 and 0.175, respectively.

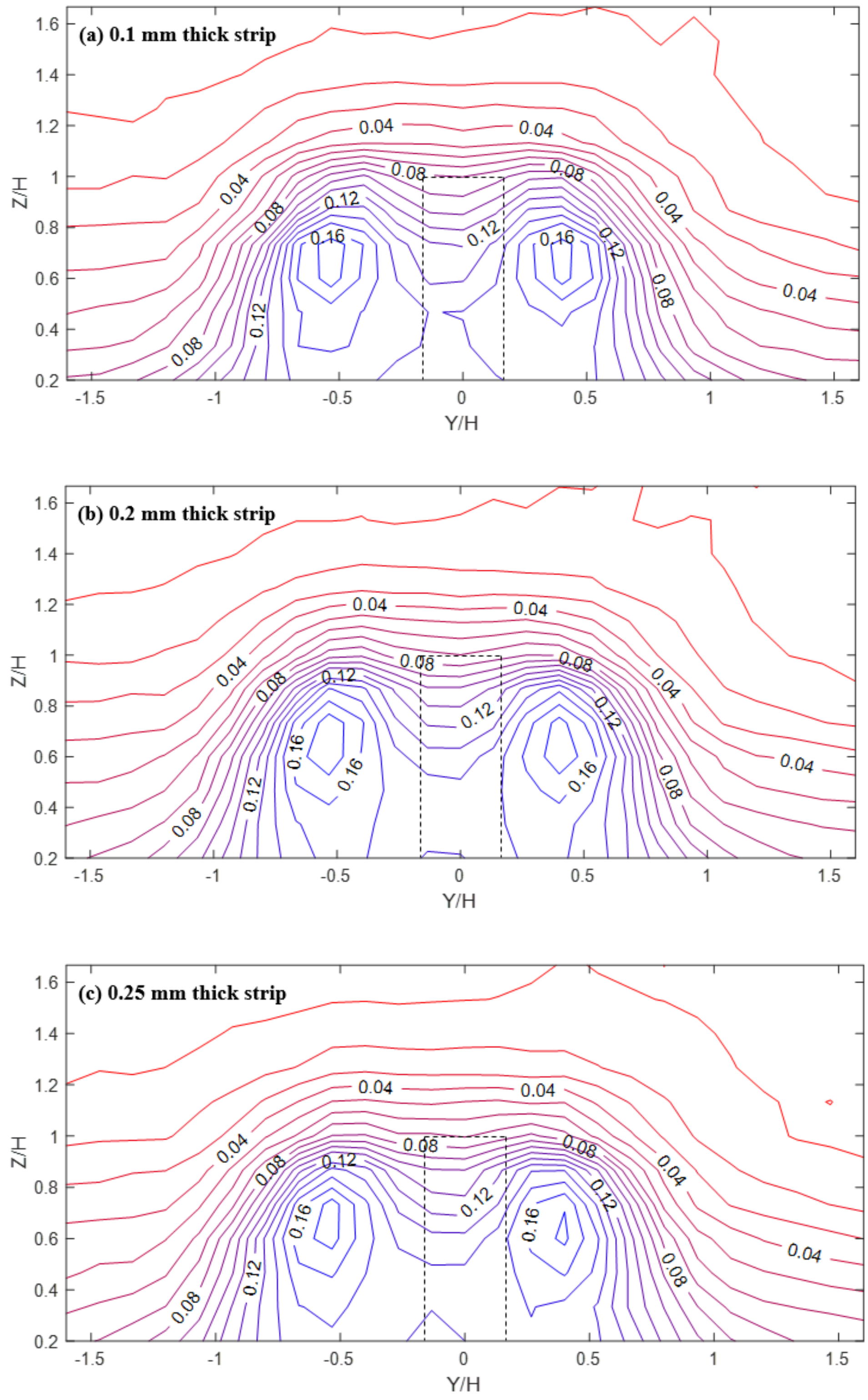

Figure 3. 6. Streamwise turbulence intensity (*Tu*) at X = 3H downstream of the flexible strip with a thickness of (a) 0.1 mm, (b) 0.2 mm and (c) 0.25 mm.

As the turbulent flow behind the strip is highly three dimensional, the total turbulent kinetic energy is also of interest. As such, the normalized turbulent kinetic energy is compiled and displayed in Figure 3.7. Due to contributions from the cross-stream and vertical directions, the contours are moderately different from that of the streamwise component alone. There is only one region – not two – of maximum *ke* behind the flexible strip, and this occurs at Y/H ≈ 0 and Z/H ≈ 0.5. Note that the turbulent kinetic energy indicates the level of velocity fluctuations, which are associated with gradients in time-averaged flow, causing increased mixing in the fluid and heat transfer enhancement [26]. And thus, the area near Y/H ≈ 0 behind the flexible strip is more likely to achieve a better heat transfer augmentation. Also, in order to compare the influence of the strip thickness on the turbulence kinetic energy, the span-averaged (from Y = -H to H) *ke* values are plotted with respect to the vertical distance in Figure 3.8. Generally speaking, the turbulence kinetic energies of the flow behind the three strips are mostly at the same level. This indicates that the chosen thickness of the studied model, and the resulting structural vibration, have little effect on the level of velocity fluctuations.

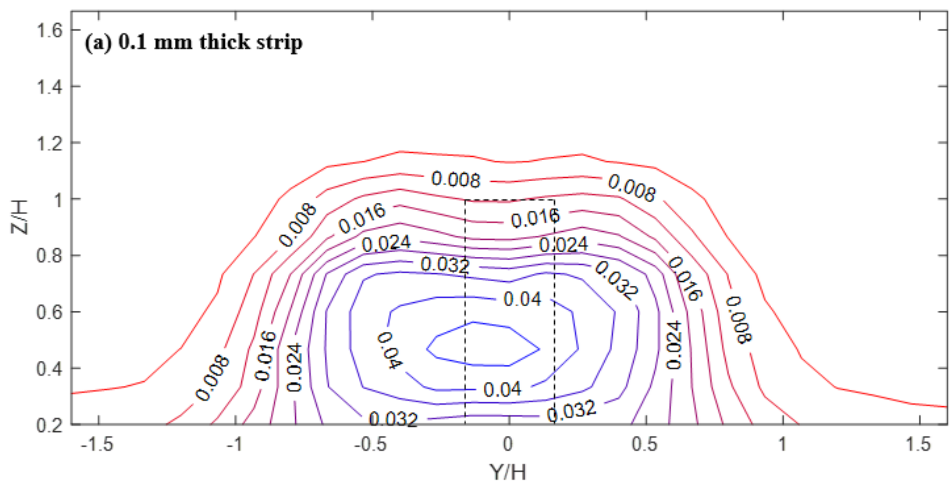

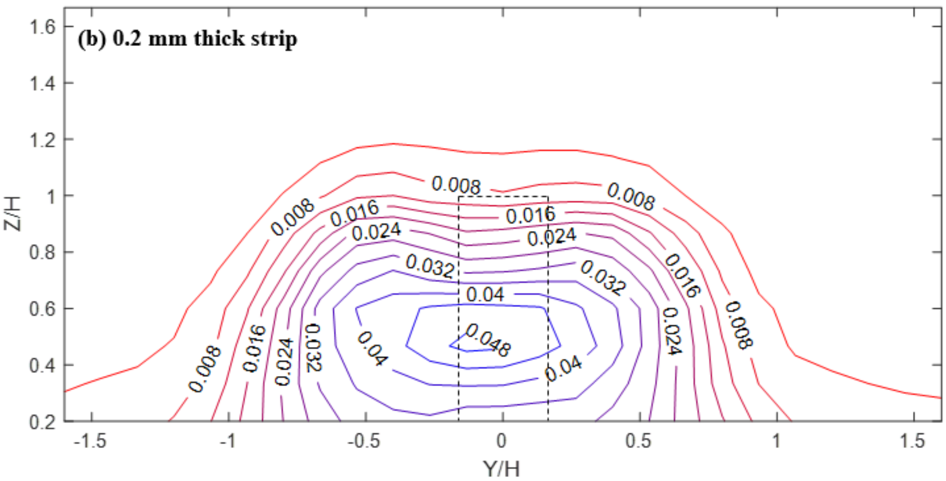

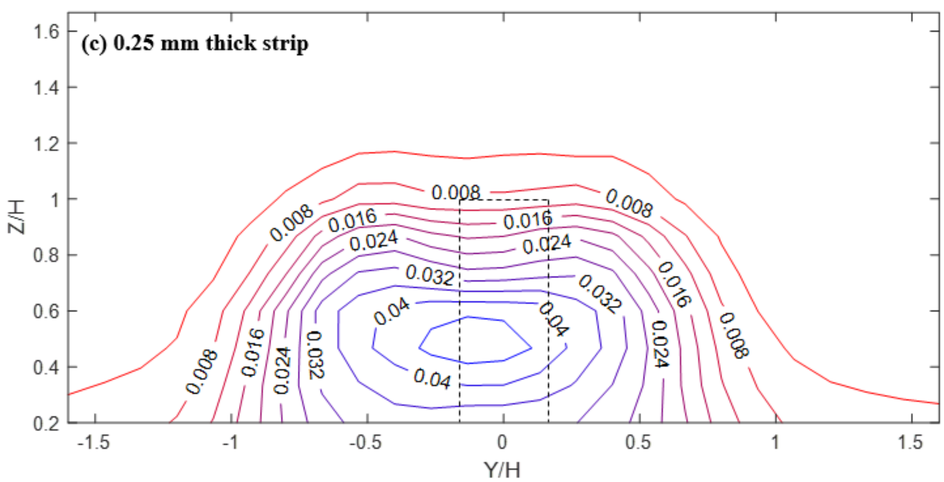

Figure 3. 7. Normalized Turbulent Kinetic Energy (*ke*) at X = 3H downstream of a flexible strip with a thickness of (a) 0.1 mm, (b) 0.2 mm, (c) 0.25 mm.

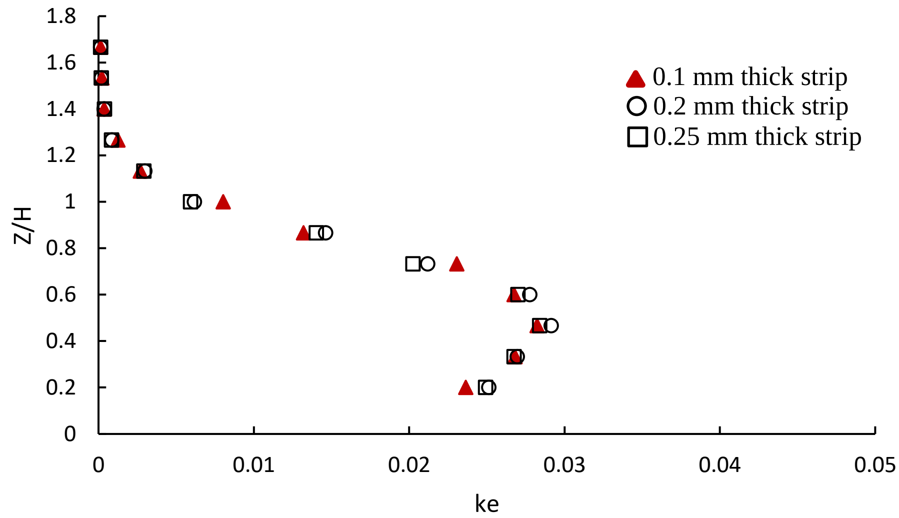

Figure 3. 8. Normalized Turbulent Kinetic Energy (*ke*) Profile (span-averaged from Y = -H to H) at X = 3H downstream of the flexible strip

3.4.2.3 Power Spectrum

The flexible strip in this study can be considered as a bluff body, resulting in the vortex shedding under certain conditions, which can play an important role in convective heat transfer over the heated plate. Thus, the power spectrum associated with this regular fluctuating velocity is analyzed. Figure 3.9 portrays the power spectrum at X=3H, Y=-0.53H, Z=0.7H, which is near the position where the highest streamwise turbulence intensity has been detected. To clearly compare the power spectrum density of the strips with different thickness, a smoother figure is preferred. The values are divided into 2^{12} sections with 50% overlap. The X, Y and Z components of the power spectrum all provide a distinct peak value at approximately 68Hz, corresponding to a Strouhal number of around 0.09 based on the strip width. This value is smaller than *St* = 0.14 ~ 0.16 obtained from an infinitely long strip [27][28]. The finite top end has been found to dampen the shedding frequency [29]. Also notable is that the largest peak amplitude value at the shedding frequency occurs for the strip with 0.1 mm thickness. This strongest vortex shedding, produced by the thinnest, 0.1 mm strip, leads to the most significant heat convection enhancement. It is worth emphasizing that at this particular location, with Y = -0.53H and Z = 0.7H, the most dominant power spectrum is observed in the X direction. This stronger power spectrum seems to correspond to the interaction of a strong Z-vortex and Y-vortex, which are shed from the left edge and the top edge of the flexible strip, respectively. The Z-component power spectrum is weaker than the others, probably due to the relatively weaker X-vortex.

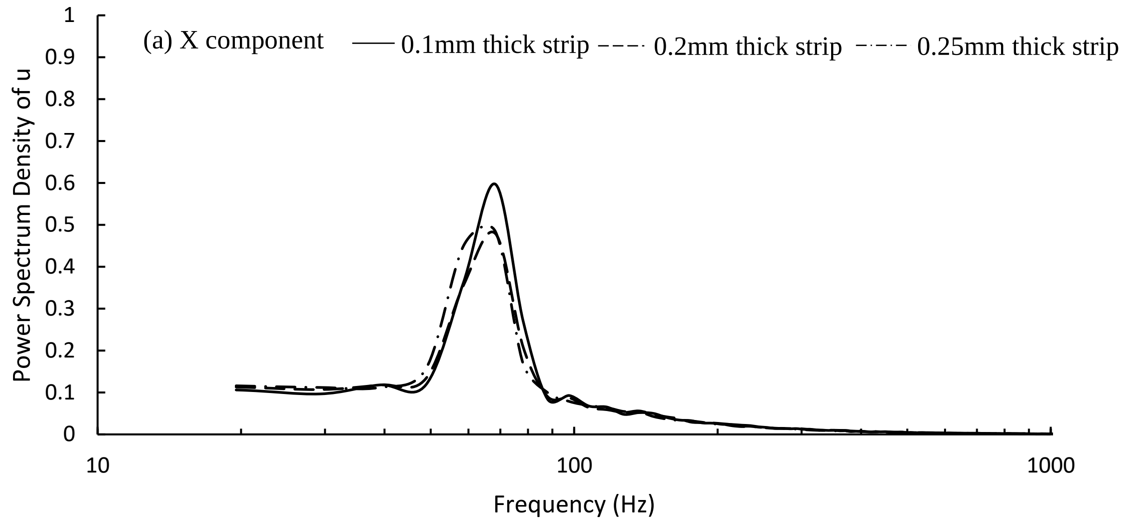
(a) X component
0.1mm thick strip
0.2mm thick strip
0.25mm thick strip
Power Spectrum Density of u
1
0.9
0.8
0.7
0.6
0.5
0.4
0.3
0.2
0.1
0
10
100
1000
Frequency (Hz)

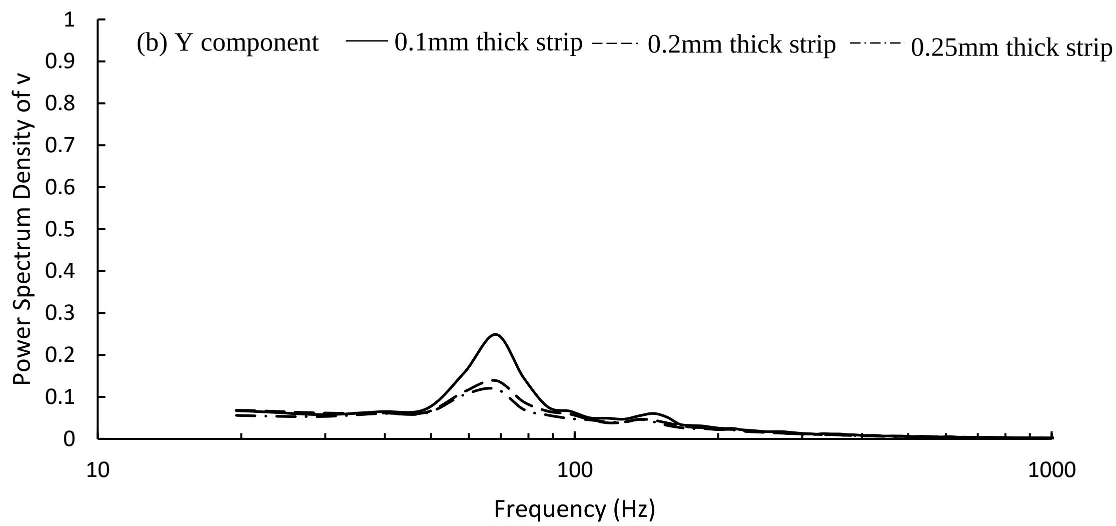
(b) Y component
0.1mm thick strip
0.2mm thick strip
0.25mm thick strip
Power Spectrum Density of v
1
0.9
0.8
0.7
0.6
0.5
0.4
0.3
0.2
0.1
0
10
100
1000
Frequency (Hz)

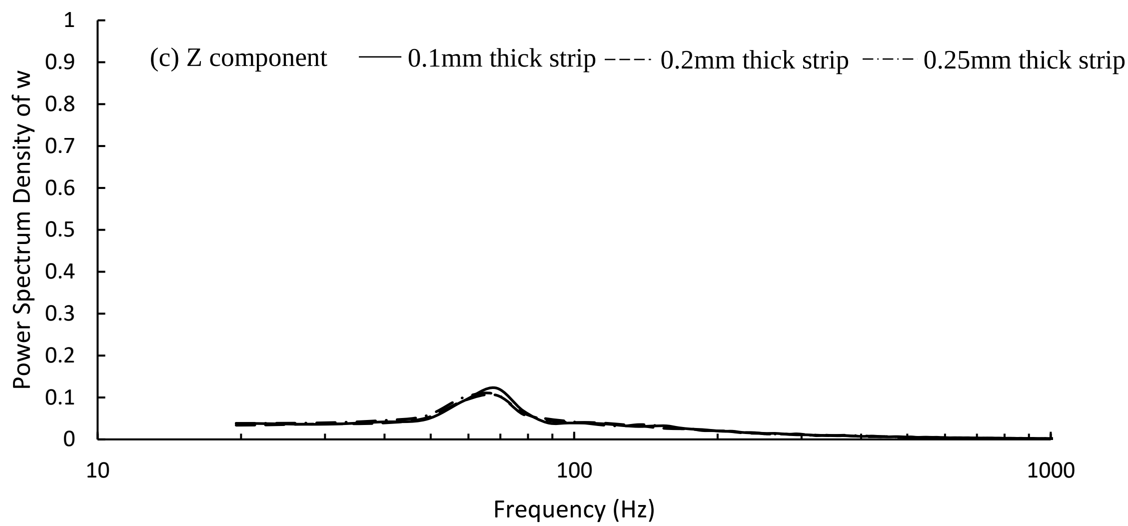

Figure 3. 9. Power spectrum at X=3H, Y=-0.53H, Z=0.7H

3.4.2.4 Integral Scale

The scale of the eddy motion reflects the effectiveness of the removal of the thermal energy from the heated surface. As such, the streamwise integral scale, normalized by the strip height, is depicted in Figure 3.10. For all three strips with different thickness, the normalized integral scale is approximately unity near Y=0, Z=0.6~1H, indicating that the magnitude of the integral scale is the same order with the obstruction dimension at the studied conditions. And thus, from the figures, it is observed that the integral scale is independent of the strip's thickness. Note that the integral scale here is calculated from X-component fluctuating velocity *u*. This contains the information of eddies shed over the side edges and the top edge, which implies the size of the width and the height. Also notable is that the largest integral scales are detected near Y=0, which have a high potential for effective heat transfer.

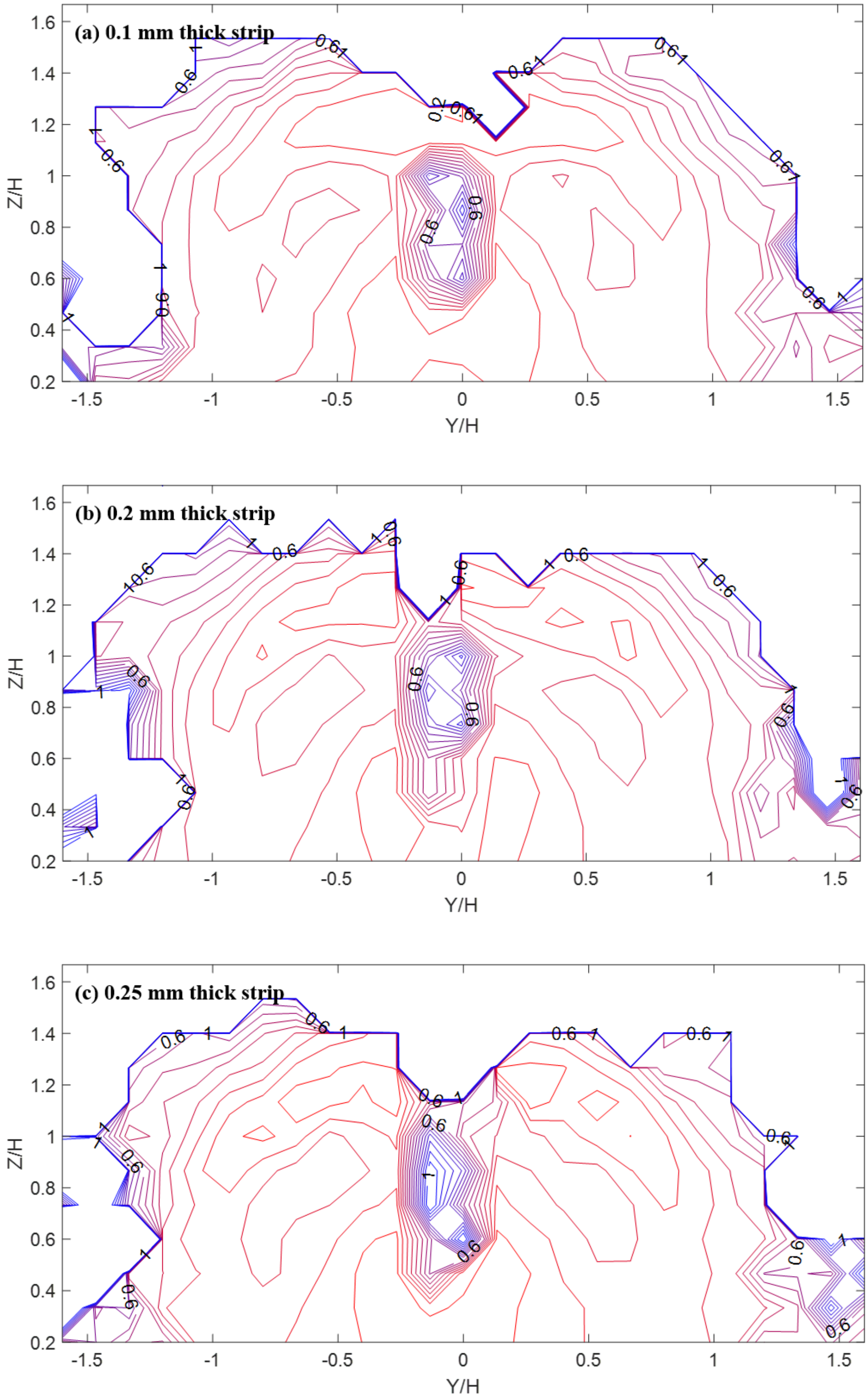

Figure 3. 10. Normalized streamwise integral scale at X = 3H downstream of a flexible strip with a thickness of (a) 0.1 mm, (b) 0.2 mm, (c) 0.25 mm.

3.4.2.5 Taylor Microscale

The most effective heat transfer enhancement is not just associated with the turbulent flow with the largest integral scale. Rather, the turbulent flow with the wider and more vigorous turbulent energy cascade is more potent when it comes to augmenting convection heat transfer. Thus, the small scale, at the other end of turbulent energy cascade, is also important for heat transfer enhancement. Figure 3.11 depicted the streamwise Taylor microscale normalized by the strip height, which is 38.1 mm. Note that the turbulence length scale has no meaning above boundary layer in this study, because the flow in those areas is largely laminar. Therefore, the length scale is only analyzed in the area below Z=1.2H. It is clear from the figure that the smallest Taylor microscale values are near Y=0. With increasing Y, the Taylor microscale increases, and this lasts until Y≈±1.3H and Z≈0.4H. The increase in Taylor microscale may be interpreted as the rapid dissipation of turbulent kinetic energy. In other words, the smaller Taylor eddies near Y=0 denote more intense local turbulence level, and thus, more effective heat transfer. It should be also noted that, the Taylor microscales for three strips are also at the same level, which indicates that the small turbulence length scale is also independent of the thickness and the resulting structural vibration.

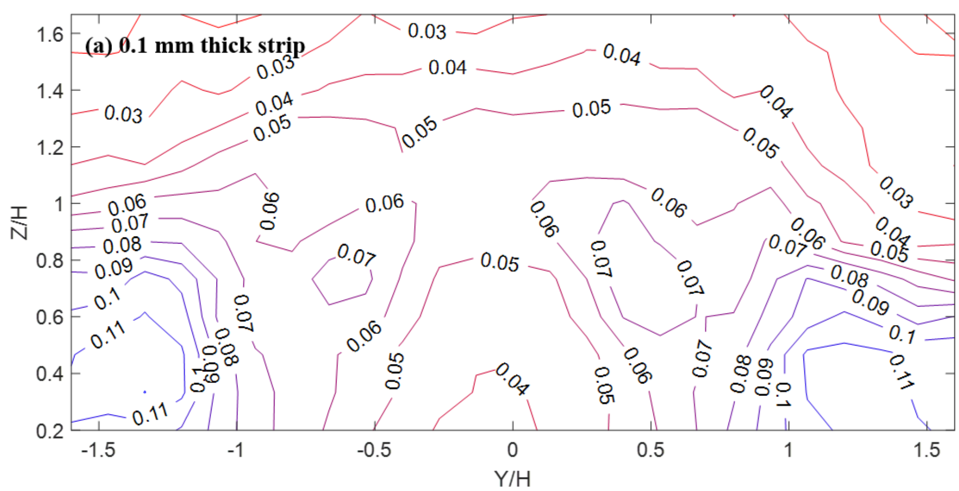

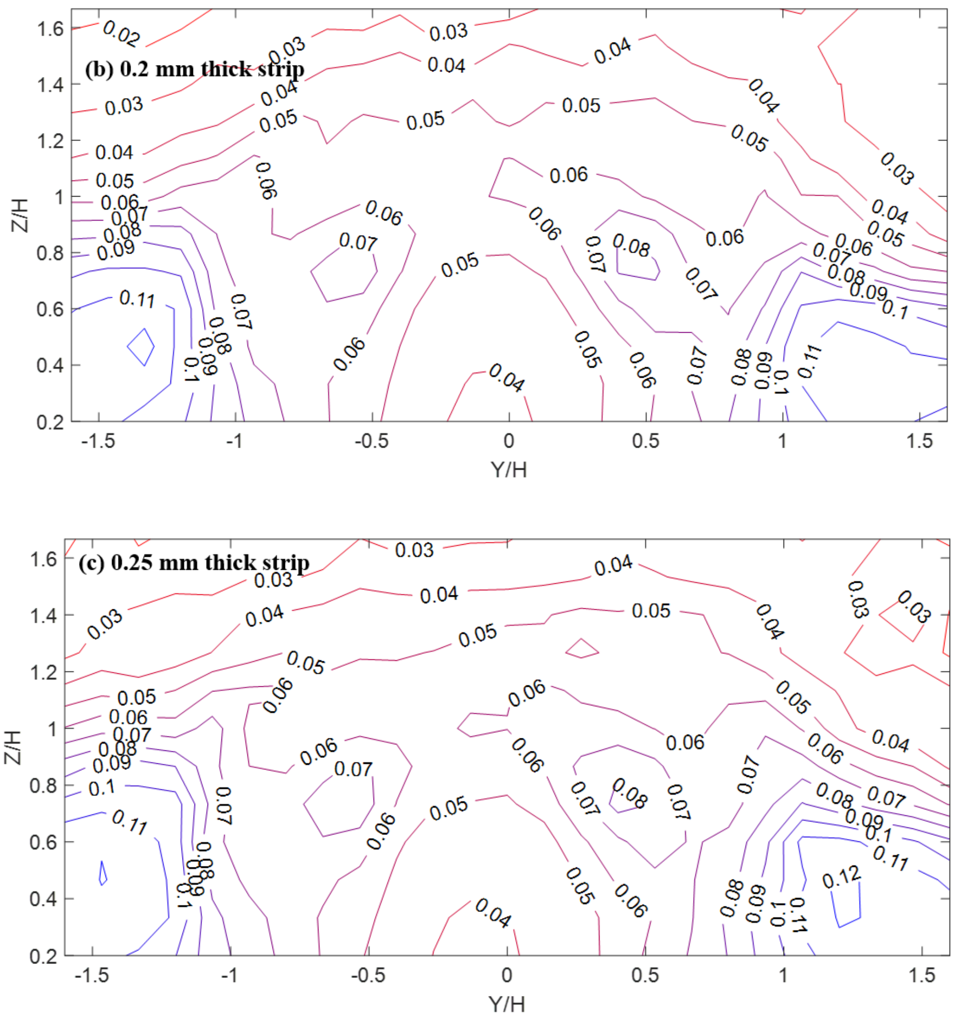

Figure 3. 11. Normalized streamwise Taylor microscale at X = 3H downstream of a flexible strip with a thickness of (a) 0.1 mm, (b) 0.2 mm, (c) 0.25 mm.

3.4.3 Heat Transfer Enhancement

The influence of the strip on the convective heat transfer performance is shown in Figure 3.12. The results are depicted in terms of the normalized Nusselt number, indicating the convective heat transfer augmentation with respect to the reference case without the strip. It is clear from the figure that the normalized Nusselt number maintains a large value, with Nu/Nu_0 approaching two, in the near-strip region until 2H downstream. The heat transfer enhancement decreases slowly at farther downstream, indicating the vortex structure behind the strip with high turbulence intensity is fading out, and the flow is gradually restoring to a less perturbed condition. It is also noted that the heat transfer enhancement of the heated surface behind the 0.1 mm-thick strip is higher than others, due to its larger-displacement vibration, and the larger secondary flow toward the heated surface, as discussed in the previous section.

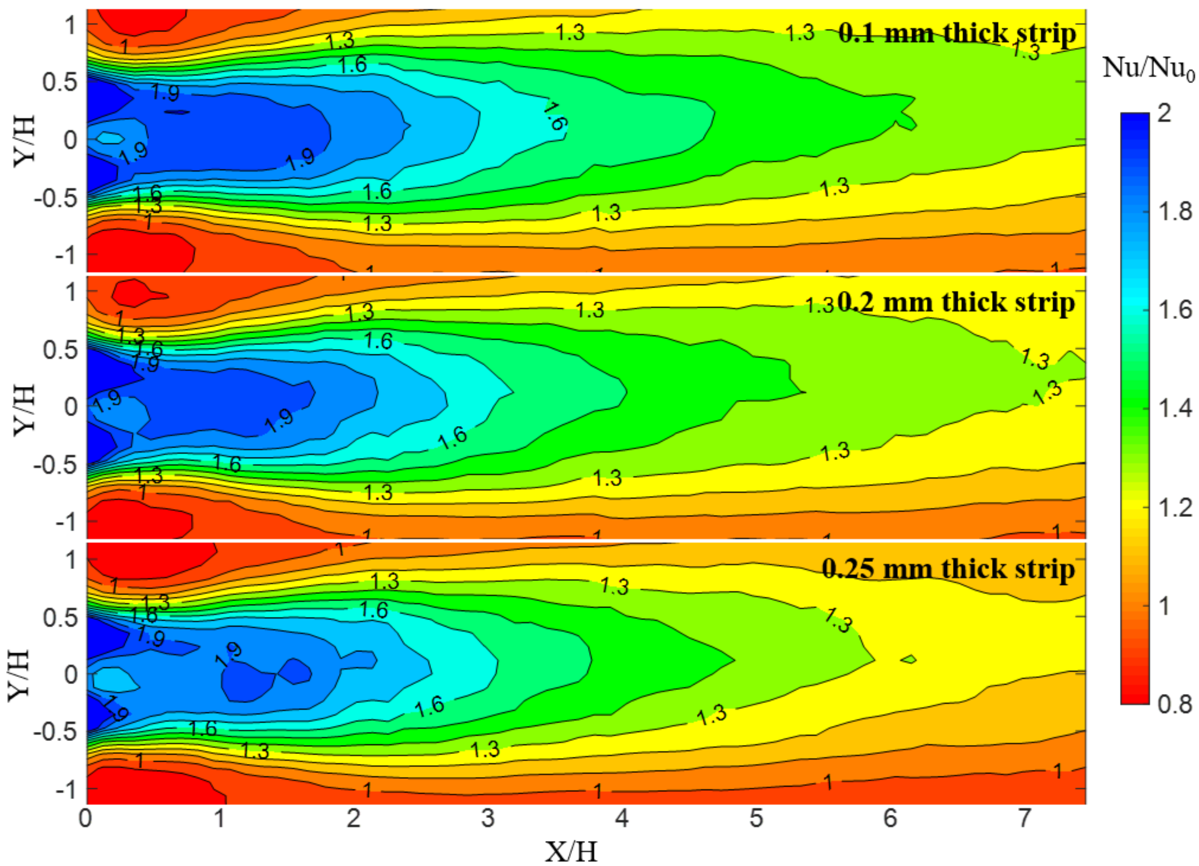

Figure 3. 12. Normalized Nusselt number (Nu/Nu_0) downstream of the strip

The streamwise distribution of the normalized Nusselt number at Y=0 is depicted in Figure 3.13(a). A relatively constant Nu/Nu_0 value of 1.9 can be observed until 1.5H downstream, beyond which an approximately exponential decay takes place. As the studied case is highly three dimensional, averaging the results across the ±1H in the Y direction can better delineate the variation of Nu/Nu_0 with respect to distance downstream of the flexible strip. This is plotted in Figure 3.13(b). It is interesting to note that, the 'slightly cross-stream averaged' Nu/Nu_0 first drops to about 1.4 right behind the flexible strip, before it increases and peaks at around 2H downstream, beyond which is a significantly more gradual decrease compared to the Y=0 result. The difference between Figure 3.13(a) and (b) can be easily inferred from Figure 3.12. The maximum Nu/Nu_0 at X=0 is probably due to the highly-conductive aluminum strip acting as an effective heat fin and the strong vortex shed from the strip. Just downstream from the strip Nu/Nu_0 is still very high, but the cross-sectional span is substantially narrower. For this reason, the Y=±1H averaged Nu/Nu_0 in Figure 3.13(b) is considerably less than the Y=0 value in Figure 3.13(a). The enhanced Nu/Nu_0 area then expands, while the enhancement gradually fades out farther downstream. Again, from the figures, 0.1 mm-thick strip was detected to have a better heat transfer augmentation among others.

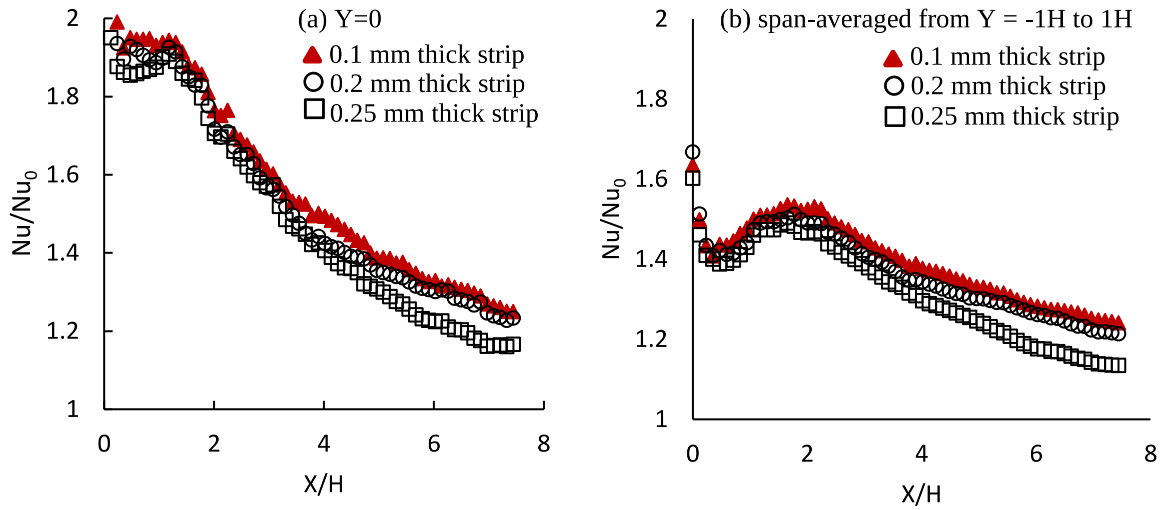

Figure 3. 13. Normalized Nusselt number downstream of the flexible strip. (a) Y = 0, (b) Y=±H.

Figure 3.14 shows the cross-stream Nu/Nu_0 profile at selected downstream distances. It is clear from the figure that the peak value of Nu/Nu_0 diminishes, while the augmented cross-stream span expands, with distance downstream. More subtly, the 0.1 mm-thick strip consistently has a marginally higher Nu/Nu_0 value, indicating better heat transfer performance. Also notable is that the local Nu/Nu_0 value is still as high as 1.5 even after five strip heights, X=5H or some 200 mm, downstream. This implies that the flexible strip can be more effective than some other type of longitudinal vortex generator, such as the delta winglet with height of 10 mm and attack angle of 30°, which was found to provide a maximum of around 40% Nusselt number boost at five heights downstream at a Reynolds number of 6000 by Wu et al. [30].

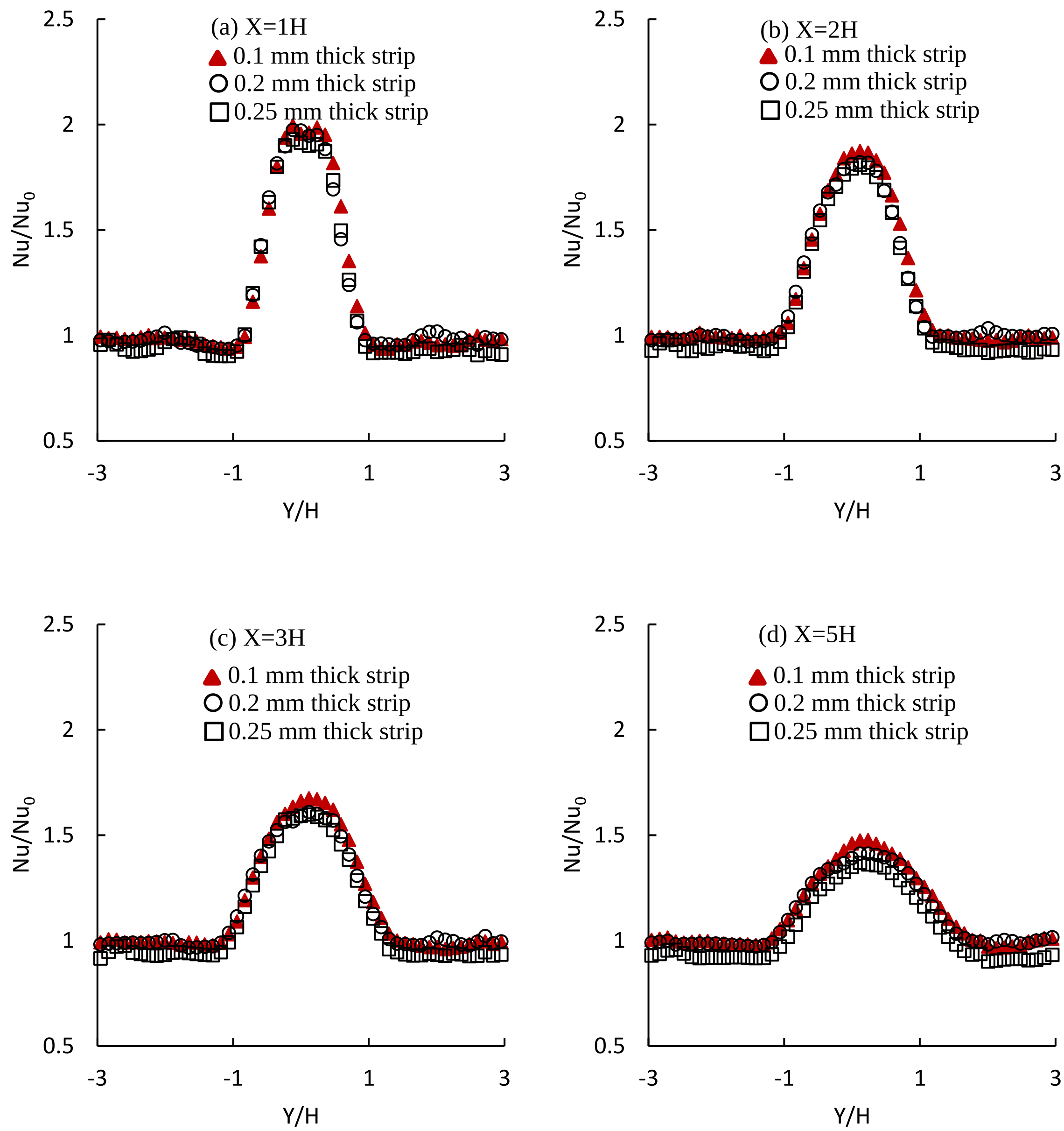

Figure 3. 14. Cross-stream normalized Nusselt number profile as a function of distance downstream. (a) X = 1H, (b) X = 2H, (c) X = 3H, (d) X = 5H.

3.5 Conclusions

A 38.1 mm tall and 12.7 mm wide aluminum strip was employed to enhance the convective heat transfer from a heated plate in a wind tunnel at 10 m/s wind velocity. The effect of the strip thickness (thickness of 0.1, 0.2 and 0.25 mm) at a Reynolds number of 8.5×10^3, based on the strip width and freestream velocity, was analyzed in terms of the normalized local Nusselt number, Nu/Nu_o, where Nu_o is the reference Nusselt number in the absence of the strip. In general, Nu/Nu_o

peaks immediately behind the strip (*X/H* < 2), and it decreases slowly farther downstream. The 0.1 mm-thick strip resulted in the highest heat transfer augmentation, with a maximum Nu/Nu_o value of 1.67 at 3H downstream, approximately 0.1 larger than that associated with the 0.25 mm-thick strip. Large wind velocity toward the heated surface and strong Strouhal fluctuations appear to promote the best heat transfer enhancement. The thinnest, most flexible, 0.1 mm thick strip has been found to be most effective in spawning these desirable flow conditions over many strip heights downstream. Also, the turbulent length scale is observed to be independent of the chosen thickness, instead, it seems to be related with the dimension of strips, i.e. the height and the width. Therefore, the optimization of the studied model needs to be continued to further the heat transfer enhancement.

Acknowledgments

This work was made possible by Natural Sciences and Engineering Research Council of Canada and Ontario Centres of Excellence.

References

[1] E. Marumo, K. Suzuki, and T. Sato, “Turbulent heat transfer in a flat plate boundary layer disturbed by a cylinder,” Int. J. Heat Fluid Flow, vol. 6, no. 4, pp. 241–248, 1985.

[2] L. Wang and B. Sundén, “Experimental Investigation of Local Heat Transfer in a Square Duct With Continuous and Truncated Ribs,” Exp. Heat Transf., vol. 18, no. 3, pp. 179–197, 2005.

[3] R. Kamali and A. R. Binesh, “The importance of rib shape effects on the local heat transfer and flow friction characteristics of square ducts with ribbed internal surfaces,” Int. Commun. Heat Mass Transf., vol. 35, no. 8, pp. 1032–1040, 2008.

[4] B. V. Ravi, P. Singh, and S. V. Ekkad, “Numerical investigation of turbulent flow and heat transfer in two-pass ribbed channels,” Int. J. Therm. Sci., vol. 112, pp. 31–43, Feb. 2017.

[5] G. Biswas, H. Chattopadhyay, and A. Sinha, “Augmentation of heat transfer by creation of streamwise longitudinal vortices using vortex generators,” Heat Transf. Eng., vol. 33, no. 4–5, pp. 406–424, 2012.

[6] Z. Qian, Q. Wang, and J. Cheng, “Analysis of heat and resistance performance of plate fin-and-tube heat exchanger with rectangle-winglet vortex generator,” Int. J. Heat Mass Transf., vol. 124, pp. 1198–1211, Sep. 2018.

[7] A. Khanjian, C. Habchi, S. Russeil, D. Bougeard, and T. Lemenand, “Effect of rectangular winglet pair roll angle on the heat transfer enhancement in laminar channel flow,” Int. J. Therm. Sci., vol. 114, pp. 1–14, Apr. 2017.

[8] A. T. Wijayanta, T. Istanto, K. Kariya, and A. Miyara, "Heat transfer enhancement of internal flow by inserting punched delta winglet vortex generators with various attack angles," Exp. Therm. Fluid Sci., vol. 87, pp. 141–148, 2017.

[9] G. Zhou and Z. Feng, "Experimental investigations of heat transfer enhancement by plane and curved winglet type vortex generators with punched holes," Int. J. Therm. Sci., vol. 78, pp. 26–35, 2014.

[10] B. Gong, L.-B. Wang, and Z.-M. Lin, "Heat transfer characteristics of a circular tube bank fin heat exchanger with fins punched curve rectangular vortex generators in the wake regions of the tubes," Appl. Therm. Eng., vol. 75, pp. 224–238, 2015.

[11] M. Oneissi, C. Habchi, S. Russeil, D. Bougeard, and T. Lemenand, "Novel design of delta winglet pair vortex generator for heat transfer enhancement," Int. J. Therm. Sci., vol. 109, pp. 1–9, 2016.

[12] R. K. B. Gallegos and R. N. Sharma, "Flags as vortex generators for heat transfer enhancement: Gaps and challenges," Renew. Sustain. Energy Rev., vol. 76, pp. 950–962, 2017.

[13] J. S. Go et al., "Heat transfer enhancement using flow-induced vibration of a microfin array," Sensors Actuators A Phys., vol. 90, no. 3, pp. 232–239, 2001.

[14] J. Shi, S. R. Schafer, and C. L. C. L. Chen, "Vortex-induced vibration for heat transfer enhancement," in Proceedings of the ASME 2014 International Mechanical Engineering Congress and Exposition, 2014, pp. 1–8.

[15] S. Mohammadshahi, M. Nili-Ahmadabadi, H. Samsam-Khayani, and M. R. Salimpour, "Numerical study of a vortex-induced vibration technique for passive heat transfer enhancement in internal turbulent flow," Eur. J. Mech. B/Fluids, vol. 72, pp. 103–113, 2018.

[16] S. Ali, C. Habchi, S. Menanteau, T. Lemenand, and J.-L. Harion, "Heat transfer and mixing enhancement by free elastic flaps oscillation," Int. J. Heat Mass Transf., vol. 85, pp. 250–264, Jun. 2015.

[17] S. Ali, S. Menanteau, C. Habchi, T. Lemenand, and J. L. Harion, "Heat transfer and mixing enhancement by using multiple freely oscillating flexible vortex generators," Appl. Therm. Eng., vol. 105, pp. 276–289, 2016.

[18] S. Ali, C. Habchi, T. Lemenand, and J.-L. Harion, "Towards self-sustained oscillations of multiple flexible vortex generators," Fluid Dyn. Res., vol. 51, no. 2, p. 025507, 2019.

[19] S. Ali, C. Habchi, S. Menanteau, T. Lemenand, and J. L. Harion, "Three-dimensional numerical study of heat transfer and mixing enhancement in a circular pipe using self-sustained oscillating flexible vorticity generators," Chem. Eng. Sci., vol. 162, pp. 152–174, 2017.

[20] “Thermal Conductivity of common Materials and Gases.” [Online]. Available: https://www.engineeringtoolbox.com/thermal-conductivity-d_429.html. [Accessed: 04-Apr-2019].

[21] “Emissivity Coefficients Materials.” [Online]. Available: https://www.engineeringtoolbox.com/emissivity-coefficients-d_447.html. [Accessed: 04-Apr-2019].

[22] “Radiation Heat Transfer.” [Online]. Available: https://www.engineeringtoolbox.com/radiation-heat-transfer-d_431.html. [Accessed: 04-Apr-2019].

[23] D. Ting, Basics of engineering turbulence. Academic Press, New York, 2016.

[24] G. I. Taylor, “The spectrum of turbulence,” Proc. R. Soc., vol. 164, pp. 476–490, 1938.

[25] R. Bourguet, G. E. Karniadakis, and M. S. Triantafyllou, “Lock-in of the vortex-induced vibrations of a long tensioned beam in shear flow,” J. Fluids Struct., vol. 27, no. 5–6, pp. 838–847, Jul. 2011.

[26] A. Tariq, P. K. Panigrahi, and K. Muralidhar, “Flow and heat transfer in the wake of a surface-mounted rib with a slit,” Exp. Fluids, vol. 37, no. 5, pp. 701–719, 2004.

[27] V. D. Narasimhamurthy and H. I. Andersson, “Numerical simulation of the turbulent wake behind a normal flat plate,” Int. J. Heat Fluid Flow, vol. 30, no. 6, pp. 1037–1043, 2009.

[28] M. Kiya and M. Matsumura, “Incoherent turbulence structure in the near wake of a normal plate,” J. Fluid Mech., vol. 190, pp. 343–356, 1988.

[29] A. Faucett and T. Ameel, “Computational determination of the modified vortex shedding frequency for a rigid, truncated, wall-mounted cylinder in cross flow,” in Proceedings of the ASME 2014 International Mechanical Engineering Congress and Exposition, 2014, pp. 1–7.

[30] H. Wu, D. S.-K. Ting, and S. Ray, “The effect of delta winglet attack angle on the heat transfer performance of a flat surface,” Int. J. Heat Mass Transf., vol. 120, pp. 117–126, 2018.

CHAPTER 4
ON FLEXIBLE RECTANGULAR STRIP HEIGHT ON FLAT PLATE HEAT CONVECTION

Y. Yang, D. S-K. Ting, S. Ray, "On flexible rectangular strip height on flat plate heat convection," International Journal of Heat and Mass Transfer 150 (2020) 119269

4.1 Introduction

Many engineering systems lean on enhancing heat transfer rates to improve their performance. This is also the case with one of the most promising renewable energy technologies – solar photovoltaic ("PV"). The output power of the solar PV panel with crystalline silicon cells can increase by 0.65% per 1℃ drop in the cell temperature [1]. Therefore, much effort has been invested in removing heat from the panels as they generate electricity.

Among others, turbulence/vortex generators, one of the passive cooling techniques, have drawn great attention in recent years due to their structural simplicity, robustness, and effectiveness. Skullong et al. [2] explored the effect of staggered-winglet perforated-tapes (WPT) on the heat transfer in a round tube for Reynolds number from 4000 to 30000. They concluded that the WPT provides the heat transfer augmentation up to 240%~470% compared to that of the plain tube. They reported a maximum thermal enhancement factor of 1.71, around 11~13% higher than that associated with the staggered-winglet without perforated tapes. Gholami et al. [3] numerically studied the heat transfer enhancement of fin-and-tube compact heat exchangers with wavy rectangular winglets. Their results showed that the winglets vortex generators have a significant effect on the flow behavior, reducing the recirculation regions behind the tubes and enhancing the thermal mixing of the fluid. Moreover, they found that the Nusselt number of the heat exchanger with the wavy winglets can be increased by up to 22% compared to the conventional flat rectangular winglet. In another study, the inclined projected winglet pair vortex generators with protrusions were investigated by Oneissi et al. [4]. According to their numerical results, the inclined projected winglet pair with a protrusion provided an additional 7.1% heat transfer augmentation above that of a conventional delta winglet pair. Haik et al. [5] numerically demonstrated the heat transfer characteristics of the curved rectangular winglet placed in a channel. They pointed out that, because of the wider horseshoe vortices and higher strength of longitudinal vortices, the concave-curved winglet generated more disruption in boundary layer growth and fluid mixing, resulting in a higher heat transfer enhancement as well as pressure loss. Within their studied cases, the maximum enhancement occurred using the concave-curved winglet with 75° arc angle, approximately 22% higher than the clean channel without the winglet. Ayli et al. [6] experimentally and numerically explored the optimal dimension and spacing of rectangular fins in a square channel for forced convection. Over the studied conditions, the smallest clearance ratio (width of the plate / height of the fin) and the largest inter-fin distance led to the maximum heat transfer rate. Subsequently, they placed vortex promoters on the finned surface to further enhance the heat transfer rate [7]. These vortex promoters significantly augmented the heat transfer rate. In another study, Beig et al. [8] investigated the optimal position of a vortex generator for heat transfer enhancement of three electronic chips. Their results revealed that the optimal position is above the second chip.

Besides the aforementioned rigid turbulence generators, the flexible and oscillating structures also offer the significant potential in heat transfer augmentation [9]. Ali et al. [10] proposed flexible vortex generators for heat transfer enhancement in a channel. They illustrated that the flexible flap oscillated with a large amplitude when the frequency of oscillation is close to the frequency of vortex shedding, providing higher heat and mass transfer performances. For their studied conditions, 134% heat transfer enhancement was observed when using the flexible flaps instead of the rigid flaps. Sun et al. [11] numerically investigated the effect of the flexible fin on the heat transfer from a circular cylinder. They also observed large-amplitude vibrations when the vortex shedding frequency approaches the natural frequency. This vibrating motion advanced the vortex shedding process, reducing the ‘dead water’ region behind the cylinder, providing approximately 11% heat transfer augmentation. In another study, the heat transfer enhancement of the channel using a cylinder with a flexible plate was investigated by Soti et al. [12]. They concluded that stronger vorticity was generated behind the cylinder with the flexible plate, enhancing the mixing of cooler fluid in the center of the channel and the hotter fluid near the channel walls. Thus, the thermal boundary layer thickness reduces and the Nusselt number at the channel walls increases. Finally, Sastre and Velazquez [13] conducted an experimental study to analyze the heat transfer enhancement of the water channel using a moving prism. They found that the moving prism doubled the Nusselt number value with respect to the clean channel.

It is clear that the heat transfer performance can be significantly improved by well-designed oscillating turbulence generators. Much achievement has been made in recent years, but much more remains to be developed. The thickness effect of the rectangular flexible strip on the convective heat transfer was explored by Yang et al [14]. The vortices with the larger velocity toward the heated surface and the stronger Strouhal fluctuations were observed behind the thinnest strip among the studied models, leading to better heat transfer augmentation. The vortices behind the strip are surmised to be strongly correlated with the mixing between the cooler freestream air and the hotter air near the surface. Thus, the location of the vortices is supposed to have a significant influence on the heat transfer enhancement. The current study aims at furthering the research of the rectangular flexible strip, by focusing on the height of the strip. The height is expected to affect the vortex location, and hence, the resulting heat transfer augmentation.

4.2 Experimentation

This experimental study was carried out in a closed loop wind tunnel with a 76 cm by 76 cm cross-section. A *PTFE* (polytetrafluoroethylene) plate, with an emissivity of 0.92 [15] and a thermal conductivity of 0.25 $Wm^{-1}K^{-1}$ [16], was inlaid in the middle of the fiberglass test section base. The experimental setup is illustrated in Figure 4.1. A basin of water under the *PTFE* plate was heated to boil, maintaining the bottom surface of the *PTFE* plate at a uniform and constant temperature of 100°C by the generated steam. A FLIR C2 thermal camera, with resolution of 60 by 80 pixels, was employed to obtain the local temperature distribution of the top surface of the heated plate. The 0.1 mm-thick and 12.7 mm-wide rectangular flexible strips were made from an aluminum sheet. To demonstrate the effect of strip height on the heat transfer augmentation, three strips with heights of 25.4, 38.1 and 50.8 mm were investigated in this study. The studied strip was located in front of the *PTFE* plate at an incoming wind of 10 m/s, a Reynolds number of approximately 8500 based on the strip width. The orthogonal *X*, *Y*, *Z* in Figure 4.1 represent streamwise, widthwise and vertical directions respectively. The flow-induced vibration of the strips was captured by a Hotshot CC high speed camera at 500 frames per second. The turbulent flow generated by the strips was measured using a 3D hotwire probe (type 55P95) with a constant-temperature anemometer. According to our preliminary study, the turbulent flow is more-or-less developed at 9W downstream of the strips, from which the distinguished difference of the heat transfer of the three studied strips occurs. In other words, 9W represents the stretch of cooling enhancement. Therefore, the 3D hotwire probe was placed at 9W downstream. To avoid aliasing, 10^6 measurements were low passed at 30 kHz, and sampled at 80 kHz.

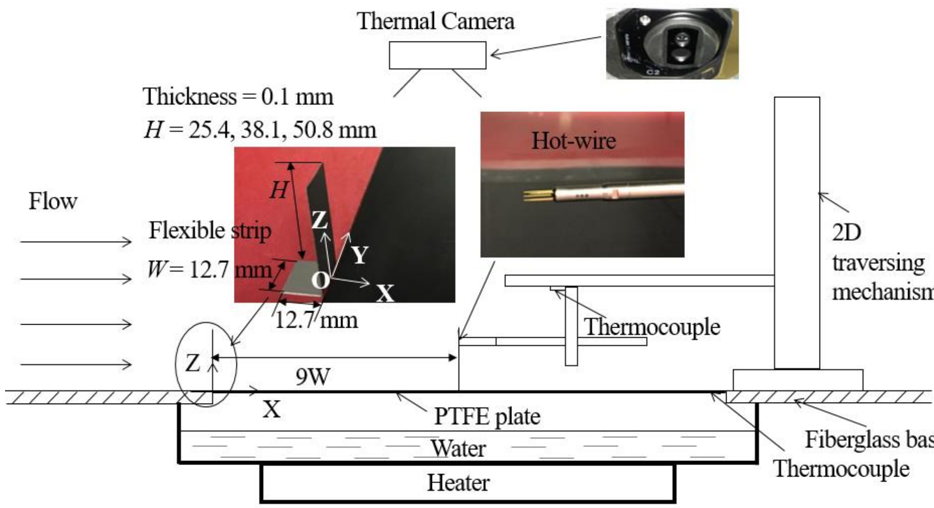

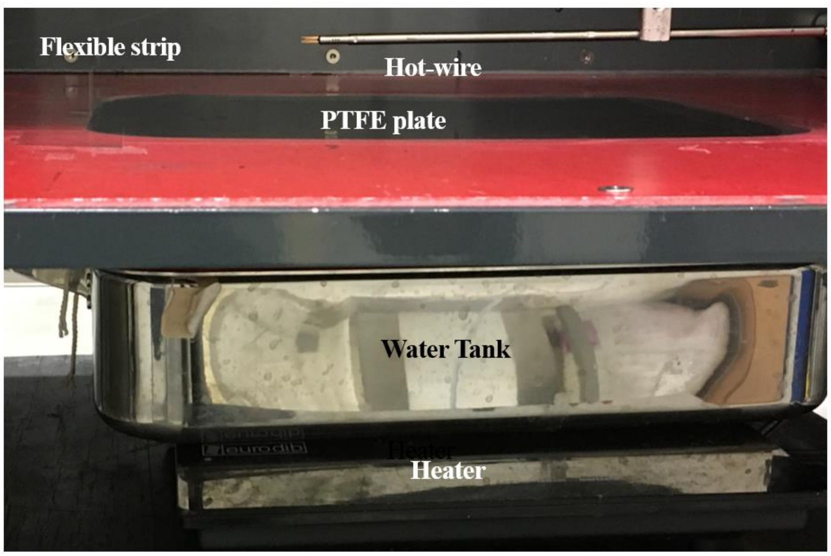

Figure 4. 1. The experimental setup.

4.3 Data Processing

The rate of the total heat transferred from the heated surface can be obtained from,

$$\dot{Q}_{total} = K_{PTFE}A(\frac{T_{bottom} - T_{top}}{t_{PTFE}}) \tag{4.1}$$

where the thermal conductivity of the *PTFE* plate, K_{PTFE}, is 0.25 $Wm^{-1}K^{-1}$, the area of the plate, *A*, is 295 mm by 380 mm, the thickness of the plate, t_{PTFE}, is 3 mm, the bottom surface temperature of the heated plate, T_{bottom} is 100°C. The local temperature of the top surface, T_{top} was measured by a FLIR C2 thermal camera.

Because of the negligible conduction loss, the heat transfers from the *PTFE* plate took place via radiation and convection. Therefore, the rate of convective heat transfer,

$$\dot{Q}_{convection} = \dot{Q}_{total} - \dot{Q}_{radiation} \tag{4.2}$$

Here, $\dot{Q}_{radiation}$ is the rate of radiation heat transfer, which can be obtained from,

$$\dot{Q}_{radiation} = \varepsilon\sigma A(T_{top}^4 - T_{wall}^4) \tag{4.3}$$

where Boltzmann's constant, σ is 5.67x10^{-8} Wm^{-2}K^{-4} [17], emissivity ε is 0.92 [15], and T_{wall} is the wall temperature of the wind tunnel. Here, T_{wall} is assumed to be equal to the air temperature T_{air}, which was measured by a thermocouple; see Figure 4.1.

Then, the coefficient of convective heat transfer is deduced,

$$h = \frac{\dot{Q}_{convection}}{A(T_{top} - T_{air})} \tag{4.4}$$

The corresponding non-dimensional Nusselt number is,

$$Nu = \frac{hL}{K_{air}} \tag{4.5}$$

Here, L and K_{air} are the characteristic length and the thermal conductivity of the ambient air, respectively. To estimate the augmentation of the convective heat transfer, *Nu* is normalized by the reference Nusselt number, i.e.,

$$\frac{Nu}{Nu_0} = \frac{h}{h_0} \tag{4.6}$$

where Nu_0 and h_0 are the Nusselt number and the convective heat transfer coefficient, respectively, for the unperturbed reference case in the absence of the flexible strip. It should be noted that the size of the studied model is negligible compared to the wind tunnel cross-section, and thus, the pressure drop is not considered in the current study.

With the 3D hotwire probe, the instantaneous velocities in streamwise, widthwise and vertical directions can be deduced,

$$U_i = \overline{U} + u \,;\, V_i = \overline{V} + v \,;\, W_i = \overline{W} + w \tag{4.7}$$

Here, $\overline{U}, \overline{V}, \overline{W}$ are the corresponding time-averaged velocities, which can be obtained from

$$\bar{U} = \frac{1}{N}\sum_{i=1}^{N} U_i \; ; \; \bar{V} = \frac{1}{N}\sum_{i=1}^{N} V_i \; ; \; \bar{W} = \frac{1}{N}\sum_{i=1}^{N} W_i \tag{4.8}$$

The sample size, N=10^6. From the instantaneous fluctuating velocities, u, v, and w, the corresponding root-mean-square velocities can be calculated,

$$u_{rms} = \sqrt{\sum_{i=1}^{N} \frac{{u_i}^2}{N-1}} \; ; \; v_{rms} = \sqrt{\sum_{i=1}^{N} \frac{{v_i}^2}{N-1}} \; ; \; w_{rms} = \sqrt{\sum_{i=1}^{N} \frac{{w_i}^2}{N-1}} \tag{4.9}$$

The relative turbulence intensity is

$$Tu = \frac{u_{rms}}{U_\infty} \tag{4.10}$$

where U_∞ is the freestream velocity.

As turbulent flow induced by the studied model is highly three dimensional [18], to better illustrate the total turbulence level, the normalized turbulent kinetic energy,

$$ke = \frac{1}{2}\frac{(u_{rms}^2 + v_{rms}^2 + w_{rms}^2)}{U_\infty^2} \tag{4.11}$$

is introduced.

The studied flexible strip can be viewed as a bluff body subjected to the incoming flow, generating vortex shedding of certain frequency. This frequency can be normalized with respect to the freestream velocity and the width of the strip to give the Strouhal number,

$$St = \frac{fW}{U_\infty} \tag{4.12}$$

Also, based on the freestream velocity, U_∞, and the width of the strip, W, the Reynolds number can be calculated as,

$$Re_W = \frac{WU_\infty}{\nu} \tag{4.13}$$

where ν is kinematic viscosity, and the Reynolds number in the current study is around 8500.

The intensity of the vortex structures behind the flexible strip can be described by the X-vorticity,

$$\omega = \frac{\partial \bar{W}}{\partial Y} - \frac{\partial \bar{V}}{\partial Z} \tag{4.14}$$

This vorticity can be normalized by the width of the strip and the time-averaged freestream velocity, i.e.,

$$\Omega = \frac{\omega W}{U_\infty} \tag{4.15}$$

Other than the local heat transfer enhancement, equally important is the overall improvement over the entire panel. Therefore, appropriate span-wise averages are also of interest. The span-averaged values can be defined as

$$\bar{P} = \frac{1}{n}\sum_{i=1}^{n} P_i \tag{4.16}$$

where P is the parameter of interest, such as normalized Nusselt number and velocity, and n is the number of values used in the averaging. For the average across the ±3W in the Y-direction, n = 19, and this is used for the span-averaged Nu/Nu_0 profile.

4.4 Results and Discussion

4.4.1 Flow-induced Vibration

As mentioned earlier, the vibration of the vortex generator has been found to be helpful in furthering the heat and mass transfer rate [10]. Accordingly, the vibrating displacement of the top edge of the strip and the corresponding power spectrum are depicted in Figure 4.2. Here, the power spectrum was obtained according to the Fourier analysis, indicating the power distribution of the vibrating displacement with respect to frequency. With the increase in strip height, the vibration frequency decreases. The distinct peak value of the power spectrum density occurs at approximately 120Hz, 62Hz, and 22Hz for the 25.4, 38.1, and 50.8 mm-height strips, respectively. Meanwhile, the displacement of the vibration tends to increase, which may lead to better heat transfer enhancement. However, due to the difference in strip height, the vortex structure behind each strip is likely to take place at different locations. The location and extent of this secondary flow structure are also expected to affect the heat transfer. Therefore, the flow characteristics will be discussed in the next section, in an effort to understand the heat transfer augmentation.

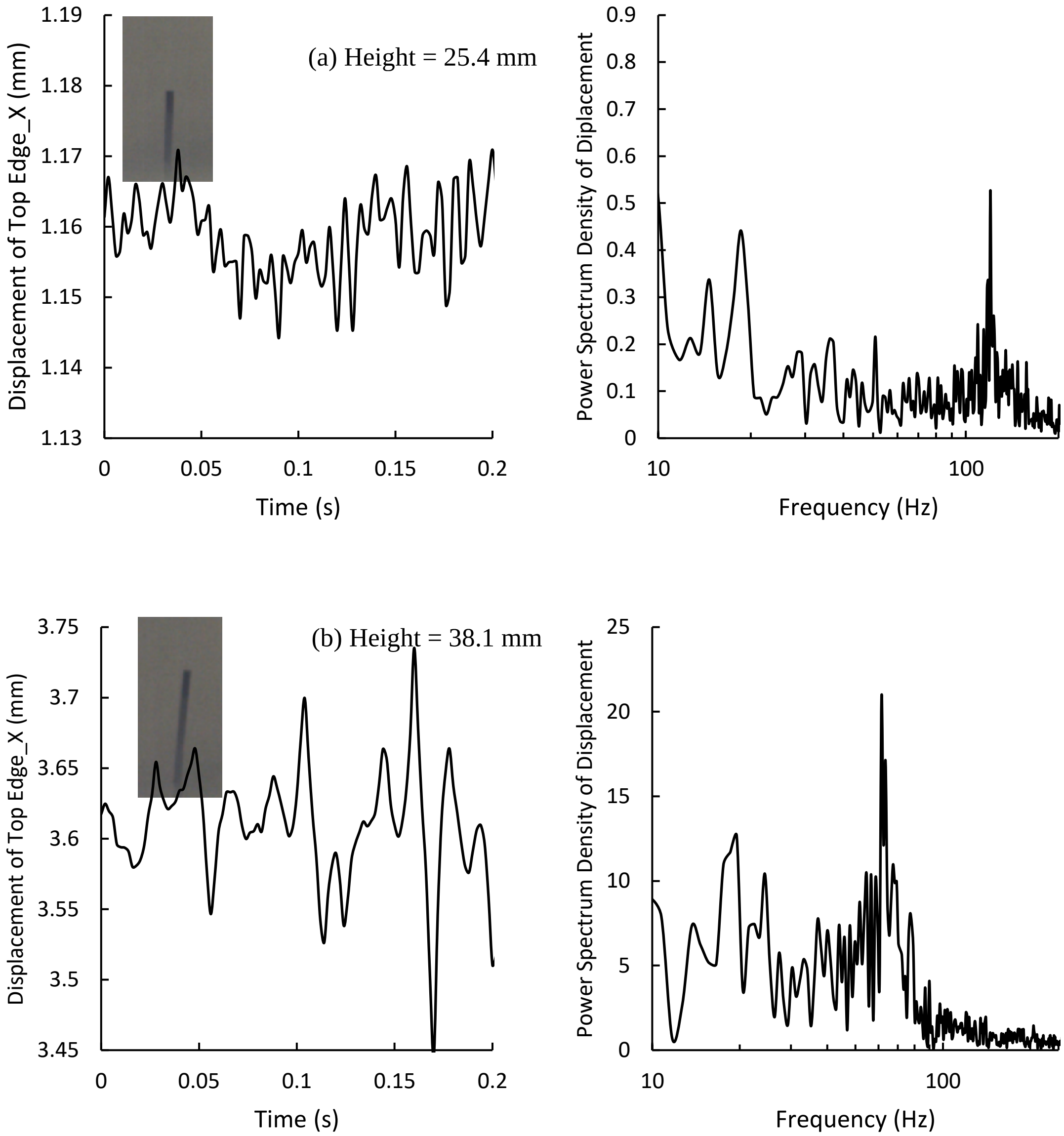
(a) Height = 25.4 mm
Displacement of Top Edge_X (mm)
1.19
1.18
1.17
1.16
1.15
1.14
1.13
0
0.05
0.1
0.15
0.2
Time (s)
Power Spectrum Density of Displacement
0.9
0.8
0.7
0.6
0.5
0.4
0.3
0.2
0.1
0
10
100
Frequency (Hz)
(b) Height = 38.1 mm
Displacement of Top Edge_X (mm)
3.75
3.7
3.65
3.6
3.55
3.5
3.45
0
0.05
0.1
0.15
0.2
Time (s)
Power Spectrum Density of Displacement
25
20
15
10
5
0
10
100
Frequency (Hz)

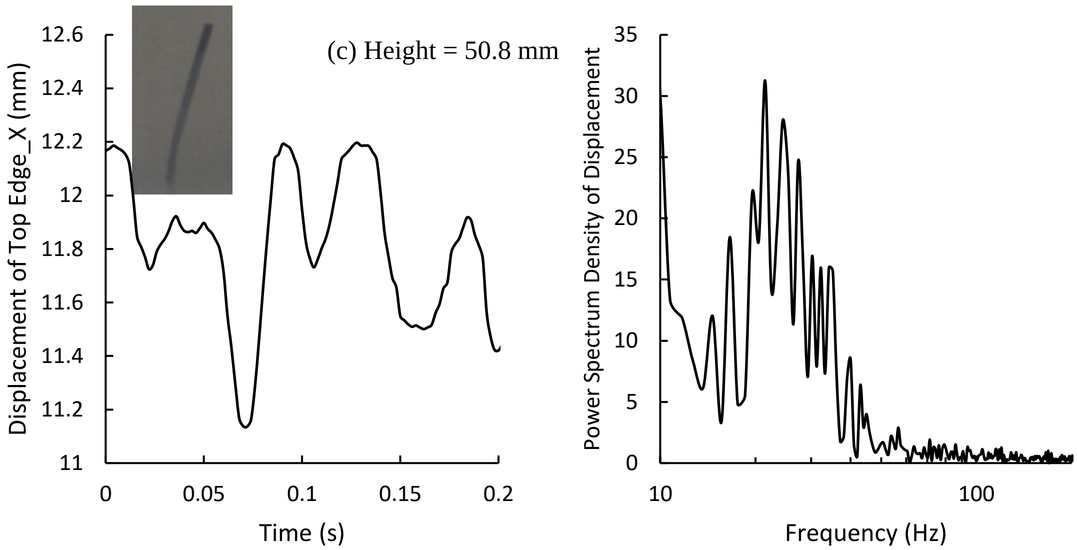

Figure 4. 2. Displacement of the top edge of the strip and the power spectrum density of the displacement (a) strip height = 25.4 mm (b) strip height = 38.1 mm (c) strip height = 50.8 mm.

4.4.2 Flow Characteristics

4.4.2.1 Velocity Profile

In standard heat transfer textbooks such as [19], the local heat transfer coefficient over a flat plate is proportional to $Re^{0.5}$ and $Re^{0.8}$ for laminar flow and turbulent flow, respectively. This indicates that both the magnitude and profile of the velocity are important in convection heat transfer. Specifically, the thermal energy of a heated surface would be more effectively swept away by a larger local velocity, especially if the flow is turbulent. A numerical study on the effect of wind convection on the photovoltaic panel thermal condition was explored by Assila et al [20]. The thermal benefit of forced convection is observed to be strongly dependent on the wind speed. The averaged heat transfer coefficient increases from approximately 22 to 40 $WK^{-1}m^{-2}$ with increasing wind velocity from 5 to 10 ms^{-1}. With this backdrop, the time-averaged streamwise velocity profile normalized by the freestream velocity at 9W downstream of the strip is depicted in Figure 4.3, with uncertainty of approximately 0.023; see Appendix A. It is clear from the figure that the 25.4 mm-height strip provides the largest near-wall velocity, which is approximately $0.7U_{\infty}$ at X=9W, Y=0, and Z=1W. This value is approximately 11.7% and 19.8% higher than that associated with the 38.1 mm-height and 50.8 mm-height strips, respectively. This infers that the streamwise flow condition induced by the 25.4 mm-height strip is likely more effective in convecting heat away from the hot plate.

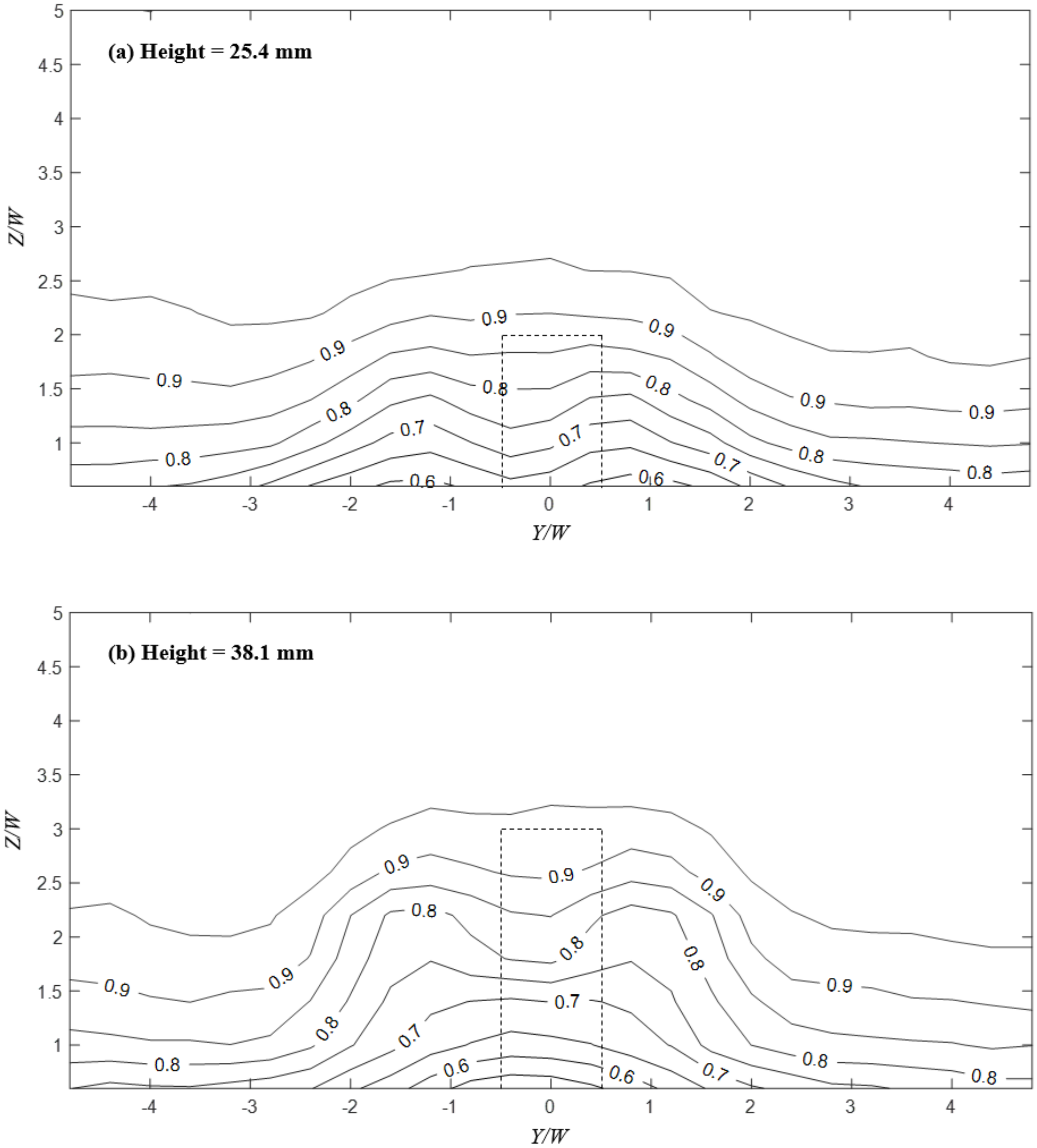
(a) Height = 25.4 mm
Z/W
Y/W
0.9
0.8
0.7
0.6
(b) Height = 38.1 mm
Z/W
Y/W
0.9
0.8
0.7
0.6

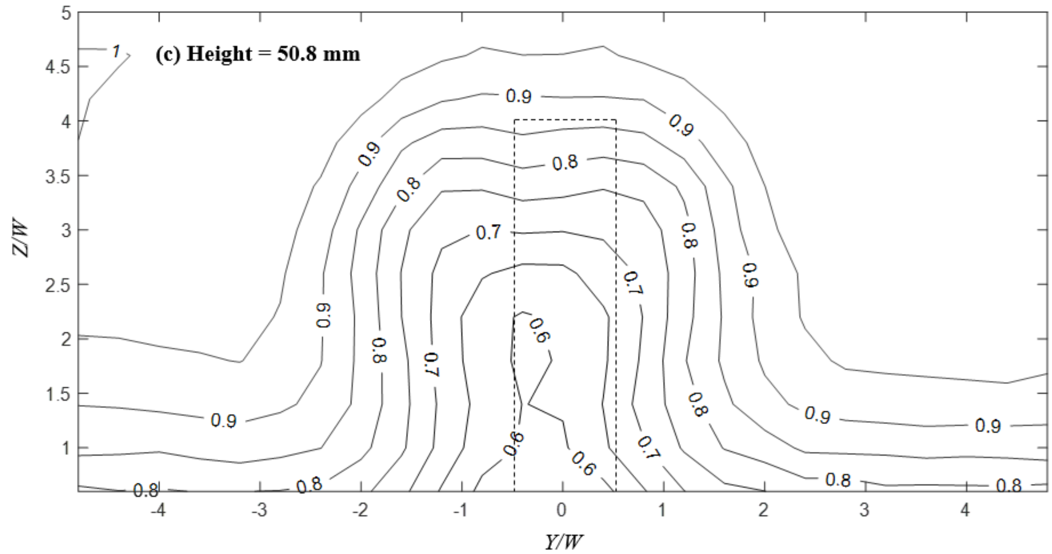

Figure 4. 3. Normalized streamwise velocity profile at 9W downstream of the strip (a) stripe height = 25.4 mm (b) strip height = 38.1 mm (c) strip height = 50.8 mm.

Figure 4.4 shows the contours of X-vorticity normalized by the width of the strip ($W = 12.7$ mm) and the freestream velocity ($U_{\infty} \approx 10$ m/s). To indicate the local flow behavior, cross-stream velocity vectors are also depicted. The swirling motions can be easily distinguished in the figures. It is interesting to notice that these vortical motions seem to generate a couple of notable flow movements toward the heated surface. As far as convective heat transfer is concerned, the downwash flow velocity, towards the heated surface, has significance. An experimental study regarding the flow and heat transfer in the wake of a surface-mounted, rigid rib was conducted by Tariq et al. [21]. They found that the heat transfer mechanism was strongly related to the cross-streamwise velocity component. The reduction of the cross-streamwise velocity can be correlated with a reduction of the momentum transport in the direction normal to the wall, resulting in a decrease of the heat transfer augmentation. In another study, the effect of the impinging jet velocity on heat transfer was investigated [22]. Increase in the Nusselt number peak value was observed with the increase of the cross-flow velocity. In the current study, the aforementioned downwash velocity is able to influence the cooler freestream air more effectively toward the hot plate, increasing the fluid mixing and the resulting heat transfer augmentation near Y/W=0. Also, with decreasing strip height from 50.8 to 25.4 mm, the location of the vortex core moves from 3.4W to 1.4W above the plate. This is attributed to the interaction of vortices shed from the side edges and the top edge of the strip [14]. These close-to-wall vortices have been found to be more beneficial to the mixing of the cooler air with the hotter air near the heated surface [12]. With the 25.4 mm high strip resulting in the vortex core closes to the hot plate at Z = 1.4W, the corresponding heat transfer augmentation is expected to be greatest. The intensity of these vortical structures is also of importance, i.e., a stronger vorticity has been linked to the strongest mixing [12]. However, among the three studied cases, the vortex behind the 25.4 mm-height strip is observed to be slightly weaker than the other two. This implies that the location of the vorticity seems to have more effect on the heat transfer augmentation than the strength of the vorticity. As the location and the vortex intensity are of different dimensions, a definite, quantitative comparison is not practically possible. The point is that it is better to have some swirling motion near the plate to sweep away the heat, rather than a strong swirl that does not penetrate into the highly-thermally-resistive boundary layer.

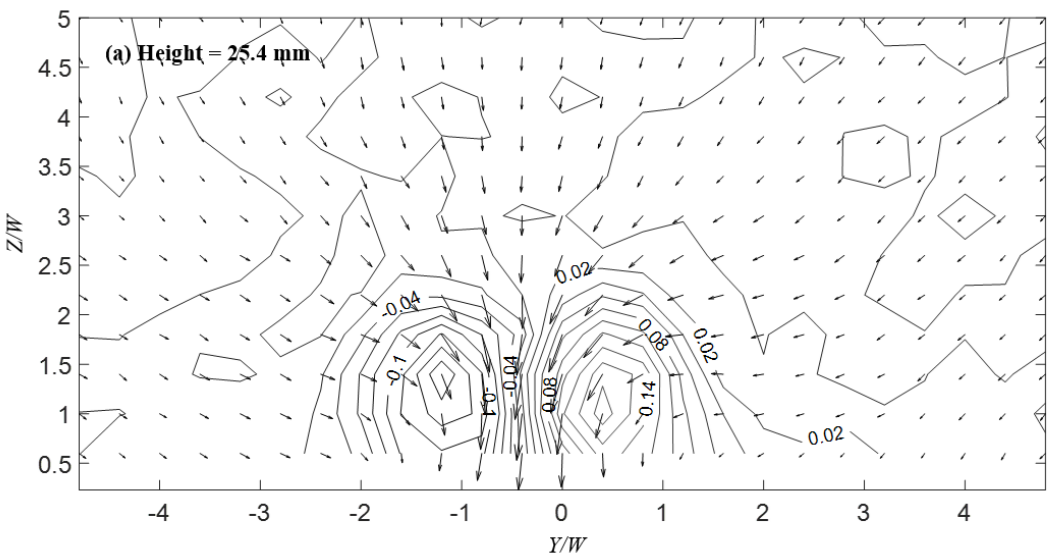

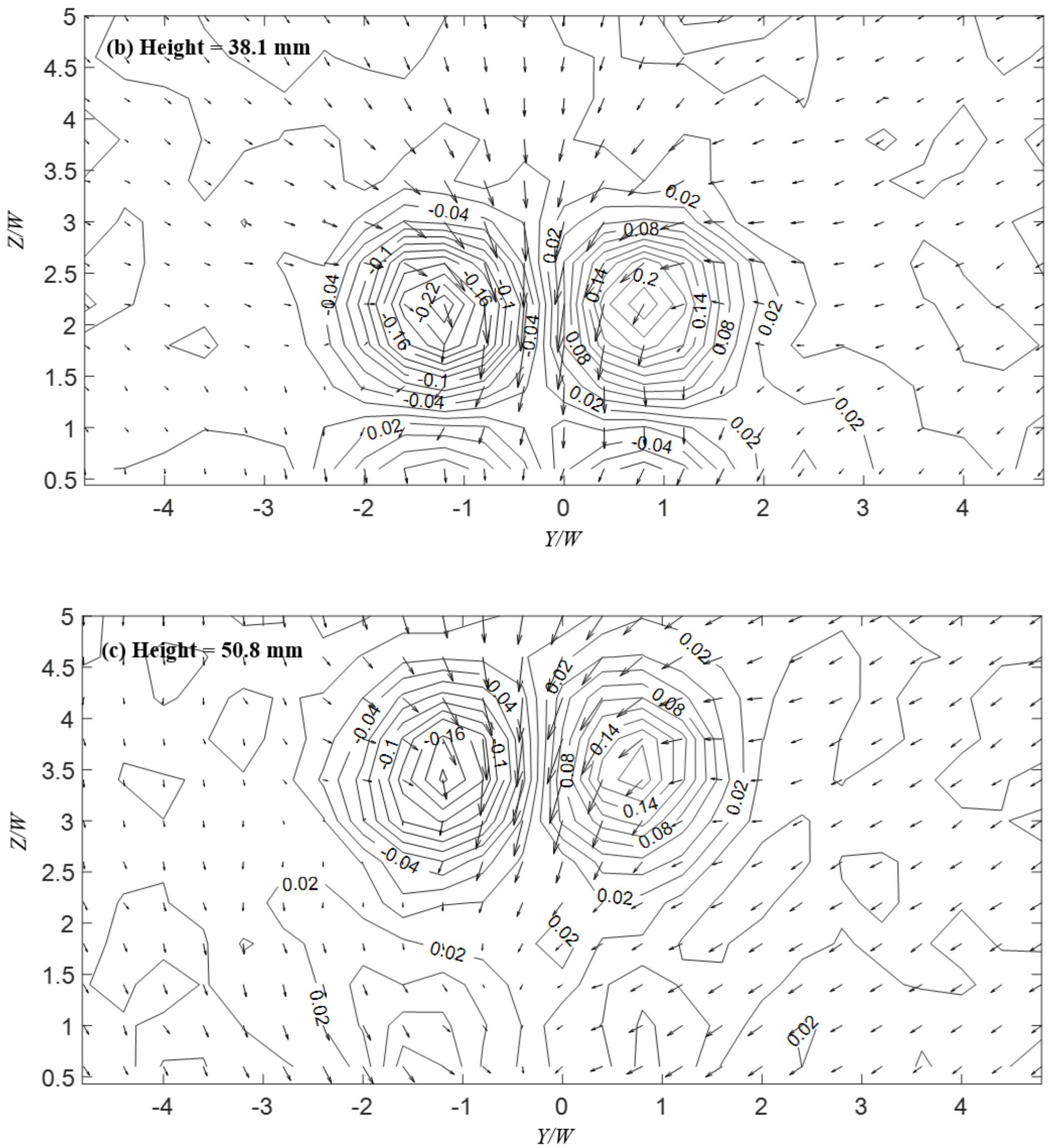

Figure 4. 4. Non-dimensional X-vorticity contour and velocity vector in YZ plane at 9*W* downstream of the strip (a) strip height = 25.4 mm (b) strip height = 38.1 mm (c) strip height = 50.8 mm.

The velocity toward the heated surface is also important. The $\overline{W}$ profile normalized by the freestream velocity is shown in Figure 4.5 to further illustrate the difference in the secondary flow generated by the strips of different height. The uncertainty of normalized $\overline{W}$ is around 0.005; see Appendix A. Since the turbulent flow behind the studied model is highly three dimensions, the span-averaged values are utilized. These span-averaged values correspond to the average over *Y*=±1.2*W*, encompassing the vortex cores behind the strip. From Figure 4.5, the negative peak values can be observed at around Z=1.5W, 2.5W, and 4W behind the 25.4 mm, 38.1 mm and 50.8

mm-high strip, respectively. This indicates that a significant amount of air circulates downward from the top edge of the strip. It is notable that the 25.4 mm-high strip induced the largest near-wall negative $\overline{W}/U_\infty$. The span-averaged downward velocity of 25.4 mm strip is approximately $0.089U_\infty$ at Z=1W, much larger than that of 38.1 mm and 50.8 mm strips, which are around $0.066U_\infty$ and $0.020U_\infty$, respectively. As this occurs just above the heated surface, the resulting cooling effect is expected to be most significant.

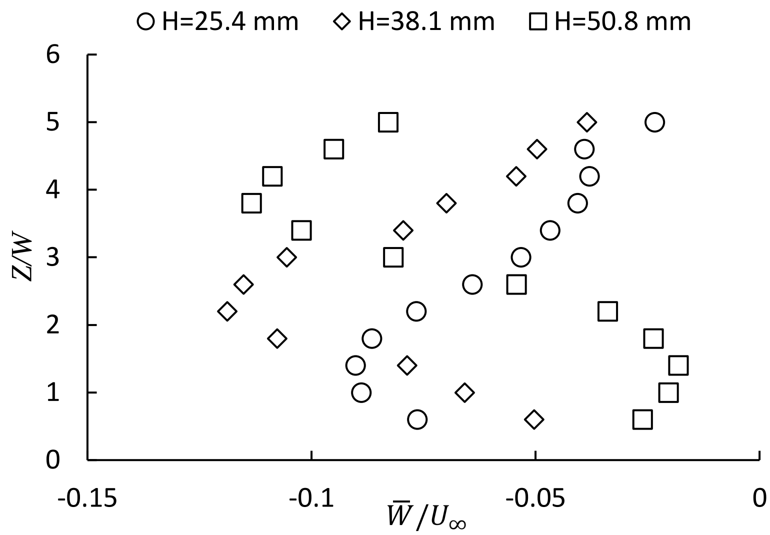

Figure 4. 5. $\overline{W}/U_\infty$ profile at 9*W* downstream of the flexible strip (span-averaged across *Y*=±1.2*W*).

4.4.2.2 Power Spectrum

To further understand the regular vortex structures shed from the strip, the power spectrum of the fluctuating velocity is analyzed. Figure 4.6 demonstrates the power spectrum density at X=9W, Y=-1.2W, Z=1.4W for the 25.4 mm-high strip, X=9W, Y=-1.2W, Z=2.2W for 38.1 mm-high strip, and X=9W, Y=-1.2W, Z=3.4W for 50.8 mm-high strip. Their locations correspond closely to the vortex cores identified in Figure 4.4. The fast Fourier transformed values are divided into 2^{14} sections with 50% overlap to obtain a smoother graph for clarity. It is clear from Figure 4.6 that distinct peaks occur at approximately 63 Hz, 73 Hz, and 78 Hz for 25.4 mm, 38.1 mm and 50.8 mm-high strip, respectively. This corresponds to a Strouhal number of approximately 0.08, 0.09, and 0.10 based on the width of the strip. Compared to the infinitely long strip, which St = 0.14 ~ 0.16 [23], the Strouhal number of the strip of finite height is smaller, presumably due to the fact that the vortices shed from the top edge tend to dampen the Kármán vortex street from the sides [24]. Moreover, increasing in the strip height tends to result in an increase in *St*. This is in agreement with the experimental results obtained by Beitel et al. [25], which showed that at low aspect ratios (cylinder height / cylinder diameter < 3±1.5), the increase of aspect ratios leads to a larger and wider recirculation zone and the increase of *St*. It is also interesting to note that, the 25.4 mm-high strip induced the smallest peak value at the vortex shedding frequency, probably due to the smallest-displacement vibration associated with the shortest dimension (height). From the perspective of vortex power spectrum alone, the shortest strip, i.e. 25.4 mm-height strip, is supposed to have the worst effect on the heat transfer enhancement.

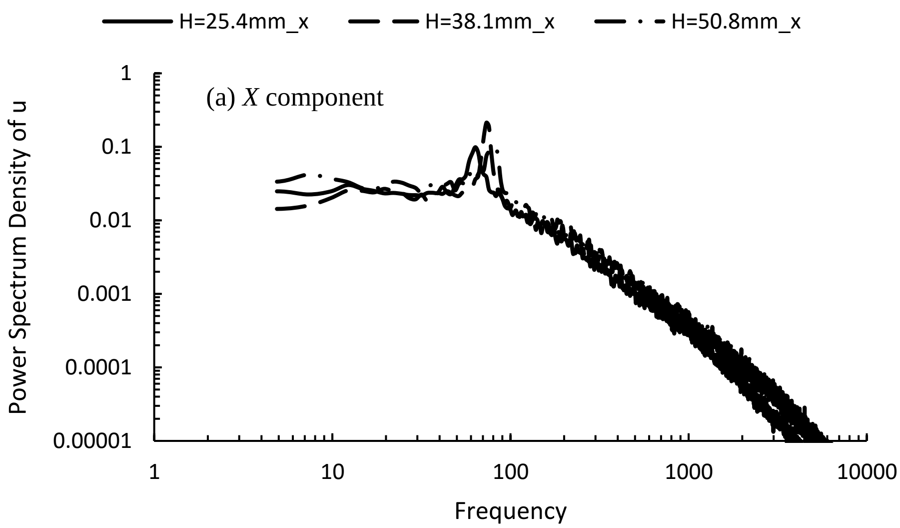

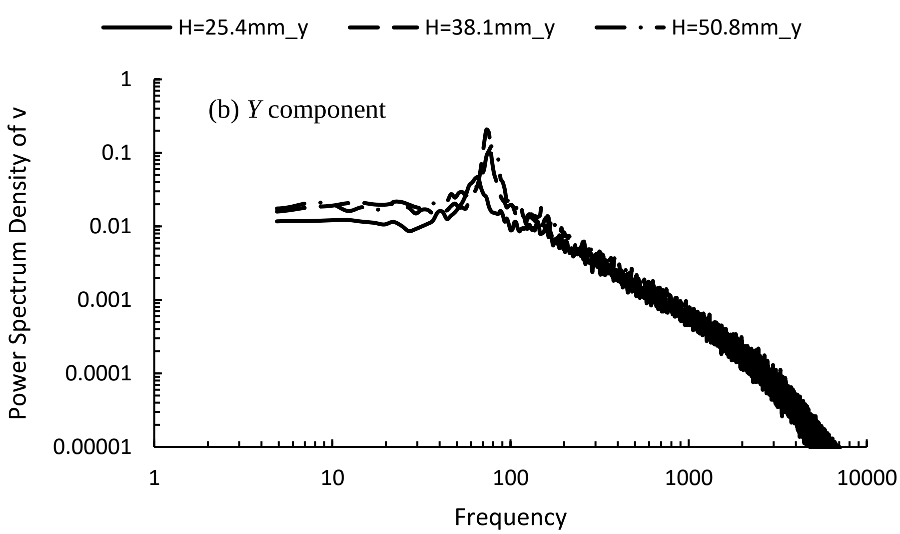

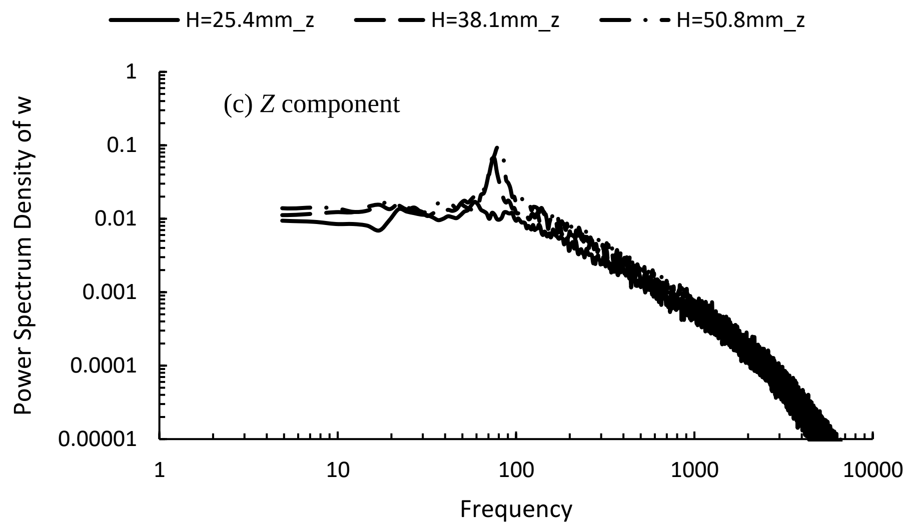

Figure 4. 6. Power spectrum density of fluctuating velocity at X=9W, Y=-1.2W, Z=1.4W for the 25.4 mm-high strip, X=9W, Y=-1.2W, Z=2.2W for the 38.1 mm-high strip, and X=9W, Y=-1.2W, Z=3.4W for the 50.8 mm-high strip.

4.4.2.3 Turbulence Intensity and Turbulent Kinetic Energy

To further understand the vortex structure and the resulting heat transfer augmentation, fluctuating velocity is scrutinized. The root-mean-square streamwise fluctuating velocity (u_{rms}) is normalized by the freestream velocity (U_∞) to give the streamwise turbulence intensity (*Tu*), which is depicted in Figure 4.7. Two high turbulence regions can be observed at Z=1.4W for the 25.4 mm-high strip. The locations corresponding to these intense-turbulence areas shift upward to around Z=3.4W for the 50.8 mm-high strip. These intense-turbulence zones conform to the vortex motion core shown in Figure 4.4. As important, the peak turbulence intensity behind the 25.4 mm-height strip is around 0.16, roughly 0.02 lower than those of 38.1 mm and 50.8 mm-height strip. The uncertainty of *Tu* is around 0.008.

Because the turbulence induced by the studied model is highly three dimensions, the normalized total turbulent kinetic energy is also worth analyzing. The total turbulent kinetic energy signifies the total fluctuation level of velocities in all three orthogonal *X*, *Y*, and *Z* directions. It is associated with gradients in time-averaged flow, and has been linked to increasing fluid mixing and enhancement of heat transfer [26]. It is interesting to note that, only one peak region of total turbulent kinetic energy can be observed, instead of two as in the contours of streamwise turbulence intensity. This is likely due to the interaction of streamwise fluctuation with the fluctuation in widthwise and vertical directions; see Figure 4.8. These peak values occur at around Y=0, which is good for promoting heat transfer near the middle region, Y=0, of the strip. The peak *ke* value of 25.4, 38.1, and 50.8 mm-high strip is around 0.031, 0.049, and 0.055, respectively. And the uncertainty of *ke* is calculated to be approximately 0.005. Again, the 25.4 mm-high strip provides the lowest turbulence intensity and total kinetic energy. Nonetheless, the location of the peak velocity fluctuation for this shortest strip is closest to the heated surface, which is thought to be more important for flat plate heat transfer enhancement.

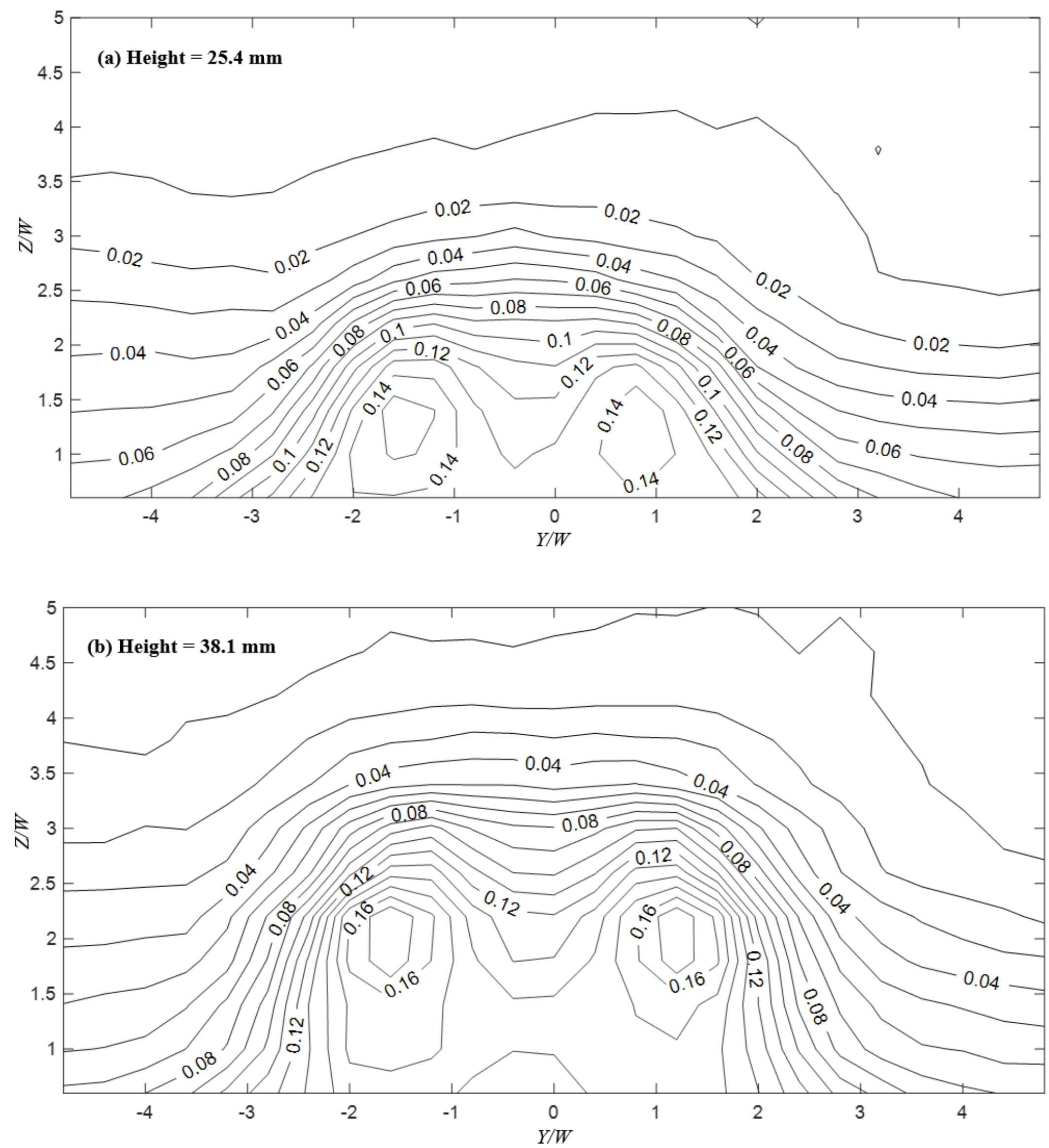

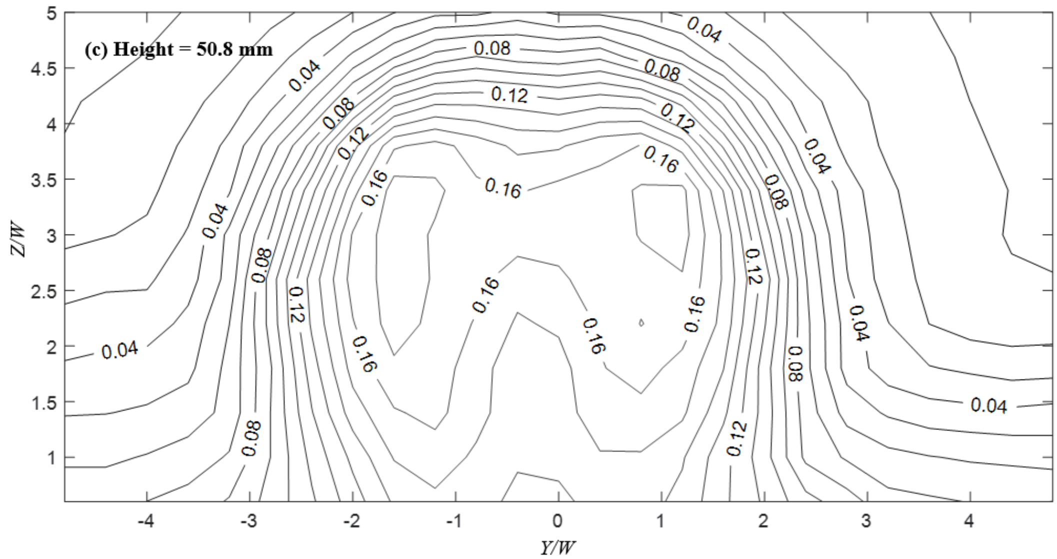

Figure 4. 7. Streamwise turbulence intensity at 9*W* downstream of the strip (a) strip height = 25.4 mm (b) strip height = 38.1 mm (c) strip height = 50.8 mm.

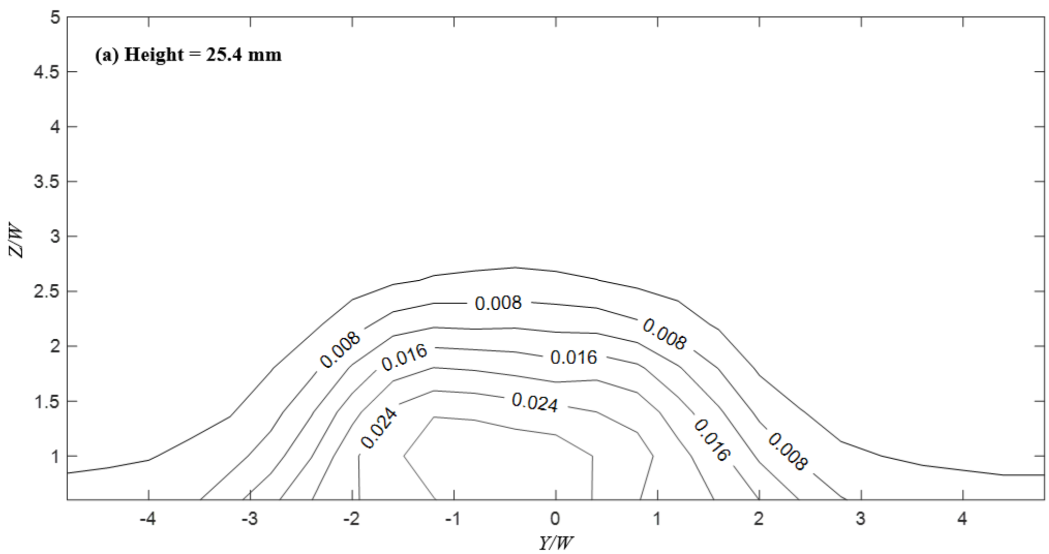

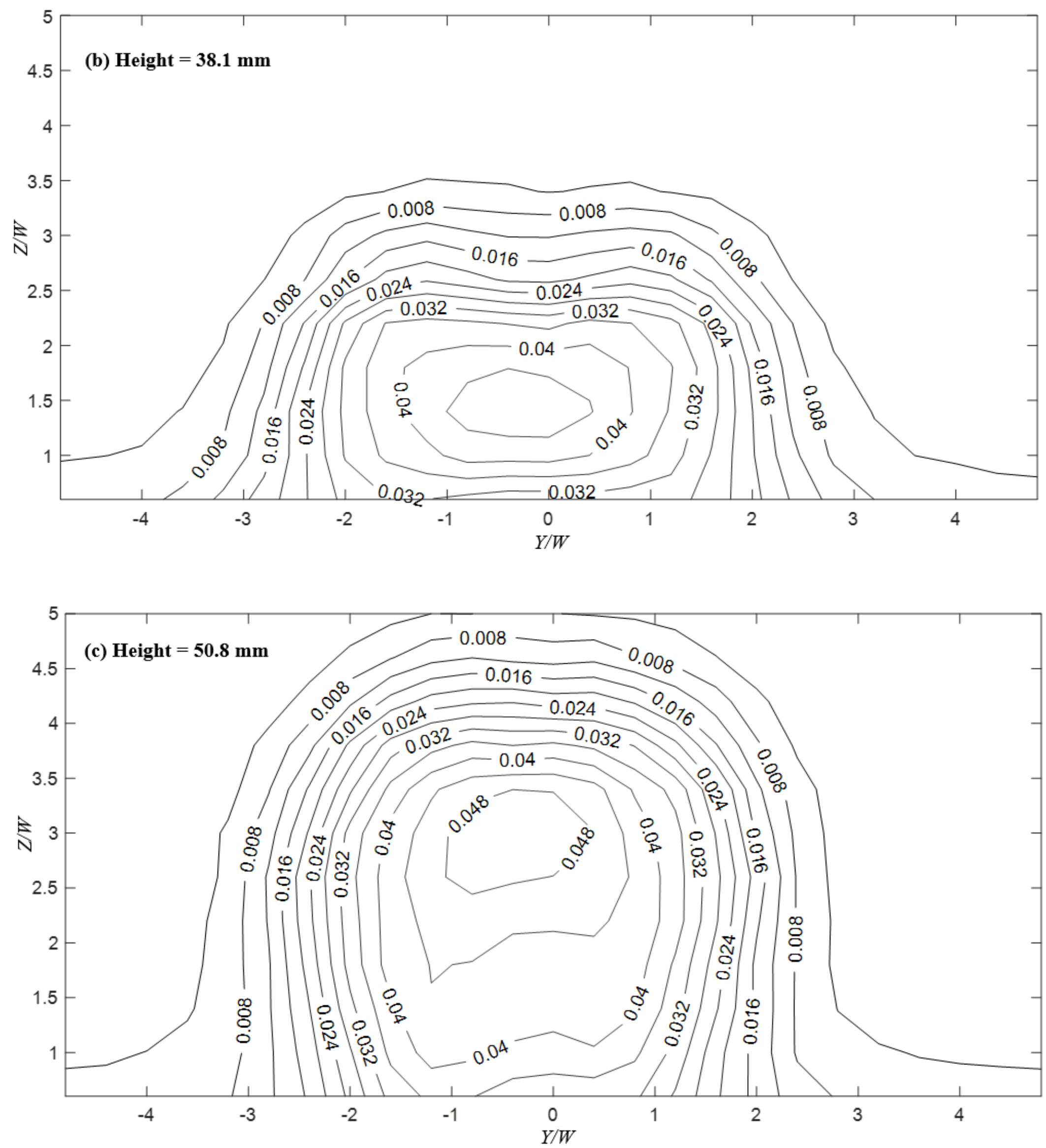

Figure 4. 8. Non-dimensional turbulent kinetic energy at 9*W* downstream of the strips with height of (a) 25.4 mm (b) 38.1 mm (c) 50.8 mm

4.4.3 Heat Transfer Enhancement

To demonstrate the effect of the strips on the convective heat transfer enhancement, contours of normalized Nusselt number are depicted in Figure 4.9. The uncertainty of local Nu/Nu_0 is estimated to be approximately 0.066; see Appendix A. A high Nu/Nu_0 value of approximately 2 can be observed in the near strip region until X/W=2, presumably due to the strong vortices shed from the strip. Moreover, the heat transfer augmentation presents a decreasing trend farther downstream, implying the decay of the vortex structure and flow turbulence. Most interestingly, a higher and long-lasting heat transfer enhancement can be found behind the 25.4 mm-high strip. This is probably due, in large part, to the larger near-surface streamwise velocity and the fact that the vortical structures generated by this shortest strip are closest to the heated surface, as discussed in the previous section; see Figure 4.3 and Figure 4.4. It is also interesting to note that the heat transfer augmentation induced by the 25.4 mm-strip is as high as 41% at the end of the heated surface, at approximately 280 mm behind the strip. It is more effective than some other longitudinal vortex generators under the open flow condition, such as the jet explored by Puzu et al. [27] and the delta-winglet proposed by Wu et al. [28], which were found to furnish a maximum of 7% and 22% enhancement on the heated flat surface at the same downstream distance, i.e. 280 mm.

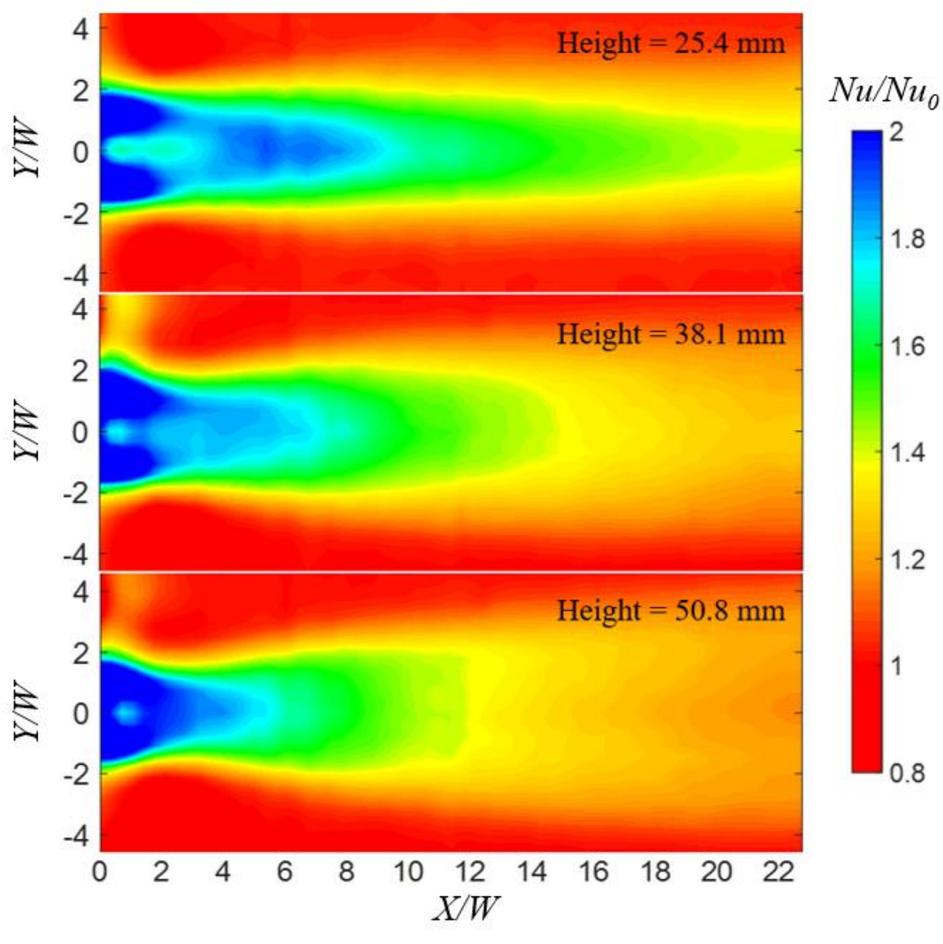

Figure 4. 9. Normalized Nusselt number (*Nu/Nu_0*) downstream of the strip

To better illustrate the heat transfer augmentation of the heated surface, the span-averaged results across ±3W in the Y direction are plotted with respect to downstream distance of the strip in Figure 4.10. The highest Nu/Nu_0 value can be found right behind the strip, where the vortex is the strongest. Then the Nu/Nu_0 value drops to approximately 1.4 at 3W downstream, beyond which it increases and peaks slightly at around 6W downstream. The increasing trend from 3W to 6W is presumably due to the expanding Nu/Nu_0 area in the Y direction (Figure 4.9). Farther downstream, Nu/Nu_0 decays gradually, concurring with the fact that the flow is slowly restoring to a less perturbed condition. Also, the 25.4 mm-high strip was observed as having the best heat transfer augmentation from 3W downstream to the end of the heated surface, approximately 0.1 larger than that of the 50.8 mm-high strip.

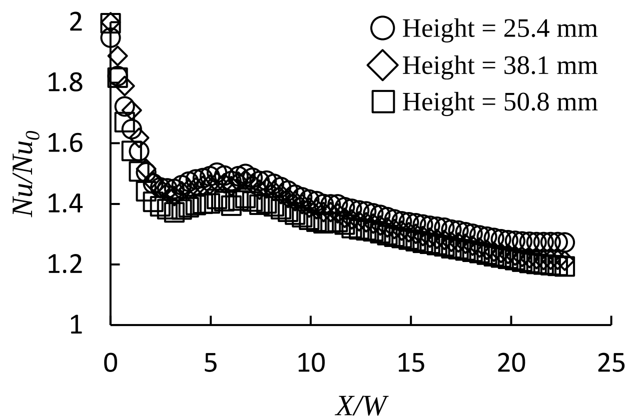

Figure 4. 10. Span-averaged (from Y = -3W to 3W) normalized Nusselt number downstream of the strip.

Figure 4.11 shows the cross-stream normalized Nusselt number profile at 3W and 9W downstream distance. It is noted from the figures that, with increasing downstream distance, the peak value of Nu/Nu_0 decreases, while the enhanced cross-stream span expands from ±2.5W to ±3.2W. It is also interesting to note that, the Nu/Nu_0 peak values of the strips with different height are approximately at the same level at 3W downstream. With the development and decay of the vortex structure, the difference in Nu/Nu_0 of the studied cases becomes distinguishable. For 25.4 mm-high strip, the heat transfer enhancement is still high at around 76% at 9W downstream. Comparatively, the Nu/Nu_0 peak value of the 50.8 mm-high strip has already decreased to 1.50 at the same downstream location. This indicates that the 25.4 mm-high strip provides the best heat transfer performance over the heated flat surface among the studied cases. Also notable is that the peak values occur at around Y=0, presumably due to the better heat and mass transporting by the larger downwash velocity and the higher turbulent kinetic energy in this area; see Figure 4.4 and Figure 4.8.

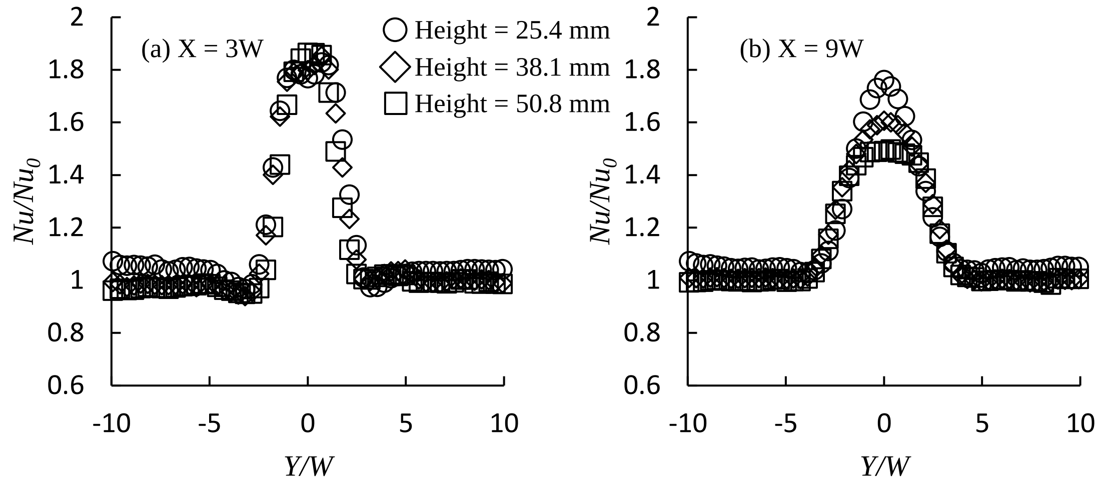

Figure 4. 11. Cross-stream normalized Nusselt number profile at (a) X = 3W, (b) X = 9W

4.5 Conclusions

Rectangular, 0.1 mm-thick, 12.7 mm wide (W), aluminum flexible strips with height of 25.4, 38.1, and 50.8 mm were investigated for their effectiveness on flat plate convective heat transfer augmentation. The heat transfer results at 10 m/s (Re_W= 8500) wind were expressed in terms of the Nusselt number normalized by the unstriped reference case (Nu/Nu_o). The 25.4 mm-high strip resulted in the most forceful heat transfer enhancement, from 3W downstream to the end of the heated surface. The corresponding span-averaged Nu/Nu_o is approximately 0.1 larger than that associated with its taller counterpart, the 50.8 mm-high strip. This superior heat enhancement occurs in spite of the weaker vortex and the less-intense turbulence spawned by the 25.4 mm-high strip. Its short height resulted in significantly lower vibration amplitude and power, but induced vortical structures significantly closer to the heated surface. The later effect caused a larger near-surface downwash velocity and a thinner boundary layer, making it effective in cooling the hot plate.

Acknowledgments

This work was made possible by Natural Sciences and Engineering Research Council of Canada and Ontario Centres of Excellence.

References

[1] E. Radziemska, “The effect of temperature on the power drop in crystalline silicon solar cells,” Renew. Energy, vol. 28, no. 1, pp. 1–12, 2003.

[2] S. Skullong, P. Promvonge, C. Thianpong, and M. Pimsarn, “Heat transfer and turbulent flow friction in a round tube with staggered-winglet perforated-tapes,” Int. J. Heat Mass Transf., vol. 95, pp. 230–242, 2016.

[3] A. A. Gholami, M. A. Wahid, and H. A. Mohammed, “Heat transfer enhancement and pressure drop for fin-and-tube compact heat exchangers with wavy rectangular winglet-type vortex generators,” Int. Commun. Heat Mass Transf., vol. 54, pp. 132–140, 2014.

[4] M. Oneissi, C. Habchi, S. Russeil, T. Lemenand, and D. Bougeard, “Heat transfer enhancement of inclined projected winglet pair vortex generators with protrusions,” Int. J. Therm. Sci., vol. 134, pp. 541–551, 2018.

[5] H. Naik, S. Harikrishnan, and S. Tiwari, “Numerical investigations on heat transfer characteristics of curved rectangular winglet placed in a channel,” Int. J. Therm. Sci., vol. 129, no. November 2017, pp. 489–503, 2018.

[6] E. Ayli, O. Bayer, and S. Aradag, “Experimental investigation and CFD analysis of rectangular profile FINS in a square channel for forced convection regimes,” Int. J. Therm. Sci., vol. 109, pp. 279–290, 2016.

[7] E. Aylı and Ö. Bayer, “Optimization of Vortex Promoter Parameters to Enhance Heat Transfer Rate in Electronic Equipment,” J. Therm. Sci. Eng. Appl., vol. 12, no. 2, pp. 1–11, 2020.

[8] S. A. Beig, E. Mirzakhalili, and F. Kowsari, “Investigation of optimal position of a vortex generator in a blocked channel for heat transfer enhancement of electronic chips,” Int. J. Heat Mass Transf., vol. 54, no. 19–20, pp. 4317–4324, 2011.

[9] R. K. B. Gallegos and R. N. Sharma, “Flags as vortex generators for heat transfer enhancement: Gaps and challenges,” Renew. Sustain. Energy Rev., vol. 76, pp. 950–962, 2017.

[10] S. Ali, C. Habchi, S. Menanteau, T. Lemenand, and J. L. Harion, “Heat transfer and mixing enhancement by free elastic flaps oscillation,” Int. J. Heat Mass Transf., vol. 85, pp. 250–264, 2015.

[11] X. Sun, Z. Ye, J. Li, K. Wen, and H. Tian, “Forced convection heat transfer from a circular cylinder with a flexible fin,” Int. J. Heat Mass Transf., vol. 128, pp. 319–334, 2019.

[12] A. K. Soti, R. Bhardwaj, and J. Sheridan, “Flow-induced deformation of a flexible thin structure as manifestation of heat transfer enhancement,” Int. J. Heat Mass Transf., vol. 84, pp. 1070–1081, 2015.

[13] F. Sastre and A. Velazquez, “Experimental study on heat transfer enhancement caused by the flow-induced vibration of a prism inside a channel,” Appl. Therm. Eng., vol. 125, pp. 412–424, 2017.

[14] Y. Yang, D. S.-K. Ting, and S. Ray, “Convective heat transfer enhancement downstream of a flexible strip normal to the freestream,” Int. J. Therm. Sci., vol. 145, p. 106059, 2019.

[15] “Emissivity Coefficients Materials.” [Online]. Available: https://www.engineeringtoolbox.com/emissivity-coefficients-d_447.html. [Accessed: 04-Apr-2019].

[16] “Thermal Conductivity of common Materials and Gases.” [Online]. Available: https://www.engineeringtoolbox.com/thermal-conductivity-d_429.html. [Accessed: 04-Apr-2019].

[17] “Radiation Heat Transfer.” [Online]. Available: https://www.engineeringtoolbox.com/radiation-heat-transfer-d_431.html. [Accessed: 04-Apr-2019].

[18] D. S.-K. Ting, Basics of engineering turbulence. Academic Press, New York, 2016.

[19] Y. A. Çengel and A. J. Ghajar, Heat and mass transfer : fundamentals & applications. McGraw Hill Education.

[20] H. Assila, E. Essadiqi, M. Faqir, M. Meziane, F. Ghanameh, and S. Ahzi, “Numerical simulation of photovoltaic panel thermal condition under wind convection,” in Proceedings of 2016 International Renewable and Sustainable Energy Conference, IRSEC 2016, 2017, pp. 653–658.

[21] A. Tariq, P. K. Panigrahi, and K. Muralidhar, “Flow and heat transfer in the wake of a surface-mounted rib with a slit,” Exp. Fluids, vol. 37, no. 5, pp. 701–719, 2004.

[22] M. Wae-hayee, P. Tekasakul, S. Eiamsa-ard, and C. Nuntadusit, “Effect of cross-flow velocity on flow and heat transfer characteristics of impinging jet with low jet-to-plate distance,” J. Mech. Sci. Technol., vol. 28, no. 7, pp. 2909–2917, 2014.

[23] V. D. Narasimhamurthy and H. I. Andersson, “Numerical simulation of the turbulent wake behind a normal flat plate,” Int. J. Heat Fluid Flow, vol. 30, no. 6, pp. 1037–1043, 2009.

[24] A. Faucett and T. Ameel, “Computational determination of the modified vortex shedding frequency for a rigid, truncated, wall-mounted cylinder in cross flow,” in Proceedings of the ASME 2014 International Mechanical Engineering Congress and Exposition, 2014, pp. 1–7.

[25] A. Beitel, H. Heng, and D. Sumner, “The effect of aspect ratio on the aerodynamic forces and bending moment for a surface-mounted finite-height cylinder,” J. Wind Eng. Ind. Aerodyn., vol. 186, pp. 204–213, 2019.

[26] F. Fouladi, P. Henshaw, and D. S.-K. Ting, “Effect of a Triangular Rib on a Flat Plate Boundary Layer,” J. Fluids Eng., vol. 138, no. 1, p. 011101, 2015.

[27] N. oh Puzu, S. Prasertsan, and C. Nuntadusit, “Heat transfer enhancement and flow characteristics of vortex generating jet on flat plate with turbulent boundary layer,” Appl. Therm. Eng., vol. 148, pp. 196–207, 2019.

[28] H. Wu, D. S.-K. Ting, and S. Ray, “The effect of delta winglet attack angle on the heat transfer performance of a flat surface,” Int. J. Heat Mass Transf., vol. 120, pp. 117–126, 2018.

CHAPTER 5

HEAT TRANSFER ENHANCEMENT OF A HEATED FLAT SURFACE VIA A FLEXIBLE STRIP PAIR

Y. Yang, D. S-K. Ting, S. Ray, "Heat transfer enhancement of a heated flat surface via a flexible strip pair," International Journal of Heat and Mass Transfer 159 (2020) 120139

5.1 Introduction

Heat exchangers are commonly used in many engineering applications, such as the air-conditioning systems, power generators, and automotive processes [1]. One familiar method for increasing performance of heat exchangers is to induce secondary flow by various swirl flow devices, i.e. vortex generators [2]. Vortex generators are usually placed near the heat transfer surface, perturbing the flow and increasing the mixing between the freestream and the near-surface fluid, and thus, augmenting the heat transfer rate.

Much effort has been invested in recent years to further heat transfer enhancement. Among others, the winglet and wind type vortex generators have shown great promise for boosting heat transfer via the secondary flow motions [3]. For example, Wu et al. [4] conducted an experimental study about the effect of delta winglet attack angle, from 30° to 60°, on the heat convection over a heated flat surface. It was revealed from their study that the heat transfer enhancement was strongly correlated to the transverse vortex induced by the winglet. Within the scope of their study, the winglet with an attack angle of 60° provided the best heat transfer performance. Khanjian et al. [5] investigated the influence of attack angle (from 10° to 30°) of a rectangular wing on the heat transfer augmentation in a channel. According to their results, the wider and more energetic vortex was generated by the wing with a larger attack angle, and this corresponded to a larger Nusselt number.

To further improve the thermal performance of the entire system, various innovative designs of winglet pairs or winglet arrays, instead of single winglets, have been proposed. An experimental study about the heat transfer enhancement of a plain-fin round-tube heat exchanger using a new type of winglet array was conducted by He et al. [6]. Based on their study, the winglet array, which is composed of two winglet pairs, was found to be more effective compared to a single winglet pair. The heat transfer improvement for the winglet array is up to 55%, with respect to the reference case without the winglet pair. On the other hand, the single winglet pair only provided heat transfer augmentation up to 32%. Khanjian et al. [7] explored the effect of rectangular winglet pair roll angle on the heat transfer augmentation in a channel. They reported that the enhancement increases with increasing roll angle, but so does the pressure drop. The overall thermal enhancement factor reaches a maximum value of 1.32 for a roll angle of 70°. Also worth mentioning is the study by Li et al. [8], who numerically investigated the arrangement of delta winglet pairs on heat transfer enhancement. Their results show that the common-flow-up configuration of a delta winglet pair has the best heat transfer performance among the studied cases, due to the stronger and slower dissipative vortices. Promvonge et al. [9] conducted an optimization investigation of rectangular winglet pairs on heat transfer augmentation in a tube. Within their study cases, the highest thermal performance enhancement of about 2 was obtained when winglet height / tube diameter = 0.15, and longitudinal pitch of winglet / tube diameter = 1. Another numerical study of delta winglet pairs was developed by Pourhedayat et al. [10]. The effect of transversal distance of the winglet (from 0 to 40 mm) was investigated. According to their research, the winglet pair with a transversal distance of 20 mm provided the maximum Nusselt number, due to the best fluid mixing condition in the cross-section of the tube. Finally, Ke et al. [11] proposed a mixed configuration of delta winglet pairs, including two groups of delta winglet pairs, to further the heat transfer enhancement in a rectangular channel. They pointed out that, the mixed configuration provided a significant improvement of heat transfer compared to only one winglet pair case, due to the generated two groups of counter-rotating vortex pairs, and thus, the fluid mixing across the whole channel cross-section.

In addition to the rigid type vortex generators, flexible and vibrating vortex generators have also drawn great attention in recent years. Shi et al. [12] numerically studied the heat transfer enhancement of a channel via vortex-induced vibration. They pointed out that the cylinder with a flexible plate provided 90% Nusselt number increase above that of an empty channel. This is superior to its rigid counterpart, a cylinder with a stationary plate, which led to only a 24% Nusselt number augmentation. In their other study, a flexible cylinder was proposed for enhancing the heat transfer of a channel [13]. The strengthened vortex interaction and the enhanced fluid mixing process can be observed behind the vibrating cylinder, resulting in 235% and 51% convective heat transfer augmentation compared to the empty channel and the channel with a stationary cylinder, respectively. Li et al. [14] conducted a numerical investigation of a vibrating vortex generator for heat transfer enhancement in a rectangular airside fin. Over studied conditions, they found that the best thermal performance occurs with the vortex generator with

Young's Modulus of 1 MPa, which produced the highest vorticity fluctuation. A numerical study of multiple flexible vortex generators was conducted by Ali et al. [15]. They illustrated that an increase in the number of flexible flaps results in larger amplitude vibration, greatly improving the fluid mixing and heat transfer. Their results indicate an increase in the global Nusselt number of up to 275%. In their other numerical study, the trapezoidal flexible vortex generator was explored for its effectiveness in heat transfer in a circular pipe [16]. They revealed that the flexible type vortex generator could provide 118% overall heat transfer enhancement compared to the empty pipe. On the other hand, the rigid type only increased the heat transfer of approximately 97%. Sastre and Velazquez [17] investigated the heat transfer augmentation via a moving prism in the water channel. They found that the moving prism could double the heat transfer rate with respect to the clean channel. In case of the fixed prism, the maximum improvement of heat transfer was 66%. Finally, Davand et al. [18] conducted a numerical study about the heat transfer enhancement of a microchannel via the flexible vortex generator. According to their results, about 18% increase of Nusselt number could be observed with respect to the rigid case.

It is clear that most of the previous studies were developed in the channel under the internal flow condition. The heat transfer enhancement under open flow conditions is also of fundamental and practical significance. One application is the cooling of a solar photovoltaic panel. For this reason, the current study focuses on the heat transfer augmentation from a heated flat surface under approximately open flow condition. This is an extension of our previous study on one standalone rectangular flexible strip [19], which showed that the more flexible the strip is, the more effective it is in augmenting heat transfer. Also notable from the brief literature review is that the heat transfer rate may be further enhanced by using a pair or an array of vortex generators. Accordingly, this study aims at uncovering the effect of the spacing between a pair of side-by-side flexible strips on heat transfer enhancement

5.2 Experimentation

The experimental setup is depicted in Figure 5.1. The closed-loop wind tunnel has a 76 cm square cross-section and a 180 cm long test section. A 3 mm-thick *PTFE* (polytetrafluoroethylene) plate is inlaid in the middle of the fiberglass test section base. The *PTFE* plate has an emissivity of 0.92 [20] and a thermal conductivity of 0.25 $Wm^{-1}K^{-1}$ [21]. A boiling tank of water under the *PTFE* plate was used to generate steam, which is continuously condensed on the bottom surface of the plate. Thus, a uniform temperature of around 100°C was obtained. Here, the local atmospheric pressure stayed around 100 kPa during the experiment. The stabilized local temperature distribution of the top surface of the *PTFE* plate was captured by a FLIR C2 thermal camera with 60 by 80 pixels, resulting in a spatial resolution of approximately 0.35*W*. The convective heat transfer coefficient, and thus, the Nusselt number, was deduced from the local surface temperature and the free-stream air temperature. The two 25.4 mm-tall and 12.7 mm-wide rectangular flexible strip were cut from a 0.1 mm-thick aluminum sheet. To investigate the vortex interaction and the resulting heat transfer improvement, the strip pairs with space of 1, 2, and 3 *W* (strip width), were used to perturb the flow. The strip pair was located just upstream of the *PTFE* plate. As an extension of our previous study [19][22], a consistent flow condition is desired. With an incoming wind of 10 m/s, a Reynolds number of 8.5×10^3 based on the width of the strip was achieved. This Reynolds number is chosen to match with that of a real PV under typical atmospheric wind. The orthogonal *X*, *Y*, *Z* denote streamwise, widthwise and vertical directions, respectively, while the origin *O* represents the middle point of the space of the strip pair; see Figure 5.1. The turbulent flow induced by the strip pair was characterized using a triple sensor hotwire probe with a constant-temperature anemometer (type 55P95), when the *PTFE* plate was at the same temperature as the flowing air. Based on our preliminary investigation, the highly-vortical flow is more-or-less developed at 9 *W* downstream of the strip pair. Accordingly, the hotwire measurements were conducted at 9 *W* downstream. At any measurement location, one million data points were low passed at 30 kHz, and sampled at 80 kHz to avoid aliasing.

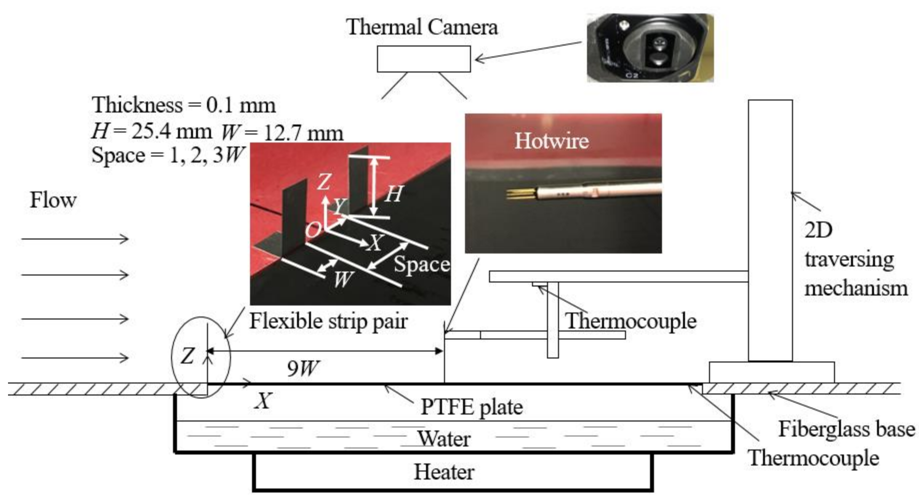

Figure 5. 1. The experimental setup

5.3 Data Processing

The total heat transfer rate from the heated *PTFE* plate consists of primarily of convection, a small amount of radiation, and negligible conduction. As such, the convective heat transfer rate can be determined from,

$$\dot{Q}_{convection} = \dot{Q}_{total} - \dot{Q}_{radiation} \tag{5.1}$$

The total heat transfer rate can be deduced from the temperature measurements via,

$$\dot{Q}_{total} = K_{PTFE}A(\frac{T_{bottom} - T_{top}}{t_{PTFE}}) \tag{5.2}$$

where the thermal conductivity of the *PTFE* plate, K_{PTFE} = 0.25 $Wm^{-1}K^{-1}$, area, A = 295 mm by 380 mm, and the thickness of the *PTFE* plate, t_{PTFE} = 3 mm. The bottom surface temperature. T_{bottom} = 100°C. The local temperature of the top surface of the *PTFE* plate, T_{top} was measured by a FLIR C2 thermal camera.

The radiation heat transfer rate $\dot{Q}_{radiation}$ can be calculated from,

$$\dot{Q}_{radiation} = \varepsilon\sigma A(T_{top}^4 - T_{wall}^4) \tag{5.3}$$

where emissivity ε = 0.92 [20], and Boltzmann's constant σ = 5.67x10^{-8} $Wm^{-2}K^{-4}$ [23]. Wall temperature of the wind tunnel, T_{wall}, is assumed to be equal to the air temperature T_{air}, which was measured by a thermocouple, as shown in Figure 5.1.

From the convective heat transfer rate, $\dot{Q}_{convection}$, the convective heat transfer coefficient can be obtained, that is,

$$h = \frac{\dot{Q}_{convection}}{A(T_{top} - T_{air})} \tag{5.4}$$

This convective heat transfer coefficient is more conveniently expressed in its non-dimensional form as the Nusselt number,

$$Nu = \frac{hL}{K_{air}} \tag{5.5}$$

where K_{air} and L are the thermal conductivity of the ambient air and the characteristic length, respectively. To determine the convective heat transfer improvement, the Nusselt number is normalized by the corresponding reference Nusselt number in the absence of the flexible strips, i.e.,

$$\frac{Nu}{Nu_0} = \frac{h}{h_0} \tag{5.6}$$

Here Nu_0 and h_0 are the Nusselt number and the convective heat transfer coefficient, respectively, for the reference case in the empty wind tunnel without the flexible strip pair.

The instantaneous velocities in streamwise (X), widthwise (Y) and vertical (Z) direction,

$$U_i = \overline{U} + u\ ; V_i = \overline{V} + v\ ; W_i = \overline{W} + w \tag{5.7}$$

were measured by the triple sensor hotwire probe, The time-averaged velocities, $\overline{U}, \overline{V}, \overline{W}$, can be calculated from,

$$\overline{U} = \frac{1}{N}\sum_{i=1}^{N} U_i\ ; \overline{V} = \frac{1}{N}\sum_{i=1}^{N} V_i\ ; \overline{W} = \frac{1}{N}\sum_{i=1}^{N} W_i \tag{5.8}$$

where N=10^6, is the sample size.

The root-mean-square velocities can be deduced from the instantaneous fluctuating velocities, u, v, and w, i.e.,

$$u_{rms} = \sqrt{\sum_{i=1}^{N} \frac{{u_i}^2}{N-1}}\ ; v_{rms} = \sqrt{\sum_{i=1}^{N} \frac{{v_i}^2}{N-1}}\ ; w_{rms} = \sqrt{\sum_{i=1}^{N} \frac{{w_i}^2}{N-1}} \tag{5.9}$$

The relative turbulence intensity can be calculated by dividing the root-mean-square velocity by the freestream velocity,

$$Tu = \frac{u_{rms}}{U_\infty} \tag{5.10}$$

In this study, the freestream velocity, U_∞, was kept at approximately 10 m/s.

As turbulent flow is highly three dimensional [24], the normalized turbulent kinetic energy can be employed to demonstrate the total turbulence level, i.e.,

$$ke = \frac{1}{2}\frac{(u_{rms}^2 + v_{rms}^2 + w_{rms}^2)}{U_\infty^2} \tag{5.11}$$

Based on the strip width (W), and the freestream velocity (U_∞), the Reynolds number can be defined as,

$$Re_W = \frac{WU_\infty}{\nu} \tag{5.12}$$

where ν is kinematic viscosity. The Reynolds number in the current study was held at approximately 8.5×10^3.

As the rectangular strip acts as a bluff body with respect to the flowing wind, regular vortex shedding is expected. The vortex shedding frequency can be cast in terms of the non-dimensional Strouhal number,

$$St = \frac{fW}{U_\infty} \tag{5.13}$$

The intensity of the vortices in the streamwise direction can be illustrated by the X-vorticity (ω),

$$\omega = \frac{\partial \bar{W}}{\partial Y} - \frac{\partial \bar{V}}{\partial Z} \tag{5.14}$$

The corresponding non-dimensional X-vorticity can be calculated as,

$$\Omega = \frac{\omega W}{U_\infty} \tag{5.15}$$

In addition to the local heat transfer augmentation, also of importance is the overall enhancement over the entire heated surface. As such, the appropriate span-averaged values are also of interest, and this can be defined as,

$$\bar{P} = \frac{1}{n}\sum_{i=1}^{n} P_i \tag{5.16}$$

Here P is the parameter of interest, the normalized Nusselt number, and n is the number of span-averaging values. For example, n = 20 for the span-averaged Nu/Nu_0 profile of the 1W-space strip pair.

5.4 Results and Discussion

5.4.1 Flow Characteristics

5.4.1.1 Velocity Profile

The contours of X-vorticity normalized by the freestream velocity ($U_\infty \approx 10$ m/s) and the strip width (W = 12.7 mm) is presented in Figure 5.2. The cross-stream (YZ plane) velocity vectors are also depicted to show the flow motion. The vortex structures are easily identifiable. As far as the convective heat transfer is concerned, these vortices are of significance, as they can disrupt the boundary layer, boost the turbulence intensity and induce secondary flow motions over the heated surface [25]. It is interesting to notice that, the swirling motions seem to produce several downward flow movements, bringing the cooler freestream air toward the heated surface, increasing the fluid mixing and the heat transfer performance [26][22]. Also notable is that, with decreasing strip pair transversal space from 3*W* to 1*W*, the interaction between the two counter-rotational vortices becomes progressively stronger, resulting in a decrease in the maximum absolute value of non-dimensional X-vorticity from approximately 0.24 to 0.15. Although the interaction between the counter-rotational vortices can degrade the vortices' intensity, the heat transfer enhancement could be improved if the transversal distance of the vortices is properly designed [27]. Song et al. [28][29] numerically studied the effect of the vortex interaction induced by delta-winglets on the heat transfer augmentation in their fin-tube heat exchanger. The transversal distances (c) between the winglets were equal to 0, 0.6, 1, 1.3 $L\sin\theta$, where L and θ are base length and attack angle of the winglet, respectively. According to their results, the vortex intensity was observed to decrease along with the decrease of the transversal distances between the winglets, presenting the same trend with our current study. The best heat transfer performance could be obtained when $c = 0.6L\sin\theta$, the second smallest transversal distance. That is to say, as for the convective heat transfer enhancement, not only the strength of the vorticity matters. Parameters such as the downwash and the streamwise velocities and the turbulence intensity are also important.

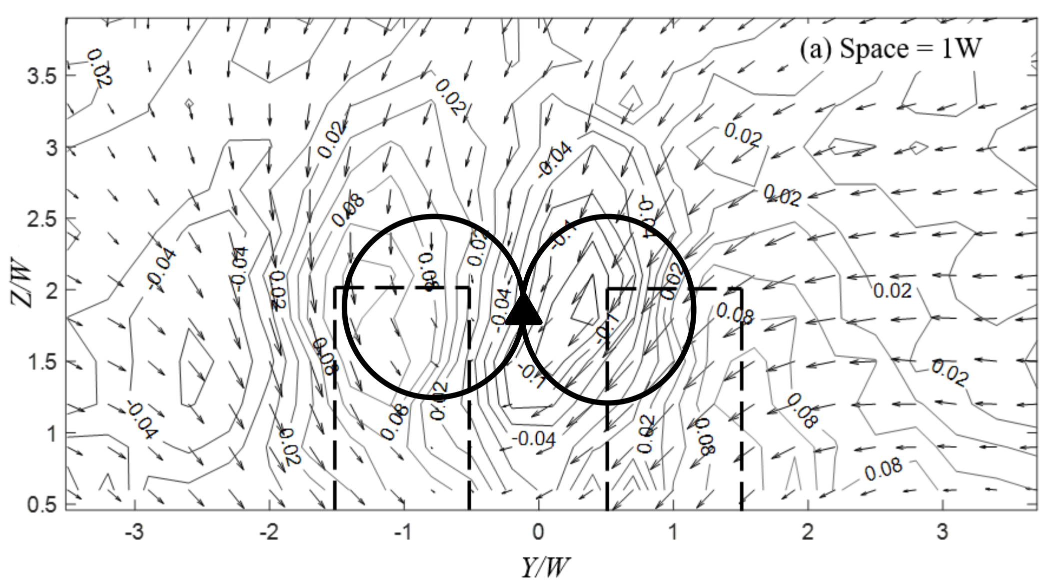

(a) Space=1*W*

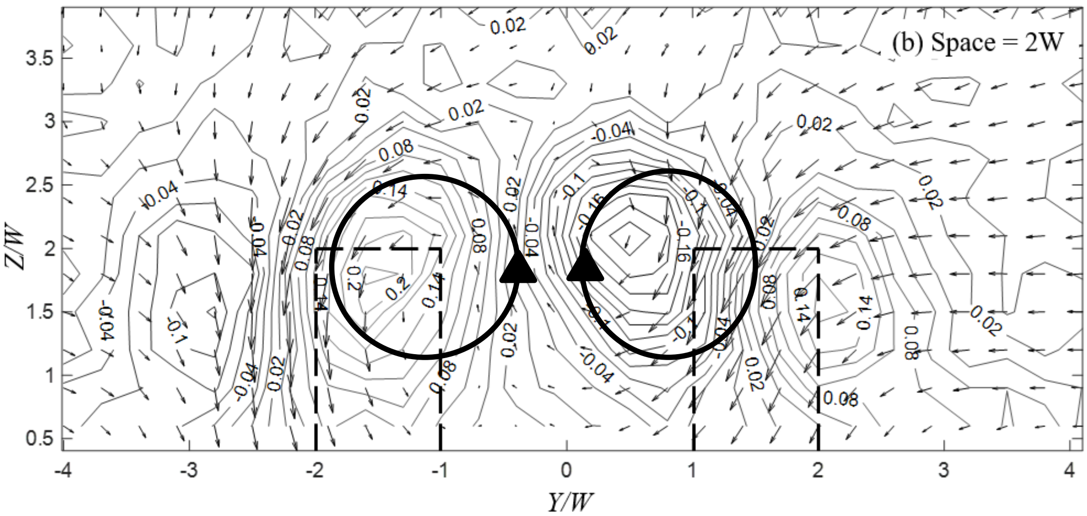

(b) Space=2*W*

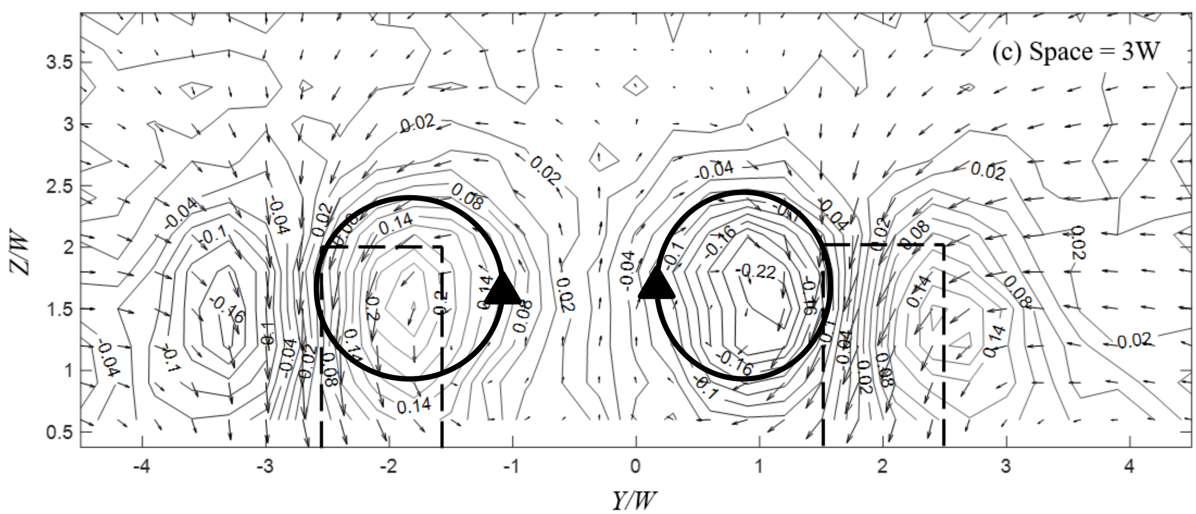

(c) Space=3*W*

Figure 5. 2. Non-dimensional X-vorticity contour and velocity vector in *YZ* plane at 9*W* downstream of the flexible strip pair separated by (a) 1*W* (b) 2*W* (c) 3*W*.

As mentioned above, the downwash flow motion is of significance. A larger downwash velocity could transport the cooler air toward the heated surface, boosting the fluid mixing and thus, the heat transfer rate. An experimental study was conducted by Sharples and Charlesworth [30] to investigate the wind effect on the heat convection from a roof-mounted flat plate solar collector. Based on their findings, a significant increase could be observed with the increase of the wind velocity toward the flat plate. In addition, a power law fitting equation of the convective heat transfer coefficient (h_w) with respect to the wind speed normal to the solar collector (V_r) was concluded, giving h_w=9.3$V_r^{0.44}$, where V_r ranged from 0.8 ms^{-1} to 6.7 ms^{-1}. With this backdrop, the normalized downwash velocity ($\overline{W}/U_\infty$) at 9W downstream distance is shown in Figure 5.3. As the flow downstream of the strip pairs was highly 3 dimensional and inhomogeneous, the span-averaged values were employed. To estimate the effect of the general vortical flow region, the span-averaged values encompassing four vortex cores behind the strip pair, Y=±2.5W, Y=±3W and Y=±3.5W for 1W-space, 2W-space, and 3W-space strip pair, respectively, were selected. From Figure 5.3, the same level of $\overline{W}/U_\infty$ can be observed from 0.6W to 1.2W height. Above Z=1.5W, the largest negative $\overline{W}/U_\infty$ values induced by 1W-space strip pair are distinguishable. For example, the span-averaged velocity toward the heated surface of 1W-space strip pair is approximately 0.062U_∞ at 2.4W height, much larger than those of 2W-space and 3W-space strip pair, which are approximately 0.050U_∞ and 0.036U_∞, respectively. Thus, the downwash flow motion of the 1W-space strip pair is expected to be most beneficial to the heat transfer augmentation.

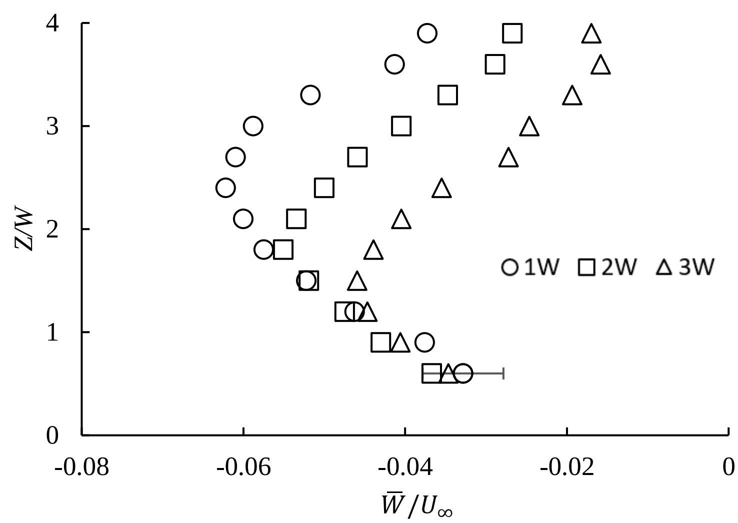

Figure 5. 3. $\overline{W}/U_\infty$ profile at 9W downstream of the flexible strip pair (span-averaged across Y=±2.5W for 1W-spaced strip pair, Y=±3W for 2W-spaced strip pair, Y=±3.5W for 3W-spaced strip pair).

Other than the downwash velocity, the profile and magnitude of the streamwise velocity are also expected to contribute to convective heat transfer enhancement. Sartori [31] conducted an investigation about the effect of wind speed on the forced convection over a flat surface. He summarized that the forced convective heat transfer coefficient was proportional to $V^{0.5}$, $V^{0.8}$, and $V^{0.8}$ for laminar, mixed and fully turbulent flows, respectively; where V was the freestream velocity. As mentioned earlier, Sharples and Charlesworth [30] correlated the convective heat transfer coefficient with $V^{0.48}$, for wind velocity between 0.8 ms^{-1} to 6.2 ms^{-1}. These studies confirmed that the heat transfer rate increases with wind speed. In other words, the larger wind speed is more effective in sweeping thermal energy from the hot surface. Accordingly, the time-averaged streamwise velocity profile normalized by the freestream velocity ($U_\infty \approx 10\ \mathrm{m/s}$) at 9*W* downstream of the strip pair is shown in Figure 5.4, where the uncertainty is around 0.023. It is noticed from the figures that, with decreasing spacing between the strips from 3*W* to 1*W*, the boundary layer (when $\overline{U}$ reaches $0.99U_\infty$) in the vortex interaction region (near *Y*=0) becomes thicker, from approximately 3*W* height to 3.9*W* height. Furthermore, the 1*W*-space strip pair resulted in the smallest near surface streamwise velocity. The smallest value of normalized streamwise velocity for 1*W*-space strip pair is around 0.32, smaller than those associated with the 2*W*-space and 3*W*-space strip pair, which are approximately 0.35 and 0.39, respectively. To further compare the strip spacing effect, Figure 5.5 depicts the span-averaged normalized streamwise velocities. The values were averaged across *Y*=±2.5*W*, *Y*=±3*W* and *Y*=±3.5*W* for 1*W*-space, 2*W*-space, and 3*W*-space strip pair, respectively. It is clear from the figure that, the 1*W*-space strip pair generates the lowest span-averaged value, which is approximately 0.44 at *Z*=0.6*W*. The span-averaged $\overline{U}/U_\infty$ for 2*W*-space and 3*W*-space strip pair in the same location are around 0.48 and 0.51, respectively. From the perspective of the streamwise velocity alone, the 1*W*-space strip pair seems to provide the worst effect on the heat transfer augmentation.

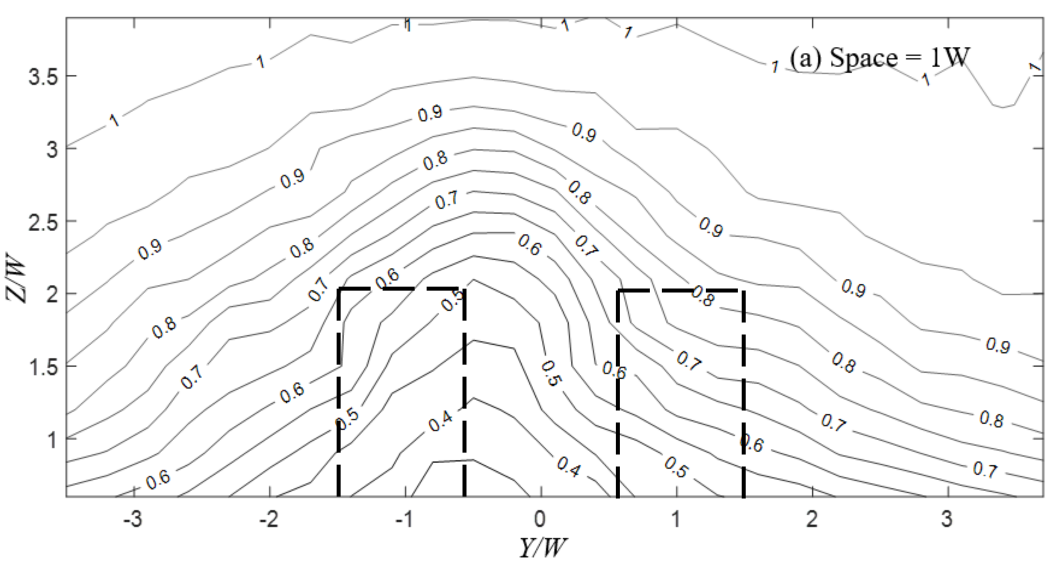

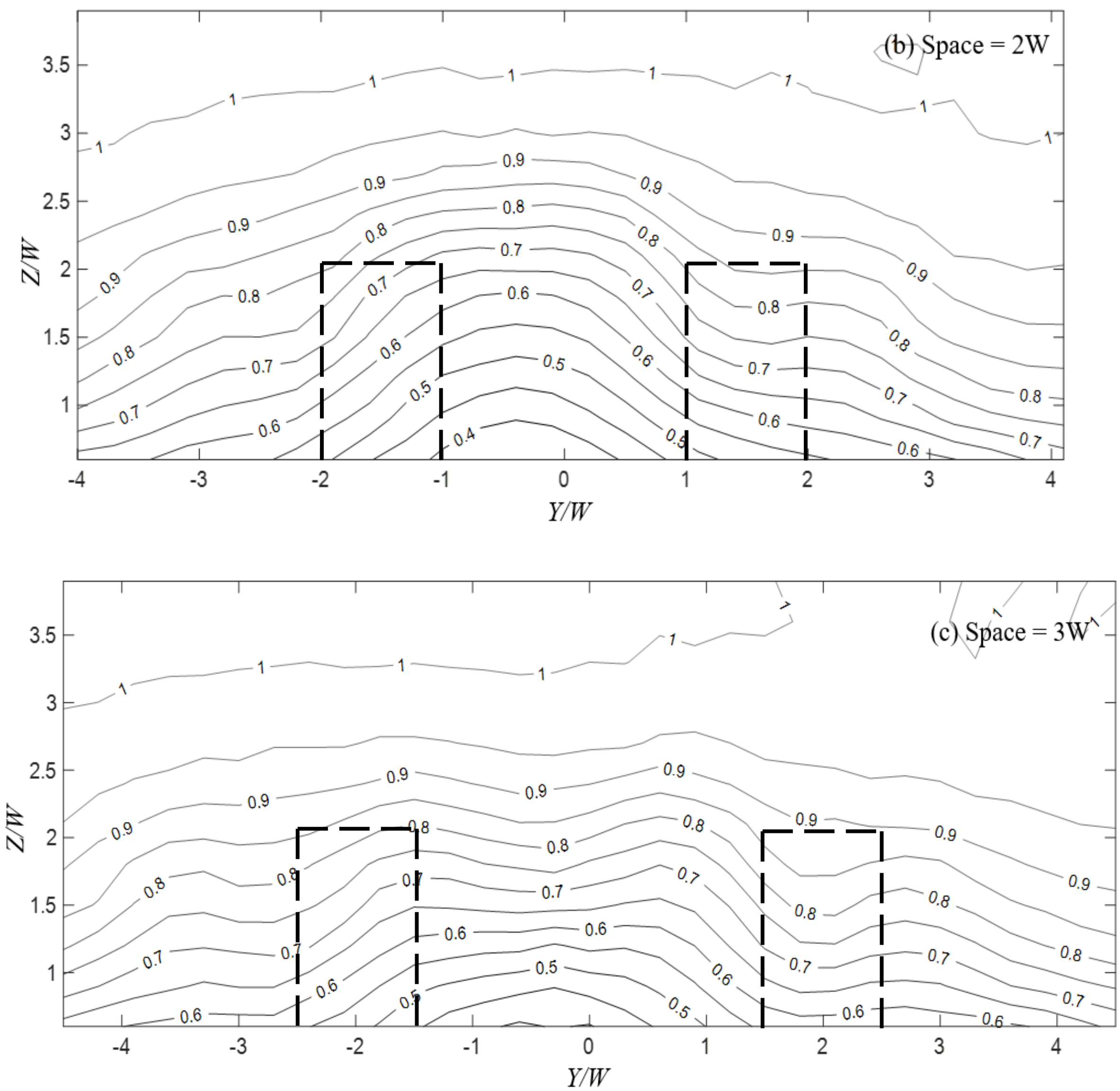

Figure 5. 4. Normalized streamwise velocity profile ($\overline{U}/U_\infty$) at 9W downstream of the flexible strip pair spaced (a) 1W (b) 2W (c) 3W.

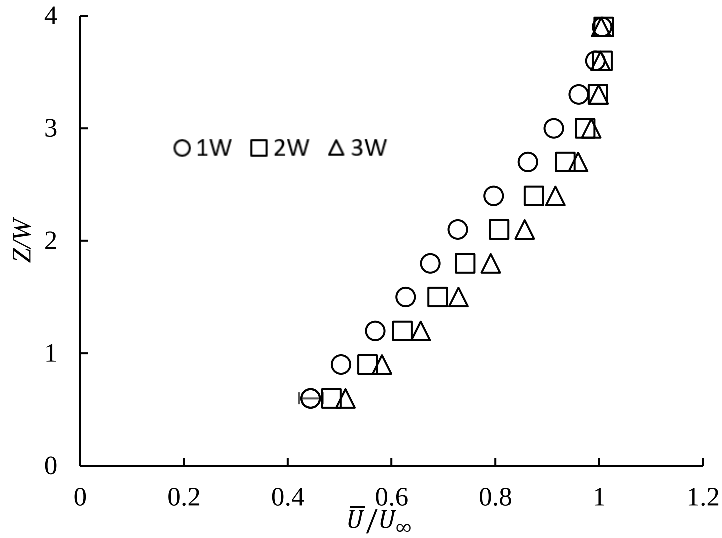

Figure 5. 5. $\overline{U}/U_\infty$ profile at 9*W* downstream of the flexible strip pair (span-averaged across *Y*=±2.5*W* for 1*W*-spaced strip pair, *Y*=±3*W* for 2*W*-spaced strip pair, *Y*=±3.5*W* for 3*W*-spaced strip pair).

5.4.1.2 Turbulence Intensity and Turbulent Kinetic Energy

With respect to heat transport in turbulent wind, the magnitude of the wind fluctuation is important, as it is closely tied with fluid mixing [32] and thus, forced convection [33][34]. Therefore, the streamwise turbulence intensity (*Tu*) and the normalized root-mean-square streamwise fluctuating velocities (u_{rms}/U_∞), is depicted in Figure 5.6. In the previous study using a single strip [22], two intense-turbulence areas which correspond to the core of the vortex motion were detected. Figure 5.6(c) depicts that when the gap between the two strips is wide at 3*W*, the two high turbulence regions resulting from the individual strip are still clearly distinguishable. With decreasing spacing, the high turbulence areas begin to interact with each other and in doing so, they merge together. Incidentally, the peak turbulence intensity downstream of the strip pair also increases. The 1*W*-spaced strip pair induces the peak *Tu* value of approximately 0.197, roughly 0.025 and 0.030 larger than those of 2*W*-space and 3*W*-space strip pair, respectively. The uncertainty of *Tu* is around 0.008.

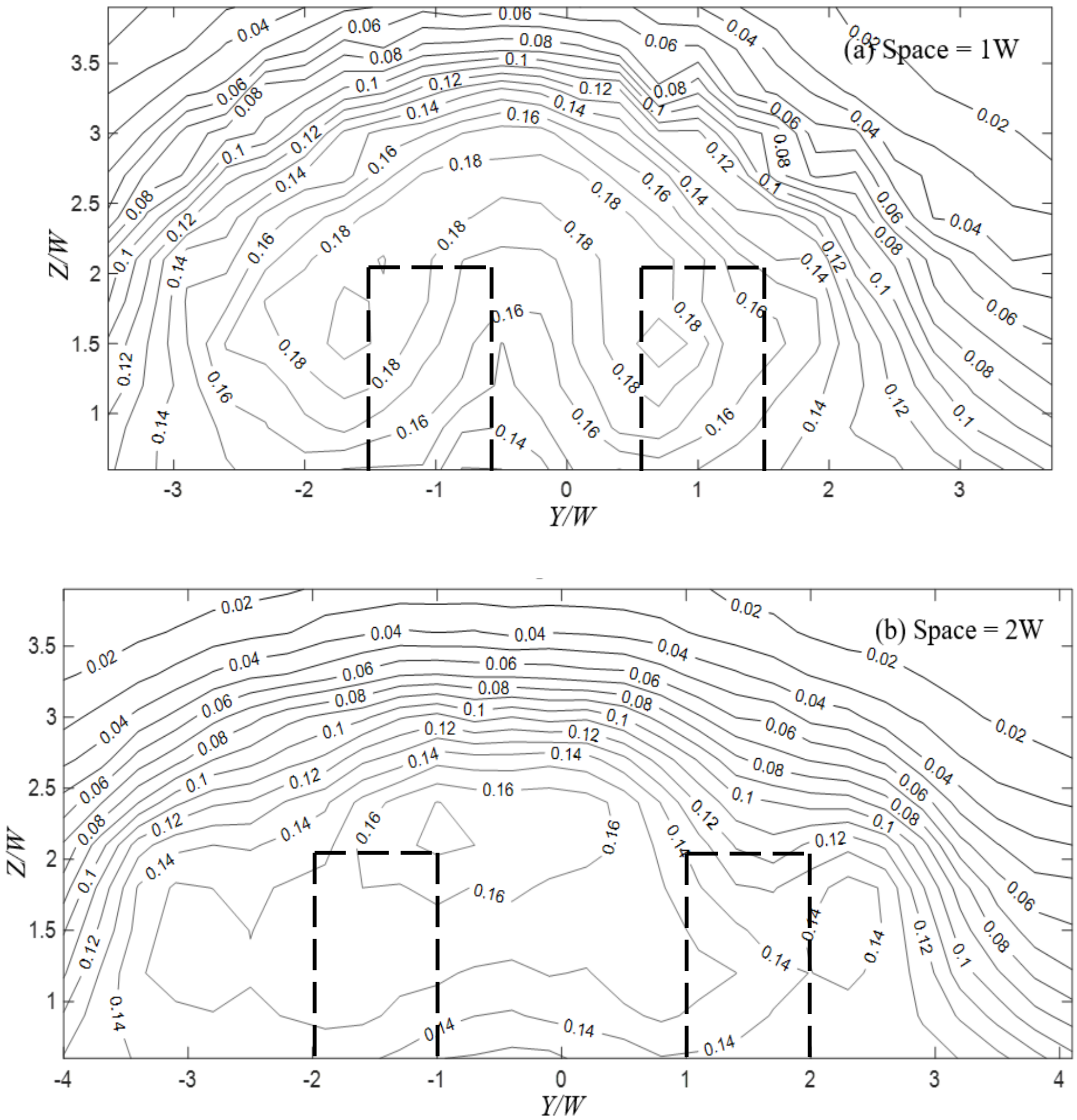

(a) Space = 1W
Z/W
Y/W
(b) Space = 2W
Z/W
Y/W

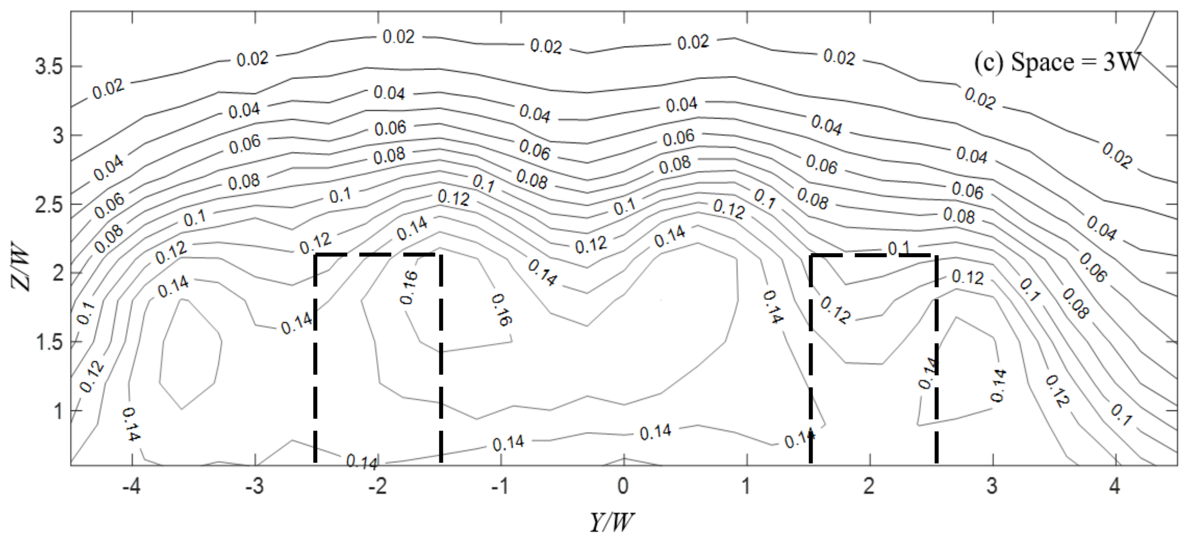

Figure 5. 6. Streamwise turbulence intensity (Tu) at 9W downstream of the flexible strip pair spaced (a) 1W (b) 2W (c) 3W.

The span-averaged turbulence intensity is presented in Figure 5.7. We can see that, the highest span-averaged turbulence intensity values are at approximately Z=1.5W, where the vortex structures locate. Also, the 1W-spaced strip pair provides the largest span-averaged Tu value, around 0.168 at Z=1.5W, approximately 0.020 and 0.023 larger than those associated with 2W-spaced and 3W-spaced strip pair. This implies that the 1W-spaced strip pair is expected to result in better heat transfer enhancement.

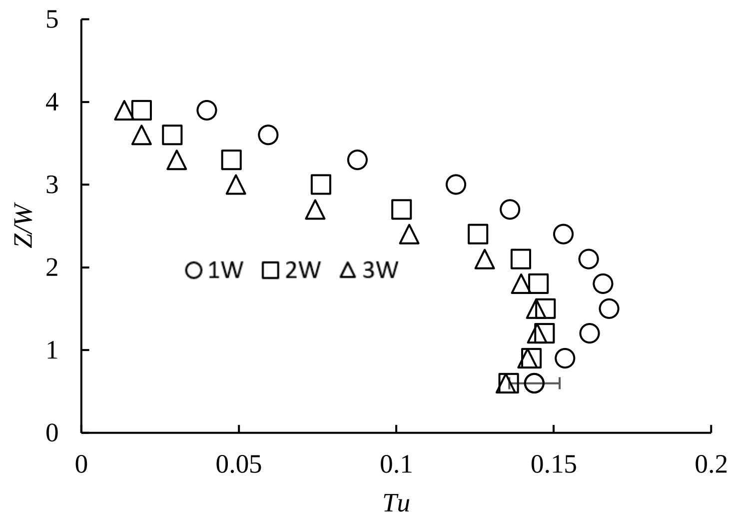

Figure 5. 7. *Tu* profile at 9*W* downstream of the flexible strip pair (span-averaged across *Y*=±2.5*W* for 1*W*-spaced strip pair, *Y*=±3*W* for 2*W*-spaced strip pair, *Y*=±3.5*W* for 3*W*-spaced strip pair).

Figure 5.8 shows the total turbulent kinetic energy downstream of the strip pair. The interaction of velocities from the three dimensions furnishes two high turbulent regions behind the 3*W*-spaced strip pair; see Figure 5.8(c). This is different from the four contours of high streamwise-only turbulence, located near the vortex cores and high X-vorticity region, as shown in Figure 5.6(c) and Figure 5.2(c). These high fluctuation areas locate at around *Y*=±2*W*, which is beneficial to improving the heat transfer near the middle region of the strip pair. With the space of the strip pair reduced to 2*W*, the high fluctuation regions come closer together, occurring at around *Y*=±1.5*W*. When it comes to the 1*W*-space strip pair, those highly fluctuating velocity regions strongly interacted with each other, merging into one highly-turbulent zone across over *Y*=±1*W* at *Z*=2*W*. It is also notable that, for the more closely-spaced strip pair, the peak value of the total turbulent kinetic energy is somewhat higher. The 1*W*-spaced strip pair provides the largest *ke* value, of approximately 0.044. The corresponding peak *ke* values of 2*W*-spaced and 3*W*-spaced strip pairs are around 0.039 and 0.035, respectively. The uncertainty of *ke* is approximately 0.005.

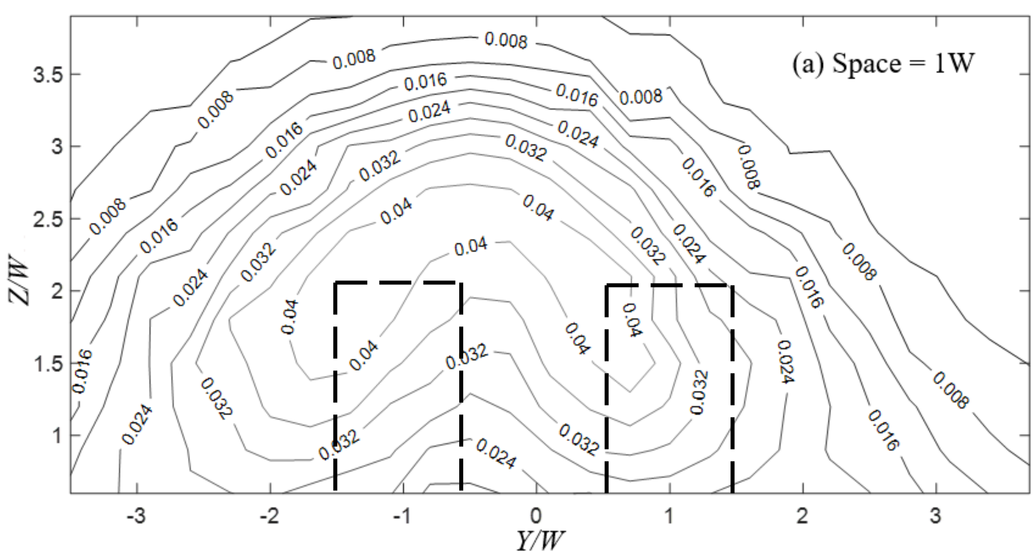

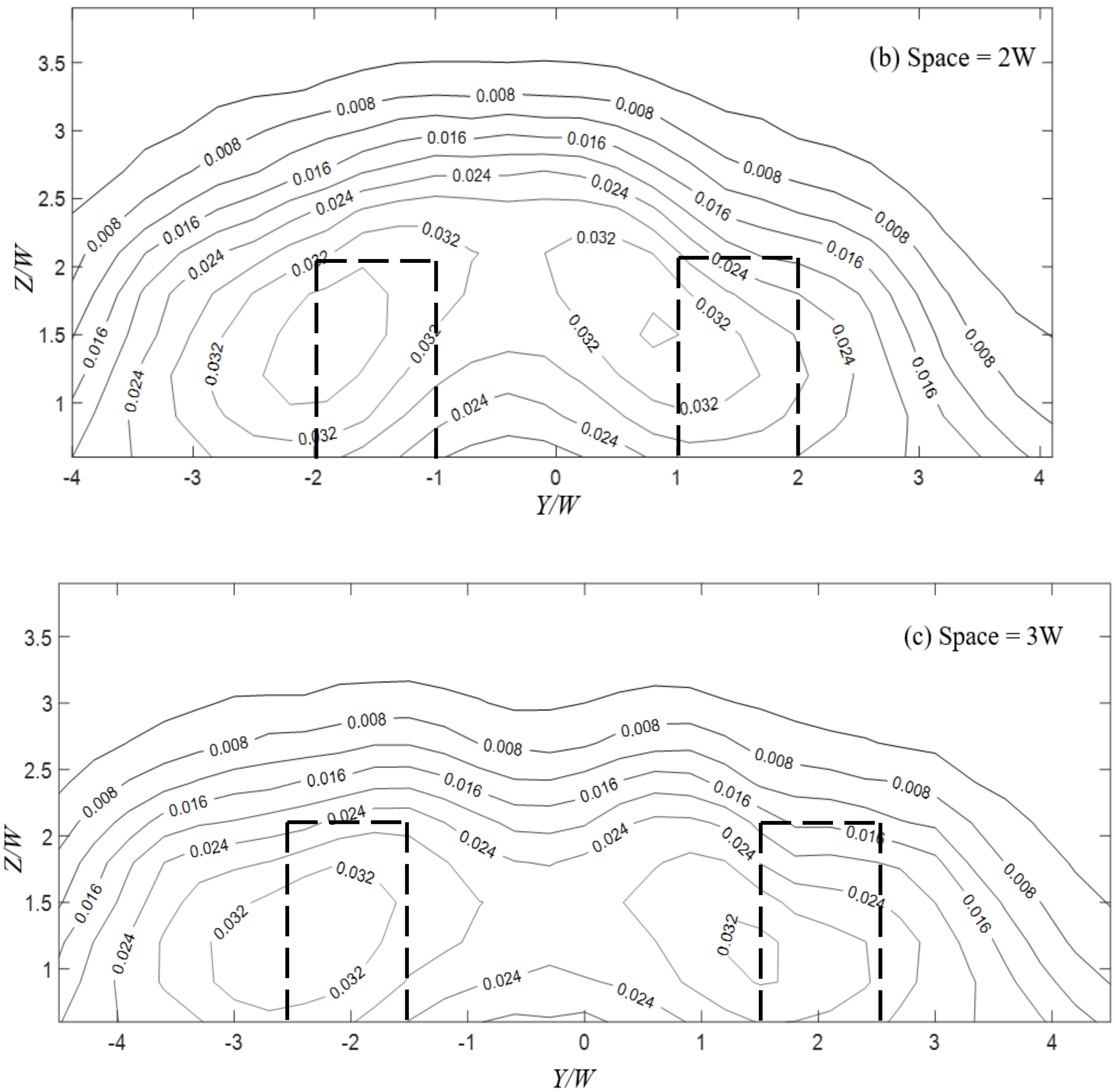

Figure 5. 8. Non-dimensional turbulent kinetic energy (*ke*) at 9*W* downstream of the flexible strips pair separated by (a) 1*W* (b) 2*W* (c) 3*W*.

Figure 5.9 depicts the span-averaged non-dimensional turbulent kinetic energy. To keep the consistency of the other span-averaged results, *Y*=±2.5*W*, *Y*=±3*W* and *Y*=±3.5*W* are still employed for 1*W*-, 2*W*- and 3*W*-spaced strip pair, respectively. From the figure, the same level of *ke* can be identified in the near surface region, from 0.6*W* to 1.2*W* height. At $Z \geq 1.5W$, where the peak *ke* values occur, a larger *ke* value can be observed for 1*W*-spaced strip pair. The *ke* value of 1W-spaced strip pair at *Z*=2.1*W* is around 0.032, slightly larger than those associated with 2*W*-spaced and 3*W*-spaced strip pairs, which are approximately 0.026 and 0.019, respectively.

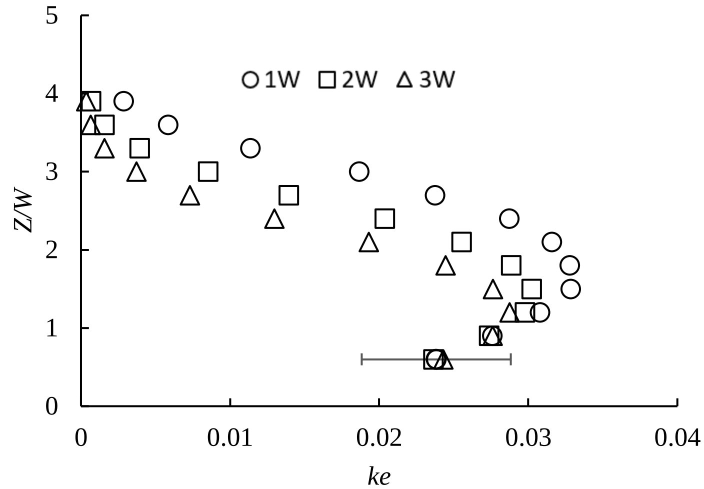

Figure 5. 9. *Ke* profile at 9*W* downstream of the flexible strip pair (span-averaged across *Y*=±2.5*W* for 1*W*-spaced strip pair, *Y*=±3*W* for 2*W*-spaced strip pair, *Y*=±3.5*W* for 3*W*-spaced strip pair).

5.4.1.3 Power Spectrum

Figure 5.10 illustrates the power spectrum density of streamwise fluctuating velocity (*u*). The studied points correspond to *X*=9*W*, *Y*=-1.3*W*, *Z*=2.1*W* for the 1*W*-spaced strip pair, *X*=9*W*, *Y*=-1.5*W*, *Z*=1.8*W* for the 2*W*-spaced strip pair, and *X*=9*W*, *Y*=-1.7*W*, *Z*=1.5*W* for the 3*W*-spaced strip pair. These are the points where the vortex cores and the highest *X*-vorticity values described in Figure 5.2 were located. To obtain a smoother graph for clarity, the Fast-Fourier-transformed values are divided into 2^{14} sections with 50% overlap. From the figure, it could be observed that the 3*W*-spaced strip pair has a distinct peak value at approximately 63 Hz, the corresponding Strouhal number of around 0.080. This is the same as the vortex shedding frequency induced by a single strip of the same dimensions [22]. Here, it should be noticed that, the sampling frequency, 80 kHz, is much larger than the vortex shedding frequency, and thus, no alias frequency occurs. The frequency of the peak value slightly decreases as the spacing between the strip pairs decreases. The peaks occur at around 58 Hz and 53 Hz for 2*W*-spaced and 1*W*-spaced strip pairs; Strouhal number of 0.073 and 0.067, respectively. This decreasing frequency with decreasing spacing result agrees with the previous finding by Yen and Liu [35], who concluded that the frequency increases with the increase of the gap spacing in the gap-flow mode (0.5 < gap spacing / width of the cylinder < 5). It is also interesting to note that, besides this peak frequency at 58 Hz, the secondary frequency appears at approximately 5 Hz for 2*W*-spaced strip pair. This is presumably due to the cross-streamwise vortex-vortex interaction [36][37]. For the 1*W*-spaced strip pair, the narrower wakes interact with each other in a more chaotic pattern [36][37], increasing the secondary frequencies, resulting in a broader power spectrum with no obvious dominant frequency. Also notable is that, the 1*W*-spaced strip pair has the largest value near the vortex shedding frequency. This strongest vortex shedding induced by the 1*W*-spaced strip pair is expected to be beneficial to heat transfer augmentation.

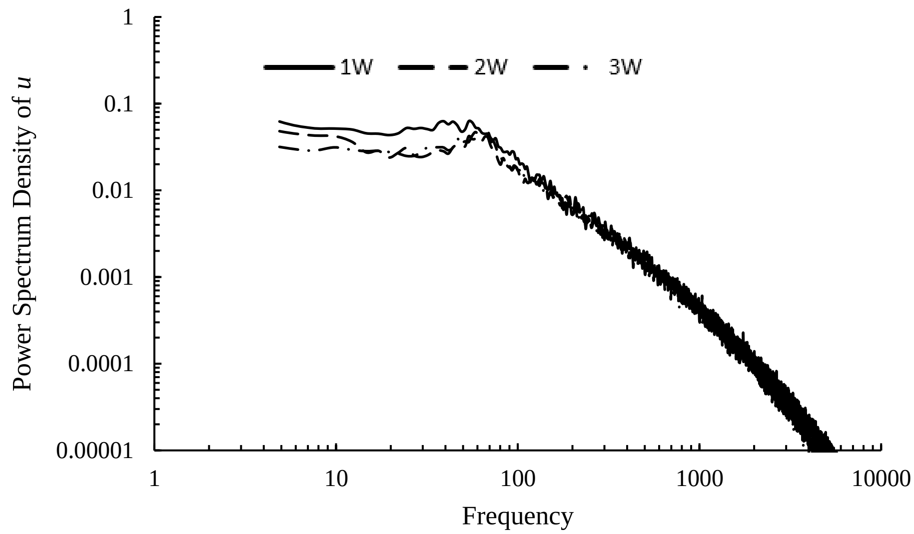

Figure 5. 10. Power spectrum density of streamwise fluctuating velocities at X=9W, Y=-1.3W, Z=2.1W for the 1W-spaced strip pair, X=9W, Y=-1.5W, Z=1.8W for the 2W-spaced strip pair, and X=9W, Y=-1.7W, Z=1.5W for the 3W-spaced strip pair.

5.4.2 Heat Transfer Enhancement

Figure 5.11 shows the temperature distribution downstream of the strip pair, in the unit of Kelvin (K). From the figures, the significant effect of the strip pair on the heat transfer of the heated surface is distinguishable. A low temperature region, as high as 10 K (°C) decrease occurs behind the strip pair. Even farther downstream at the end of the heated surface, the strip pairs still provide a 2 K (°C) decrease, compared to the no strip case. To illustrate the effect of strip pair separated by different spacing on the convective heat transfer augmentation with respect to the unperturbed reference case without the strip pair, the contours of normalized Nusselt number (Nu/Nu_0) are depicted in Figure 5.12. The uncertainty of local Nu/Nu_0 is calculated to be around 0.066. From the figure, a large normalized Nusselt number value of approximately 2.0 could be observed near the strip pair until X=2W. This is likely caused by the strong vortices induced by the strip pair. Farther downstream, the heat transfer enhancement decreases, implying that the turbulent flow and the vortices behind the strip pair are decaying. Also interesting is that, a low

Nu/Nu_0 area of around 1.1 exists at Y=0, and X=0~2W for 3W-spaced strip pair. This hints that there is a lack of interaction between the strong vortices shed from the strip pair in the near strip region. Closing the gap between the strip pair seems to promote the vortex-vortex interaction, increasing Nu/Nu_0 at the same location to approximately 1.4 and 2.0 for the 2W-spaced and 1W-spaced strip pairs, respectively. Also notable for the 3W-spaced strip pair is that, with the development of the vortical flow, the heat transfer enhancement initially improves to around 1.4 from X=2W to 4W, at Y=0, beyond which it starts to decrease. The later diminishing heat transfer enhancement is presumably due to the weakening of the vortical flow. The low Nu/Nu_0 region of approximately 1.1 appears around X=9W. For the 1W-spaced strip pair, no distinct low Nu/Nu_0 area is discernable between the two strips. This is probably attributed to the very strong interaction among the various secondary flow motions because of the narrow gap.

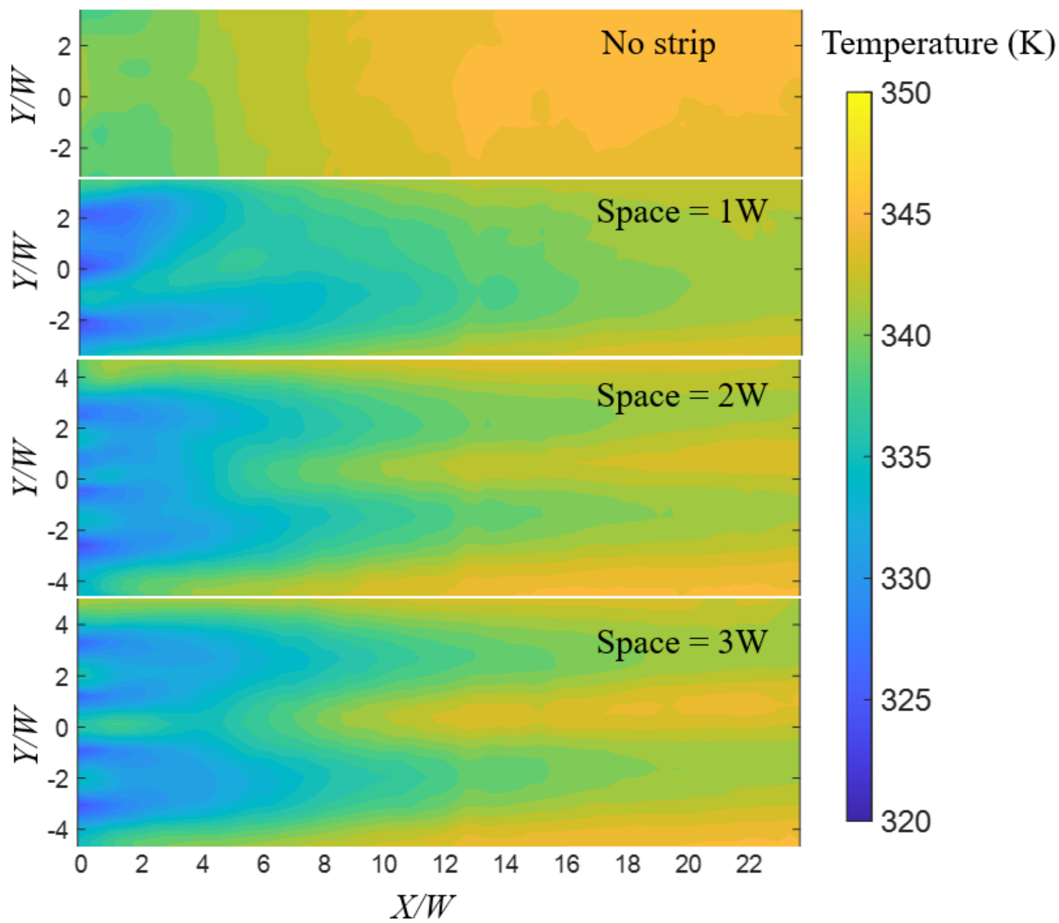

Figure 5. 11. Temperature (K) distribution downstream of the strip pair.

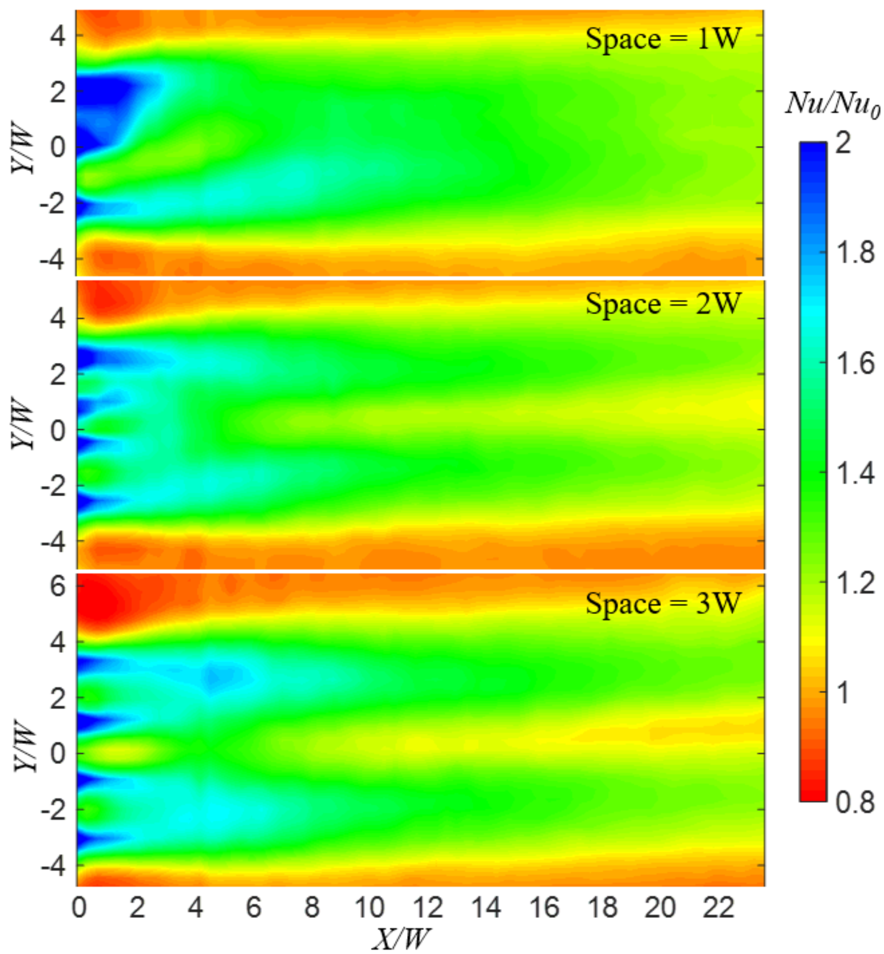

Figure 5. 12. Normalized Nusselt number (Nu/Nu_0) downstream of the strip pair.

In practice, such as the cooling of photovoltaic panels, the entire panel is of interest. Therefore, average Nu/Nu_0 for the plane shown in Figure 5.12 is sought. To see how the average Nu/Nu_0 varies with respect to distant downstream of the strip pair, the span-averaged normalized Nusselt number is plotted in Figure 5.13. These values correspond to the average over Y=±3.5W, ±4W and ±4.5W for 1W-, 2W- and 3W-spaced strip pairs, respectively. The largest Nu/Nu_0 value is observed right behind the strip pair at X=0, where the strongest vortices appear. Also notable is that, in the near strip region from X=0 to 2W, the 1W-spaced strip pair provides the best heat transfer augmentation. Apparently, the narrow gap promotes stronger vortical flow development. Just downstream, the Nu/Nu_0 value of 3W-spaced strip pair increases and even surpasses the other two cases until X=6W, beyond which the 1W-spaced strip pair regains its superior performance until the end of the studied plate. The larger downwash velocity, more intense flow turbulence level and stronger vortex shedding, as described in Figures 5.3, 5.7, 5.9 and 5.10, make the heat transfer potent.

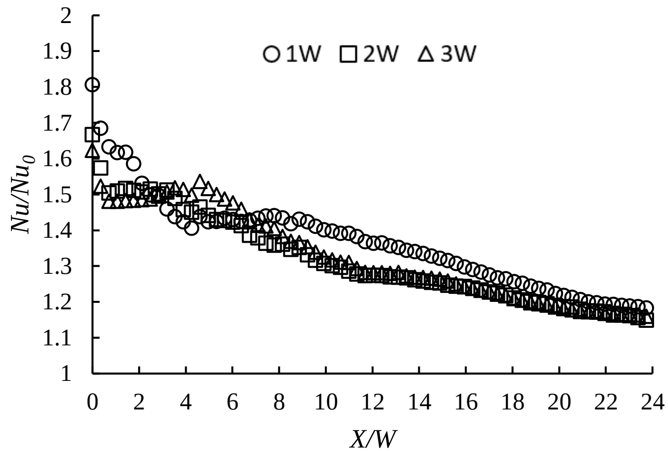

Figure 5. 13. Span-averaged normalized Nusselt number downstream of the flexible strip pair (span-averaged across *Y*=±3.5*W* for 1*W*-spaced strip pair, *Y*=±4*W* for 2*W*-spaced strip pair, *Y*=±4.5*W* for 3*W*-spaced strip pair).

The cross-stream normalized Nusselt number at *X*=9*W* and 20*W* are depicted in Figure 5.14. It is clear from the figure that the peak value of Nu/Nu_0 decreases from approximately 1.58 to 1.28 as *X* increases from 9*W* to 20*W*. Also notable is that the 1*W*-spaced strip pair provides the highest Nu/Nu_0 value of approximately 1.50 in the gap region at *X*=9*W* and *Y*=0. This value is much larger than those associated with the 2*W*- and 3*W*-spaced strip pairs, whose values are around 1.26 and 1.17, respectively. Even with significant decay in vorticity and flow turbulence when the flow reaches *X*=20*W*, the 1*W*-spaced strip pair still presents the best heat transfer performance at *Y*=0, with Nu/Nu_0 of around 1.27. On the other hand, the Nu/Nu_0 of 2*W*- and 3*W*-spaced strip pairs in the same location are approximately 1.15 and 1.07, respectively.

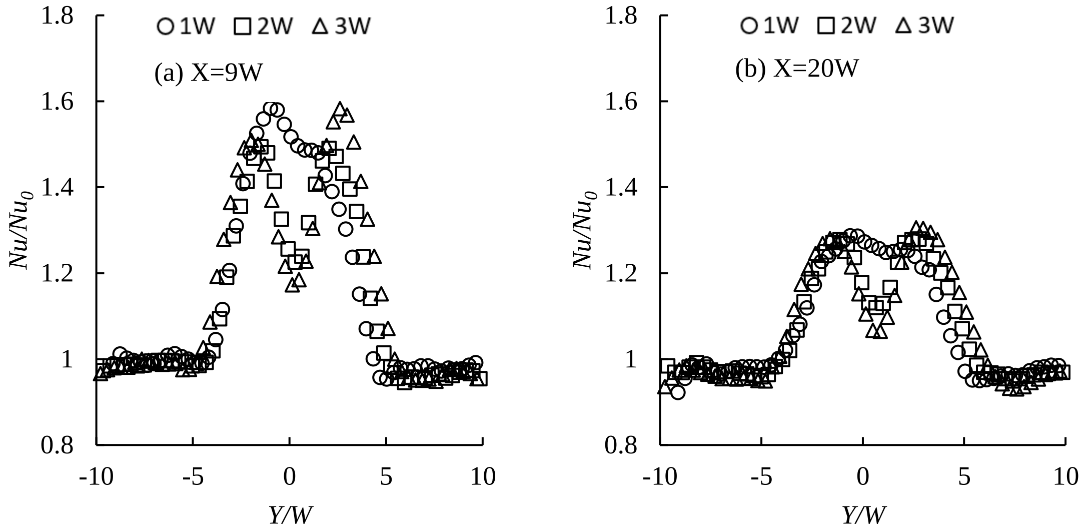

Figure 5. 14. Cross-stream normalized Nusselt number profile at (a) X = 9W, (b) X = 20W

5.4.3 Regression Analysis

From the aforementioned heat transfer enhancement results and the flow characteristics described in Section 5.4.1, we know that the heat convection augmentation is induced by the coupling effects of the multiple flow mechanisms. According to the study about the effect of delta winglet on the heat transfer investigated by Wu et al. [4], the total turbulence fluctuation has the largest effect on the heat transfer enhancement, followed by the velocity toward the heated surface, while the near-surface streamwise velocity has a moderate influence. Thus, the total turbulence fluctuation, i.e. turbulent kinetic energy, downwash velocity, and the near surface streamwise velocity, in the current study are also selected for the multiple linear regression analysis to find the weight of impact on the heat transfer enhancement. The turbulent kinetic energy (ke) and the downwash velocity ($\overline{W}/U_\infty$) chosen here were the vertical averaged values from Z=0.6W to 3W, as the trend of ke and $\overline{W}/U_\infty$ of different study cases with respect to the vertical direction (Z) is the same, as illustrated in Figure 5.9 and Figure 5.3. The near surface streamwise velocity is the velocity at the lowest measurement point of the experiment, i.e. Z=0.6W, noted as $U_{0.6}/U_\infty$. To find the weight of impact, the standardized regression coefficients (β_j^{std}) are introduced, expressed as [38],

$$\beta_j^{std} = \beta_j \frac{std_j}{std_y} \tag{5.17}$$

where β_j and std_j are the regression coefficients and the standard deviations of each individual parameter, and std_y is the standard deviation of the dependent variable (*Nu/Nu₀*). Based on the multiple linear regression results, listed in Table 5.1, the deduced standardized regression coefficients for *ke*, $\overline{W}/U_\infty$ and $U_{0.6}/U_\infty$ are 0.67, -0.49 and 0.34, respectively. The R-square for this linear regression is approximately 80%. The absolute value of the standardized regression coefficient indicates the weight of impact of each individual factor on the heat transfer augmentation. Clearly, the turbulent kinetic energy has the most significant effect on the heat transfer in the current study, while the near surface streamwise velocity has the least influence among the selected parameters. Therefore, although the 1*W*-spaced strip pair provides the lowest streamwise velocity, it still induces the best heat transfer enhancement, due to it having the strongest turbulent fluctuation and the largest downwash velocity.

Table 5. 1. Linear regression result

Parameter	*ke*	$\overline{W}/U_\infty$	$U_{0.6}/U_\infty$
Regression coefficient (β_j)	11.05	-1.45	0.45
Standardized regression coefficient (β_j^{std})	0.67	-0.49	0.34

5.5 Conclusions

A pair of 12.7 mm wide (*W*) and 25.4 mm tall rectangular flexible strips, made from 0.1 mm thick aluminum sheet, were investigated to identify their effectiveness in enhancing convective heat transfer from a heated flat surface. The strip pairs, in a side-by-side arrangement, spaced 1*W*, 2*W* and 3*W*, were studied at a wind speed of approximately 10 m/s. The Reynolds number based on the strip width (Re_W) was around 8.5×10^3. The heat transfer augmentation was analyzed in terms of the Nusselt number normalized by the unperturbed reference case in the absence of the strip pair (Nu/Nu_o). In summary, the 1*W*-spaced strip pair provided the most effective span-averaged heat transfer enhancement, from 0*W* to 2*W* downstream, and from 6*W* downstream to the end of the heated flat surface. Due to the strong vortices interaction, a larger Nu/Nu_o in the middle of the gap ($Y\approx0$) behind the 1*W*-spaced strip pair occurred. The corresponding Nu/Nu_0 value is approximately 1.50 at *X*=9*W*, *Y*=0, much larger than those associated with the 2*W*-spaced and 3*W*-spaced strip pairs, which are around 1.26 and 1.17, respectively. In spite of the decrease in streamwise velocity, which lessens the heat transfer enhancement according to the multiple linear regression result, a larger local wind velocity toward the heated surface, higher turbulence intensity and kinetic energy, and stronger flow fluctuations near vortex shedding frequency were obtained in the turbulent flow induced by the 1*W*-spaced strip pair, which resulted in the most forceful heat transfer augmentation.

Acknowledgments

This work was made possible by Natural Sciences and Engineering Research Council of Canada and Ontario Centres of Excellence.

References

[1] Y. A. Çengel and A. J. Ghajar, Heat and mass transfer : fundamentals & applications, fifth edition. McGraw Hill Education, 2015.

[2] S. Liu and M. Sakr, "A comprehensive review on passive heat transfer enhancements in pipe exchangers," Renew. Sustain. Energy Rev., vol. 19, pp. 64–81, 2013, doi: 10.1016/j.rser.2012.11.021.

[3] G. Biswas, H. Chattopadhyay, and A. Sinha, "Augmentation of heat transfer by creation of streamwise longitudinal vortices using vortex generators," Heat Transf. Eng., vol. 33, no. 4–5, pp. 406–424, 2012, doi: 10.1080/01457632.2012.614150.

[4] H. Wu, D. S.-K. Ting, and S. Ray, "The effect of delta winglet attack angle on the heat transfer performance of a flat surface," Int. J. Heat Mass Transf., vol. 120, pp. 117–126, 2018, doi: 10.1016/j.ijheatmasstransfer.2017.12.030.

[5] A. Khanjian, C. Habchi, S. Russeil, D. Bougeard, and T. Lemenand, "Effect of the angle of attack of a rectangular wing on the heat transfer enhancement in channel flow at low Reynolds number," Heat Mass Transf., vol. 54, no. 5, pp. 1441–1452, 2018, doi: 10.1007/s00231-017-2244-8.

[6] J. He, L. Liu, and A. M. Jacobi, "Air-Side Heat-Transfer Enhancement by a New Winglet-Type Vortex Generator Array in a Plain-Fin Round-Tube Heat Exchanger," J. Heat Transfer, vol. 132, no. 7, p. 071801, 2010, doi: 10.1115/1.4000988.

[7] A. Khanjian, C. Habchi, S. Russeil, D. Bougeard, and T. Lemenand, "Effect of rectangular winglet pair roll angle on the heat transfer enhancement in laminar channel flow," Int. J. Therm. Sci., vol. 114, pp. 1–14, 2017, doi: 10.1016/J.IJTHERMALSCI.2016.12.010.

[8] Y. X. Li, X. Wang, J. Zhang, L. Zhang, and J. H. Wu, “Comparison and analysis of the arrangement of delta winglet pair vortex generators in a half coiled jacket for heat transfer enhancement,” Int. J. Heat Mass Transf., vol. 129, pp. 287–298, 2019, doi: 10.1016/j.ijheatmasstransfer.2018.09.109.

[9] P. Promvonge, P. Promthaisong, and S. Skullong, “Experimental and numerical heat transfer study of turbulent tube flow through discrete V-winglets,” Int. J. Heat Mass Transf., vol. 151, p. 119351, 2020, doi: 10.1016/j.ijheatmasstransfer.2020.119351.

[10] S. Pourhedayat, S. M. Pesteei, H. E. Ghalinghie, M. Hashemian, and M. A. Ashraf, “Thermal-exergetic behavior of triangular vortex generators through the cylindrical tubes,” Int. J. Heat Mass Transf., vol. 151, 2020, doi: 10.1016/j.ijheatmasstransfer.2020.119406.

[11] Z. Ke, C. L. Chen, K. Li, S. Wang, and C. H. Chen, “Vortex dynamics and heat transfer of longitudinal vortex generators in a rectangular channel,” Int. J. Heat Mass Transf., vol. 132, pp. 871–885, 2019, doi: 10.1016/j.ijheatmasstransfer.2018.12.064.

[12] J. Shi, J. Hu, S. R. Schafer, and C. L. Chen, “Numerical study of heat transfer enhancement of channel via vortex-induced vibration,” Appl. Therm. Eng., vol. 70, no. 1, pp. 838–845, 2014, doi: 10.1016/j.applthermaleng.2014.05.096.

[13] J. Shi, J. Hu, S. R. Schafer, and C. C. L. Chen, “HEAT TRANSFER ENHANCEMENT OF CHANNEL FLOW VIA VORTEX-INDUCED VIBRATION OF FLEXIBLE CYLINDER,” in Proceedings of the ASME 2014 4th Joint US-European Fluids Engineering Division Summer Meeting, 2014, pp. 1–8.

[14] Z. Li et al., “A flapping vortex generator for heat transfer enhancement in a rectangular airside fin,” Int. J. Heat Mass Transf., vol. 118, pp. 1340–1356, 2018, doi: 10.1016/j.ijheatmasstransfer.2017.11.067.

[15] S. Ali, S. Menanteau, C. Habchi, T. Lemenand, and J. L. Harion, “Heat transfer and mixing enhancement by using multiple freely oscillating flexible vortex generators,” Appl. Therm. Eng., vol. 105, pp. 276–289, 2016, doi: 10.1016/j.applthermaleng.2016.04.130.

[16] S. Ali, C. Habchi, S. Menanteau, T. Lemenand, and J. L. Harion, “Three-dimensional numerical study of heat transfer and mixing enhancement in a circular pipe using self-

sustained oscillating flexible vorticity generators," Chem. Eng. Sci., vol. 162, pp. 152–174, 2017, doi: 10.1016/j.ces.2016.12.039.

[17] F. Sastre and A. Velazquez, "Experimental study on heat transfer enhancement caused by the flow-induced vibration of a prism inside a channel," Appl. Therm. Eng., vol. 125, pp. 412–424, 2017, doi: 10.1016/j.applthermaleng.2017.06.123.

[18] A. Dadvand, S. Hosseini, S. Aghebatandish, and B. C. Khoo, "Enhancement of heat and mass transfer in a microchannel via passive oscillation of a flexible vortex generator," Chem. Eng. Sci., vol. 207, pp. 556–580, 2019, doi: 10.1016/j.ces.2019.06.045.

[19] Y. Yang, D. S.-K. Ting, and S. Ray, "Convective heat transfer enhancement downstream of a flexible strip normal to the freestream," Int. J. Therm. Sci., vol. 145, p. 106059, 2019, doi: 10.1016/j.ijthermalsci.2019.106059.

[20] "Emissivity Coefficients Materials." [Online]. Available: https://www.engineeringtoolbox.com/emissivity-coefficients-d_447.html. [Accessed: 04-Apr-2019].

[21] "Thermal Conductivity of common Materials and Gases." [Online]. Available: https://www.engineeringtoolbox.com/thermal-conductivity-d_429.html. [Accessed: 04-Apr-2019].

[22] Y. Yang, D. S.-K. Ting, and S. Ray, "On flexible rectangular strip height on flat plate heat convection," Int. J. Heat Mass Transf., vol. 150, p. 119269, 2020, doi: 10.1016/j.ijheatmasstransfer.2019.119269.

[23] "Radiation Heat Transfer." [Online]. Available: https://www.engineeringtoolbox.com/radiation-heat-transfer-d_431.html. [Accessed: 04-Apr-2019].

[24] D. S.-K. Ting, Basics of engineering turbulence. Academic Press, New York, 2016.

[25] L. Chai and S. A. Tassou, "A review of airside heat transfer augmentation with vortex generators on heat transfer surface," Energies, vol. 11, p. 2737, 2018, doi: 10.3390/en11102737.

[26] Z. Sun, K. Zhang, W. Li, Q. Chen, and N. Zheng, "Investigations of the turbulent thermal-hydraulic performance in circular heat exchanger tubes with multiple rectangular

winglet vortex generators," Appl. Therm. Eng., vol. 168, p. 114838, 2020, doi: 10.1016/j.applthermaleng.2019.114838.

[27] K. W. Song, S. Liu, and L. B. Wang, "Interaction of counter rotating longitudinal vortices and the effect on fluid flow and heat transfer," Int. J. Heat Mass Transf., vol. 93, pp. 349–360, 2016, doi: 10.1016/j.ijheatmasstransfer.2015.10.001.

[28] K. Song and L. Wang, "Effects of longitudinal vortex interaction on periodically developed flow and heat transfer of fin-and-tube heat exchanger," Int. J. Therm. Sci., vol. 109, pp. 206–216, 2016, doi: 10.1016/j.ijthermalsci.2016.06.011.

[29] K. W. Song and T. Tagawa, "The optimal arrangement of vortex generators for best heat transfer enhancement in flat-tube-fin heat exchanger," Int. J. Therm. Sci., vol. 132, pp. 355–367, 2018, doi: 10.1016/j.ijthermalsci.2018.06.011.

[30] S. Sharples and P. S. Charlesworth, "Full-scale measurements of wind-induced: Convective heat transfer from a roof mounted flat plate solar collector," Sol. Energy, vol. 62, no. 2, pp. 69–77, 1998, doi: 10.1016/S0038-092X(97)00119-9.

[31] E. Sartori, "Convection coefficient equations for forced air flow over flat surfaces," Sol. Energy, vol. 80, no. 9, pp. 1063–1071, 2006, doi: 10.1016/j.solener.2005.11.001.

[32] A. Tariq, P. K. Panigrahi, and K. Muralidhar, "Flow and heat transfer in the wake of a surface-mounted rib with a slit," Exp. Fluids, vol. 37, no. 5, pp. 701–719, 2004, doi: 10.1007/s00348-004-0861-8.

[33] H. M. Badr, "Effect of free-stream fluctuations on laminar forced convection from a straight tube," Int. J. Heat Mass Transf., vol. 40, no. 15, pp. 3653–3662, 1997, doi: 10.1016/S0017-9310(96)00387-0.

[34] W. A. Xie and G. N. Xi, "Geometry effect on flow fluctuation and heat transfer in unsteady forced convection over backward and forward facing steps," Energy, vol. 132, pp. 49–56, 2017, doi: 10.1016/j.energy.2017.05.072.

[35] S. C. Yen and J. H. Liu, "Wake flow behind two side-by-side square cylinders," Int. J. Heat Fluid Flow, vol. 32, no. 1, pp. 41–51, 2011, doi: 10.1016/j.ijheatfluidflow.2010.09.005.

[36] S. R. Kumar, A. Sharma, and A. Agrawal, "Simulation of flow around a row of square cylinders," J. Fluid Mech., vol. 606, pp. 369–397, 2008, doi: 10.1017/S0022112008001924.

[37] D. Chatterjee, G. Biswas, and S. Amiroudine, "Numerical investigation of forced convection heat transfer in unsteady flow past a row of square cylinders," Int. J. Heat Fluid Flow, vol. 30, no. 6, pp. 1114–1128, 2009, doi: 10.1016/j.ijheatfluidflow.2009.09.004.

[38] J. L. Myers, A. (Arnold) Well, and R. F. Lorch, Research design and statistical analysis. Routledge, 2010.

CHAPTER 6

THE EFFECT OF FREESTREAM TURBULENCE ON CONVECTION ENHANCEMENT BY A FLEXIBLE STRIP

Y. Yang, D. S-K. Ting, S. Ray, "The effect of freestream turbulence on convection enhancement by a flexible strip," Experimental Thermal and Fluid Science, under review.

6.1 Introduction

Forced convective heat transfer enhancement has been widely explored for boosting engineering system performance. The enhancement techniques can be divided into active and passive approaches. The active means is often more effective. For example, a novel water spray for cooling photovoltaic (PV) panel, proposed by Nizetic et al.[1], was able to reduce the panel temperature by 28°C, boosting the electric power output by a handsome 16%. In another study, different designs of heat absorbing pipes on the back surface of the PV panel was investigated by Bhattacharjee et al. [2]. Among their studied cases, the best thermal performance occurred when using the circular spiral-shaped semi-flattened copper pipe, providing a 17% increase in the maximum power of the panel. The cost of active techniques includes the needed power to operate them and thus, reduces the overall useful power. These techniques are also more complex and they require higher initial costs and more maintenance. Therefore, the simple but effective passive approaches are preferred. Kim and Kim [3] conducted a numerical study in search of an optimal design of a rib to enhance the heat transfer in a channel. They found that the heat transfer rate increased with the increase of the rib height (H) or the decrease of the rib width (W). Other types of rib, including half-cylinder, rectangular, straight triangular, and isosceles triangular, were numerically studied by Xu et al. [4] for their effect on the heat transfer in a channel. Among others, the straight triangular rib provided the best heat transfer augmentation of 76% with respect to the clean channel without the rib. This was attributed to the strongest vortex and flow disturbance brought about by the specific rib. These blunt heat transfer enhancers, however, come with a fair amount of pressure drop and thus, additional pumping power to move the fluid at the same velocity.

Winglets have attracted much attention recently, as they tend to induce significantly less pressure drop while producing a long-lasting longitudinal vortex street. The street of vortices disturb the boundary layer and increase the turbulence intensity [5], substantially enhancing heat transfer rate. Wijayanta et al. [6] experimentally investigated the effect of delta winglets on the heat transfer enhancement in a tube. The attack angle of the winglet was varied from 30°to 70°. They found increasing heat transfer augmentation with increasing attack angle; the winglet with a 70° attack angle led to a 264% heat transfer improvement. Biswas et al. [7] examined two different longitudinal streamwise vortices generators, delta-wing and delta-winglet pair, for improving the performance of a heat exchanger. They found that the vortices generated behind the wing and winglet lead to a swirling flow moving downstream, effectively mixing the cooler stream of the vortex core with the hotter fluid from the channel wall. Stronger vortices were observed behind the delta wing, providing a heat transfer enhancement of around 34% compared to the clean channel, while the augmentation caused by the delta-winglet pair was about 14%. Another numerical investigation exploring the wing shape effect, including rectangular, triangular and trapezoidal, on the thermal characteristics of a channel was performed by Sheikhzadeh et al. [8]. From a heat transfer point of view, the rectangular wing was found to be the most effective, providing an average Nusselt number of approximately 130 at a Reynolds number of 1600. The trapezoidal and triangular wings come in second and third places, furnishing an average Nusselt number of around 115 and 100, respectively, at the same Reynolds number. Recently more unique designs have emerged; for example, the curved-winglet and the perforated-curved winglet in a circular tube were investigated by Skullong et al. [9]. The curved winglet was observed to augment the heat transfer rate by up to 476% compared to the clean tube. The perforated-curved winglet with 1.5 mm diameter holes showed superior performance, providing the thermal enhancement factor of 1.76, 7.8% higher than that associated with the curved-winglet for the same friction loss. Song et al. [10] came up with two different sizes of novel curved delta winglet, exploring their effectiveness in the heat transfer enhancement in a fin-tube heat exchanger. They pointed out that the smaller winglet is more effective at a lower Reynolds number of 500, while the larger winglet was more conducive to the heat transfer augmentation at a higher Reynolds number of 3000, with an overall heat transfer enhancement of around 19% compared to the reference case without the winglets.

In addition to the rigid turbulence generators mentioned above, flexible type of turbulence generator has also been demonstrated to boost heat convection [11]. Ali et al. [12] numerically investigated the heat transfer in a 2D channel by using oscillating flexible vortex generators. They showed that the structural oscillation can further heat transfer enhancement. Meanwhile, they revealed that the larger oscillation amplitude could result in a higher heat transfer rate. Their flexible vortex generators provided a global heat transfer augmentation up to 275% compared to the empty channel, whereas the rigid ones only led to approximately 50% improvement. In another study, the heat transfer characteristics of the heated oscillating cylinder was presented in detail by Fu and Tong [13]. They found that the highest enhancement occurred when the oscillating frequency of the cylinder approached the shedding frequency. Similarly, Yang [14] conducted a numerical investigation of the heat transfer enhancement in a channel via an oscillating bar. The heat transfer rate was found to be strongly correlated with the oscillating amplitude of the bar. Stronger vortices were produced by larger amplitude oscillation, resulting in a better mixing between the high-temperature wall flow from the heated regions and the low-temperature core flow. Furthermore, Yang and Chen [15] explored the heat transfer characteristics of heated blocks in a channel with an oscillating cylinder. The vibrating cylinder increased the overall heat transfer by 17% with respect to the reference case without the cylinder in the channel.

It is clear from the literature review that well-designed turbulence generators can significantly improve heat transfer. Various ingenious designs have been proposed in recent years, trying to maximize the heat transfer augmentation. The selected literatures are summarized in Table 6.1. Most of these recent attempts were for internal flow, where the confining walls and other structures tended to significantly alter the generated turbulent flow. More scarcely studied is the open flow condition, which is of both fundamental and practical importance. Fundamentally, it can reveal the physics of the vortices and turbulence spawn from the passive flow 'agitator' without the added complication of the confining walls. Practically, the discovery in the open flow case can substantially further renewable and other technologies such as solar photovoltaic. The 0.1 mm thick rectangular flexible strip used in our previous study [16], with an oscillating frequency of around 120Hz and a maximum oscillating amplitude of around 1.2 mm, was further exploited in the current study. The orificed perforated plate [17][18] was installed upstream of the flexible strip, to understand the role of ubiquitous wind turbulence. The aim was to understand the flexible strip in enhancing heat convection under varying level of freestream turbulence.

Table 6. 1. Summary of selected literatures

Reference	Technology for heat transfer enhancement			Brief comments
	Active / Passive	Open / Internal Flow	Studied case	
Nizetic et al. [1]	Active	-	water spray	Effective, but external power, higher initial costs and more maintenance are needed
Bhattacharjee et al. [2]	Active	-	water flow	
Kim and Kim [3]	Passive	Internal Flow	rib vortex generator	Longitudinal vortex generator (winglet / wing) attracted much more attention due to its long-last effect on heat transfer enhancement
Xu et al. [4]	Passive	Internal Flow	rib vortex generator	
Wu et al. [5]	Passive	Open Flow	winglet vortex generator	
Wijayanta et al. [6]	Passive	Internal Flow	winglet vortex generator	
Biswas et al. [7]	Passive	Internal Flow	winglet and wing vortex generator	Wing produced a better heat transfer enhancement
Sheikhzadeh et al. [8]	Passive	Internal Flow	wing vortex generator	Rectangular wing produced a better heat transfer enhancement
Skullong et al. [9]	Passive	Internal Flow	curved winglet vortex generator	Novel shape design draws attention due to its effectiveness in heat transfer enhancement
Song et al. [10]	Passive	Internal Flow	curved winglet vortex generator	
Ali et al. [12]	Passive	Internal Flow	flexible vortex generator	Flexible type could further improve the heat transfer enhancement compared to their rigid counterpart
Fu and Tong [13]	Passive	Internal Flow	flexible vortex generator	
Yang [14]	Passive	Internal Flow	flexible vortex generator	
Yang and Chen [15]	Passive	Internal Flow	flexible vortex generator	

6.2 Experimentation

Figure 6.1 depicts the experimental setup in a closed-loop wind tunnel with a 76 cm by 76 cm cross-section. A 3 mm thick 295 mm wide and 380 mm long *PTFE* (polytetrafluoroethylene) plate was inlaid in the center of fiberglass test section base. The conductivity and the emissivity of the *PTFE* plate were 0.25 $Wm^{-1}K^{-1}$ [19][20] and 0.92 [21][22], respectively. A tank of water placed under the *PTFE* plate was set to boil continuously, keeping the bottom surface of the *PTFE* plate at 100℃. A FLIR C2 thermal camera with 80 by 60 pixels was used to capture the local temperature distribution of the top surface of the heated *PTFE* plate. The 0.1 mm-thick, 12.7 mm-wide (*W*), and 25.4 mm-tall rectangular flexible strip was placed upstream of the *PTFE* plate to perturb the flow. An orificed perforated plate (*OPP*) as used in [17][23] was employed to explore the influence of freestream turbulence on the effectiveness of the flexible strip in augmenting heat convection. The 6 mm thick *OPP* has a perforation of 57% consisting of 38.1 diameter (*D*) holes each chamfered 41°. It was positioned at 10, 13 and 16 *D* upstream of the flexible strip, generating streamwise freestream turbulence intensity of approximately 11%, 9% and 7%, respectively. The reference empty-tunnel case with 0.4% background turbulence was also investigated for completeness. It should be noted that the freestream turbulence was measured at the center of the wind tunnel, at the same *X* location where the flexible strip was placed. The streamwise freestream velocity in the current study was fixed at approximately 7 m/s, resulted in a Reynolds number based on the strip width of 6000. As shown in Figure 6.1, the orthogonal streamwise, widthwise and vertical directions are represented as *X*, *Y* and *Z*.A triple sensor hotwire probe (DANTEC DYNAMICS type 55P95) with a constant-temperature anemometer was employed to characterize the flow at 9*W* downstream of the flexible strip, to detail the turbulent flow characteristics. At each cross-sectional point, 10^6 measurements were sampled at 80 kHz and low passed at 30 kHz to avoid aliasing.

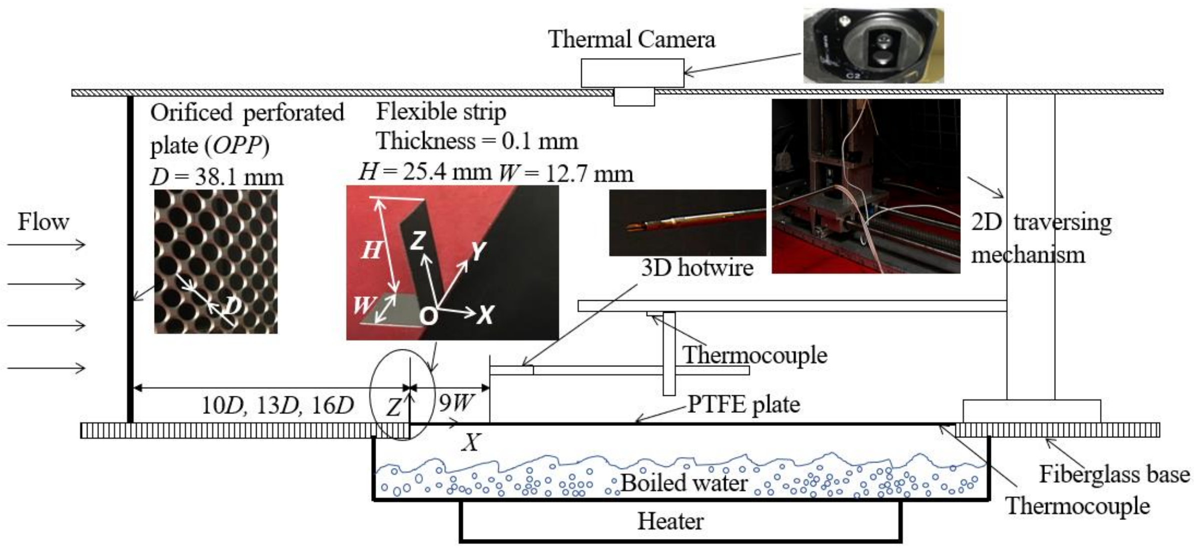

Figure 6. 1. The experimental setup

6.3 Data Processing

The total heat transfer rate from the heated *PTFE* plate was calculated from,

$$\dot{Q}_{total} = K_{PTFE} A (\frac{T_{bottom} - T_{top}}{t_{PTFE}}) \tag{6.1}$$

where the thermal conduction, K_{PTFE} was 0.25 $Wm^{-1}K^{-1}$, surface area, *A* was 295 mm times 380 mm, and thickness, t_{PTFE} was 3 mm. Due to small thermal conductivity of the PTFE plate (0.25 $Wm^{-1}K^{-1}$) and the surrounding fiberglass test section base (0.04 $Wm^{-1}K^{-1}$), the heat transfer parallel to the flat plate was considerably smaller than that normal to it. Therefore, the heat transfer was predominantly one-dimensional, in the direction normal to the flat plate. The temperature of the lower surface of the *PTFE* plate, T_{bottom} was maintained at 100℃, and the top surface temperature, T_{top}, was measured by a FLIR C2 thermal camera.

With negligible heat conduction to the base of the wind tunnel test section, the convective heat transfer rate,

$$\dot{Q}_{convection} = \dot{Q}_{total} - \dot{Q}_{radiation} \tag{6.2}$$

The radiation heat transfer rate, accounting for approximately 18% of the total heat transfer rate, could be calculated as,

$$\dot{Q}_{radiation} = \varepsilon\sigma A(T_{top}^4 - T_{wall}^4) \quad (6.3)$$

where emissivity ε is 0.92 [21], and Stefan-Boltzmann constant σ = 5.67x10^{-8} Wm^{-2}K^{-4} [24]. The wind tunnel wall temperature T_{wall} was assumed to be equal to the air temperature, T_{air}, which was measured by a thermocouple; see Figure 6.1.

From the convective heat transfer rate, the convection heat transfer coefficient was deduced from

$$h = \frac{\dot{Q}_{convection}}{A(T_{top} - T_{air})} \quad (6.4)$$

The corresponding non-dimensional Nusselt number was obtained from

$$Nu = \frac{hL}{K_{air}} \quad (6.5)$$

where K_{air} was the thermal conductivity of the wind tunnel air and the characteristic length, L, was measured from the leading edge of the *PTFE* plate. The normalized Nusselt number is introduced, to evaluate the convective heat transfer augmentation, i.e.,

$$\frac{Nu}{Nu_0} = \frac{h}{h_0} \quad (6.6)$$

Here, Nu_0 and h_0 are the Nusselt number and the coefficient of convective heat transfer, respectively, for the base case without the flexible strip, but in the presence of the *OPP*. Also used as a reference is Nu_{00} which corresponds to no *OPP* and no flexible strip case. The background turbulence for this case is 0.4%.

The instantaneous velocities in streamwise (*X*), widthwise (*Y*) and vertical (*Z*) directions were obtained from a triple sensor hotwire probe. It can be shown that,

$$U_i = \bar{U} + u\,; V_i = \bar{V} + v\,; W_i = \bar{W} + w \quad (6.7)$$

where the corresponding time-averaged velocities are denoted as $\bar{U}, \bar{V}, \bar{W}$, and the instantaneous fluctuating velocities are represented by u, v, and w .

From the root-mean-square fluctuating velocities, $u_{rms} = \sqrt{\sum_{i=1}^{N} \frac{{u_i}^2}{N-1}}$, the relative turbulence intensity can be defined as

$$Tu = \frac{u_{rms}}{U_\infty} \tag{6.8}$$

where the freestream velocity U_∞ was maintained at around 7 m/s. *Tu* denotes streamwise *freestream* turbulence intensity, where the fluctuating velocity was calculated from the freestream flow.

Due to the highly three-dimensional nature of the turbulent flow [25], the normalized turbulent kinetic energy was used to represent the total turbulence level, i.e.,

$$ke = \frac{1}{2}\frac{(u_{rms}^2 + v_{rms}^2 + w_{rms}^2)}{U_\infty^2} \tag{6.9}$$

The Reynolds number was defined based on the strip width (*W*) and the freestream velocity (U_∞), i.e.,

$$Re_W = \frac{WU_\infty}{\nu} \tag{6.10}$$

where ν is the kinematic viscosity of air. The Reynolds number was held at approximately 6000.

Based on *W* and U_∞, the non-dimensional vortex shedding frequency, Strouhal number, was defined as

$$St = \frac{fW}{U_\infty} \tag{6.11}$$

Here f is the vortex shedding frequency.

To describe the intensity of the vortices, the X-vorticity at point (*i*, *j*) [26],

$$\begin{aligned}\omega = [\, &\Delta Y\left(\bar{V}_{i-1,j-1} + 2\bar{V}_{i,j-1} + \bar{V}_{i+1,j-1}\right) + \Delta Z\left(\bar{W}_{i+1,j-1} + 2\bar{W}_{i+1,j} + \bar{W}_{i+1,j+1}\right) \\ &-\Delta Y\left(\bar{V}_{i+1,j+1} + 2\bar{V}_{i,j+1} + \bar{V}_{i-1,j+1}\right) \\ &\qquad - \Delta Z\left(\bar{W}_{i-1,j+1} + 2\bar{W}_{i-1,j} + \bar{W}_{i-1,j-1}\right)]/(8\Delta Y \Delta Z)\end{aligned} \tag{6.12}$$

was employed. Normalizing this by *W* and U_∞, the corresponding non-dimensional X-vorticity,

$$\Omega = \frac{\omega W}{U_\infty} \tag{6.13}$$

6.4 Results and Discussion

In this section, first the heat transfer results are presented. Subsequently, the underlying fluid mechanics are detailed, in an effort to delineate the underlying happenings.

6.4.1 Heat Transfer Enhancement

Figure 6.2 presents the contours of the normalized Nusselt number (Nu/Nu_0) under different freestream turbulence conditions, revealing the convective heat transfer enhancement with respect to the reference case. Keep in mind that there was also no *OPP*, in addition to no strip, for the *Tu* = 0.4% case. In other words, the first (top) case in Figure 6.2 depicts Nu/Nu_{00}; while the other cases show Nu/Nu_0. The uncertainty of Nu/Nu_0 was estimated to be approximately 0.07. In general, a large normalized Nusselt number region at approximately 2.5 occurs in the near-strip area until X/W=2. This is due to the strong vortical structures immediately behind the strip. Following that, a decreasing trend of the heat transfer augmentation could be identified, indicating that the vortices and the highly intense turbulence are decaying. More interestingly, the freestream turbulence tends to degrade the *relative* heat transfer augmentation by the flexible strip. For example, the local Nu/Nu_0, or more correctly Nu/Nu_{00}, induced by the strip under 0.4% freestream turbulence remained largely above 1.3 by the end of the studied heated surface, i.e. X=23W downstream of the strip. The large Nu/Nu_0 region becomes shorter and narrower with increasing *Tu*. In other words *Nu* with respect to Nu_0 is lessening with increasing *Tu*. From these results alone, we cannot tell how much of this diminishment is due to decreasing *Nu*, if any, and how much of it is due to increasing Nu_0 with *Tu*.

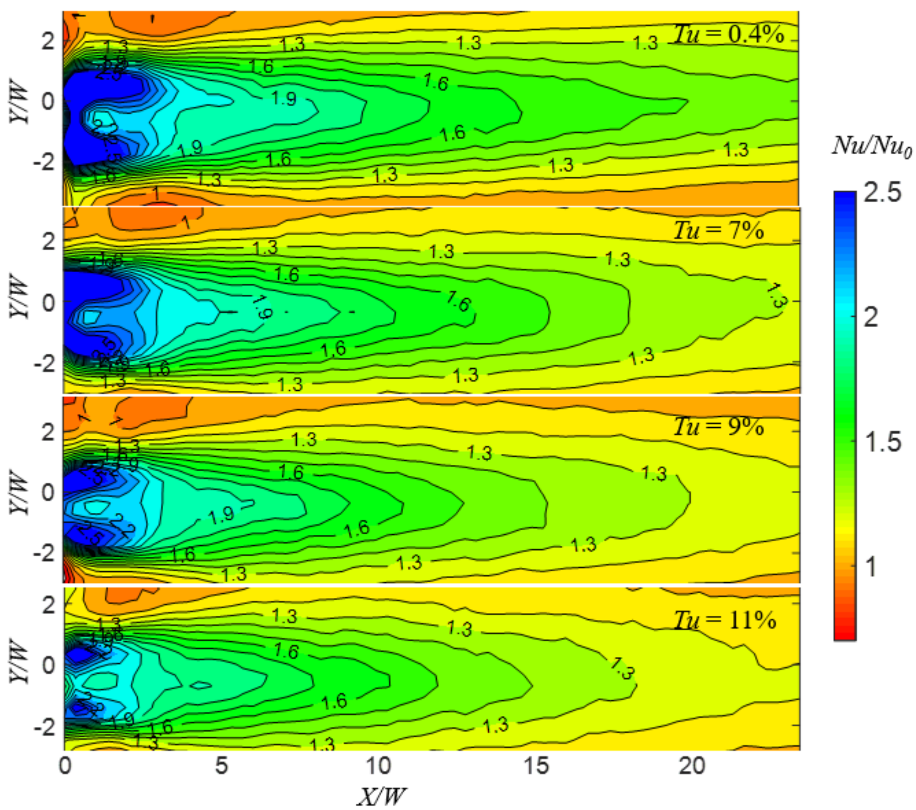

Figure 6. 2. Normalized Nusselt number (*Nu/Nu₀*) downstream of the flexible strip

To further describe the heat transfer enhancement of the entire heated surface, the span-averaged results across $Y=\pm4W$ are depicted with respect to downstream distance in Figure 6.3, which is of practical interest. It is clear from the figure that Nu/Nu_0 peaks right behind the strip, probably a by-product of the newly formed intense vortical flow structures. The span-averaged Nu/Nu_0 is as high as 1.93 for the Tu = 0.4% case. It decays rapidly (exponentially) to 1.43 at X=4W, beyond which it decreases gradually, to around 1.23 at X=23W. Also notable, the flexible strip under the most intense freestream turbulence induces the worst *relative* heat transfer enhancement, approximately 0.3 and 0.1 smaller Nu/Nu_0 than that associated with the 0.4% freestream turbulence, in the near strip region and at the end of the heated surface, respectively. It is of practical significance to note that even at a very high freestream turbulence of 11%, where the freestream turbulence is inducing consequential heat transfer enhancement, the flexible strip can still notably further the heat transfer rate.

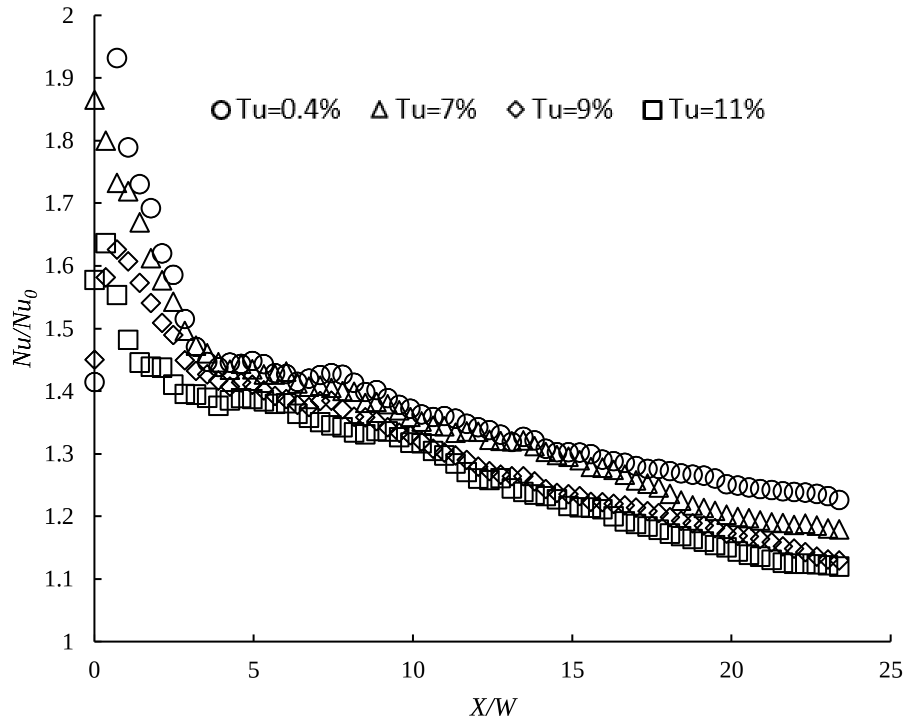

Figure 6. 3. Span-averaged (across Y=±4W) Nu/Nu_0 downstream of the flexible strip

Figure 6.4 illustrates the cross-stream Nu/Nu_0 profile at X=9W and X=20W. We see that the peak Nu/Nu_0 decreases from X = 9W to 20W; from 1.87, 1.80, 1.72 and 1.68 under 0.4%, 7%, 9% and 11% freestream turbulence, respectively, to around 1.49, 1.35, 1.29 and 1.23. Also note that the decay in peak Nu/Nu_0 with distance is somewhat more drastic at more turbulent freestream. The heat transfer improvement, Nu/Nu_0, or more correctly, Nu/Nu_{00}, by the strip under 0.4% freestream turbulence is as high as 1.87 at X=9W. When it is in 11% freestream turbulence, the strip is less effective, only providing peak Nu/Nu_0 value of around 1.68. We will scrutinize the underlying flow characteristics to better understand the happenings in a later section.

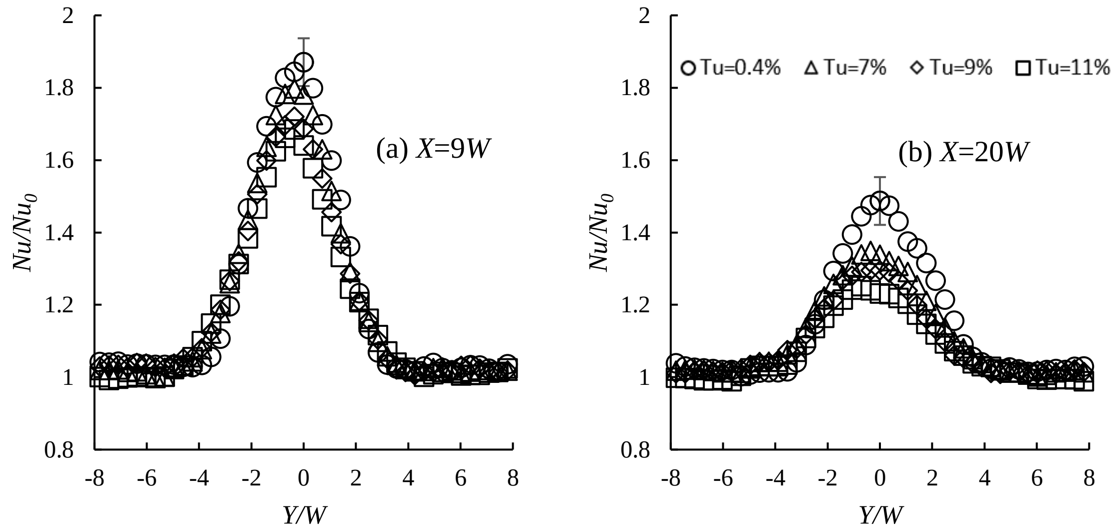

Figure 6. 4. Cross-stream profile of Nu/Nu_0 at (a) X = 9W, (b) X = 20W

To have a more complete picture, let us compare and contrast the heat transfer enhancement by the flexible strip, under the various levels of freestream turbulence, Nu/Nu_0, with respect to that of the completely empty wind tunnel in the absence of both the *OPP* and the flexible strip, Nu/Nu_{00}. Comparing these Nu/Nu_{00} results with those Nu/Nu_0 results presented earlier will give a sense of the relative enhancement contribution by the flexible strip with respect to that caused by freestream turbulence. Figure 6.5 shows the span-averaged (across Y=±4W) Nusselt number, in the presence of the strip (and *OPP*, except for the Tu=0.4% case without the *OPP*), relative to the Nusselt number in the absence of both strip and *OPP*, i.e., Nu/Nu_{00}. Note that the Nu_0 case corresponding to Tu=0.4% presented in Figures 6.2 to 6.4 is equal to Nu_{00}. Figure 6.5 clearly illustrates increasing Nu/Nu_{00} with Tu. There is a drastic jump in Nu/Nu_{00} from a largely unperturbed wind stream with Tu of 0.4% to 7%. When Tu further increases from 7% to 9%, and to 11%, a slight increase in Nu/Nu_{00} occurred. To put it another way, the heat transfer rate is drastically augmented when the ‘laminar’ wind becomes turbulent, any further intensification of wind turbulence leads to relatively smaller, but still definite, increment of heat transfer enhancement.

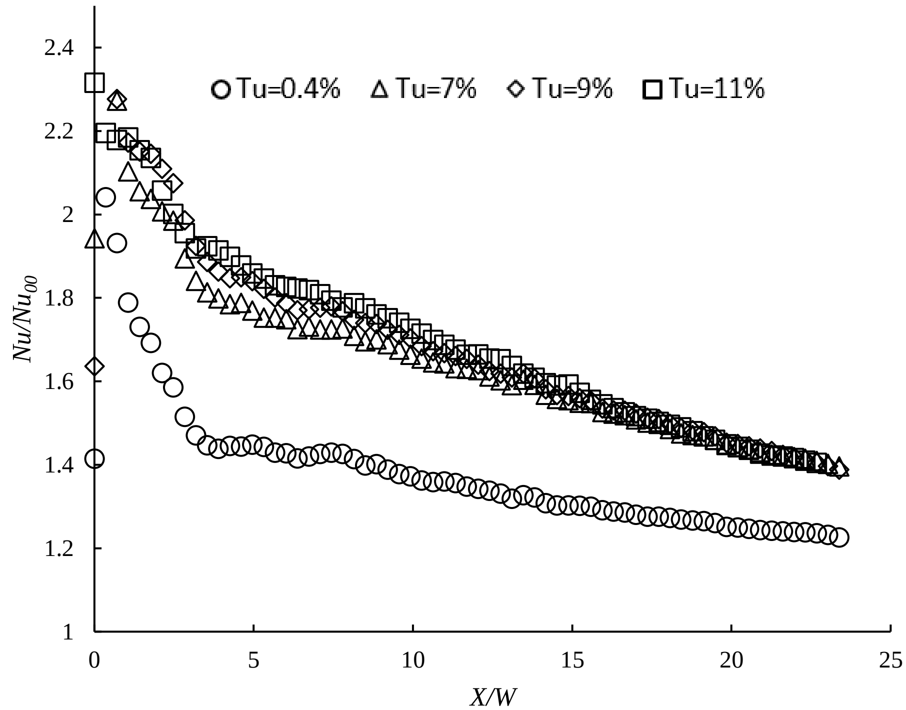

Figure 6. 5. Span-averaged (across Y=±4W) Nu/Nu_{00} as a function of distance downstream of the strip

The cross-stream profiles of Nu/Nu_{00} at X=9W are plotted in Figure 6.6. The peak value of Nu/Nu_{00} for 11% freestream turbulence case is just over 2.2, which is 0.4 larger than that associated with 0.4% freestream turbulence. It is interesting to note that the peak Nu/Nu_{00} values under 7%, 9%, and 11% freestream turbulence are roughly at the same level. The small gain in Nu/Nu_{00} with increasing Tu beyond 7% takes place away from the peak Nu/Nu_{00} region, i.e., outside of Y=±2W. This indicates that in the region behind the strip, within Y = ±2W, the larger wake structures dominate the augmentation of the heat transfer rate, more than doubling Nu. The relatively milder influence of Tu becomes only distinguishable outside of the wake region.

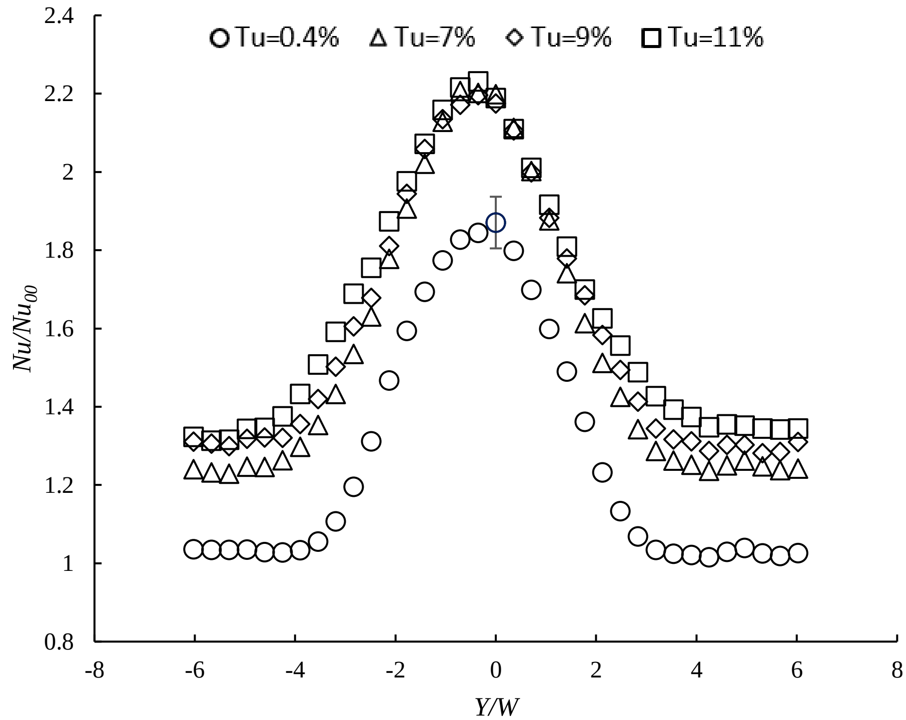

Figure 6. 6. Cross-stream profile of Nu/Nu_{00} at X = 9W

To better depict the effect of Tu, span-averaged (across Y=±4W) Nu_0/Nu_{00} is plotted as a function of distance downstream of the strip. Recall that Nu_0 signifies the no-strip condition with the *OPP* upstream generating the desirable wind turbulence, whereas Nu_{00} denotes the no-strip case in the absence of the *OPP*. The effect of the 2% incremental freestream turbulence intensity, Tu, from 7% to 9% and to 11%, is obvious. To put it in context, high wind turbulence is quite effective in enhancing the heat transfer rate, boosting Nu from 20 to 50% in the absence of the flexible strip. Therefore, the additional improvement in heat transfer caused by the strip was partially masked by that due to increasing Tu. Namely, the values of Nu/Nu_0, Figures 6.2-6.4, are less than those of Nu/Nu_{00}, Figures 6.5-6.6, because freestream turbulence causes Nu_0 to become significantly larger than Nu_{00}, Figure 6.7. In practice, there is always a gain with the strip and with increasing wind turbulence. Higher wind turbulence may reduce Nu/Nu_0 somewhat by increasing Nu_0, but the resulting absolute value of Nu in the presence of the flexible strip is always larger. In short, the heat transfer performance is invariably improved in the presence of the strip, and the total improvement is consistently more than that due to wind turbulence alone.

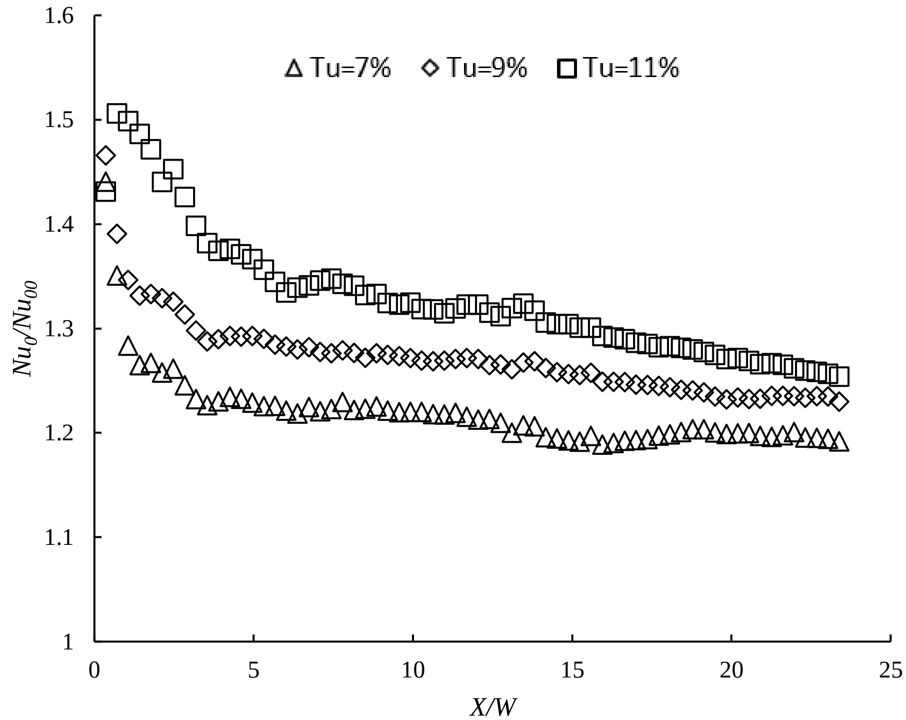

Figure 6. 7. Span-averaged (across Y=±4W) Nu_0/Nu_{00} as a function of distance downstream of the strip

6.4.2 Flow Characteristics

To understand the underlying physics behind the heat transfer results, the flow characteristics measured by a triple hotwire, without heating the plate, are detailed here. Selected locations downstream of the flexible strip are chosen to reveal the evolution of the perturbed flow.

6.4.2.1 X-Vorticity

Figure 6.8 illustrates the contour of X-vorticity normalized by the freestream velocity ($U_\infty \approx 7\ \mathrm{m/s}$) and the width of the strip (W = 12.7 mm), $\Omega = \frac{\omega W}{U_\infty}$.The cross-stream velocity vectors (in the YZ plane) are also included to present the flow motion. It is worth mentioning that the velocity vectors are a little asymmetric. This is presumably due to the imperfection of the experimental work, such as a little flow non-uniformity, a minute misalignment, etc. which could significantly disturb the turbulent flow. The thick dashed rectangle traces the strip in the YZ plane, looking upstream at 9W downstream distance. The vortical structures with swirling motions are clearly distinguishable. These flow motions promote the large-scale mixing of fluid and, thus, thermal energy, and they interrupt the thin but highly-thermal-resistive boundary layer next to the plate [27][28]. Note that the strength of the vortex pair is progressively weakened as the streamwise freestream turbulence intensifies from 0.4% to 11%. The peak value of the normalized X-vorticity induced by the strip under a freestream turbulence of 0.4% is approximately 0.18, and it decreases to around 0.17, 0.16 and 0.15 as *Tu* increases to 7%, 9% and 11%, respectively. Furthermore, the size of the vortical structure also increases with freestream turbulence. For example, the X-vorticity contour of -0.04 spans 1.3*W*, from *Y*=-0.5*W* to -1.8*W*, when *Tu* = 0.4%. This same vorticity contour spans 2*W*, from *Y*=-0.5*W* to -2.5*W*, when *Tu* is at 11%. These findings are in agreement with Miloud et al. [29], who found the circulation of their wingtip generated vortex to decrease, while the vortex radius increases, with increasing freestream turbulence.

Increasing vortex intensity has been correlated with enhanced heat transfer rate [30]. Freestream turbulence, tends to weaken coherent vortex structures, potentially lessens the vortex-induced heat transfer augmentation. The effect of this weakening in the X-vorticity seems to manifest itself in terms of the maximum heat transfer enhancement (Nu/Nu_{00}) shown in Figure 6.6. Case in point, the 11% freestream turbulence weakened the X-vorticity to a maximum value of only 0.15 such that the corresponding maximum Nu/Nu_{00} is at the same level at those at *Tu* of 7% and 9%, Nu/Nu_{00} = 2.2. As the vortex weakens, it tends to enlarge. The increase in vortex size can improve the span of the vortex-induced heat transfer enhancement. For example, the span-averaged Nu/Nu_{00} is around 1.77 at 9*W* downstream for the maximum X-vorticity of 0.15 (*Tu*=11%) case, marginally higher than that under the maximum X-vorticity of 0.17 (*Tu*=7%), which is approximately 1.70, although their peak Nu/Nu_{00} values are almost the same; see Figures 6.5 and 6.6. Keep in mind that a larger vortical eddy encompasses a larger volume of air (i.e., more freestream cool air is brought in contact with the hot plate). Notwithstanding, it is difficult to differentiate this enhancement from that brought about by the increase in wind turbulence. Besides, parameters such as the velocities toward, across and away from the heated surface are also expected to play a consequential role. We will examine these details next.

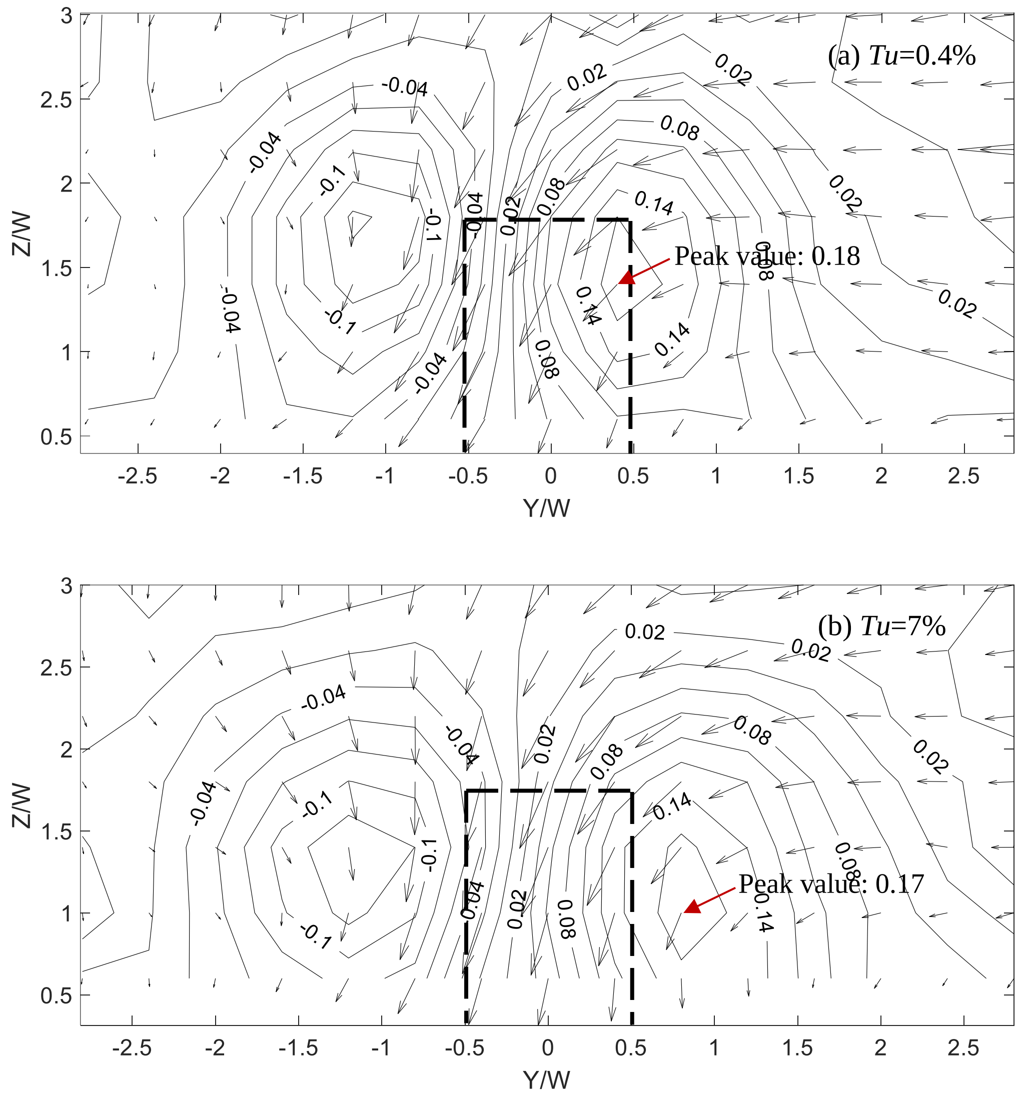

(a) Tu=0.4%
Peak value: 0.18
(b) Tu=7%
Peak value: 0.17
Z/W
Y/W

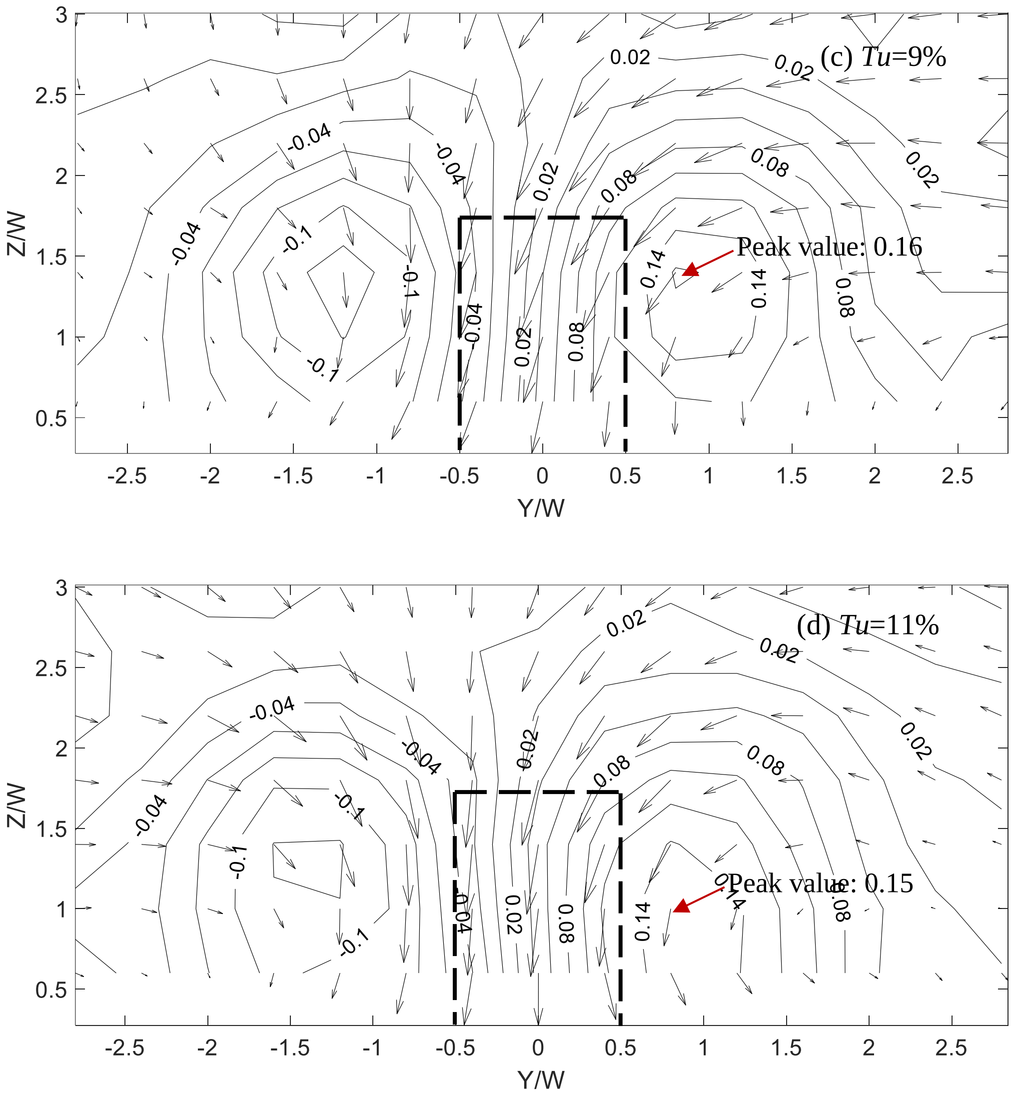

Figure 6. 8. Non-dimensional X-vorticity contour and velocity vector in *YZ* plane at 9*W* downstream of the flexible strip under streamwise freestream turbulence intensity of (a) *Tu* = 0.4% (b) *Tu* = 7% (c) *Tu* = 9% (d) *Tu* = 11%

To reiterate, it is a common knowledge that the wind bringing cooler air toward a heated flat surface can effectively promote the cooling of the surface [31][32][33]. Figure 6.9 presents the profile of the normalized velocity toward the heated horizontal surface ($\overline{W}/U_\infty$) in the vertical direction at 9*W* downstream of the strip. Each data point corresponds to a span-averaged value covering *Y*=±0.4*W*. As such, they encompass the downwash region behind the strip shown in Figure 6.8; as we are particularly interested in the flow toward the heated surface. Over the studied *Z* range, the normal velocity toward the plate increases ($\overline{W}/U_\infty$ becomes more negative), peaks at around Z=1.4W, and then decreases with increasing Z. The most negative $\overline{W}/U_\infty$ point corresponds approximately to the vertical level where the centers of the two vortices are located in Figure 6.8. This is somewhat expected as the tangential velocity of the two vortices along this height is directed vertically downward. It is perplexing to see that when there is negligible freestream turbulence to disturb the vortices (with Tu=0.4% in the absence of OPP), the downwash velocity is the smallest. This smallest $\overline{W}/U_\infty$ is expected to induce the worst absolute heat transfer performance Nu/Nu_{00} as shown in Figure 6.5. Moreover, the strip under the 7% freestream turbulence induces the largest downwash velocity, which indicates that the moderately intense (7%) freestream turbulence is supposed to provide the most effective flow condition to the heat transfer augmentation from the point of view of downwash velocity alone. Further increase of the freestream turbulence to 11%, the span-averaged downwash velocity decreased marginally, implying that the most intense freestream turbulence has a small negative effect on the heat transfer performance as far as the downwash velocity is concerned. However, notwithstanding the largest $\overline{W}/U_\infty$ occurs under the Tu=7% condition, it does not provide the most effective absolute heat transfer augmentation Nu/Nu_{00}; see Figure 6.5. Its induced span-averaged Nu/Nu_{00} is approximately 1.70 at 9W downstream, around 0.07 smaller than that of Tu = 11%, under which $\overline{W}/U_\infty$is observed to be smaller. This seems to imply that the effects of other influential parameters, such as streamwise velocity ($\overline{U}/U_\infty$) and the local turbulence fluctuation (ke) [22], have overshadowed the effect of $\overline{W}/U_\infty$. The effects of these additional parameters are examined next.

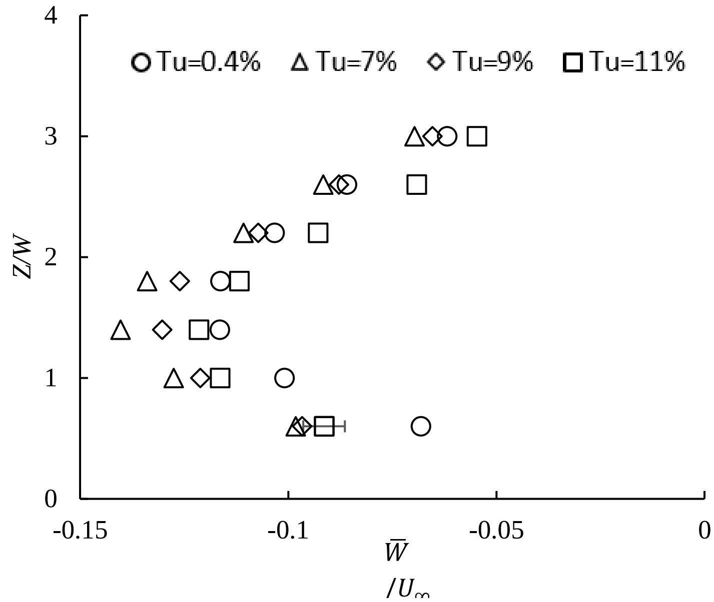

Figure 6. 9. Span-averaged (across Y=±0.4W) $\overline{W}/U_\infty$ profile at 9W downstream of the flexible strip

In addition to the flow toward the heated surface, also important is the streamwise velocity, which has been found to correlate strongly with forced heat convection. The standard Nusselt-Reynolds relations for a horizontal flat plate are $Nu = 0.664Re^{0.5}Pr^{1/3}$ and $Nu = 0.037Re^{0.8}Pr^{1/3}$, for laminar and turbulent flow, respectively [24]. These relationships bespeak increasing *Nu* with streamwise velocity, *Re*; more so when the flow is turbulent. With respect to that, the time-averaged streamwise velocity profile at 9W downstream of the strip is depicted in Figure 6.10. The dashed rectangle encompasses the measurement locations of the hotwire probe. The time-averaged streamwise velocity normalized by the freestream velocity ($U_\infty \approx 7$ m/s) has an uncertainty of around 0.023; see the appendix. As expected, freestream turbulence flattens the velocity profile, reducing the 'boundary layer,' augmenting the near-surface streamwise velocity. The normalized streamwise velocity induced by the strip under 0.4% freestream turbulence is approximately 0.53 at Y=0 and Z=0.6W. It increased to around 0.61, 0.63 and 0.69 when the freestream turbulence is increased to 7%, 9% and 11%, respectively.

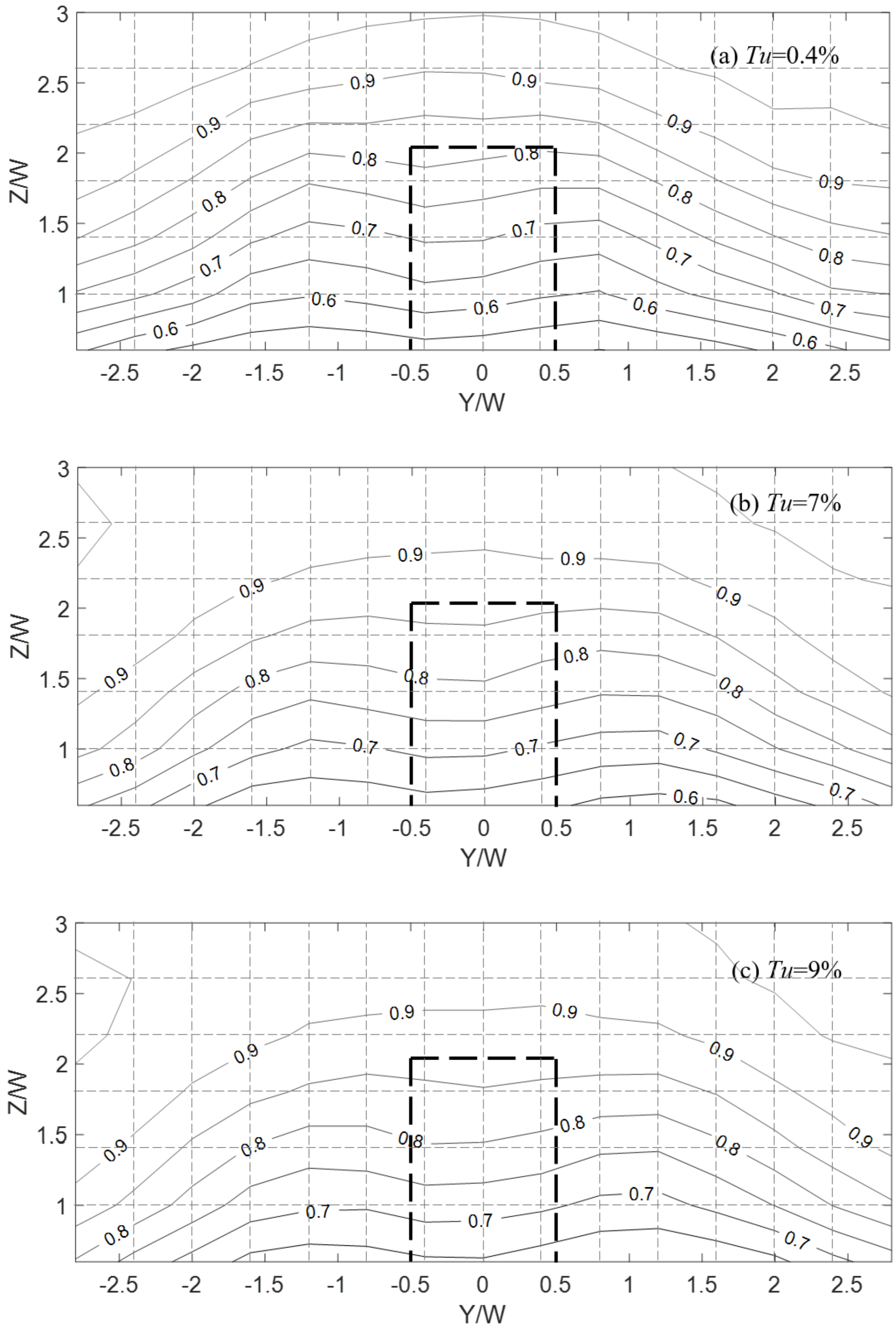
(a) Tu=0.4%
(b) Tu=7%
(c) Tu=9%
Z/W
Y/W

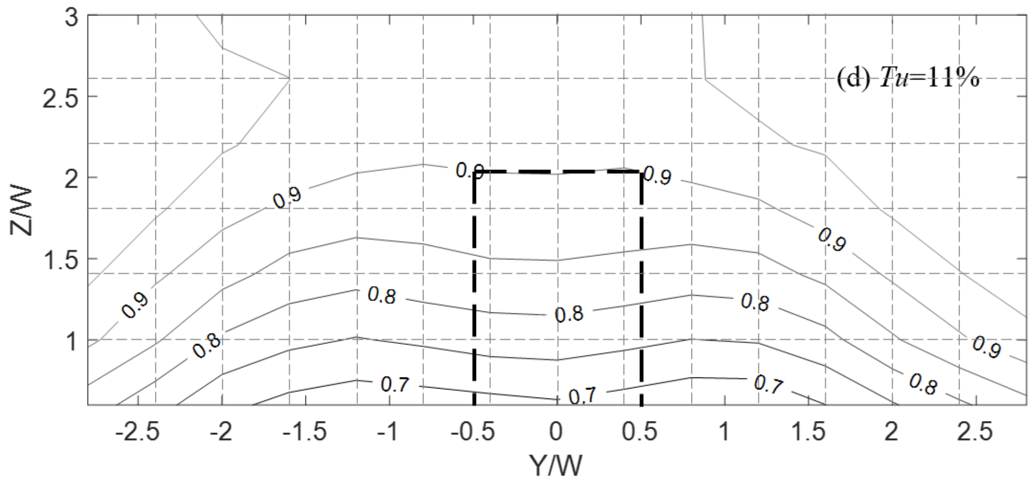

Figure 6. 10. Normalized streamwise velocity profile ($\overline{U}/U_\infty$) at 9*W* downstream of the flexible strip under streamwise freestream turbulence intensity of (a) *Tu* = 0.4% (b) *Tu* = 7% (c) *Tu* = 9% (d) *Tu* = 11%

In order to identify their overall effect, the span-averaged $\overline{U}/U_\infty$ value with respect to the vertical direction (*Z*) is plotted in Figure 6.11. The span-averaged values across *Y*=±1.6*W*, encompassing the two vortex cores behind the strip shown in Figure 6.8, were selected to evaluate the overall vortical flow region. From Figure 6.11, the largest $\overline{U}/U_\infty$values in the near-surface region under the 11% freestream turbulence is distinguishable, which is around 0.69 at *Z*=0.6*W*, approximately 33% higher than that associated with 0.4% freestream turbulence condition. This indicates that freestream turbulence improves the streamwise flow condition in terms of promoting convective heat transfer parallel to the hot surface. And this increasing trend of $\overline{U}/U_\infty$ presumably contributed to the increase of span-averaged Nu/Nu_{00} from 1.40 at 9*W* downstream under 0.4% freestream turbulence to around 1.70, 1.73, and 1.77 for 7%, 9%, and 11% freestream turbulence, respectively; see Figure 6.5. It is also interesting to note that the increasing trend of $\overline{U}/U_\infty$ from *Tu* = 0.4% to 11% is not linear. A significant increase between *Tu* = 0.4% and 7%, *Tu* = 9% and 11% could be clearly observed. However, only marginal increase is found from *Tu* = 7% to 9%. This indicates that freestream turbulence is not the only parameter affecting the $\overline{U}/U_\infty$ profile. The vortex structures, such as the downwash flow motion, the intensity and size of the vortex shown in Figure 6.8, also have a significant coupling effect on the $\overline{U}/U_\infty$ profile.

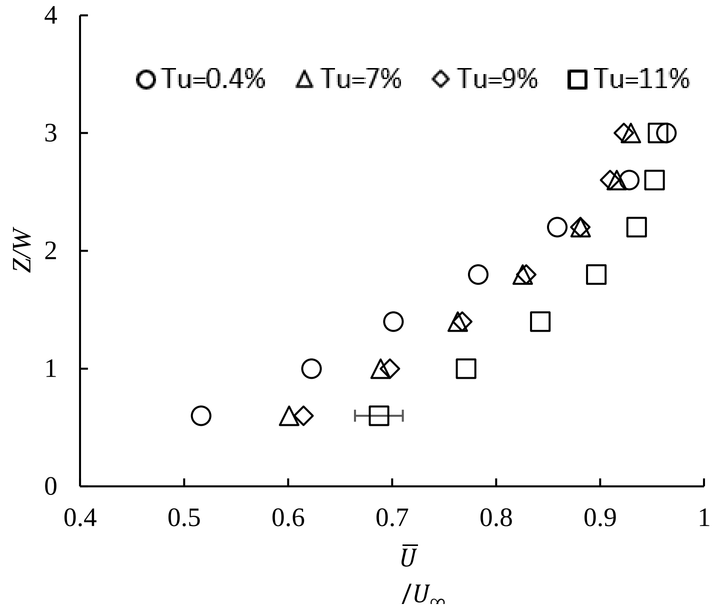

Figure 6. 11. Span-averaged (across *Y*=±1.6*W*) local velocity normalized by freestream velocity, $\overline{U}/U_\infty$, vertical profile at 9*W* downstream of the flexible strip

6.4.2.2 Streamwise Local Turbulence Intensity and Turbulent Kinetic Energy

Aside from flow velocity, the level of turbulence in the flow is another important factor in convection heat transfer. Experimental research regarding the turbulence intensity effect on heat transfer for a flat surface was conducted by Blair [34]. According to their study, a significant increase in heat transfer coefficient was linked to the increase in turbulence intensity. Approximately 15% enhancement was obtained under the turbulence intensity of 7%, compared to 0.3%. From another experimental investigation explored by Melina et al. [35], a similar correlation between heat transfer and turbulence intensity was observed. They found that the heat transfer augmentation was increased from around 5% to 20% when the turbulence intensity increased from 2.5% to 12%. Therefore, the total turbulent level, turbulent kinetic energy (*ke*), is discussed in this section.

The non-dimensional total turbulent kinetic energy (*ke*), which indicates the total turbulent level of all three orthogonal *X*, *Y* and *Z* directions, is shown in Figure 6.12. As the vortex structures behind the current studied model, wall-mounted finite height bluff body, are highly three dimensional [36], the turbulent kinetic energy may be more closely correlated, than the streamwise component alone, with the heat transfer enhancement. Figure 6.12 reveals that there is one intense total turbulence region near *Y*=0, and this entails effective heat transfer enhancement to occur in the middle region of the strip. This is indeed the case as illustrated in Figure 6.6. Furthermore, the peak value of the total turbulent kinetic energy slightly increases with freestream turbulence. These peak values are approximately 0.033, 0.037, 0.038 and 0.042 for 0.4%, 7%, 9% and 11% freestream turbulence, respectively. As far as the heat transfer is concerned, this increasing *ke*, from 0.033 to 0.042, seems to consistently provide a positive contribution to the absolute heat convection enhancement (Nu/Nu_{00}), boosting the span-averaged Nu/Nu_{00} from 1.40 to 1.70, 1.73 and 1.77 at 9*W* downstream, accordingly.

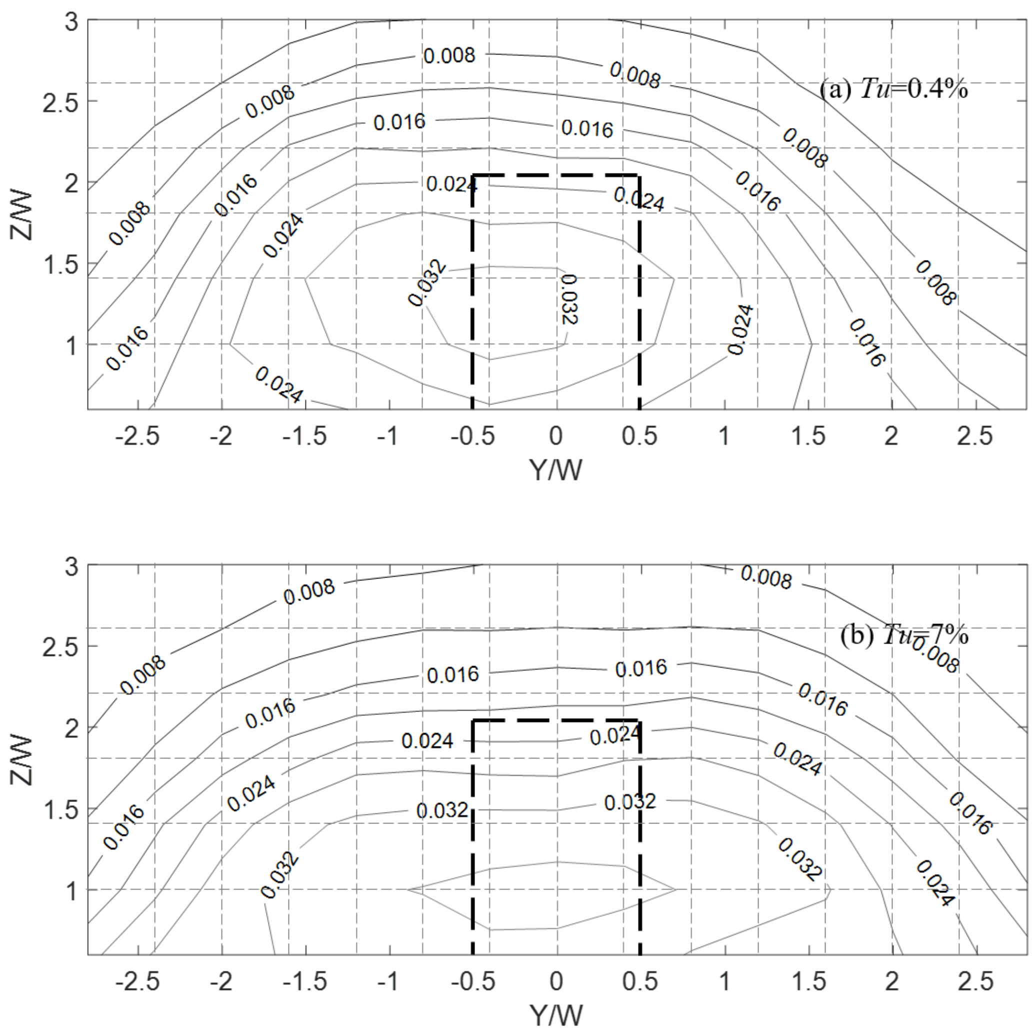

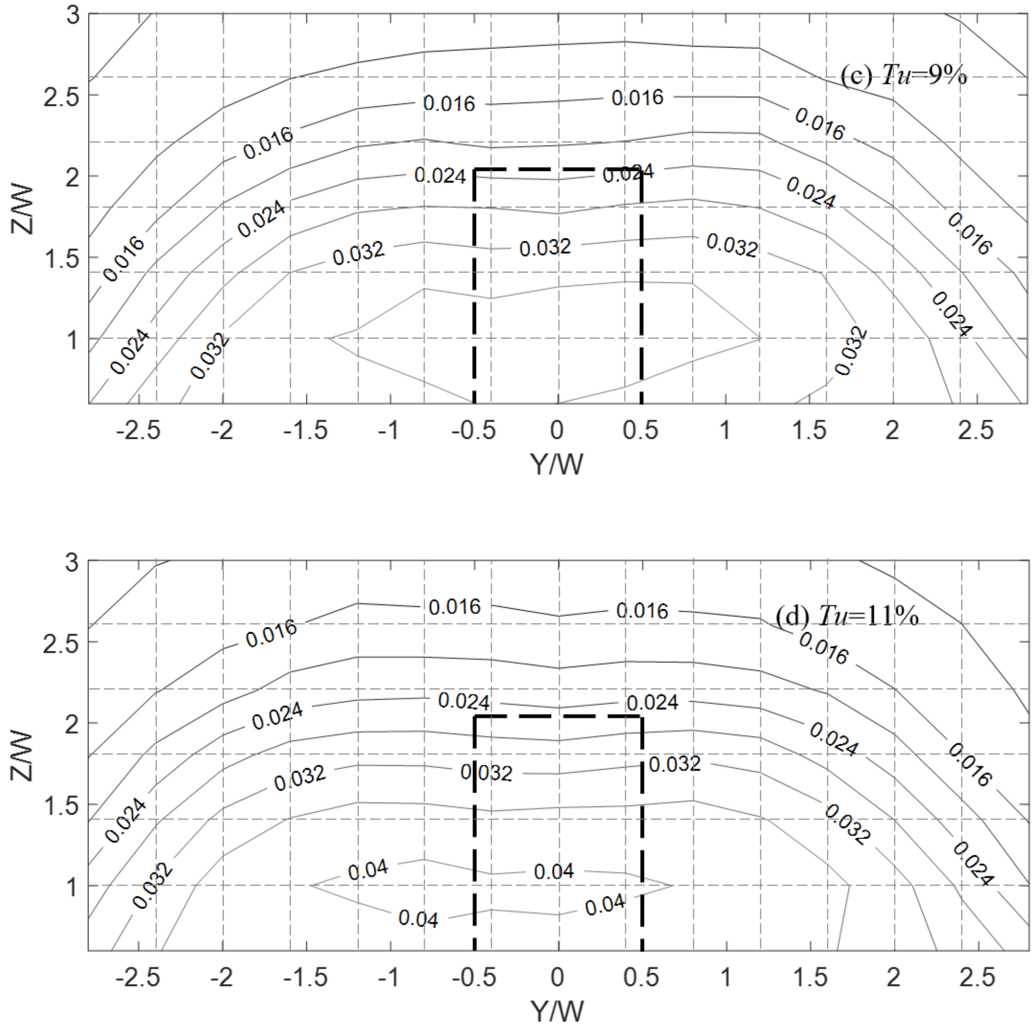

Figure 6. 12. Non-dimensional total turbulent kinetic energy (*ke*) at 9*W* downstream of the flexible strip under streamwise freestream turbulence intensity of (a) *Tu* = 0.4% (b) *Tu* = 7% (c) *Tu* = 9% (d) *Tu* = 11%

Let us zoom in to the cross-sectional area behind the strip at 9*W* downstream. Figure 6.13 shows the span-averaged values (averaged across *Y*=±1.6*W*) of the total turbulent kinetic energy profile. The highest turbulent kinetic energy associated with the shear over the top of the strip at approximately 1*W* above the flat plate is clearly visible. Within the considered region, the local turbulent kinetic energy increases with increasing freestream turbulence. It is interesting to note that the enhancement in *ke* with 2% increment in *Tu* from 9% to 11% is significantly more substantial than that from *Tu* = 7% to 9%. In fact, this augmentation in *ke* with 2% increment in *Tu* is as consequential as that caused by 6.4% increase in *Tu* from 0.4% to 7%. The upsurge in *ke* from *Tu* of 0.4% is largely due to the flow transitioning into a turbulent one, while that from *Tu* of 9% to 11% is presumably due to the shear flow around the flexible strip interacting with the intense freestream turbulence. The positive effect of the span-averaged *ke* on the heat transfer augmentation is clear. Due to the largest span-averaged *ke*, the strip at 11% freestream turbulence condition resulted in the best heat transfer performance, with the span-averaged Nu/Nu_{00} value of 1.77 at 9*W* downstream. At the other end, the strip under *Tu* = 0.4%, where the smallest *ke* is identified, resulted in the least effective heat transfer augmentation in terms of Nu/Nu_{00}. The span-averaged Nu/Nu_{00} value at 9*W* downstream for 0.4%, 7% and 9% are approximately 1.40, 1.70 and 1.73, respectively.

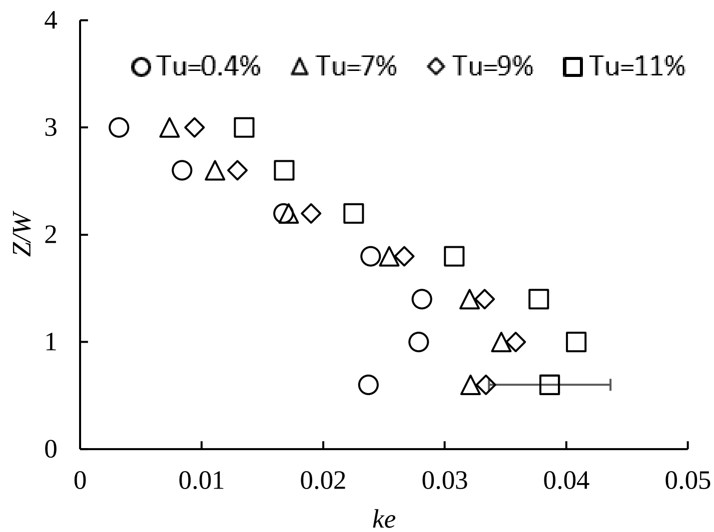

Figure 6. 13. Span-averaged (across *Y*=±1.6*W*) local turbulent kinetic energy, *ke*, vertical profile at 9*W* downstream of the flexible strip

What about the local turbulent kinetic energy relative to the freestream turbulent kinetic energy, ke/ke_∞? Figure 6.14 reveals that ke/ke_∞ decreaseds with increasing ke_∞. Here, the freestream turbulent kinetic energy (ke_∞) under 0.4%, 7%, 9% and 11% freestream turbulence are 0.0002, 0.007, 0.010, and 0.018, respectively. To put it another way, the span-averaged kinetic energy enhancement induced by the strip diminishes rapidly with increasing freestream turbulence. This is especially true from *Tu* of 0.4% to 7%; for example, ke/ke_∞ is around 152 at *Z*=0.6*W* and it drops to around 4.5 when the freestream turbulence is increased to 7%. This is due to the jump in the freestream turbulent kinetic energy, ke_∞ from the predominantly laminar *Tu* = 0.4% case to the next level up studied, *Tu* of 7%, with the *OPP* upstream is overriding. Further increase in ke_∞ beyond the fully turbulent freestream *Tu* of 7% is sure, though comparatively moderate when expressed in terms of ke/ke_{∞}. This is because ke_{∞} increases more rapidly with increasing Tu than ke. This relative enhancement of turbulent kinetic energy (ke/ke_{∞}) correlates with the relative heat transfer enhancement (Nu/Nu_0). As mentioned, the strip in Tu = 0.4% provides the largest span-averaged ke/ke_{∞} value at 9*W* downstream. This also leads to the highest span-averaged Nu/Nu_0 with a value of approximately 1.40; see Figure 6.3. The Nu/Nu_0 value decreases with decreasing ke/ke_{∞}. When it comes to 11% freestream turbulence, the smallest ke/ke_{∞} case, the span-averaged Nu/Nu_0 is around 1.33, as shown in Figure 6.3.

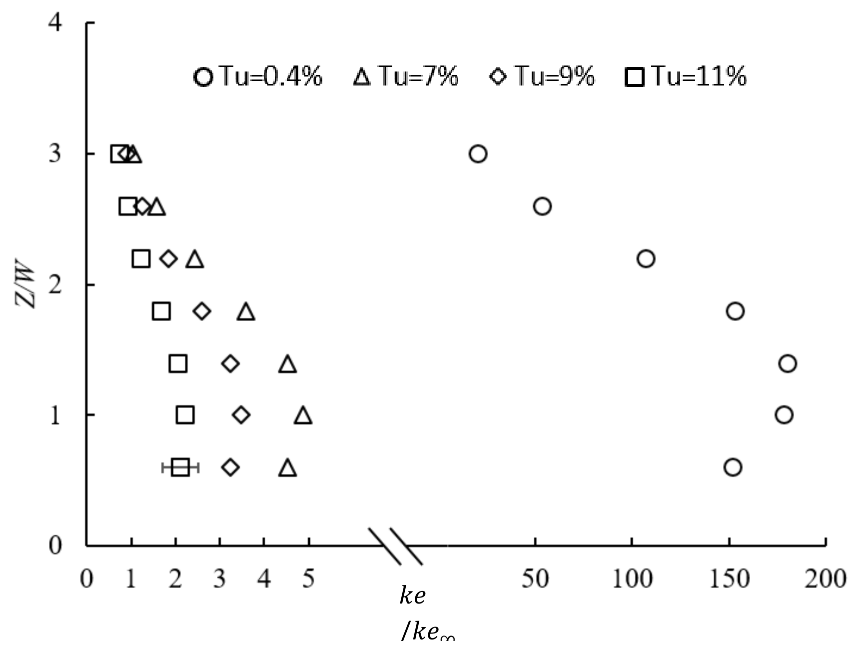

Figure 6. 14. Span-averaged (across *Y*=±1.6*W*) local turbulent kinetic energy with respect to the freestream turbulent kinetic energy, ke/ke_{∞}, vertical profile at 9*W* downstream of the flexible strip

6.4.2.3 Power Spectrum

To further characterize the vortex structure induced by the strip under different freestream turbulence, the power spectrum of the streamwise fluctuating velocity is illustrated in Figure 6.15. These studied points are at *X*=9*W*, *Y*=0.4*W*, *Z*=1.4*W* for 0.4% freestream turbulence, and at *X*=9*W*, *Y*=0.8*W*, *Z*=1.4*W* for Tu = 7%, 9% and 11%, which correspond to the position near the center of the vortex structure detected in Figure 6.8. In other words, the vortex center shifted by about 0.4*W* in the *Y* direction from the largely laminar Tu = 0.4% case to 'fully' turbulent cases. The time series data is Fast-Fourier-Transformed into 2^{14} sections with 50% overlap. The peak value of the power spectrum could be observed at approximately 42 Hz for the largely laminar Tu = 0.4% case. This corresponds to a Strouhal number, based on the strip width and the freestream velocity, of around 0.08. When the freestream turbulence increases, a slight increase of the peak value can be observed, to a frequency of around 50 Hz, a Strouhal number of 0.09, for *Tu* = 7%, 9%. When it comes to *Tu* = 11%, the peak frequency is found at around 61 Hz, a Strouhal number of 0.11. This small increase in Strouhal number with freestream turbulence, from *Tu* of 0.4%, agrees with the experimental investigation conducted by Mannini et al. [37], which revealed an increasing trend of the Strouhal number with the freestream turbulence intensity. Figure 6.15 also depicts increasing energy content over the entire frequency range with increasing *Tu*, confirming that the overall velocity fluctuation intensifies with freestream turbulence, providing a marginal improvement in span-averaged Nu/Nu_{00} as shown in Figure 6.5.

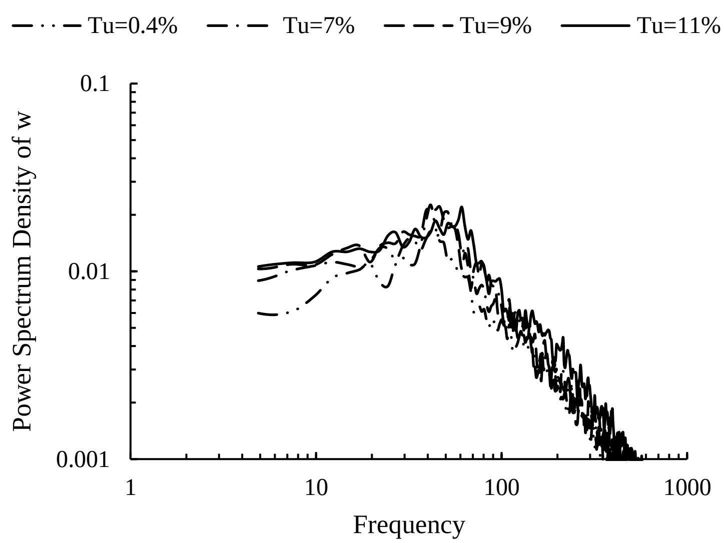

Figure 6. 15. Power spectrum density of streamwise fluctuating velocity, w, at *X*=9*W*, *Y*=0.4*W*, *Z*=1.4*W* for the strip under *Tu* = 0.4%, *X*=9*W*, *Y*=0.8*W*, *Z*=1.4*W* for the strip under *Tu* = 7%, 9% and 11%

6.5 Conclusions

A 25.4 mm tall, 12.7 mm wide (*W*) and 0.1 mm thick rectangular flexible strip was studied experimentally in a closed-loop wind tunnel, to explore its effect on the convective heat transfer enhancement over a heated flat surface under different freestream turbulence condition. A 76 cm by 76 cm orificed perforated plate (*OPP*) with holes of 38.1 mm diameter was employed to generate streamwise freestream turbulence intensity of approximately 11%, 9% and 7%. The streamwise freestream velocity in the current study was fixed at approximately 7 m/s, a Reynolds number of about 6000 based on the strip width. The heat convection augmentation was analyzed in terms of the Nusselt number with respect to the reference case in the absence of the strip (Nu/Nu_0). In general, the increase in the freestream turbulence diminishes the relative effect of flexible strip on the convective heat transfer enhancement. The strip under the highest studied freestream turbulence (*Tu*=11%) induces the smallest peak and span-averaged Nu/Nu_0 values. This is largely due to the significant increase of Nu_0 with increasing freestream turbulence. To put it another way, the flexible strip always furthers the heat transfer enhancement in terms of an increase in *Nu*, even though Nu/Nu_0 tends to decrease with increasing *Tu*. The largest heat transfer rate is realized at the highest freestream turbulence in the presence of the flexible strip. The streamwise vorticity, the velocity toward the heated plate, the streamwise velocity, the local turbulence intensity and kinetic energy all correlate positively with *Nu*. Due to complex coupling among them, it is not possible to quantify the independent effect due to the individual parameters.

Acknowledgments

This work was made possible by Natural Sciences and Engineering Research Council of Canada and Ontario Centres of Excellence.

References

[1] S. Nižetić, D. Čoko, A. Yadav, and F. Grubišić-Čabo, "Water spray cooling technique applied on a photovoltaic panel: The performance response," Energy Convers. Manag., vol. 108, pp. 287–296, 2016, doi: 10.1016/j.enconman.2015.10.079.

[2] S. Bhattacharjee et al., "An investigational back surface cooling approach with different designs of heat-absorbing pipe for PV/T system," Int. J. Energy Res., vol. 42, no. 5, pp. 1921–1933, 2018, doi: 10.1002/er.3977.

[3] H. M. Kim and K. Y. Kim, "Design optimization of rib-roughened channel to enhance turbulent heat transfer," Int. J. Heat Mass Transf., vol. 47, no. 23, pp. 5159–5168, 2004, doi: 10.1016/j.ijheatmasstransfer.2004.05.035.

[4] Z. Xu, Z. Han, J. Wang, and Z. Liu, "The characteristics of heat transfer and flow resistance in a rectangular channel with vortex generators," Int. J. Heat Mass Transf., vol. 116, pp. 61–72, 2018, doi: 10.1016/j.ijheatmasstransfer.2017.08.083.

[5] H. Wu, D. S. K. Ting, and S. Ray, "An experimental study of turbulent flow behind a delta winglet," Exp. Therm. Fluid Sci., vol. 88, pp. 46–54, 2017, doi: 10.1016/j.expthermflusci.2017.05.012.

[6] A. T. Wijayanta, T. Istanto, K. Kariya, and A. Miyara, "Heat transfer enhancement of internal flow by inserting punched delta winglet vortex generators with various attack

angles," Exp. Therm. Fluid Sci., vol. 87, pp. 141–148, 2017, doi: 10.1016/J.EXPTHERMFLUSCI.2017.05.002.

[7] G. Biswas, P. Deb, and S. Biswas, "Generation of longitudinal streamwise vortices—a device for improving heat exchanger design," J. Heat Transfer, vol. 116, no. 3, pp. 588–597, 1994, doi: 10.1115/1.2910910.

[8] G. A. Sheikhzadeh, F. N. Barzoki, A. A. A. Arani, and F. Pourfattah, "Wings shape effect on behavior of hybrid nanofluid inside a channel having vortex generator," Heat Mass Transf. und Stoffuebertragung, vol. 55, no. 7, pp. 1969–1983, 2019, doi: 10.1007/s00231-018-2489-x.

[9] S. Skullong, P. Promvonge, C. Thianpong, N. Jayranaiwachira, and M. Pimsarn, "Thermal performance of heat exchanger tube inserted with curved-winglet tapes," Appl. Therm. Eng., vol. 129, pp. 1197–1211, 2018, doi: 10.1016/j.applthermaleng.2017.10.110.

[10] K. W. Song, Z. P. Xi, M. Su, L. C. Wang, X. Wu, and L. B. Wang, "Effect of geometric size of curved delta winglet vortex generators and tube pitch on heat transfer characteristics of fin-tube heat exchanger," Exp. Therm. Fluid Sci., vol. 82, pp. 8–18, 2017, doi: 10.1016/j.expthermflusci.2016.11.002.

[11] R. K. B. Gallegos and R. N. Sharma, "Flags as vortex generators for heat transfer enhancement: Gaps and challenges," Renew. Sustain. Energy Rev., vol. 76, pp. 950–962, 2017, doi: 10.1016/j.rser.2017.03.115.

[12] S. Ali, S. Menanteau, C. Habchi, T. Lemenand, and J. L. Harion, "Heat transfer and mixing enhancement by using multiple freely oscillating flexible vortex generators," Appl. Therm. Eng., vol. 105, pp. 276–289, 2016, doi: 10.1016/j.applthermaleng.2016.04.130.

[13] W. S. Fu and B. H. Tong, "Numerical investigation of heat transfer from a heated oscillating cylinder in cross flow," Int. J. Heat Mass Transf., vol. 45, no. 14, pp. 3033–3043, 2002, doi: 10.1016/S0017-9310(02)00016-9.

[14] S. J. Yang, "Numerical study of heat transfer enhancement in a channel flow using an oscillating vortex generator," Heat Mass Transf. und Stoffuebertragung, vol. 39, no. 3, pp. 257–265, 2003, doi: 10.1007/s00231-002-0299-6.

[15] Y. T. Yang and C. H. Chen, "Numerical simulation of turbulent fluid flow and heat transfer characteristics of heated blocks in the channel with an oscillating cylinder," Int. J. Heat Mass Transf., vol. 51, no. 7–8, pp. 1603–1612, 2008, doi: 10.1016/j.ijheatmasstransfer.2007.07.010.

[16] Y. Yang, D. S.-K. Ting, and S. Ray, "On flexible rectangular strip height on flat plate heat convection," Int. J. Heat Mass Transf., vol. 150, p. 119269, 2020, doi: 10.1016/j.ijheatmasstransfer.2019.119269.

[17] R. Liu and D. S.-K. Ting, "Turbulent flow downstream of a perforated plate: Sharp-edged orifice versus finite-thickness holes," J. Fluids Eng. Trans. ASME, vol. 129, no. 9, pp. 1164–1171, 2007, doi: 10.1115/1.2754314.

[18] R. Liu, D. S.-K. Ting, and M. David Checkel, "Constant Reynolds number turbulence downstream of an orificed perforated plate," Exp. Therm. Fluid Sci., vol. 31, no. 8, pp. 897–908, 2007, doi: 10.1016/j.expthermflusci.2006.09.007.

[19] "Thermal Conductivity of common Materials and Gases." [Online]. Available: https://www.engineeringtoolbox.com/thermal-conductivity-d_429.html. [Accessed: 26-Aug-2020].

[20] D. M. Price and M. Jarratt, "Thermal conductivity of PTFE and PTFE composites," Thermochim. Acta, vol. 392–393, pp. 231–236, 2002, doi: 10.1016/S0040-6031(02)00105-3.

[21] "Emissivity Coefficients Materials." [Online]. Available: https://www.engineeringtoolbox.com/emissivity-coefficients-d_447.html. [Accessed: 26-Aug-2020].

[22] H. Wu, D. S.-K. Ting, and S. Ray, "The effect of delta winglet attack angle on the heat transfer performance of a flat surface," Int. J. Heat Mass Transf., vol. 120, pp. 117–126, 2018, doi: 10.1016/j.ijheatmasstransfer.2017.12.030.

[23] Y. Yang, D. S. K. Ting, and S. Ray, "Perforated-plate turbulence: Orifice versus converging nozzle," in Proceedings of the ASME 2018, 5th Joint US-European Fluids Engineering Division Summer Meeting, 2018, pp. 1–9, doi: 10.1115/FEDSM2018-83038.

[24] Y. A. Çengel and A. J. Ghajar, Heat and mass transfer : fundamentals & applications, fifth edition. McGraw Hill Education, 2015.

[25] D. S.-K. Ting, Basics of engineering turbulence. Academic Press, New York, 2016.

[26] M. Raffel, C. E. Willert, F. Scarano, C. J. Kähler, S. T. Wereley, and J. Kompenhans, Particle image velocimetry: a practical guide, Third Edition. Springer, 2018.

[27] A. Kumar and M. H. Kim, “Convective heat transfer enhancement in solar air channels,” Appl. Therm. Eng., vol. 89, pp. 239–261, 2015, doi: 10.1016/j.applthermaleng.2015.06.015.

[28] M. Sheikholeslami, M. Gorji-Bandpy, and D. D. Ganji, “Review of heat transfer enhancement methods: Focus on passive methods using swirl flow devices,” Renew. Sustain. Energy Rev., vol. 49, pp. 444–469, 2015, doi: 10.1016/j.rser.2015.04.113.

[29] K. Ben Miloud, H. Fellouah, M. Dghim, and M. Ferchichi, “Wing tip vortex development under a grid generated turbulent flow,” in American Society of Mechanical Engineers, Fluids Engineering Division (FEDSM), 2018, doi: 10.1115/FEDSM2018-83478.

[30] A. K. Soti, R. Bhardwaj, and J. Sheridan, “Flow-induced deformation of a flexible thin structure as manifestation of heat transfer enhancement,” Int. J. Heat Mass Transf., vol. 84, pp. 1070–1081, 2015, doi: 10.1016/j.ijheatmasstransfer.2015.01.048.

[31] T. Defraeye, B. Blocken, and J. Carmeliet, “Convective heat transfer coefficients for exterior building surfaces: Existing correlations and CFD modelling,” Energy Convers. Manag., vol. 52, pp. 512–522, 2011, doi: 10.1016/j.enconman.2010.07.026.

[32] M. G. Emmel, M. O. Abadie, and N. Mendes, “New external convective heat transfer coefficient correlations for isolated low-rise buildings,” Energy Build., vol. 39, no. 3, pp. 335–342, 2007, doi: 10.1016/j.enbuild.2006.08.001.

[33] M. T. Kahsay, G. Bitsuamlak, and F. Tariku, “Numerical analysis of convective heat transfer coefficient for building facades,” J. Build. Phys., vol. 42, no. 6, pp. 727–749, 2019, doi: 10.1177/1744259118791207.

[34] M. F. Blair, “Influence of free-stream turbulence on turbulent boundary layer heat transfer and mean profile development, part II—analysis of results,” J. Heat Transfer, vol. 105, no. 1, pp. 41–47, 1983, doi: 10.1115/1.3245557.

[35] G. Melina, P. J. K. Bruce, J. Nedić, S. Tavoularis, and J. C. Vassilicos, "Heat transfer from a flat plate in inhomogeneous regions of grid-generated turbulence," Int. J. Heat Mass Transf., vol. 123, pp. 1068–1086, 2018, doi: 10.1016/j.ijheatmasstransfer.2018.03.019.

[36] H. Y. Zhu, C. Y. Wang, H. P. Wang, and J. J. Wang, "Tomographic PIV investigation on 3D wake structures for flow over a wall-mounted short cylinder," J. Fluid Mech., vol. 831, pp. 743–778, 2017, doi: 10.1017/jfm.2017.647.

[37] C. Mannini, A. M. Marra, L. Pigolotti, and G. Bartoli, "The effects of free-stream turbulence and angle of attack on the aerodynamics of a cylinder with rectangular 5:1 cross section," J. Wind Eng. Ind. Aerodyn., vol. 161, pp. 42–58, 2017, doi: 10.1016/j.jweia.2016.12.001.

[38] R. S. Figliola and D. E. Beasley, Theory and design for mechanical measurements, Fourth edition. Wiley, New York, 2006.

[39] S. Yavuzkurt, "A Guide to Uncertainty Analysis of Hot-Wire Data," J. Fluids Eng., vol. 106, no. 2, p. 181, 1984, doi: 10.1115/1.3243096.

[40] H. Tyagi, R. Liu, D. S.-K. Ting, and C. R. Johnston, "Measurement of wake properties of a sphere in freestream turbulence," Exp. Therm. Fluid Sci., vol. 30, no. 6, pp. 587–604, 2006, doi: 10.1016/J.EXPTHERMFLUSCI.2005.12.004.

CHAPTER 7

MECHANISMS UNDERLYING FLAT SURFACE FORCED CONVECTION ENHANCEMENT BY RETANGULAR FLEXIBLE STRIPS

Y. Yang, D. S-K. Ting, S. Ray, "Mechanisms Underlying Flat Surface Forced Convection Enhancement by Rectangular Flexible Strips," Thermal Science and Engineering Progress, under review.

7.1 Introduction

Among the various innovative strategies for improving forced convection and thus the efficiency of engineering systems involving convective heat exchange, utilizing passive turbulence generators [1] is one viable approach as it generally does not require input power, complicated structures, high initial cost and maintenance. Many researchers have conducted studies on improving the design of turbulence generators in recent years. These include many attempts on the rib/baffle and the twisted tapes. For example, Boonloi and Jedsadaratanachai [2] numerically explored the heat transfer characteristics in a square channel equipped with V-baffle. Their V-baffle induced a vortex flow in the channel, leading to enhanced fluid mixing and hence, an increase in Nusselt number by a factor of six. In another numerical study, the effect of V-baffle on the heat transfer performance of a channel heat exchanger was illustrated by Ameur et al. [3]. Their V-baffle boosted the heat transfer coefficient by up to 400%. Tamna et al. [4] conducted an experimental study, demonstrating the heat transfer augmentation in a tubular heat exchanger with V-ribbed twisted-tapes. They achieved a Nusselt number augmentation of around 2.3. Arjmandi et al. [5] numerically investigated the effect of combined vortex generator and twisted tape on a double pipe heat exchanger. Their turbulence generator with pitch ratio of 0.09 and angle of 30° led to a maximal enhancement of heat transfer performance of 400% compared to the heat exchanger with no vortex generator.

Other than the sample of investigations highlighted above, the literature is also rich in studies on longitudinal vortex generators, such as wings and winglets. This is due to their ability to generate long-lasting longitudinal vortices, producing swirling flow motions and increasing the turbulence intensity [6]. Making these vortex generators flexible has shown promise in furthering the heat transfer augmentation [7]. For example, Dadvand et al. [8] conducted a numerical investigation, exploring the effect of flexible vortex generator on the heat transfer enhancement in a channel. They found that the flexible type provided 18% Nusselt number improvement with respect to its rigid counterpart. Shi et al. [9] showed that their oscillating cylinder could provide a stronger and closer-to-wall vortices, reinforcing the interaction between the cooler freestream fluid and the hotter fluid near the channel wall surface. Therefore, it enhanced the average Nusselt number by around 51% compared to the stationary cylinder.

Destabilization is a key flow mechanism for passive heat transfer enhancement [10]. It is known that the velocity fluctuations expressed in terms of turbulence intensity have a direct effect on the convective heat transfer coefficient. For example, an experimental investigation conducted by Blair [11] showed that the heat transfer coefficient over a heated surface was enhanced by around 15% when the turbulence intensity increased from 0.3% to 7%. Kondjoyan and Daudin [12] experimentally explored the heat transfer rate of a circular cylinder under various turbulence intensity. Based on their results, the Nusselt number of the cylinder was around 160 under a turbulence intensity of 40%, which is approximately 100% larger than that under a turbulence intensity of 1.5%. Other than the fluctuating velocity, also worth mentioning is the flow motion toward the heated surface, by which the cooler freestream flow could be effectively transported into the hot fluid near the surface and vice versa. This consequently enhanced the fluid mixing and, hence, the heat transfer rate. Defraeye et al. [13] conducted a numerical study to investigate the heat convection of the windward surface. They pointed out that the convective heat transfer coefficient increased with the increase of the flow velocity toward the heated surface. Emmel et al. [14] and Kahsay et al. [15] also revealed similar findings, concluding a correlation between the heat convection coefficient (h) and the velocity toward the heated surface (V), as $h = 5.15V^{0.81}$ and $h = 4.39V^{0.96}$, respectively. Furthermore, the streamwise velocity is also of significance as far as heat convection is concerned. A typical correlation between the forced heat convection and the streamwise velocity over a flat surface is $Nu = 0.664Re^{0.5}Pr^{1/3}$ for laminar flow, and $Nu = 0.037Re^{0.8}Pr^{1/3}$ for turbulent flow [16]. This implies that a higher streamwise velocity is better at sweeping thermal energy away with the flow stream.

Efforts in furthering forced convection enhancement remain a focus. The vast majority of the efforts on this, however, deal with internal flow and heat transfer inside a conduit. Also practically significant but seldom explored is the heat transfer under the open flow condition, which could be employed in the cooling of solar photovoltaic panel. With this backdrop, the current research focuses on the heat convection enhancement over a heated flat surface under the open-flow condition. This study is an extension of our ongoing research on rectangular flexible strips [17][18][19], combining the advantage of longitudinal vortex generator and oscillating vortex generator. The focus here is to reveal the key underlying mechanisms involved in promoting heat convection. As such, we analyze the turbulence, downwash velocity and streamwise velocity to establish the correlations between the convective heat transfer augmentation and the primary flow parameters.

7.2 Experimentation and Test Matrix

We conducted the experiment in a closed-loop wind tunnel with a 760 mm by 760 mm square cross-section. For the study, we laid a 3 mm thick *PTFE* (polytetrafluoroethylene) plate in the middle of the test section as depicted in Figure 7.1. The 380 mm long and 295 mm wide *PTFE* plate has a thermal conductivity of $0.25 Wm^{-1}K^{-1}$ [20] and an emissivity of 0.92 [21]. A basin water placed under the PTFE plate was set to boil, maintaining the lower surface of the plate at 100°C. We employed a FLIR C2 thermal camera to capture the top surface temperature. The local heat transfer rate was determined from the temperature difference across the thickness of the plate.

We used a single or a pair of 12.7 mm wide rectangular flexible aluminum strips to generate turbulent flow over the surface of the plate. We employed aluminum sheets with thickness of 0.1 mm, 0.2 mm and 0.25 mm to alter the flexibility of the turbulence generator. We changed the strip height from 25.4 mm to 38.1 mm to 50.8 mm to vary the proximity of the generated longitudinal vortices with respect to the plate. In addition, the interaction between vortices generated by side-by-side strip pair was also of interest. For this, we studied strip-strip spacing of 12.7, 25.4 and 38.1 mm. The Reynolds number based on the strip width was set at 6000 and 8500. To investigate the influence of freestream turbulence, we secured an orificed perforated plate (OPP) at different locations upstream of the strip or strip pair to increase the freestream turbulence from 0.4% to 7%, 9% and 11%. In total, we studied a combination of 12 cases as summarized in Table 7.1.

We utilized a DANTEC DYNAMICS 3D hotwire probe to characterize the turbulent flow downstream of the strip or strip pair. Specifically, we detailed the cross-sectional flow field at 9W downstream of the flexible strip. At each measurement location, we acquired the signal at 80 kHz for 12.5 seconds, resulting in 10^6 data points. The sampled signal was low-passed at 30 kHz to avoid aliasing.

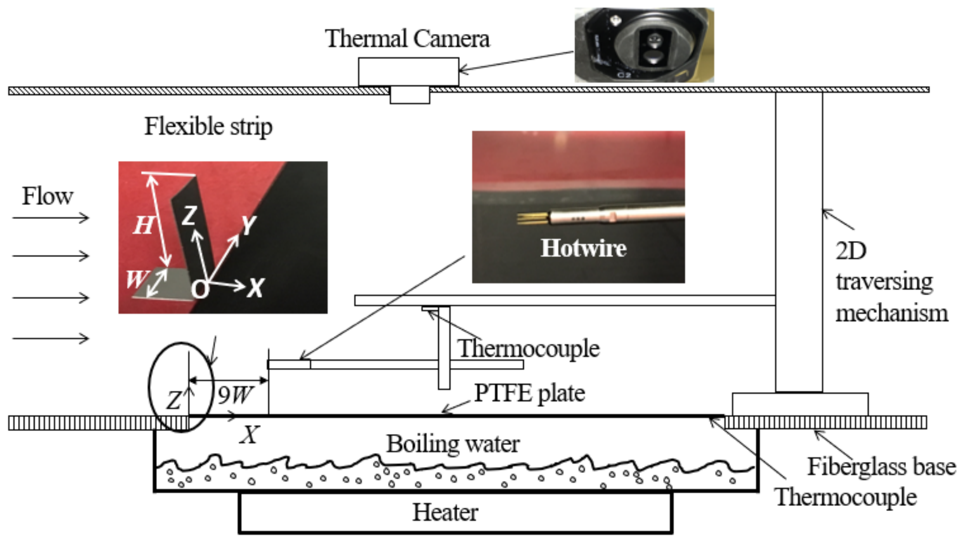

Figure 7. 1. Experimental setup

Table 7. 1. Studied cases

Case	Thickness (mm)	Height (mm)	Spacing (mm)	Freestream turbulence intensity	Reynolds number (base on strip width)
1	0.1	38.1	/ (single)	0.4%	8500
2	0.2	38.1	/ (single)	0.4%	8500
3	0.25	38.1	/ (single)	0.4%	8500
4	0.1	25.4	/ (single)	0.4%	8500
5	0.1	50.8	/ (single)	0.4%	8500
6	0.1	25.4	12.7	0.4%	8500
7	0.1	25.4	25.4	0.4%	8500
8	0.1	25.4	38.1	0.4%	8500
9	0.1	25.4	/ (single)	0.4%	6000
10	0.1	25.4	/ (single)	7%	6000
11	0.1	25.4	/ (single)	9%	6000
12	0.1	25.4	/ (single)	11%	6000

7.3 Methodology

The total heat transferred through the entire plate of interest came from the condensing steam from the lower surface. The heat is lost via conduction through the plate to the cool convecting air over the upper surface. The total heat transfer rate,

$$\dot{Q}_{total} = K_{PTFE}A(\frac{T_{bottom} - T_{top}}{t_{PTFE}}) \tag{7.1}$$

The thermal conductivity of the plate, K_{PTFE}, was 0.25 Wm^{-1}K^{-1}. The area of the plate, A, was 380 mm by 295 mm, and the plate thickness, t_{PTFE} was 3 mm. The bottom surface temperature, T_{bottom}, was 100°C, and the top surface temperature, T_{top} was measured by a FLIR C2 thermal camera. With negligible conduction loss to the base of the wind tunnel, the convective heat transfer rate was

$$\dot{Q}_{convection} = \dot{Q}_{total} - \dot{Q}_{radiation} \tag{7.2}$$

where the radiation heat transfer rate,

$$\dot{Q}_{radiation} = \varepsilon\sigma A(T_{top}^4 - T_{wall}^4) \tag{7.3}$$

For the PTFE plate, the surface emissivity, ε = 0.92. The Stefan-Boltzmann constant, σ = 5.67x10^{-8} Wm^{-2}K^{-4} [16]. The wall temperature of the wind tunnel, T_{wall}, was assumed to be equal to the air temperature, T_{air}.

We calculated the convective heat transfer coefficient (h) from

$$h = \frac{\dot{Q}_{convection}}{A(T_{top} - T_{air})} \tag{7.4}$$

Normalized this by the thermal conductivity of the ambient air (K_{air}) and the characteristic length (L), the non-dimensional Nusselt number became

$$Nu = \frac{hL}{K_{air}} \tag{7.5}$$

This Nusselt number was cast with respect to the reference Nusselt number, Nu_0, in the absence of rectangular strips and OPP. Doing so leads to the resulting heat convection enhancement,

$$\frac{Nu}{Nu_0} = \frac{h}{h_0} \tag{7.6}$$

We employed a 3D hotwire probe to characterize the turbulent flow behind the strip. We measured the instantaneous velocities in streamwise (X), widthwise (Y) and vertical (Z) directions simultaneously. These velocities consisted of mean and fluctuating components, that is,

$$U_i = \overline{U} + u \; ; V_i = \overline{V} + v \; ; W_i = \overline{W} + w \tag{7.7}$$

where $\overline{U}, \overline{V}, \overline{W}$ and u, v, w denote the time-averaged velocities and the instantaneous fluctuating velocities, respectively. To evaluate the velocity fluctuation level, we deduced the root-mean-square fluctuating velocities,

$$u_{rms} = \sqrt{\sum_{i=1}^{N} \frac{{u_i}^2}{N-1}} \; ; v_{rms} = \sqrt{\sum_{i=1}^{N} \frac{{v_i}^2}{N-1}} \; ; w_{rms} = \sqrt{\sum_{i=1}^{N} \frac{{w_i}^2}{N-1}} \tag{7.8}$$

Normalized by the freestream velocity (U_∞), the non-dimensional velocity fluctuation, i.e., turbulence intensity,

$$Tu = \frac{u_{rms}}{U_\infty} \tag{7.9}$$

was obtained. As the studied turbulence was highly three dimensional [22], the turbulence kinetic energy was of interest. The total turbulence level,

$$ke = \frac{1}{2} \frac{(u_{rms}^2 + v_{rms}^2 + w_{rms}^2)}{U_\infty^2} \tag{7.10}$$

The Reynolds number in the current study was defined based on the freestream velocity (U_∞) and the strip width (W), giving,

$$Re = \frac{WU_\infty}{\nu} \tag{7.11}$$

where ν is kinematic viscosity of air.

We invoked multiple linear regression to determine the correlations between the strip and flow parameters with on the heat transfer enhancement in terms of the normalized Nusselt number. Namely,

$$\frac{Nu}{Nu_0} = \sum \beta_j (parameter)_j \tag{7.12}$$

where β_j is the regression coefficient of each individual parameter. Furthermore, to find the weight of each impact, the standardized regression coefficients,

$$\beta_j^{std} = \beta_j \frac{std_j}{std_y} \tag{7.13}$$

were calculated. Here, std_j signifies the standard deviation of each parameter, and std_y denotes the standard deviation of the dependent variable, i.e., Nu/Nu_0.

7.4 Results and Discussion

7.4.1 Statistical optimization for averaged normalized Nusselt number

Figure 7.2 illustrates the convective heat transfer augmentation, in terms of the normalized Nusselt number, downstream of the rectangular flexible strip for Case 1 and Case 8; see Table 7.1. X and Y denote the streamwise and the widthwise direction, and the origin (X=0, Y=0) represents the middle position of the isolated strip for Case 1. For the strip pair case, such as Case 8, the origin represents the middle of the gap. The red solid line in the leading edge shows the position of the strip. The uncertainty of the local Nu/Nu_0 is around 0.066. Due to the strong vortices with intense turbulence generated by the strip, an effective cooling area with Nu/Nu_0 up to around 2 is found immediately behind the strip. Farther downstream, with increasing X/W, the cooling effect tends to decrease, implying that the turbulence is decaying. Nevertheless, thanks to the long-lasting longitudinal vortices, the strip still provides around 30% convective heat transfer enhancement at far downstream, i.e. X/W=23, with respect to the reference case in the absence of the strip.

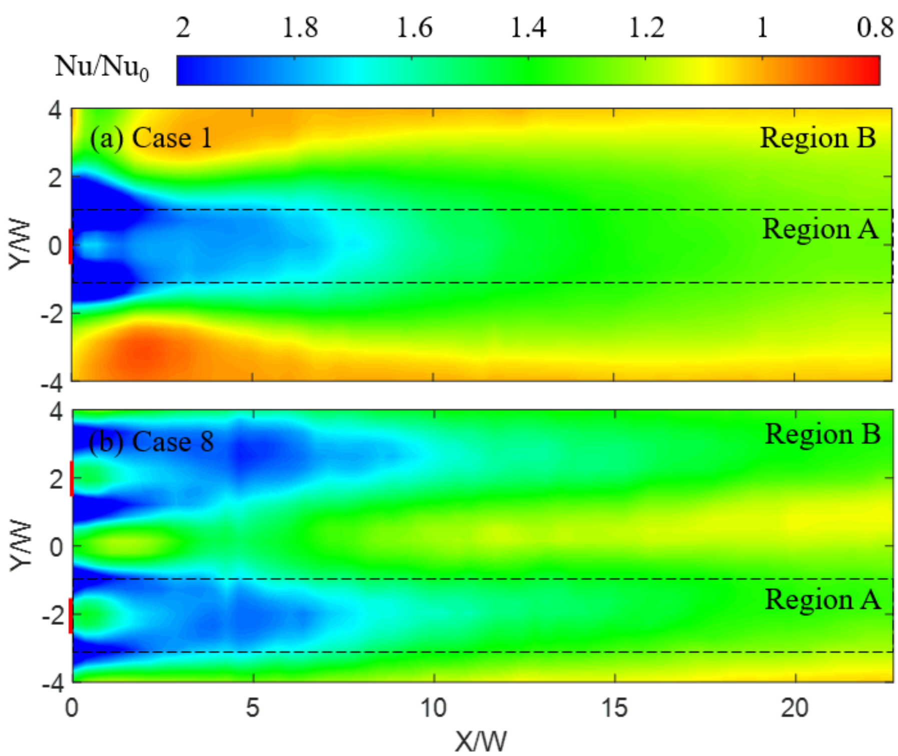

Figure 7. 2. Normalized Nusselt number (Nu/Nu_0) downstream of the rectangular flexible strip, (a) Case 1 (b) Case 8

The cooling effect of the entire heated surface is of practical significance. Therefore, the averaged normalized Nusselt number was determined and summarized in Table 7.2. Note that the downstream region from X/W=0 to 23 was selected, incorporating the long-lasting effect such as over an entire span of a photovoltaic panel. In practical applications such as cooling of photovoltaic panels, flexible strips can be positioned side-by-side along the frame of each panel. It is, however, more challenging to place them onto the panel itself in staggered or tandem arrangements. Region A, enclosed by a dashed rectangle, in Figure 7.2 represents the immediate narrow width, Y =±1W with respect to the middle position of the isolated strip (i.e. Y/W=0 for Cases 1 to 5, and 9 to 12). For the strip pair cases, Region A is defined by Y/W=0 to -2 for Case 6, Y/W=-0.5 to -2.5 for Case 7, Y/W=-1 to -3 for Case 8. Seeing the extended area of significant heat transfer enhancement, it is also of interest to determine if the flexible strip can cover a widened area. Therefore, the normalized Nusselt number averaged across Y/W=±4 was also calculated to assess the enlarged effect over the entire solid border, Region B in Figure 7.2.

For Cases 1 to 3, a decreasing trend of averaged Nusselt number enhancement with increasing strip thickness is observed; see Table 7.2, refer to Table 7.1 for the specifications of each case. This agrees with the finding of Ali et al. [24][25], demonstrating that the flexibility of the vortex generators could provide a positive influence on heat transfer enhancement. When the height of strip decreased from H/W=4 (Case 5) to H/W=2 (Case 4), the averaged Nu/Nu_0 increased by around 0.14 and 0.05, for Region A and Region B, respectively. This is due to the closer-to-surface longitudinal vortices induced by the shorter strip [18]. Variation in averaged Nu/Nu_0 with respect to the transversal spacing (S/W) is illustrated by Cases 6 to 8. It is interesting to note that, for Region A, the averaged Nu/Nu_0 tends to increase with decreasing spacing. This is presumably due to the build-up of vortex-vortex interaction and intensification of turbulence in the gap as the vortices formed from the two neighboring edges approach each other. On the contrary, the averaged Nu/Nu_0 decreases with decreasing spacing when considering the enlarged area defined by Region B. This implies that the span of significantly enhanced heat convection area decreases with decreasing spacing between the two side-by-side strips. In other words, the squashing and intensification of the two vortices through the gap as the gap narrows resulted in a serious decrease in the sweeping surface by the otherwise large and mostly independent pair of vortices.

Besides the geometry and the arrangement of the strips, the freestream conditions can also influence the heat convection augmentation. With decreasing Reynolds number from 8500 to 6000, the cooling effect tends to increase; see Cases 4 and 9. The averaged Nu/Nu_0 increases from around 1.65 to 1.75 for Region A and from 1.32 to 1.38 for Region B. Also notable is the freestream turbulence effect. The averaged Nu/Nu_0 increases drastically from the predominantly laminar freestream with Tu=0.4% (Case 9) to highly turbulent freestream with Tu=7% (Case 10). When Tu further increases from 7% to 9% to 11%, we detected opposite trends in the two regions designated as Region A and Region B. Specifically, Nu/Nu_0 in the narrow region defined by 1W from the middle of the concerned strip followed a downward trend with increasing Tu from 7% to 9% to 11%. On the other hand, Nu/Nu_0 of the wider span within bounded by 4W from the middle of the strip of interest continued to increase with increasing freestream turbulence intensity from Tu = 7% to 11%. These opposing trends are due to the weakening of the vortex intensity along with increasing vortex size with increasing freestream turbulence. These are in agreement with Ben Miloud et al [26], where the circulation of the vortex decreased while the vortex radius increased with increasing turbulence intensity in the freestream. Thus, Tu=7% resulted in a more intense vortex than that at Tu of 9% and 11%, improving the heat transfer in the narrower region, Region A. On the other hand, Tu=11% led to a larger (though weaker) vortex than that at Tu of 9% and 7%, which swept through a wider area, resulting in a relatively better overall cooling effect over the extended region, Region B.

Table 7. 2. Averaged normalized Nusselt number results

Case	1	2	3	4	5	6	7	8	9	10	11	12
t/W	0.008	0.016	0.020	0.008	0.008	0.008	0.008	0.008	0.008	0.008	0.008	0.008
H/W	3	3	3	2	4	2	2	2	2	2	2	2
S/W	0	0	0	0	0	1	2	3	0	0	0	0
Tu	0.4%	0.4%	0.4%	0.4%	0.4%	0.4%	0.4%	0.4%	0.4%	7%	9%	11%
Re	8500	8500	8500	8500	8500	8500	8500	8500	6000	6000	6000	6000
Averaged Nu/Nu_0 (region A)	1.571	1.575	1.530	1.654	1.515	1.428	1.392	1.404	1.749	2.083	2.065	2.055
Averaged Nu/Nu_0 (region	1.303	1.241	1.192	1.321	1.275	1.330	1.326	1.347	1.384	1.665	1.687	1.723

B)													

With multiple linear regression analysis, the standardized regression coefficients (β_j^{std}) were deduced to allow across the board comparison of the significance of the studied parameters on heat transfer enhancement. Table 7.3 is a summary of the obtained results. The tabulated values indicate the weight of impact of each parameter on the averaged heat convection augmentation. The R-square for this linear regression is around 0.96 and 0.99 for Region A and Region B, respectively. Clearly, the freestream conditions, i.e. Tu and Re have the largest impact on the averaged heat transfer improvement over the studied conditions. The standardized regression coefficient, β_j^{std}, of the freestream turbulence intensity, Tu, for Region B of 0.72 is the largest. This confirms that Tu has the greatest positive effect in augmenting the extended area of the plate. The second largest β_j^{std} corresponds to the narrower span defined as Region A. The second most important factor is Re, which has a negative influence, that is, heat transfer augmentation decreases with increasing Re. In other words, the Reynolds number has a negative correlation with Nu/Nu_0, more so in Region A than in Region B. After Re, the decreasing order of significance is the spacing of the strip pair, S/W, for Region A, the thickness of the strip, t/W, for Region B, the height of the strip, H/W, for Region A followed by Region B. The correlation between Nu/Nu_0 in Region B and the spacing of the strip pair, S/W, and that between Nu/Nu_0 of Region A and the strip thickness, t/W, are the weakest.

Table 7. 3. Multiple linear regression results

Parameters		*Tu*	*Re*	*S/W*	*H/W*	*t/W*
Averaged Nu/Nu_0 (region A)	Regression coefficient (β_j)	3.15	-7.6x10^{-5}	-0.08	-0.03	-1.15
	Standardized regression coefficient (β_j^{std})	0.48	-0.36	-0.31	-0.09	-0.02
Averaged Nu/Nu_0 (region B)	Regression coefficient (β_j)	3.31	-3.2x10^{-5}	0.01	-0.02	-8.63
	Standardized regression coefficient (β_j^{std})	0.72	-0.21	0.04	-0.08	-0.18

7.4.2 Correlation between local normalized Nusselt number and turbulence characteristics behind the strips

The total turbulence fluctuations, downwash velocities toward the heated surface, and the streamwise velocities are of significant interest as far as the underlying mechanisms behind heat convection performance. Therefore, the turbulent generated by the strip is detailed in this section to reveal the strip-induced turbulent flow characteristics. More importantly, we attempt to understand how these flow characteristics affect the local convective heat transfer.

7.4.2.1 Freestream turbulence effect

Figure 7.3 depicts the cross-stream profiles of local Nu/Nu_0, turbulent kinetic energy (ke), downwash velocity ($\overline{W}/U_\infty$) and near-surface streamwise velocity ($U_{0.6}/U_\infty$) under different freestream turbulence; which is found to have the largest impact on the averaged heat transfer enhancement as shown in Table 7.3. Note that ke and $\overline{W}/U_\infty$ conveyed here are the averaged values with respect to vertical (Z/W) distance from 0.6 to 3. Meanwhile, $U_{0.6}/U_\infty$ is the velocity at the lowest measurement point of the experiment, i.e. Z/W=0.6. A jump in local Nu/Nu_0 could be identified from the largely "laminar" case, i.e. Tu=0.4%, to the turbulent cases (Tu≥7%). The local Nu/Nu_0 peak for the Tu=11% case reaches around 2.2 at Y/W=0. This is approximately 0.4 larger than that associated with Tu=0.4% case; see Figure 7.3(a). This drastic improvement in local heat transfer is resulted from the increase of turbulent kinetic energy and near-surface streamwise velocity; see Figure 7.3(b) and 3(d). It is interesting to note that the peak value of the local Nu/Nu_0 for Tu=7% case is roughly the same as that of the Tu=11% case. Although the values of ke and $U_{0.6}/U_\infty$ at this peak Nu/Nu_0 cross-stream (Y/W) location for the Tu=7% case are smaller than those for the Tu=11% condition, the largest downwash velocity was observed for the Tu=7% case; see Figure 7.3(c). This largest downwash provided the added boost in local heat transfer enhancement for the lower free-stream turbulence case with Tu=7%.

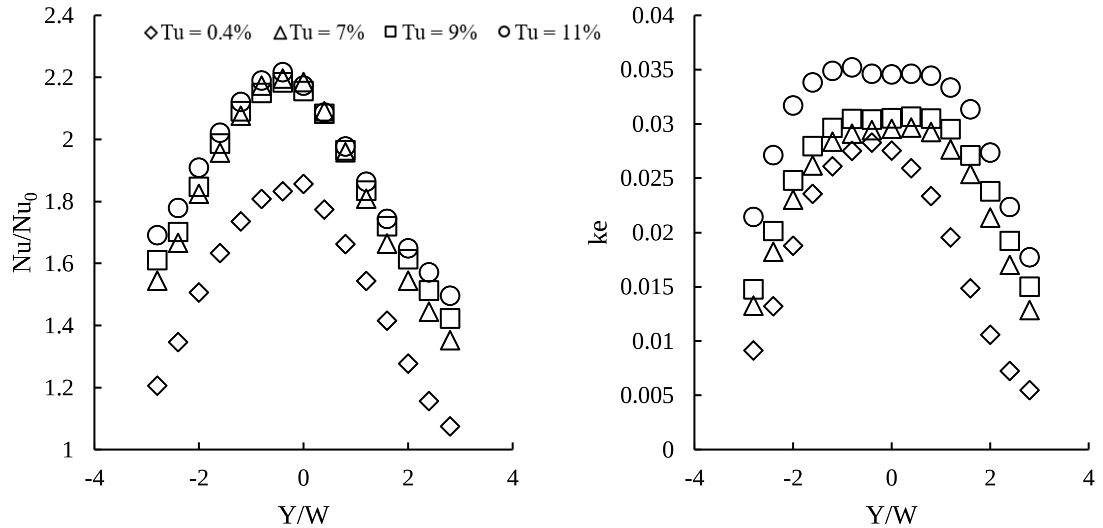

(a) local normalized Nusselt number (b) vertical averaged turbulent kinetic energy

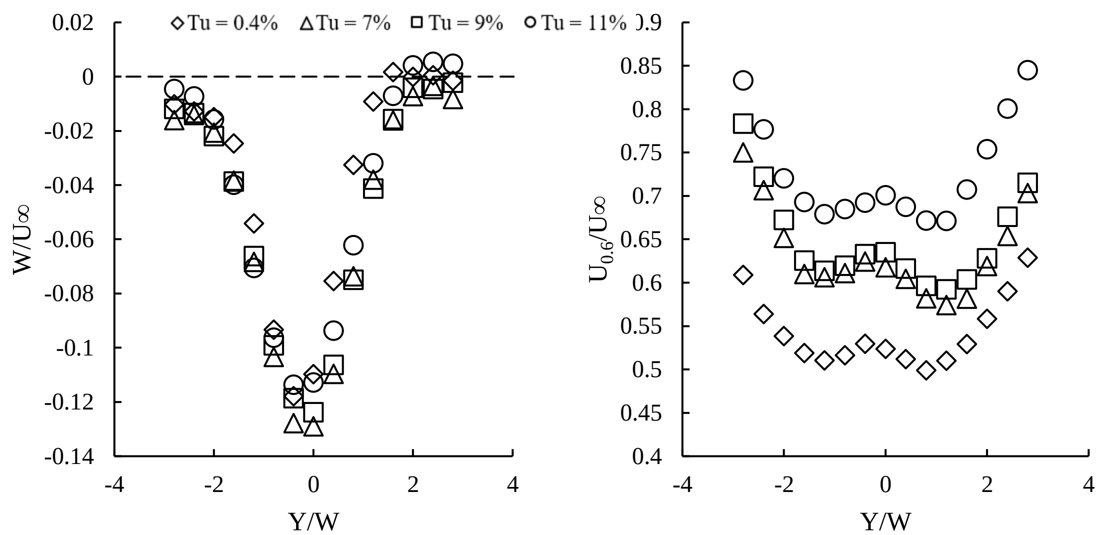

(c) vertical averaged downwash velocity (d) near-surface streamwise velocity

Figure 7. 3. Cross-stream profile at 9W downstream, for Case 9, 10, 11, 12 (freestream turbulence effect)

7.4.2.2 Reynolds number effect

The effects of Reynolds number on the local heat transfer augmentation, turbulent kinetic energy, downwash velocity and streamwise velocity at 9W downstream are presented in Figure 7.4. With decreasing Reynolds number from 8500 to 6000, the local Nu/Nu_0 peak increases from around 1.78 to 1.86; see Figure 7.4(a). The local turbulent kinetic energy, ke, downstream of the strip also increased with decreasing Reynolds number as shown in Figure 7.4(b). The peak ke value intensified from 0.024 to 0.028 as Re decreased from 8500 to 6000. On the other hand, the magnitude of the downwash velocity lowered marginally while the near-surface velocity decreased substantially with decreasing Re from 8500 to 6000; see Figure 7.4(c) and 7.4(d). These results indicate the predominating turbulent kinetic energy role. The regression analysis presented later will confirm this observation.

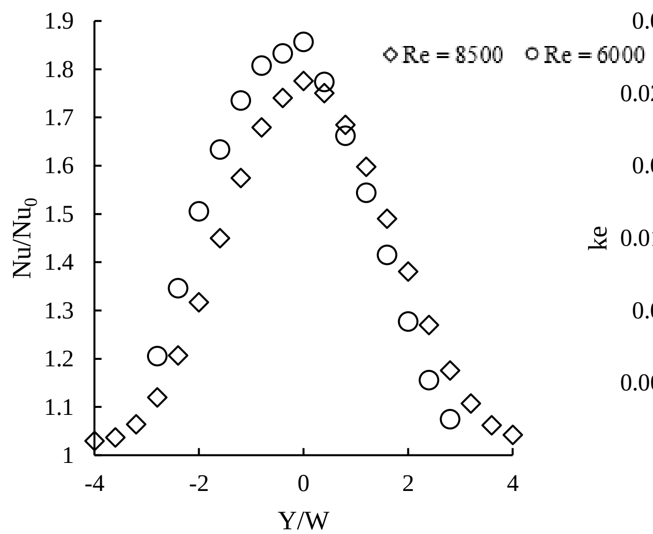

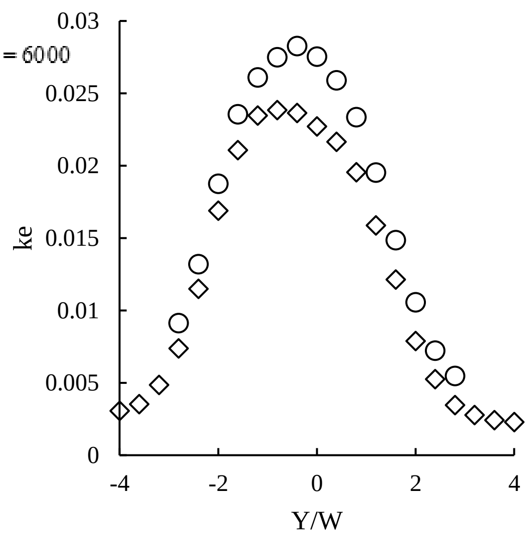

(a) local normalized Nusselt number

(b) vertical averaged turbulent kinetic energy

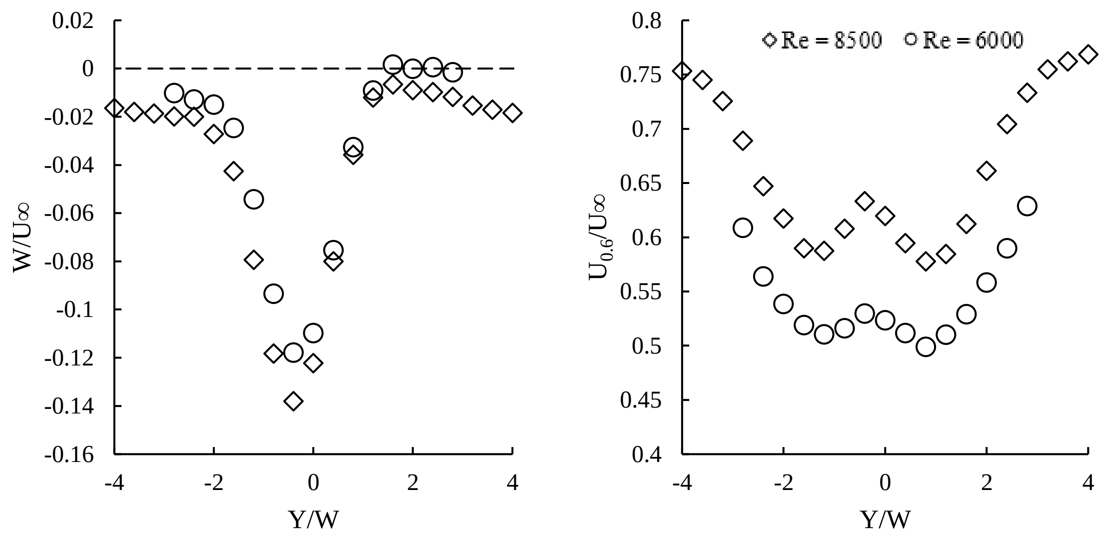

(c) vertical averaged downwash velocity (d) near-surface streamwise velocity

Figure 7. 4. Cross-stream profile at 9W downstream, for Case 4, 9 (Reynolds number effect)

7.4.2.3 Spacing effect

Variations in local Nu/Nu_0, ke, $\overline{W}/U_\infty$ and $U_{0.6}/U_\infty$ with respect to transversal spacing between the pair of side-by-side strips are illustrated in Figure 7.5. It should be mentioned that Y/W=0 represents the middle point of the strip pair. We see that the 12.7 mm-spaced strip pair induced the highest local heat convection augmentation in the gap region, providing the local Nu/Nu_0 up to 1.60 at around Y/W=0. When the spacing increased to 25.4 mm and 38.1 mm, the local Nu/Nu_0 decreased to approximately 1.27 and 1.19 at the same location, respectively. This variation of heat transfer performance at gap region is largely due to vortex-vortex interaction. The vortex-vortex interaction intensified as the vortices from the two approaching strip edges progressively mingled with each other [19], resulting in a higher turbulent kinetic energy and a larger downwash velocity in the gap region; see Figure 7.5(b) and 7.5(c). Also worth mentioning is that, outside the gap region, the best heat transfer augmentation is found when the 38.1 mm-spaced strip pair is employed. For example, at Y/W=2.4, the local Nu/Nu_0 for the 38.1 mm-spaced strip pair is around 1.60, much larger than that of the 12.7 mm-spaced strip pair, which is around 1.44. This indicates that the strip pair with wider spacing could affect more area, providing a better overall heat transfer enhancement of the entire heated surface; see Table 7.2.

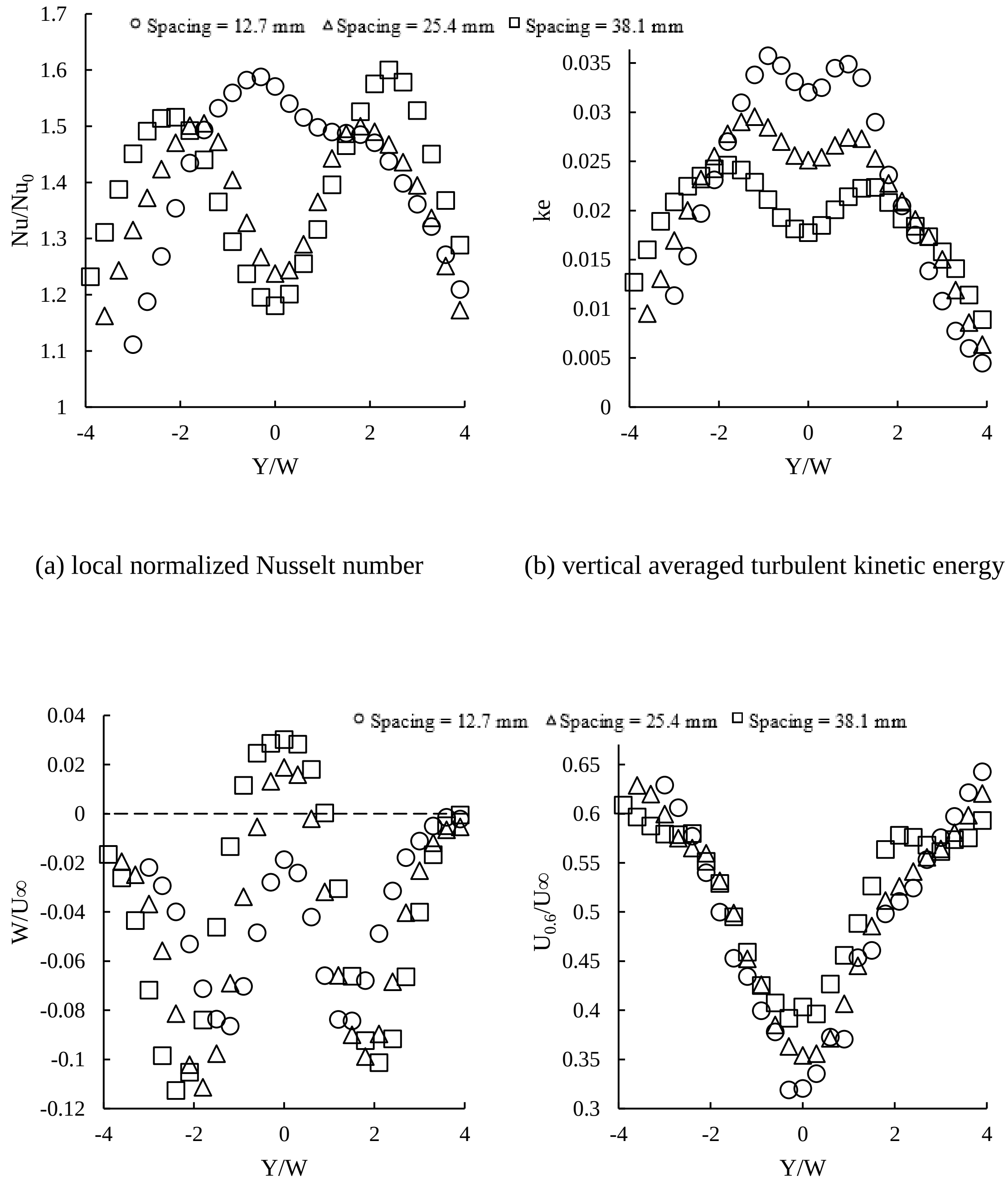

(a) local normalized Nusselt number (b) vertical averaged turbulent kinetic energy

(c) vertical averaged downwash velocity (d) near-surface streamwise velocity

Figure 7. 5. Cross-stream profile at 9W downstream, for Case 6, 7, 8 (spacing effect)

7.4.2.4 Height effect

The effects of the flexible strip height on the local heat transfer and the turbulent flow characteristics are depicted in Figure 7.6. Figure 7.6(a) shows that the peak of local Nu/Nu_0

increased significantly with decreasing strip height. This increase in Nu/Nu_0 with decreasing strip height is not due to an increase in the turbulent kinetic energy, ke. Contrary to the increasing Nu/Nu_0 with decreasing strip height trend, the average ke decreases with decreasing strip height as shown in Figure 7.6(b). Nevertheless, due to the closer-to-base vortex and the thinner velocity boundary layer [18], the shortest 25.4 mm-high strip provided the largest downwash velocity, Figure 7.6(c), as well as the highest near-surface streamwise velocity around Y/W=0, Figure 7.6(d). These two factors contributed to greatest local heat transfer enhancement in the neighborhood of Y/W=0.

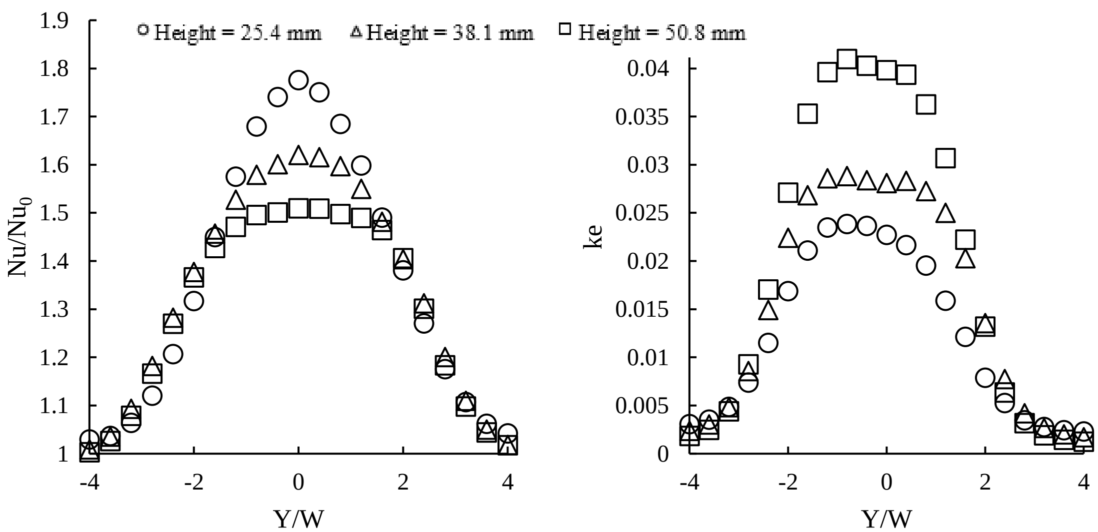

(a) local normalized Nusselt number (b) vertical averaged turbulent kinetic energy

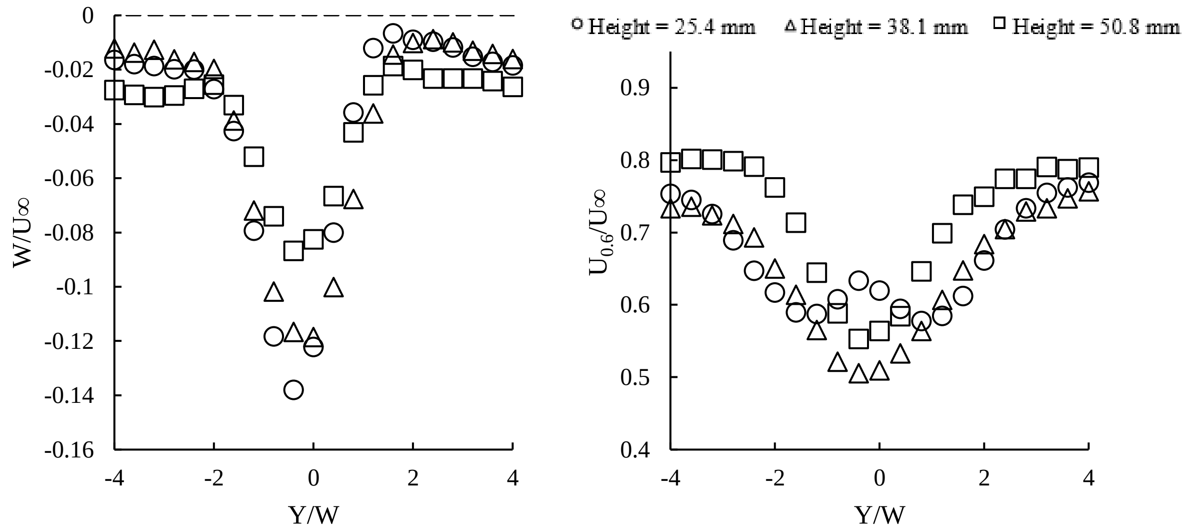

(c) vertical averaged downwash velocity (d) near-surface streamwise velocity

Figure 7. 6. Cross-stream profile at 9W downstream, for Case 1, 4, 5 (height effect)

7.4.2.5 Thickness effect

Figure 7.7 exhibits the role the strip thickness plays on the local heat transfer improvement and the flow characteristics in terms of turbulent kinetic energy, downwash velocity and the streamwise velocity. The figure shows that at nine strip widths (X/W=9) downstream, the difference in all considered heat and flow parameters for 0.1 mm, 0.2 mm and 0.25 mm-thick flexible strips are negligible. Recall that the thinnest 0.1 mm strip provided the best overall Nu/Nu_0, around 0.11 larger than that of 0.25 mm strip over the wide and extended plate, Region B; see Table 7.2. This implies that the thinner, more flexible strip can provide a farther-reaching and longer-lasting heat transfer enhancement. This is significantly beneficial in practice as fewer strips are required to promote heat convection over a larger area.

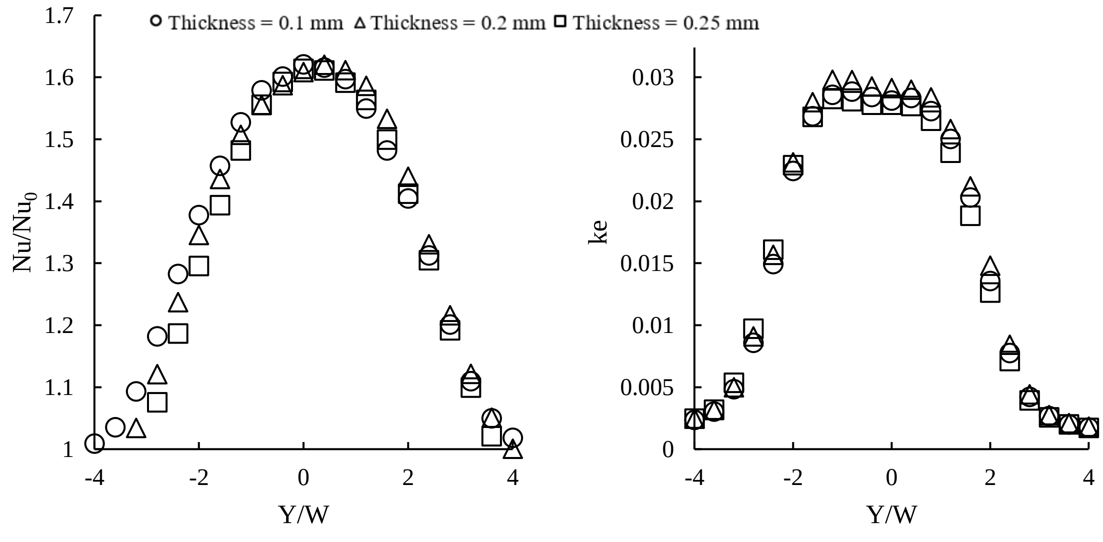

(a) local normalized Nusselt number

(b) vertical averaged turbulent kinetic energy

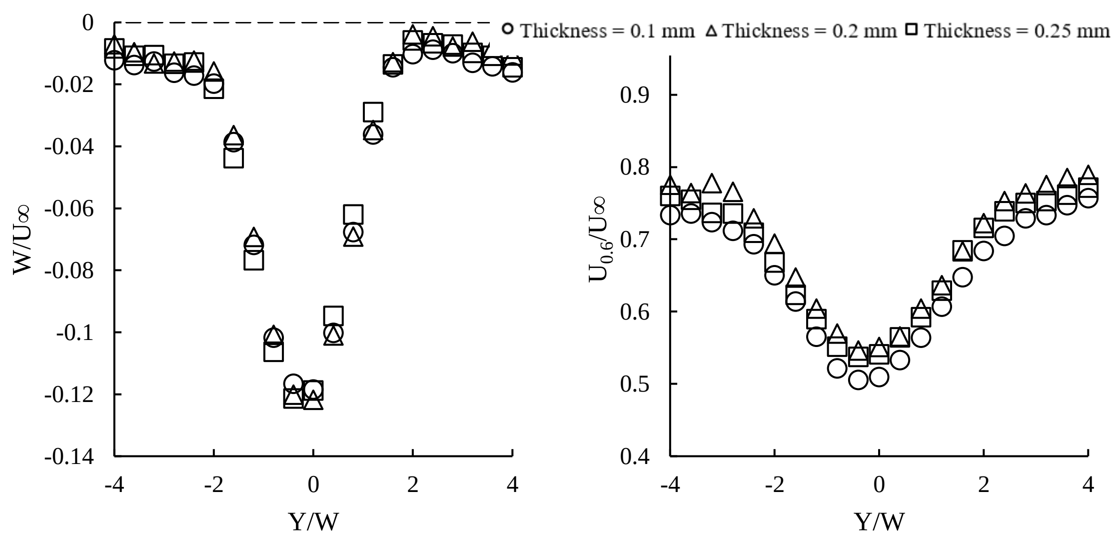

(c) vertical averaged downwash velocity

(d) near-surface streamwise velocity

Figure 7. 7. Cross-stream profile at 9W downstream, for Case 1, 2, 3 (thickness effect)

7.4.2.6 Multiple linear regression result

Given our findings, we fully appreciate the complex coupling among the studied factors in promoting heat convection. To reveal the underlying correlations between local Nu/Nu_0 and the studied parameters, a multiple linear regression analysis was conducted. Table 7.4 is a summary of the results. The R-square for this linear regression is around 0.71, which is moderate because of the limited ranges of considered conditions along with strong coupling between the studied variables. It is obvious from Table 7.4 that the turbulent kinetic energy has the most significant effect on the local heat convection enhancement. The standardized regression coefficient (β_j^{std}) for ke is 0.83, implying that an increase in ke leads to a strong increase in Nu/Nu_0. This standardized regression coefficient is notably larger than those of Tu associated with the average Nu/Nu_0 over extended areas, Region A and Region B, as shown in Table 7.3. This is an expected result as we are correlating the local heat transfer enhancement with the local flow characteristics here; whereas Table 7.3 pertains to correlations between the flow characteristics at a typical location downstream of the strip with the average heat transfer augmentation over 23 strip widths downstream over cross-sections of 2 strip widths and 8 strip widths. The near-surface streamwise velocity $U_{0.6}/U_\infty$ also correlates positively with Nu/Nu_0 with a solid standardized regression coefficient of 0.22. The downwash, or into the plate velocity, $\overline{W}/U_\infty$, also affects the local heat transfer significantly with β_j^{std} of approximately -0.19. The negative sign is because downwash velocity is negative, opposing the positive Z coordinate, which is pointing upward; see Figure 7.1.

Table 7. 4. Correlation between local normalized Nusselt number and turbulence parameters

Parameters	ke	$U_{0.6}/U_\infty$	$\overline{W}/U_\infty$
Regression coefficient (β_j)	23.0	0.58	-1.51
Standardized regression coefficient (β_j^{std})	0.83	0.22	-0.19

7.5 Conclusions

12.7 mm wide (W) rectangular flexible strips were explored experimentally in a wind tunnel in an effort to further convective heat transfer augmentation of a flat surface. Strip thickness (0.1 mm, 0.2 mm and 0.25 mm), strip height (25.4 mm, 38.1 mm and 50.8 mm), and strip spacing (12.7 mm, 25.4 mm and 38.1 mm) were investigated under different freestream conditions (Reynolds number of 8500 and 6000, freestream turbulence intensity of 0.4%, 7%, 9% and 11%). The main findings are highlighted as follows.

1. The freestream turbulence intensity has the largest positive effect on the overall heat transfer enhancement. The averaged Nu/Nu_0, the maximal averaged Nu/Nu_0 along a narrow path defined by $Y=\pm W$ cross-stream and up to $Z=23W$ downstream was observed for the $Tu=7\%$ case, while the largest averaged Nu/Nu_0 for the extended surface area of 8 strip widths was obtained when $Tu=11\%$.

2. The averaged Nu/Nu_0 increases with decreasing Reynolds number, decreasing strip thickness, and decreasing strip height.

3. When a strip pair, instead of an isolated strip, is used, the transversal spacing has a negative influence on the heat transfer enhancement of the narrow band defined by $Y=\pm W$ cross-section and up to $Z=23W$ downstream. This transversal spacing only has a weak positive effect, with a standardized regression coefficient (β_j^{std}) of 0.04, on the extended area of 8 strip widths.

4. As expected, localized correlations relating the local Nu/Nu_0 with the local flow characteristics are strongest. The local turbulent kinetic energy significantly and positively affected the local Nu/Nu_0. As such, promoting local flow turbulence is the key in promoting heat convection. Increasing near-surface streamwise and/or downwash velocities can also notably boost local Nu/Nu_0.

Acknowledgments

This work was made possible by Natural Sciences and Engineering Research Council of Canada and Ontario Centres of Excellence.

References

[1] M. Awais and A. A. Bhuiyan, "Heat transfer enhancement using different types of vortex generators (VGs): A review on experimental and numerical activities," Therm. Sci. Eng. Prog., vol. 5, no. August 2017, pp. 524–545, 2018, doi: 10.1016/j.tsep.2018.02.007.

[2] A. Boonloi and W. Jedsadaratanachai, "Numerical investigation on turbulent forced convection and heat transfer characteristic in a square channel with discrete combined V-baffle and V-orifice," Case Stud. Therm. Eng., vol. 8, pp. 226–235, 2016, doi: 10.1016/j.csite.2016.07.003.

[3] H. Ameur, D. Sahel, and Y. Menni, “Enhancement of the cooling of shear-thinning fluids in channel heat exchangers by using the V-baffling technique,” Therm. Sci. Eng. Prog., vol. 18, no. October 2019, p. 100534, 2020, doi: 10.1016/j.tsep.2020.100534.

[4] S. Tamna, Y. Kaewkohkiat, S. Skullong, and P. Promvonge, “Heat transfer enhancement in tubular heat exchanger with double V-ribbed twisted-tapes,” Case Stud. Therm. Eng., vol. 7, pp. 14–24, 2016, doi: 10.1016/j.csite.2016.01.002.

[5] H. Arjmandi, P. Amiri, and M. Saffari Pour, “Geometric optimization of a double pipe heat exchanger with combined vortex generator and twisted tape: A CFD and response surface methodology (RSM) study,” Therm. Sci. Eng. Prog., vol. 18, no. December 2019, p. 100514, 2020, doi: 10.1016/j.tsep.2020.100514.

[6] L. Chai and S. A. Tassou, “A review of airside heat transfer augmentation with vortex generators on heat transfer surface,” Energies, vol. 11, p. 2737, 2018, doi: 10.3390/en11102737.

[7] R. K. B. Gallegos and R. N. Sharma, “Flags as vortex generators for heat transfer enhancement: Gaps and challenges,” Renew. Sustain. Energy Rev., vol. 76, pp. 950–962, 2017, doi: 10.1016/j.rser.2017.03.115.

[8] A. Dadvand, S. Hosseini, S. Aghebatandish, and B. C. Khoo, “Enhancement of heat and mass transfer in a microchannel via passive oscillation of a flexible vortex generator,” Chem. Eng. Sci., vol. 207, pp. 556–580, 2019, doi: 10.1016/j.ces.2019.06.045.

[9] J. Shi, S. R. Schafer, and C. L. C. L. Chen, “Vortex-induced vibration for heat transfer enhancement,” in Proceedings of the ASME 2014 International Mechanical Engineering Congress and Exposition, 2014, pp. 1–8.

[10] Y. L. He, P. Chu, W. Q. Tao, Y. W. Zhang, and T. Xie, “Analysis of heat transfer and pressure drop for fin-and-tube heat exchangers with rectangular winglet-type vortex generators,” Appl. Therm. Eng., vol. 61, no. 2, pp. 770–783, 2013, doi: 10.1016/j.applthermaleng.2012.02.040.

[11] M. F. Blair, “Influence of free-stream turbulence on turbulent boundary layer heat transfer and mean profile development, part II—analysis of results,” J. Heat Transfer, vol. 105, no. 1, pp. 41–47, 1983, doi: 10.1115/1.3245557.

[12] A. Kondjoyan and J. D. Daudin, “Effects of free stream turbulence intensity on heat and mass transfers at the surface of a circular cylinder and an elliptical cylinder, axis ratio 4,” Int. J. Heat Mass Transf., vol. 38, no. 10, pp. 1735–1749, 1995, doi: 10.1016/0017-9310(94)00338-V.

[13] T. Defraeye, B. Blocken, and J. Carmeliet, “Convective heat transfer coefficients for exterior building surfaces: Existing correlations and CFD modelling,” Energy Convers. Manag., vol. 52, pp. 512–522, 2011, doi: 10.1016/j.enconman.2010.07.026.

[14] M. G. Emmel, M. O. Abadie, and N. Mendes, “New external convective heat transfer coefficient correlations for isolated low-rise buildings,” Energy Build., vol. 39, no. 3, pp. 335–342, 2007, doi: 10.1016/j.enbuild.2006.08.001.

[15] M. T. Kahsay, G. Bitsuamlak, and F. Tariku, “Numerical analysis of convective heat transfer coefficient for building facades,” J. Build. Phys., vol. 42, no. 6, pp. 727–749, 2019, doi: 10.1177/1744259118791207.

[16] Y. A. Çengel and A. J. Ghajar, Heat and mass transfer : fundamentals & applications, fifth edition. McGraw Hill Education, 2015.

[17] Y. Yang, D. S.-K. Ting, and S. Ray, “Convective heat transfer enhancement downstream of a flexible strip normal to the freestream,” Int. J. Therm. Sci., vol. 145, p. 106059, 2019, doi: 10.1016/j.ijthermalsci.2019.106059.

[18] Y. Yang, D. S.-K. Ting, and S. Ray, “On flexible rectangular strip height on flat plate heat convection,” Int. J. Heat Mass Transf., vol. 150, p. 119269, 2020, doi: 10.1016/j.ijheatmasstransfer.2019.119269.

[19] Y. Yang, D. S. K. Ting, and S. Ray, “Heat transfer enhancement of a heated flat surface via a flexible strip pair,” Int. J. Heat Mass Transf., vol. 159, p. 120139, 2020, doi: 10.1016/j.ijheatmasstransfer.2020.120139.

[20] “Thermal Conductivity of common Materials and Gases.” [Online]. Available: https://www.engineeringtoolbox.com/thermal-conductivity-d_429.html. [Accessed: 26-Aug-2020].

[21] “Emissivity Coefficients Materials.” [Online]. Available: https://www.engineeringtoolbox.com/emissivity-coefficients-d_447.html. [Accessed: 26-Aug-2020].

[22] D. S.-K. Ting, Basics of engineering turbulence. Academic Press, New York, 2016.

[23] J. L. Myers, A. (Arnold) Well, and R. F. Lorch, Research design and statistical analysis. Routledge, 2010.

[24] S. Ali, S. Menanteau, C. Habchi, T. Lemenand, and J. L. Harion, “Heat transfer and mixing enhancement by using multiple freely oscillating flexible vortex generators,” Appl. Therm. Eng., vol. 105, pp. 276–289, 2016, doi: 10.1016/j.applthermaleng.2016.04.130.

[25] S. Ali, C. Habchi, T. Lemenand, and J.-L. Harion, “Towards self-sustained oscillations of multiple flexible vortex generators,” Fluid Dyn. Res., vol. 51, no. 2, p. 025507, 2019, doi: 10.1088/1873-7005/aaeced.

[26] K. Ben Miloud, H. Fellouah, M. Dghim, and M. Ferchichi, “Wing tip vortex development under a grid generated turbulent flow,” in American Society of Mechanical Engineers, Fluids Engineering Division (FEDSM), 2018, doi: 10.1115/FEDSM2018-83478.

[27] R. S. Figliola and D. E. Beasley, Theory and design for mechanical measurements, Fourth edition. Wiley, New York, 2006.

[28] S. Yavuzkurt, “A Guide to Uncertainty Analysis of Hot-Wire Data,” J. Fluids Eng., vol. 106, no. 2, p. 181, 1984, doi: 10.1115/1.3243096.

CHAPTER 8

CONCLUSIONS AND RECOMMENDATIONS

8.1 Summary and Conclusions

The overall objective of this study was to explore the effect of flexible strips on the convective heat transfer enhancement of a heated flat surface under an open flow condition. It was shown from the study that the chosen flexible strip has a significant potential in promoting the heat transfer. The main findings are summarized here.

8.1.1 Thickness Effect

The influence of the flexible strip thickness, 0.1, 0.2 and 0.25 mm, was investigated in a wind tunnel at a Reynolds number of 8500, based on the strip width and freestream velocity. The convective heat transfer enhancement was analyzed in terms of the normalized local Nusselt number, Nu/Nu_o. It was found that the peak value of Nu/Nu_0 occurs immediately behind the strip, after which it decays gradually. Also, the thinnest, most flexible, 0.1 mm-thick strip induced a larger wind velocity toward the heated surface and the stronger Strouhal fluctuation, providing the most desirable flow condition for the heat transfer augmentation, with a peak Nu/Nu_o value of around 1.67 at 3H downstream, 0.1 higher than that of 0.25 mm-thick strip.

8.1.2 Height Effect

Flexible strips with height of 25.4, 38.1, and 50.8 mm were explored at a Reynolds number of 8500. The shortest, 25.4 mm high strip resulted in the most effective heat transfer enhancement. The corresponding span-averaged Nu/Nu_0 is around 0.1 higher than its taller counterpart, the 50.8 mm strip, in spite of the lower vibration amplitude, weaker vortex and the less intense turbulence. The 25.4 mm strip induced the vortex significantly closer to the heated surface, resulting in a larger near surface downwash velocity and a thinner boundary layer, and thus, a more effective cooling from a heated surface.

8.1.3 Transversal Spacing Effect

The strip pairs, in a side-by-side arrangement, spaced 1W (strip width), 2W and 3W, were studied. The Reynolds number in this study was also maintained at around 8500, based on the strip width. Generally speaking, the 1W-spaced strip pair provided the most effective span-averaged heat transfer enhancement, due to the strong vortex-vortex interaction. In spite of the decrease in streamwise velocity, which induced a negative effect on the heat transfer augmentation, the 1W-spaced strip pair provided a larger downwash velocity, and a higher turbulence level. According to the multiple linear regression results, the later effect seemed to have a more significant impact, leading to the most forceful heat transfer enhancement behind the 1W-spaced strip pair.

8.1.4 Freestream Turbulence Effect

A 76 cm by 76 cm orificed perforated plate (OPP), was placed at 10D (hole diameter, of 38.1 mm), 13D, and 16D upstream of the flexible strip to achieve the streamwise freestream turbulence intensity (*Tu*) of approximately 11%, 9%, and 7%. The Reynolds number, based on the strip width, was around 6000 in this study. With increasing freestream turbulence, the relative effect of flexible strip on the heat transfer augmentation decreases. The strip in the most intense 11% freestream turbulence provided the smallest Nu/Nu_0 values. In other words, with increasing *Tu*, the flexible strip could promote less heat transfer augmentation from the already highly-effective turbulent heat convection in the presence of the OPP. More importantly, the flexible strip always further *Nu* beyond that caused by a high-turbulent wind.

8.1.5 Multiple Linear Regression Analysis

All the dataset, including strip thickness (0.1 mm, 0.2 mm and 0.25 mm), strip height (25.4 mm, 38.1 mm and 50.8 mm), and strip spacing (12.7 mm, 25.4 mm and 38.1 mm) were investigated under different freestream conditions (Reynolds number of 8500 and 6000, freestream turbulence intensity of 0.4%, 7%, 9% and 11%). The main findings are highlighted as follows.

1. The freestream turbulence intensity has the largest positive effect on the overall heat transfer enhancement. The averaged Nu/Nu_0, the maximal averaged Nu/Nu_0 along a narrow path defined by Y=±W cross-stream and up to Z=23W downstream was observed for the Tu=7% case, while the largest averaged Nu/Nu_0 for the extended surface area of 8 strip widths was obtained when Tu=11%.

2. The averaged Nu/Nu_0 increases with decreasing Reynolds number, decreasing strip thickness, and decreasing strip height.

3. When a strip pair, instead of an isolated strip, is used, the transversal spacing has a negative influence on the heat transfer enhancement of the narrow band defined by Y=±W cross-section and up to Z=23W downstream. This transversal spacing only has a weak positive effect, with a standardized regression coefficient (β_j^{std}) of 0.04, on the extended area of 8 strip widths.

4. As expected, localized correlations relating the local Nu/Nu_0 with the local flow characteristics are strongest. The local turbulent kinetic energy significantly and positively affected the local Nu/Nu_0. As such, promoting local flow turbulence is the key in promoting heat convection. Increasing near-surface streamwise and/or downwash velocities can also notably boost local Nu/Nu_0.

8.2 Recommendations

The most effective strip design, including the 1W gap between two side-by-side strips, should be implemented on real solar PV panels and compare the performance of the portions of PV array that serve as the control group. In-situ data, including the weather conditions, gathered over the seasons are needed to evaluate the real impact of these simple and potent turbulence generators. Different type and age of PV panels should also be monitored. Also of importance are the different environmental conditions such as the weather, latitude, geography and urban versus suburban settings.

Appendix A UNCERTAINTY ANALYSIS

The total uncertainty of the experiment (E) consists of bias and precision [1]:

$$E = \sqrt{\mathrm{Bias}^2 + \mathrm{Precision}^2} \tag{A.1}$$

In the current study, the precision was calculated from a ten-time repeated measurement, using the Student's t distribution method with a 95% confidence interval. Based on the propagation rule of the uncertainty [1], the uncertainty of the other dependent parameter, $y = f(x_1, x_1, \dots, x_n)$, can be calculated,

$$E(y) = \sqrt{\sum\nolimits_{i=1}^{n} [\frac{\partial y}{\partial x_i} E(x_i)]^2} \tag{A.2}$$

Based on Equation (A.1), the uncertainty of the top surface temperature of the *PTFE* plate can be deduced. From this uncertainty, the uncertainty of Nu/Nu_0 can be calculated. Sample heat transfer uncertainties are tabulated in Table A.1.

Table A. 1. Uncertainties of the thermal camera and the thermocouple

	Thermal Camera	Thermocouple	Nu / Nu_0
Uncertainty	2 °C	0.5 °C	0.066

For the hotwire probe measurement, the total uncertainties of $\overline{U}$ and u_{rms} were determined from the calibration error [2]. The uncertainties of typical flow parameters are summarized in Table A.2. And the uncertainties of the resulting parameters in the chapters were deduced via the propagation role of the uncertainties based on Ref [3]. These uncertainties are summarized in Table A.3.

Table A. 2. Typical uncertainties of mean and root-mean-square velocities.

Parameter	$\overline{U}$	u_{rms}	$\overline{V}$	v_{rms}	$\overline{W}$	w_{rms}
Uncertainty	0.166 ms^{-1}	0.068 ms^{-1}	0.045 ms^{-1}	0.059 ms^{-1}	0.044 ms^{-1}	0.055 ms^{-1}

Table A. 3. Representative uncertainties of studied parameters.

Parameter	Nu/Nu_0	$\bar{U}/U_\infty$	$\bar{V}/U_\infty$	$\bar{W}/U_\infty$	u_{rms}/U_∞
Uncertainty	0.066	0.023	0.005	0.005	0.008
Parameter	ke	Ω	Λ/H	λ/H	
Uncertainty	0.005	0.017	0.040	0.003	

References

[1] R. S. Figliola and D. E. Beasley, Theory and design for mechanical measurements, Fourth edition. Wiley, New York, 2006.

[2] S. Yavuzkurt, "A Guide to Uncertainty Analysis of Hot-Wire Data," J. Fluids Eng., vol. 106, no. 2, p. 181, 2009, doi: 10.1115/1.3243096.

[3] H. Tyagi, R. Liu, D. S.-K. Ting, and C. R. Johnston, "Measurement of wake properties of a sphere in freestream turbulence," Exp. Therm. Fluid Sci., vol. 30, no. 6, pp. 587–604, 2006, doi: 10.1016/J.EXPTHERMFLUSCI.2005.12.004.

Appendix B PERFORATED-PLATE TURBULENCE: ORIFICE VERSUS CONVERGING NOZZLE

Y. Yang, D. S-K. Ting, S. Ray, "Perforated-plate turbulence: orifice versus converging nozzle," Proceedings of the 5th Joint US-European Fluids Engineering Summer Conference, 2018.

Nomenclature

$CNPP$	Converging-nozzled perforated plate
D	Grid hole diameter (m)
$f(r)$	Spatial autocorrelation function
$f(\tau)$	Temporal autocorrelation function
Re	Reynolds number
r	Spatial distance (m)
N	Sampling number
OPP	Orificed perforated plate
Tu	Turbulence intensity
Tu_{mean}	Cross-sectional area averaged turbulence intensity
U	Instantaneous velocities (m/s)
$\overline{U}$	Time-averaged velocity (m/s)
U_{mean}	Cross-sectional-area-averaged velocity (m/s)
u	Instantaneous fluctuating velocity (m/s)
u_{rms}	Root-mean-square velocity (m/s)
Λ	Integral length scale (m)
Λ_{mean}	Cross-sectional-area-averaged integral length scale (m)
λ	Taylor microscale (m)
λ_{mean}	Cross-sectional-area-averaged Taylor microscale (m)
μ	Air dynamic viscosity (Pa · s)
ρ	Air density (kg/m^3)
τ	Temporal distance (s)
τ_Λ	Integral time scale (s)
τ_λ	Taylor time scale (s)

B.1 Introduction

As one of the common turbulence promoters, the grids are widely used in engineering applications, such as for enhancing heat transfer [1-2], reducing low frequency noise [3], and increasing the turbulent combustion rate [4]. A large number of studies on grid turbulence have been carried out since the pioneering work of Taylor [5]. These include many attempts on the effect of grid geometry. For instance, Uberio & Wallis [6] explored the decay of turbulence using biplane grids, inclined rod grids and honeycomb grids. They concluded that the isotropy level is essentially constant during the normal decay period, and it varies with grid geometry. Among others, Liu and Ting [7] illustrated that the turbulence intensity and the degree of homogeneity depend on the hole size and the solidity ratio. Subsequently, they investigated turbulent flow generated by perforated plates with sharp-edged orifices and finite-thickness straight openings, and found that the orificed plate produces a higher level of turbulence [8]. Recently, fractal grids became popular, resulting in a series of publications such as Seoud & Vassilicos [9], Hurst & Vassilicos [10] and Hearst & Lavoie [11]. Among the most recent grid studies, Liu et al. [12] experimentally and numerically explored two different sizes of square-mesh grid, and found that the resulting turbulence can be enhanced by an increase in the grid solidity.

It is clear from the highlighted sample of studies that the so thought "simple grid turbulence" is actually complex; that is, the resulting flow turbulence depends on numerous geometrical and operating parameters. In spite of great effort, there remains much mystery behind grid turbulence. The current study aims at furthering the delineation of the influence of the flow passage on the resulting turbulence generated by a perforated plate. To do so, the orificed perforated plate (OPP) of Ref [8] is revisited and contrasted with its reverse counterpart, the converging-nozzled perforated plate (CNPP).

B.2 Experimentation

The experiment was conducted in a closed-loop wind tunnel with a 760mm by 760mm cross-section. The 760mm by 760mm perforated plate, Figure B.1, was made from a 6mm thick aluminum sheet. The holes in the plate were cut at an angle of 41°, resulting in 38mm circular openings. Two types of the perforated plate were studied, the orificed perforated plate (OPP) and the converging-nozzled perforated plate (CNPP).

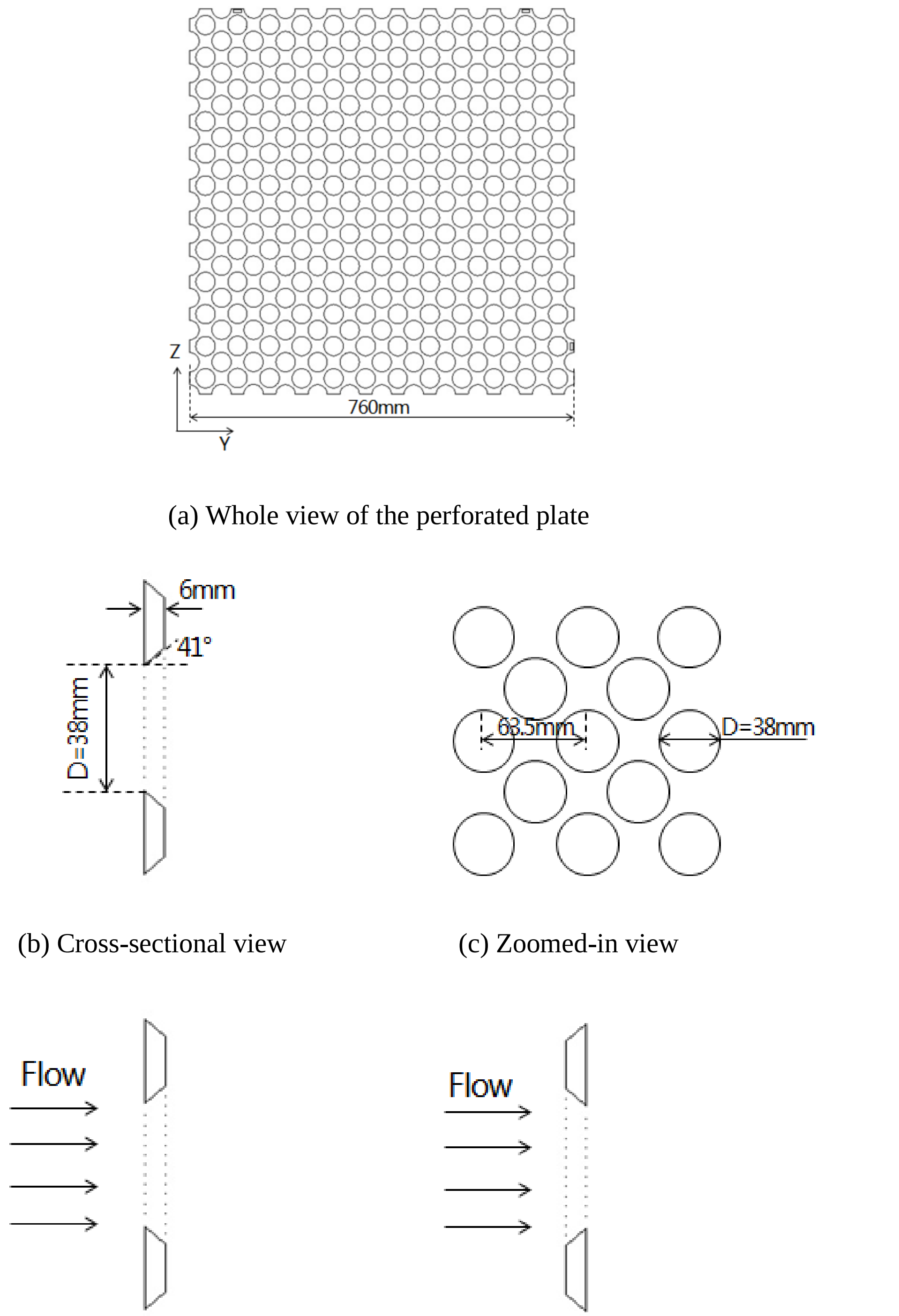

(a) Whole view of the perforated plate

(b) Cross-sectional view

(c) Zoomed-in view

(d) Orificed Perforated Plate (OPP)

(e) Converging-Nozzled Perforated Plate (CNPP)

Figure B. 1. Details of the Perforated Plate

Figure B.2 depicts the experimental setup in the wind tunnel. The perforated plate was mounted normal to the air flow. X, Y and Z represent streamwise, widthwise, and vertical direction, respectively. The triple sensor hotwire probe (type 55P95) with a constant temperature anemometer was employed to obtain the velocities at 10*D* and 20*D* downstream of the perforated plate. Each measured plane was 127 mm by 127 mm at the middle of the cross-section of the wind tunnel, with a spatial resolution of 15.875mm (0.625inch). The velocity signals were low passed at 30 kHz, and 10^6 measurements were sampled at 80 kHz.

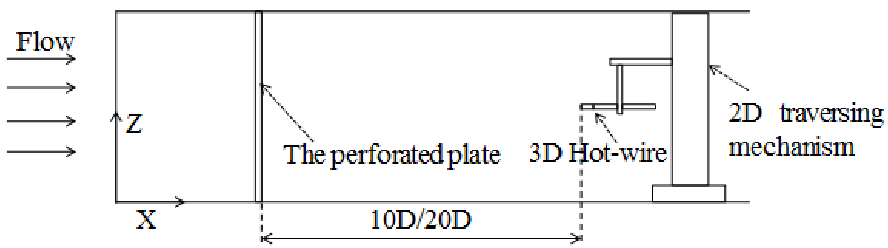

(a) Experimental setup in the wind tunnel

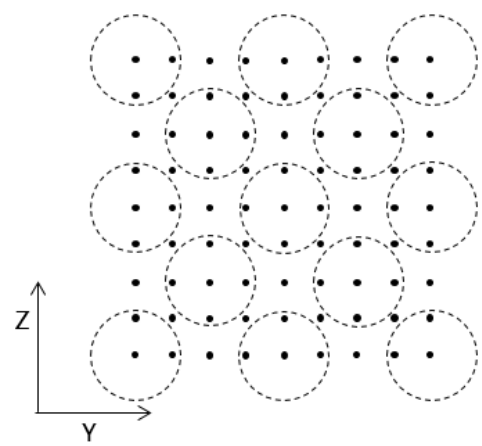

(b) Measuring points

Figure B. 2. Experimental setup and measuring points

B.3 Studied Parameters

With the 3D hotwire, the instantaneous velocities in the X, Y and Z directions were measured simultaneously. The instantaneous velocities in the streamwise direction can be expressed as:

$$U = \overline{U} + u \tag{B.1}$$

where $\overline{U}$ is the time-averaged velocity, and u is the instantaneous fluctuating velocity. The time-averaged velocity can be calculated from:

$$\overline{U} = \frac{1}{N}\sum_{i=1}^{N} U_i \tag{B.2}$$

the sampling number N=10^6.

The root-mean-square velocity,

$$u_{rms} = \sqrt{\sum_{i=1}^{N} \frac{{u_i}^2}{N-1}} \tag{B.3}$$

This fluctuating velocity can be normalized by the cross-sectional-area-averaged velocity to give the relative turbulence intensity,

$$Tu = \frac{u_{rms}}{U_{mean}} \tag{B.4}$$

The Reynolds number can be defined as

$$Re = \frac{\rho D U_{mean}}{\mu} \tag{B.5}$$

where *D*=38mm is hole diameter, ρ and μ are air density and air dynamic viscosity, respectively.

Other than velocity fluctuation, turbulence length scale is another key parameter to describe the turbulence [13]. The integral scale, representing the energy-containing large eddies, can be derived from the autocorrelation function of turbulence fluctuating velocities. The autocorrelation function in the temporal distance is

$$f(\tau) = \frac{\overline{u(t)u(t+\tau)}}{\overline{u^2(t)}} \tag{B.6}$$

This can be converted into the corresponding spatial autocorrelation function based on Taylor frozen hypothesis [14],

$$f(r) = f(\tau)\overline{U} \tag{B.7}$$

The integral time scale is defined as:

$$\tau_\Lambda = \int_0^\infty f(\tau)d\tau \tag{B.8}$$

From this, invoking the Taylor frozen hypothesis [14] gives

$$\Lambda = \overline{U}\tau_\Lambda \tag{B.9}$$

At the other end of the turbulence energy cascade, the Taylor microscale associated with the dissipation is

$$\lambda = \overline{U}\tau_{\lambda} \tag{B.10}$$

The Taylor timescale,

$$\tau_{\lambda} = \sqrt{\frac{\overline{2u^2}}{(\frac{du}{dt})^2}} \tag{B.11}$$

B.4 Results and Discussion

To delineate the role of the perforated plate turbulence generator, contours of time-averaged velocity, turbulence intensity, the integral scale and the Taylor microscale were inspected. The contours of these parameters at 10D downstream of the OPP and the CNPP are presented in Figures B.3, B.4, B.6, and B.7, respectively. The studied cross-sectional area averaged velocities (U_{mean}) were approximately 7 m/s and 11 m/s. These results are discussed under the following subheadings. The uncertainties of U, Tu, Λ and $\lambda$are estimated to be approximately ±0.2 m/s, ±0.005, ±0.002m and ±0.0002m, respectively. These were deduced for the 11 m/s wind case at 9 typical measurement locations, following Ref [15].

B.4.1 Velocity Profile

Figure B.3 depicts the normalized streamwise time-averaged velocity ($\overline{U}/U_{mean}$) at 10*D* downstream of the perforated plate, position as an OPP versus that of a CNPP. For the lower wind speed with $U_{mean} = 7.39$ m/s, the maximum variation of the local time-averaged velocity from the U_{mean} value is less than 4% for both the OPP and the CNPP; see Figures B.3(a) and B.3(b). This indicates that the flow evolving from the multiple wakes and jets generated by the perforated plate has become homogeneous across the studied cross section at 10*D*.

At a higher wind speed, U_{mean} of 11 m/s, the largest deviation of the local time-averaged velocity for the OPP remains small at about 4%; see Figure B.3(c). At the same wind speed and distance downstream, the CNPP shows a lesser spatial homogeneity in the time-averaged local velocity, with a maximum deviation from the cross-sectional mean of about 10%; see Figure B.3(d).

The time-averaged velocity results farther downstream at 20*D* are summarized in Table B.1. At the lower wind speed of roughly 7 m/s, the cross-sectional homogeneity in $\overline{U}$ deteriorated marginally for the OPP case. The maximum deviation increased slightly from 4% at 10*D* to 5% at

20*D*. Increasing the wind to about 11 m/s resulted in the preservation of slightly better spatial homogeneity in $\overline{U}$ of less than 4% for the OPP case.

For the turbulent flow generated by the CNPP at a wind speed of around 7 m/s, the cross-sectional $\overline{U}$ homogeneity lessened with distance downstream, from 4% at 10*D* to 7% at 20*D*. Surprisingly, this homogeneity improved from 10% to about 2% at the higher wind speed of 11 m/s.

Table B. 1. Cross-sectional time-averaged velocity at 20D

Plate	U_{mean} [m/s]	Maximum deviation
OPP	7.3	5.3%
CNPP	7.5	6.9%
OPP	10.9	3.6%
CNPP	10.9	2.1%

From the time-averaged velocity results, we can surmise that the CNPP is less capable of generating homogeneous turbulence in general; except for the higher wind speed case at 20*D*. Projecting from the time-averaged velocity spatial homogeneity outcome, one could speculate that the turbulence resulting from the OPP is more consistently isotropic. Let us proceed and examine the turbulence intensity results

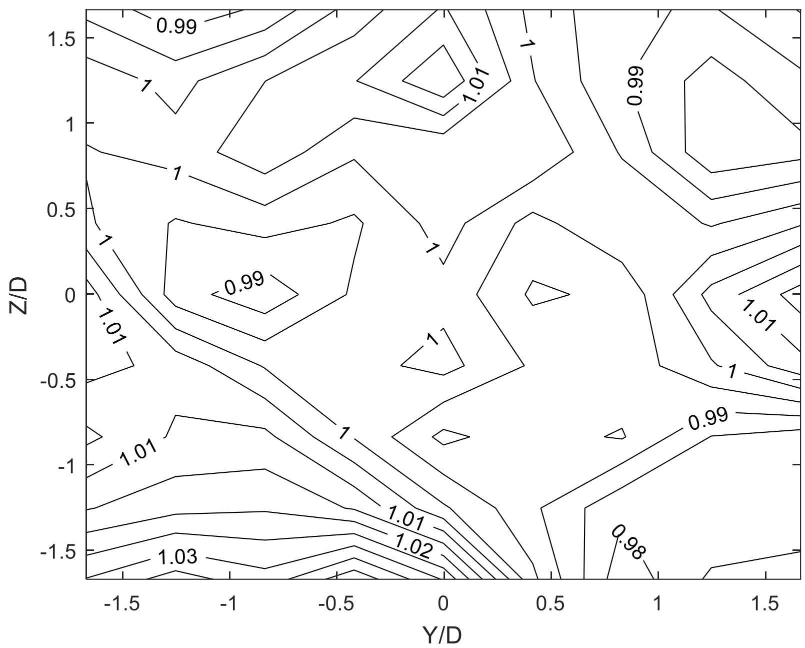

(a) OPP ($U_{mean} = 7.4$m/s, $Re = 1.87\ \times 10^4$)

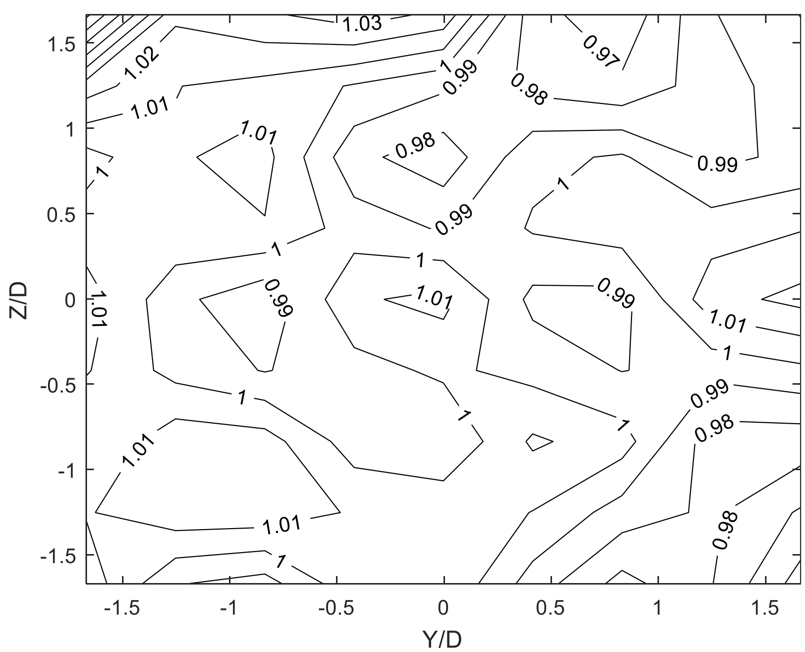

(b) CNPP ($U_{mean} = 7.4$m/s, $Re = 1.87\ \times 10^4$)

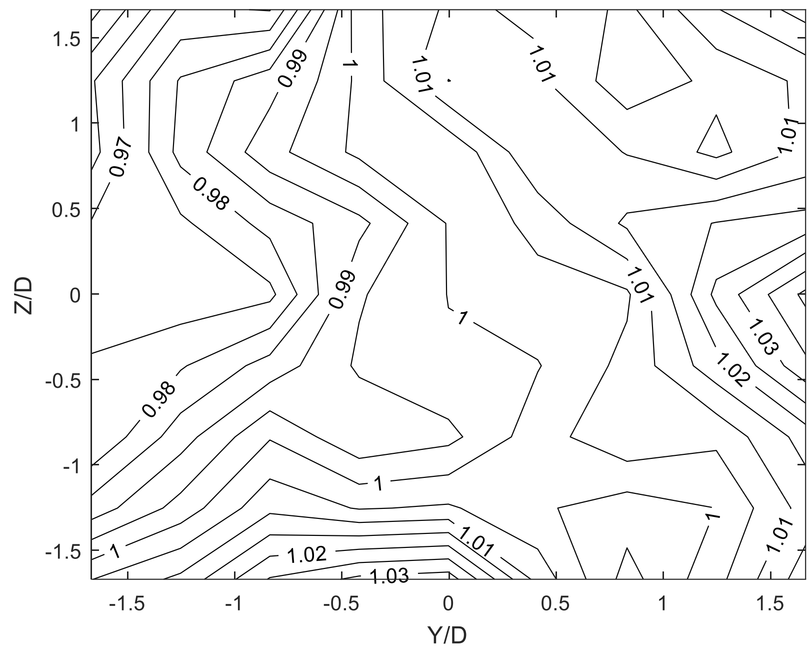

(c) OPP ($U_{mean} = 11.1$m/s, $Re = 2.80 \times 10^4$)

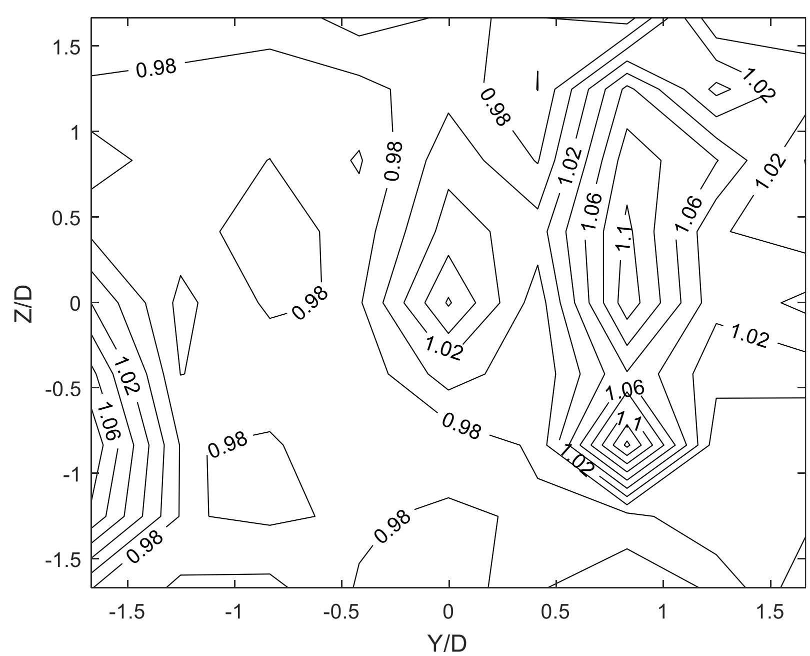

(d) CNPP ($U_{mean} = 11.2$m/s, $Re = 2.84 \times 10^4$)

Figure B. 3. Normalized streamwise time-averaged velocity ($\overline{U}/U_{mean}$) at 10D downstream of the perforated plate.

B.4.2 Turbulence Intensity

Figure B.4 shows the turbulence intensity (Tu) contours at 10*D*. Turbulence intensity contours at 20*D* downstream look similar and thus, the plots are not included due to space limitation. It is clear from Figure B.4 that the turbulence resulting from the OPP is of higher intensity than that of the CNPP. For instance, at $U_{mean} = 7.39$m/s, the cross-sectional area averaged turbulence intensity (Tu_{mean}) of the OPP is 0.115, with a largest deviation of 6%. On the other hand, the Tu_{mean} value of the CNPP is 0.108, and the maximum variation is about 9%; Figures B.4(a) and B.4(b). At a higher wind speed U_{mean} of approximately 11 m/s; see Figures B.4(c) and B.4(d), the Tu_{mean} value of the OPP is 0.116, 8% higher (compared to 6% at the lower wind speed) than that associated with the CNPP.

By the time that the turbulent flow reaches 20*D* downstream, plots not shown, its intensity Tu_{mean} has decayed to approximately 47% of that at 10*D* for the OPP. The somewhat less intense CNPP turbulence decayed marginally slower, to 49% of its 10*D* value at 20*D*. The cross-sectional homogeneity for both OPP and CNPP is approximately 4% at 20*D*; maximum deviation of 4.1% for OPP and 4.2% for CNPP. In other words, the turbulent flow field has become more homogeneous by the time the flow reaches 20*D*.

To see a fuller picture, the respective inertia and dissipative eddies need to be scrutinized. For this purpose, we choose the integral scale and the Taylor microscale. These have been deduced via autocorrelation, as discussed next.

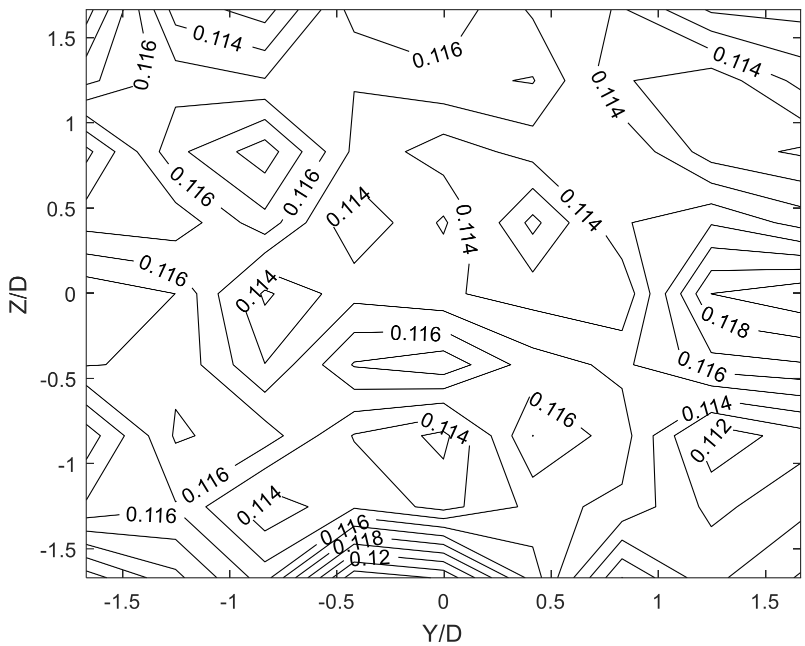

(a) OPP ($U_{mean} = 7.4$m/s, $Re = 1.87 \times 10^4$)

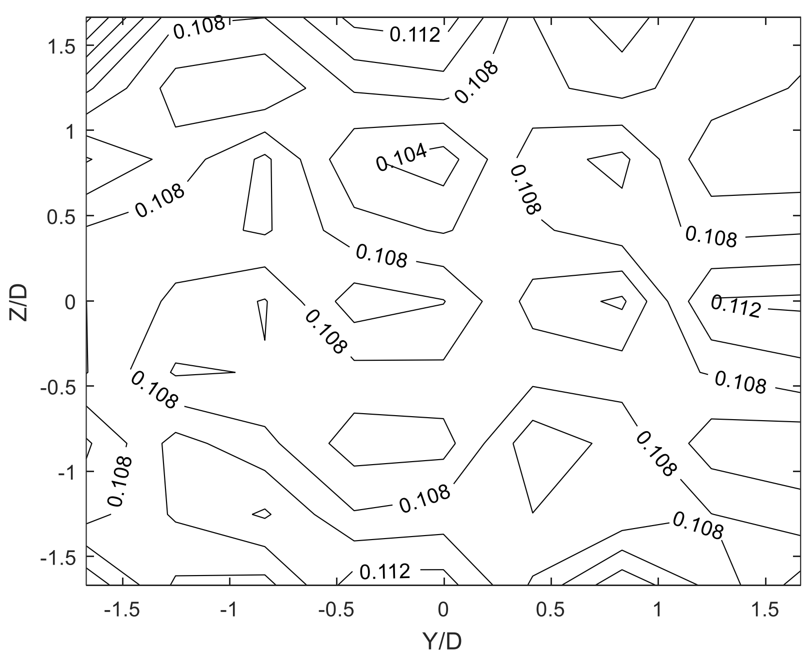

(b) CNPP ($U_{mean} = 7.4$m/s, $Re = 1.87 \times 10^4$)

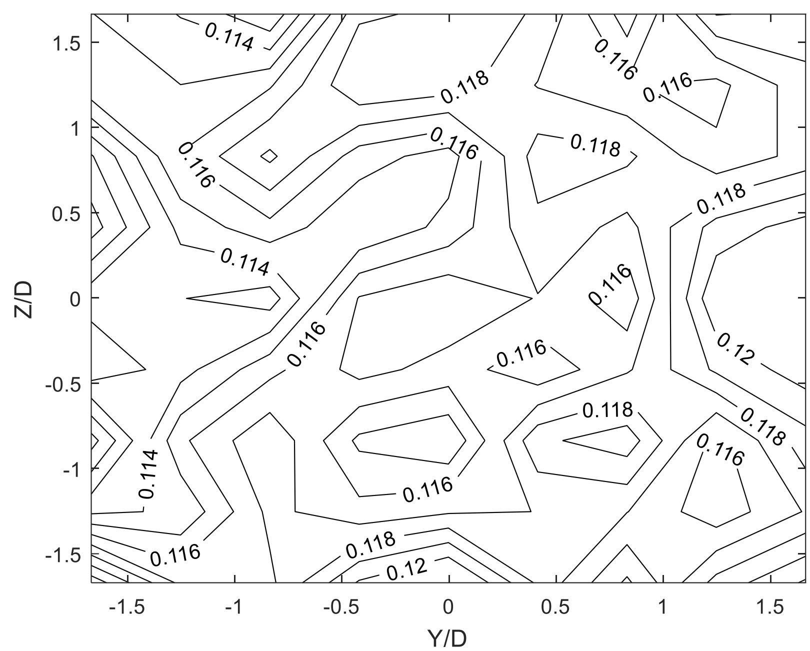

(c) OPP ($U_{mean} = 11.1\text{m/s}$, $Re = 2.80\ \times 10^4$)

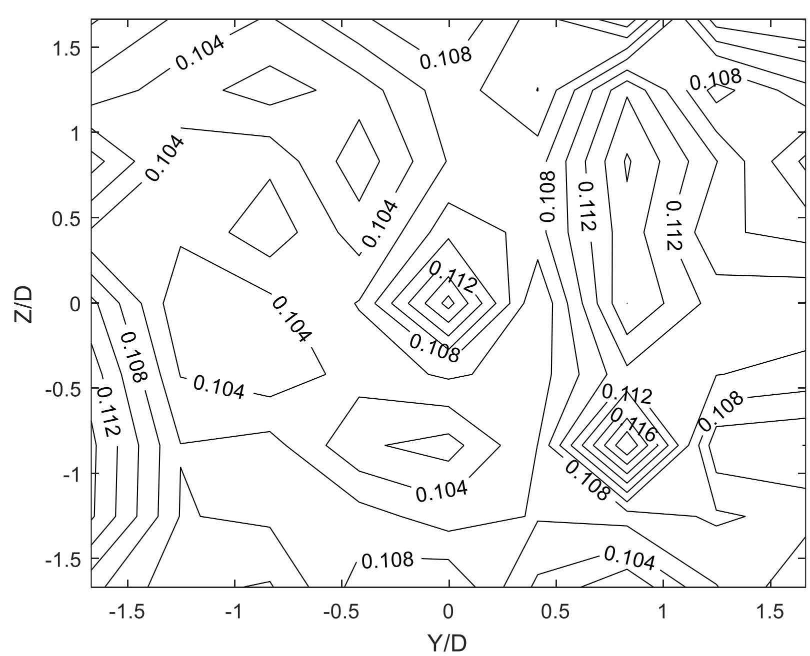

(d) CNPP ($U_{mean} = 11.2\text{m/s}$, $Re = 2.84\ \times 10^4$)

Figure B. 4. Turbulence intensity *Tu* at 10*D* downstream of the perforated plate

B.4.3 Autocorrelation Function

The autocorrelation function of the velocity at the center point of the measurement grid, Figure B.2(b), has been deduced. These results are plotted in Figure B.5. We can see that, at the same location, the area underneath the autocorrelation function *f(r)* of the OPP is a little larger than that associated with the CNPP, indicating the integral scale of the OPP is larger. With more energy near the peak of turbulence production at 10D, the corresponding turbulence is more intense, and this has been discussed earlier when interpreting the results portrayed in Figure B.4. Farther downstream, the turbulence decays rapidly, and thus, the enlarged area underneath the autocorrelation function *f(r)*.

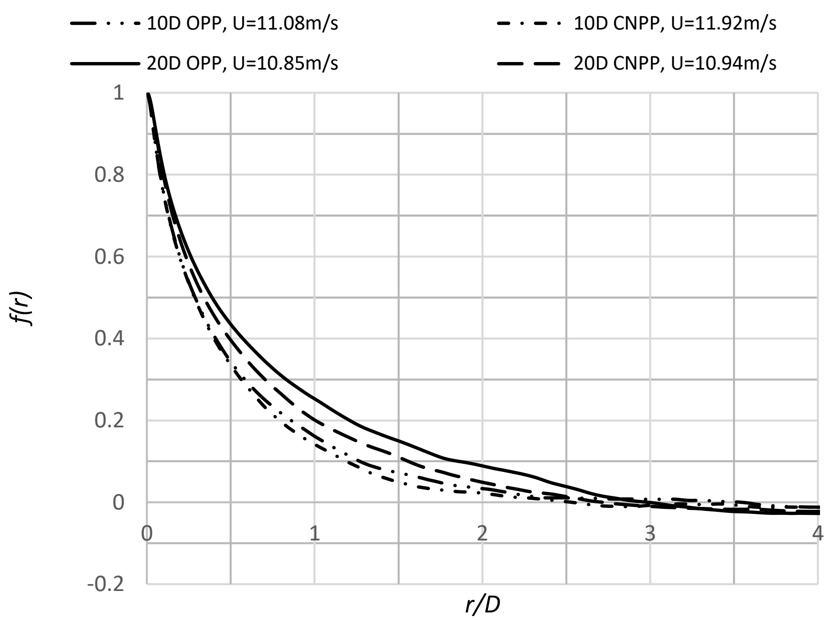

Figure B. 5. Streamwise spatial autocorrelation function *f(r)*

B.4.4 Integral Scale

The integral scale distribution across the measurement cross sections are displayed in Figure B.6. The contours correspond to the integral length scale normalized by the hole diameter (Λ/D, D=38mm).

It is clear from Figure B.6 that the integral length of the OPP generated turbulence at 10D is slightly larger than that associated with the CNPP. For instance, at $U_{mean} = 7.4$m/s, the cross-sectional-area-averaged integral length scale of the OPP, Λ_{mean}/D, is 0.47, while that of the CNPP is 0.43. The maximum variations of the local integral length over the studied cross-section are about 16% and 13%, respectively, for the OPP and the CNPP; see Figures B.6(a) and B.6(b).

The OPP Λ_{mean}/D value increased marginally from 0.47 to 0.49, while the largest variation across the measured section decreased significantly from 16% to 10.5%, at a higher wind speed of 11.1 m/s. The corresponding CNPP value also increased slightly, from 0.43 to 0.45, with increasing wind speed from 7.4 to 11.2 m/s. The deviation of the local integral length from the cross-sectional mean, however, remained largely unaltered at about 13% over this range of wind speed.

It is evident from the above integral length results, which are in agreement with the *Tu* findings, that the OPP tends to produce somewhat larger integral scales. These larger energy-containing eddies connote the higher intensity turbulence generated by the OPP, versus that of CNPP, at the same wind speed and downstream location.

By the time the OPP turbulence decayed to 20*D* downstream, Λ_{mean}/D increased by 25%, with respect to that at 10*D*, for a 7.4 m/s speed. Even though the corresponding increase in CNPP Λ_{mean}/D was slightly larger at 27%, the OPP turbulence intensity remained somewhat higher at 20*D*. The maximum variations are approximately 11.5% and 12% for the OPP and CNPP, respectively. In short, the OPP seems to consistently produce more homogeneous turbulence. The CNPP, on the other hand, attempts to attain equal status in terms of generating clean, isotropic turbulence. It appears to achieve some level of success at higher Reynolds number and farther downstream. The farther downstream recovery also seems to imply that the turbulence generated by the CNPP takes a longer time and/or distance to become fully developed. This could be clarified with more streamwise measurements over an extended range, including the near-wake region.

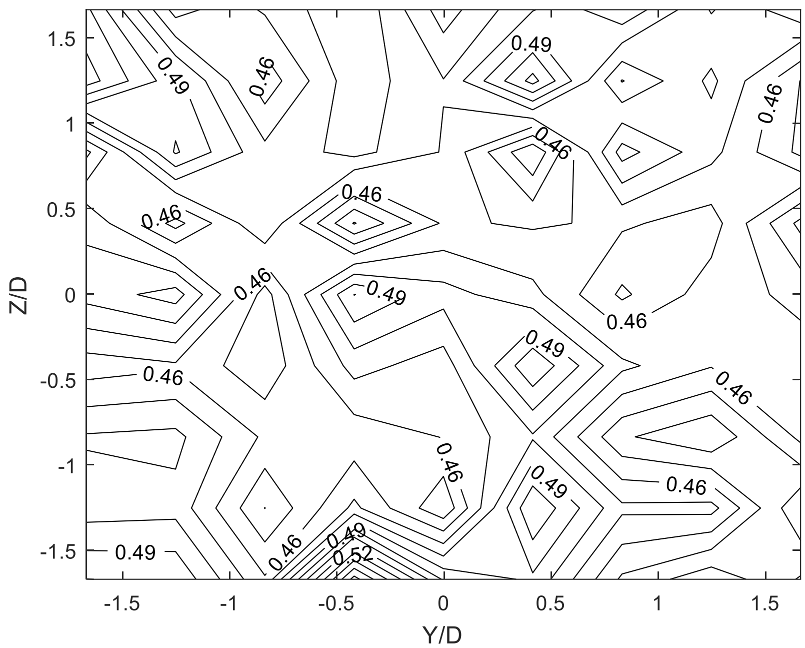

(a) OPP ($U_{mean} = 7.4$m/s, $Re = 1.87 \times 10^4$)

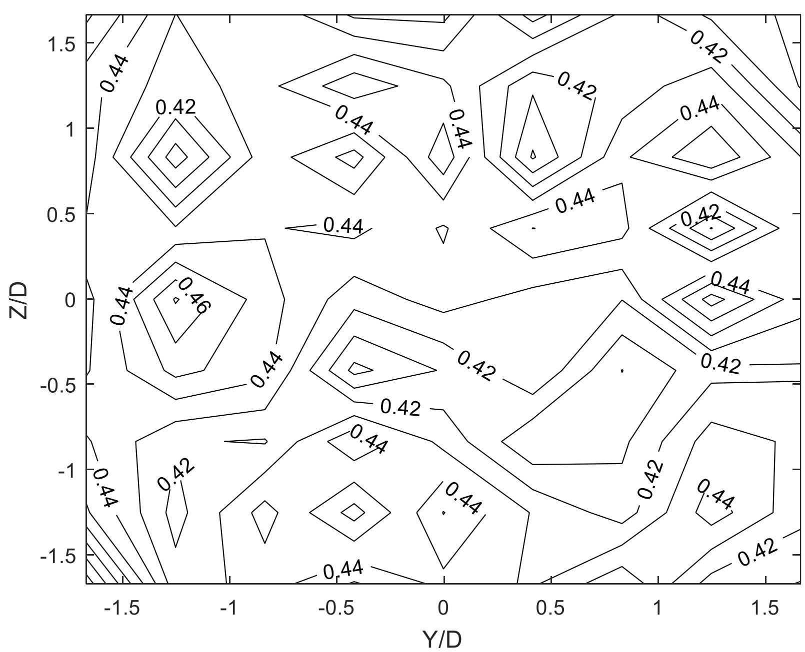

(b) CNPP ($U_{mean} = 7.4$m/s, $Re = 1.87 \times 10^4$)

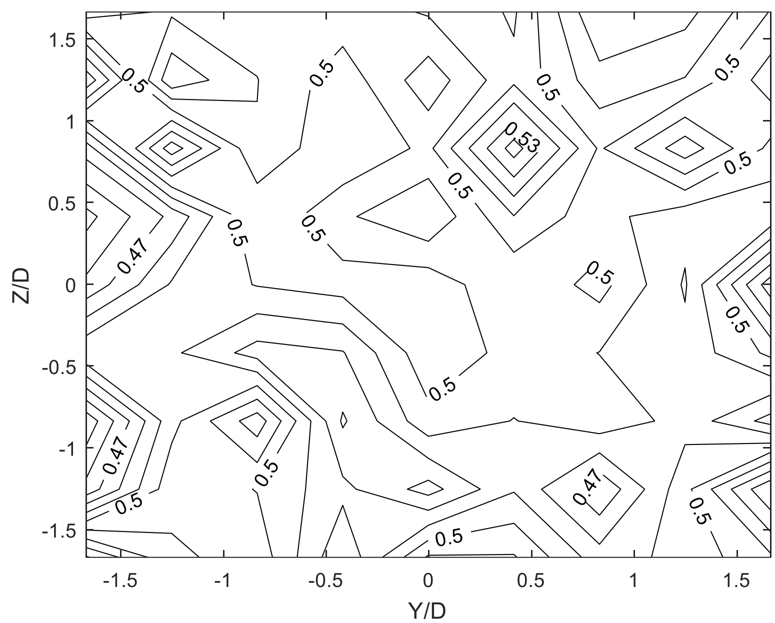

(c) OPP ($U_{mean} = 11.1$m/s, $Re = 2.80 \times 10^4$)

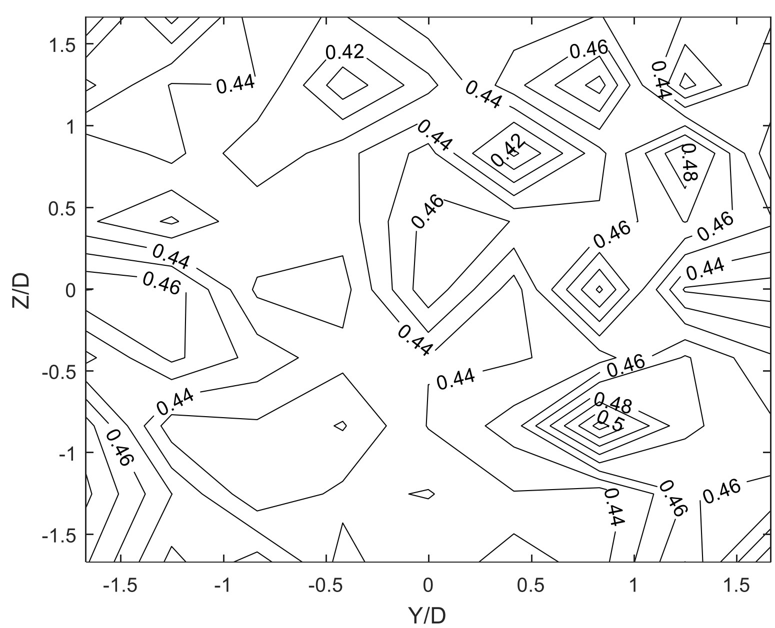

(d) CNPP ($U_{mean} = 11.2$m/s, $Re = 2.84 \times 10^4$)

Figure B. 6. Normalized streamwise integral length scale (Λ/D, D=38mm) at 10D downstream of the perforated plate

B.4.5 Taylor Microscale

To complement the turbulence intensity and integral length results, the dissipative eddies represented by the Taylor microscale are also analyzed. The contours of the normalized Taylor microscale (λ/D, D=38mm) of the OPP and the CNPP are shown in Figure B.7.

At U_{mean} of 7.4 m/s, the cross-sectional-area-averaged normalized Taylor microscale (λ_{mean}/D) of the OPP is 0.0986, and the maximum variation is approximately 4%. The CNPP-generated Taylor microscale is almost of the exact same size, λ_{mean}/D = 0.0985. The spatial homogeneity, however, is less with a largest variation of 6.8%. Increasing the wind speed to approximately 11 m/s resulted in the expected decrease in λ_{mean}/D; 0.097 and 0.094 for the OPP and the CNPP, respectively. The spatial homogeneity of the OPP worsened slightly at 11m/s wind, increasing the maximum deviation to 5.1%. On the other hand, higher wind speed improved the cross-sectional homogeneity of the Taylor microscale produced by the CNPP, lowering the maximum variation from 6.8 to 6.0%.

With continuous decay as the turbulent flow moves downstream, the corresponding Taylor microscale enlarges. For the higher wind speed case, the λ_{mean}/D value of the OPP is 0.135, 14.3% higher than that associated with the CNPP at the same location of 20*D*. In other words, the respective λ_{mean}/D increased by 28% and 19% from those at 10*D*. The maximum cross-sectional variations for the OPP and the CNPP cases are about 4.3% and 4.8%, respectively. The conclusion concerning the OPP is clear, i.e., it generates higher and more isotropic turbulence at a shorter distance downstream. The verdict for CNPP is not so obvious. While it produces slightly lower intensity turbulence of a lesser cross-sectional homogeneity at 10*D*, the created turbulence seems to evolve into a more isotropic one which decays slower farther downstream

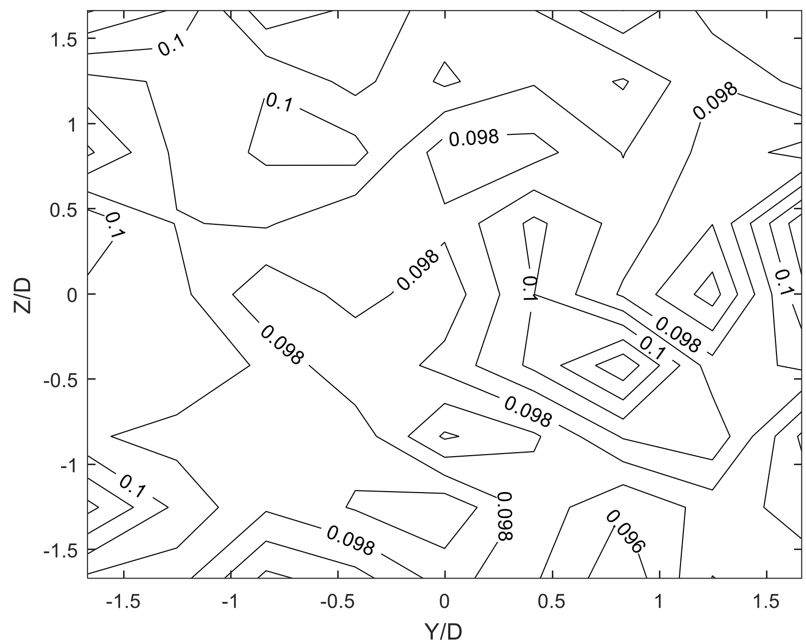

(a) OPP ($U_{mean} = 7.4$m/s, $Re = 1.87 \times 10^4$)

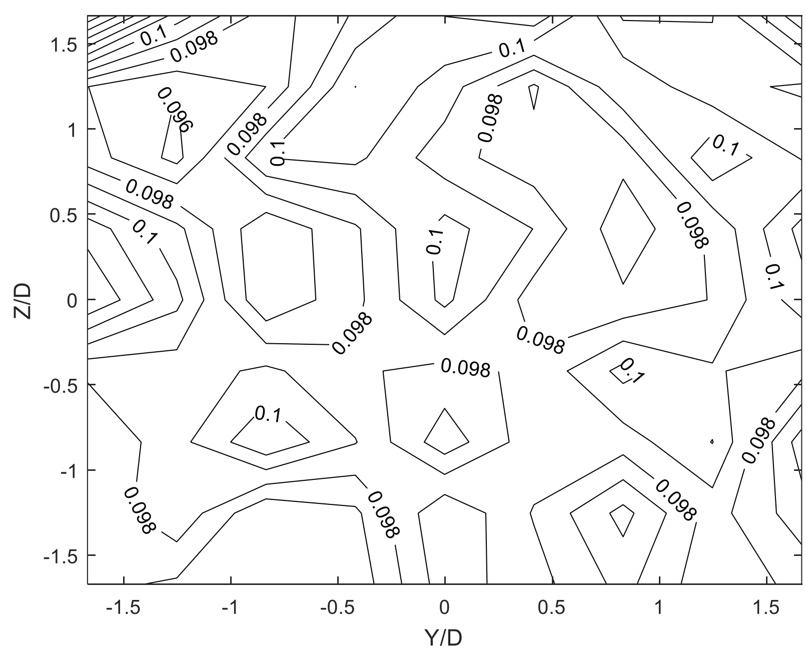

(b) CNPP ($U_{mean} = 7.4$m/s, $Re = 1.87 \times 10^4$)

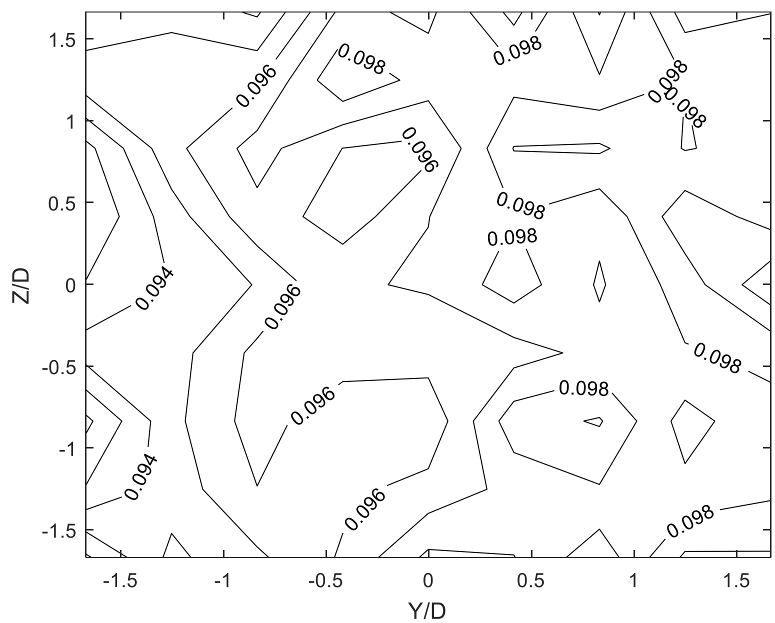

(c) OPP ($U_{mean} = 11.1$m/s, $Re = \ 2.80 \times 10^4$)

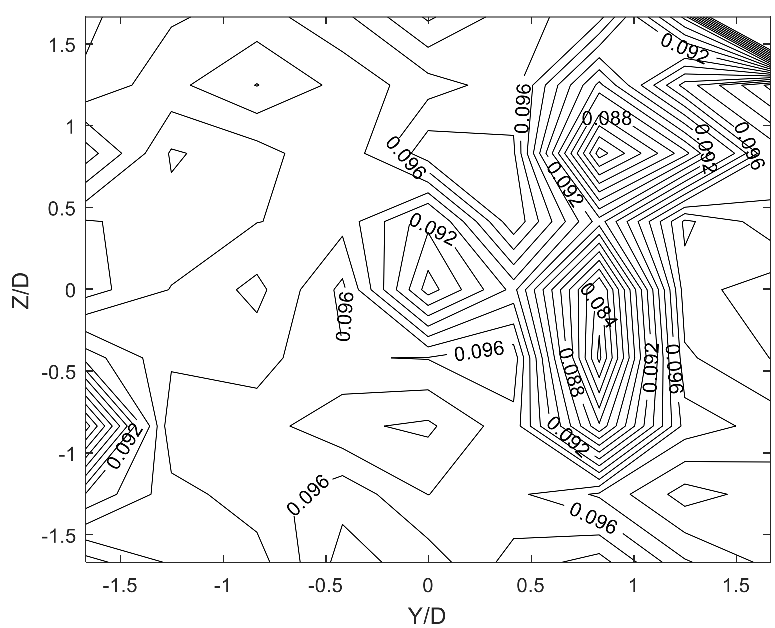

(d) CNPP ($U_{mean} = 11.2$m/s, $Re = \ 2.84 \times 10^4$)

Figure B. 7. Normalized streamwise Taylor microscale (λ/D, D=38mm) at 10D downstream of the perforated plate

B.5 Conclusion

To better appreciate the difference in the turbulent flow generated by an OPP and its reversed counterpart, an CNPP, wind tunnel tests were conducted. The time-averaged velocity, turbulence intensity, integral length and Taylor microscale were analyzed at 10*D* and 20*D* at wind speeds of approximately 7 and 11 m/s. The main findings are:

Turbulence intensity of the OPP is slightly higher than that associated with the CNPP at the same location (10*D*). The higher intensity OPP turbulence also decays somewhat faster than that produced by the CNPP. Increasing the wind speed from 7 to 11 m/s improved the quality of the resulting turbulence in terms of reduced cross-sectional inhomogeneity. This is particularly true for the CNPP.

The OPP turbulence at 10*D* composes of somewhat larger integral length, encompassing the larger amount of turbulent kinetic energy. The dissipative Taylor microscale, however, is almost of the exact same size for both OPP and CNPP. The increase in Taylor microscale farther downstream at 20*D* is notably more rapid for the OPP turbulence.

OPP is more consistent in producing high intensity, isotropic turbulence. The resulting turbulence decays speedily downstream. CNPP, on the other hand, is less reliable when it comes to generating intense and isotropic turbulence. The jet-wake interactions seem to require a longer time or distance to develop into fully developed turbulence. Interestingly, it appears to be able to recover from its shortcomings at higher wind speed and/or farther downstream. In fact, it can outperform OPP in the sense that the created turbulence does not decay as rapidly farther downstream.

Acknowledgments

This work was made possible by Natural Sciences and Engineering Research Council of Canada and Ontario Centres of Excellence.

References

[1] S. V. Ekkad et al., 1997, “Combined effect of grid turbulence and unsteady wake on film effectiveness and heat transfer coefficient of a gas turbine blade with air and CO2 film injection,” Journal of Turbomachinery 119(3): 594-600

[2] G. Melina et al., 2018, “Heat transfer from a flat plate in inhomogeneous regions of grid-generated turbulence”, International Journal of Heat and Mass Transfer 123: 1068–1086.

[3] J. Nedic et al., 2012, “Aeroacoustic Performance of Fractal Spoilers,” AIAA Journal 50(12): 2695-2710.

[4] D. S-K. Ting, M.D. Checkel, 1997, “The importance of turbulence intensity, eddy size and flame size in spark ignited, premixed flame growth,” Proceedings of the Institution of Mechanical Engineers, Part D, Journal of Automobile Engineering, 211: 83-86.

[5] G. I. Taylor, 1935, “Statistical Theory of Turbulence,” Proceedings of the Royal Society of London, Series A, Mathematical and Physical Sciences, 151: 421–444.

[6] M. S. Uberio, S. Wallis, 1967, “Effect of grid geometry on turbulence decay,” Physics of Fluids 10: 1216-1224.

[7] R. Liu, D. S-K. Ting, G. Rankin, 2004, “On the generation of turbulence with a perforated plate,” Experimental Thermal and Fluid Science 28: 307–316.

[8] R. Liu, D. S-K. Ting, 2007, “Turbulent flow downstream of a perforated plate: sharp-edged orifice versus finite-thickness holes,” Journal of Fluids Engineering, 129: 1164-1171.

[9] R. E. Seoud, J. C. Vassilicos, 2007, “Dissipation and decay of fractal-generated turbulence,” Physics of Fluids 19: 105108.

[10] D. Hurst, J. C. Vassilicos, 2007, “Scalings and decay of fractal-generated turbulence,” Physics of Fluids 19: 035103.

[11] R. Hearst, P. Lavoie, 2016, “Effects of multi-scale and regular grid geometries on decaying turbulence,” Journal of Fluid Mechanics, 803: 528-555.

[12] L. Liu et al., 2017, “Numerical and experimental studies on grid-generated turbulence in wind tunnel,” Journal of Engineering Science and Technology Review 10(3): 159-169.

[13] D. S-K. Ting, 2016, “Basics of engineering turbulence,” Academic Press, New York.

[14] G.I. Taylor, 1938, “The spectrum of turbulence,” Proceedings of the Royal Society, London, 164(919): 476–490.

[15] R. S. Figliola and D. E. Beasley, 2006, “Theory and design for mechanical measurements, Fourth edition,” Wiley, New York.

Appendix C THE INFLUENCE OF SQUARE WIRE ATTACK ANGLE ON THE HEAT CONVECTION FROM A SURROGATE PV PANEL

Y. Yang, A. Ahmed, D. S-K. Ting, S. Ray, "The influence of square wire attack angle on the heat convection from a surrogate PV panel," The Energy Mix for Sustaining Our Future, Springer, 2018, pp. 103-128.

Nomenclature

A	Area of the *PTFE* plate
D	Width of the square wire
f	Frequency
G_T	Solar irradiance
h	Heat transfer coefficient
K_{air}	Thermal conductivity of air
K_{PTFE}	Thermal conductivity of *PTFE* plate
Re	Reynolds number
Nu	Nusselt number
Nu_0	Nusselt number without the square wire
P	Electric power output
P_0	Electric power output without the square wire
$PTFE$	Polytetrafluoroethylene
PV	Solar photovoltaics
$Q_{convection}$	Convective heat transfer
$Q_{radiation}$	Radiation heat transfer
Q_{total}	Total heat transfer
St	Strouhal Number
T_{air}	Temperature of the ambient air
T_c	Cell temperature of *PV* panel
T_{bottom}	Temperature of the bottom surface of the *PTFE* plate
T_{ref}	Reference temperature
T_{top}	Temperature of the top surface of the *PTFE* plate
$T_{top,0}$	Temperature of the top surface of the *PTFE* plate without the wire

T_{wall}	Wall temperature of the wind tunnel
t_{PTFE}	Thickness of the *PTFE* plate
Tu, Tv, Tw	Turbulence intensity in X, Y, and Z direction, respectively
U, V, W	Instantaneous velocity in X, Y, and Z direction, respectively
$\bar{U}, \bar{V}, \bar{W}$	Time-averaged velocity in X, Y, and Z direction, respectively
U_∞	Free stream velocity in X direction
u, v, w	Instantaneous fluctuating velocity in X, Y, and Z direction, respectively
$u_{rms}, v_{rms}, w_{rms}$	Root mean square velocity in X, Y, and Z direction, respectively
X	Streamwise direction
Y	Widthwise direction
Z	Vertical direction
β	Temperature coefficient
ε	Emissivity
η	Electric efficiency
η_{ref}	Efficiency at reference temperature
Θ	Square wire attack angle
Λ	Integral length scale
λ	Taylor microscale
ν	Kinematic viscosity
τ	Temporal distance
τ_Λ	Integral time scale
τ_λ	Taylor time scale

C.1 Introduction

Global energy needs will expand by 30% from 2017 to 2040. Among worldwide end-uses of energy, the demand of the electricity keeps rising, making up 40% of the increase in final consumption to 2040 [1]. To meet the rising demand of the electricity and the challenge of decarbonising power supply, the global investment in electricity has already overtaken that of oil and gas in 2016. Among others, due to the rapid development of solar photovoltaics (*PV*), solar energy has the potential to become the largest source of low-carbon capacity by 2040, by which time the share of all renewables in total power generation will reach 40% [1].

The power output efficiency of *PV* panels is influenced by solar irradiance and their cell temperature. For *PV* panels with polycrystalline modules, the efficiency can drop to 9.1% if cell temperature is above 60℃ [2]. Thus, much effort has been invested in finding better ways to keep *PV* panels cool. The numerous attempts can be divided into two groups; active versus passive cooling approaches. Drawing water across the back of the *PV* panel is an effective means. For example, Baloch et al. [3] investigated the effect of converging angle of water cooling channel on *PV* cooling and concluded that the two-degree angle was observed to have the best thermal performance, which reduced cell temperature from 71 ℃ to 45 ℃, and improved power output by 35.5% in the month of June. An experimental study of a novel *PV* cooling technique with water spray was conducted by Nizetic et al. [4]. Their results showed that it was possible to achieve an increase of 16.3% in electric power output on a summer day, by reducing the *PV* panel temperature from 52℃ up to 24℃. Moreover, Bhattacharjee et al. [5] investigated the back surface cooling approach with different designs of heat-absorbing pipe (semi-oval serpentine, circular spiral, and circular spiral semi-flattened). They found that the circular spiral-shaped semi-flattened copper pipe showed the best performance and helped the maximum power of the panel increase by 16.8% (from 22.6 to 26.39W). However, the active techniques mentioned above require external power.

Due to the considerations of overall power conservation and cost, many passive *PV*-cooling techniques have also widely been explored. For example, Rajput and Yang [6] investigated the cooling effect of a clear coated aluminum heat sink. It was determined by their study that natural convection was present from the heat sink facing downwards, reducing temperature by 25 ℃ given an 88.1 ℃ *PV* panel. Also promising is the passive technique of enhancing convective heat transfer, as turbulent generators have drawn great attention in recent years. For example, Fouladi et al [7] investigated the turbulent flow behind a finite-height perforated plate and concluded that the turbulent flow was not in its continuous decay mode with downstream distance due to the interference of the flow over the upper edge of the perforated plate, resulting in an increase of turbulence intensities with downstream distance at some points, which is helpful to enhance convective heat transfer. Subsequently, they explored the effect of the triangular rib and the square rib on a flat plate [8,9]. They found that the rib caused a larger boundary layer and a higher level of turbulence intensity in the area close to the wall, which are predicted to affect the heat transfer from the surface. Moreover, Wu at el focused on the studies about the turbulent flow behind a delta winglet [10,11], and illustrated that vortices were observed downstream of the winglet, resulting in a higher level of turbulence, which is expected to have a higher heat transfer rate than that associated with the base flat plate case.

Among different type of turbulence generators, the studies about the ribs were widely developed due to their structural simplicity. Marumo et al. [12] investigated the turbulent heat transfer in a flat plate behind a cylinder and found that the gap between the cylinder and the plate was helpful for heat transfer in the near wake. Wang and Sundén [13] studied the heat transfer behind the truncated ribs, and concluded that the vortices generated from the end effect was able to sweep cooler fluid towards the wall, resulting in a better heat transfer in the close-rib region. In another study, the rib shape effect on heat transfer was explored by Kamali and Binesh [14], which illustrated the trapezoidal shaped rib had a better heat transfer performance than others. Subsequently, an experimental investigation associated with the effect of the trapezoidal rib chamfering angle on the heat transfer was conducted by Ali et al. [15], which points out the changing angle had an influence on the location of separation and reattachment, and the resulting augmentation of heat transfer. Besides, the arrangements of the rib also draw a great deal of attention recently. For example, Liu et al. [16] explored the heat transfer using different arrangements of the square ribs, and concluded that the flow path become more complex by the staggered arrangements, leading to a larger heat transfer enhancement. A numerical investigation of heat transfer in two-pass ribbed channels was developed by Ravi et al. [17]. And they found that the V-shaped-arranged ribs provided the maximum heat transfer enhancement in the first and second pass, while the M-shaped-arranged ribs provided the best thermal performance in the bend region. It is clear from the sample of studies that heat transfer performance behind a rib is significantly influenced by its geometry, operating parameters and arrangements. In spite of great efforts, much remains to be discovered about the heat transfer behind the rib. The current study aims at furthering the state-of-the-art knowledge by focusing on the promising influence of the attack angle of a square wire on the heat transfer from a flat surface.

C.2 Experimentation

The experiment was carried out in a closed-loop wind tunnel with a 760 mm square cross-section. A 295 mm by 380 mm polytetrafluoroethylene (*PTFE)* plate was inlaid in the center of the test section base, which is made of 10 mm thick fiberglass with thermal conductivity of 0.04 $Wm^{-1}K^{-1}$. The 3 mm thick *PTFE* plate has a thermal conductivity of 0.25W $m^{-1}K^{-1}$ and an emissivity of 0.92 [18, 19]. A water tank was heated up to generate steam, keeping the bottom surface of the *PTFE* plate at a uniform and constant temperature of 100°C. A FLIR C2 thermal camera was used to capture the temperature distribution of the top surface. The thermal image had 60 by 80 pixels, resulting in a spatial resolution of approximately 4.5 mm.

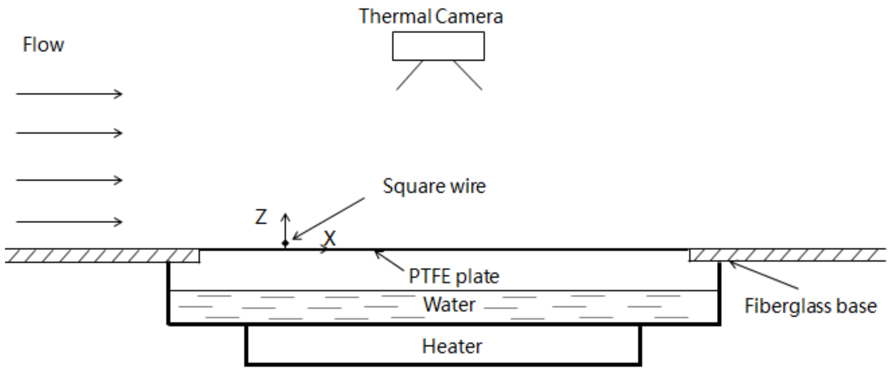

Figure C. 1. Heat transfer experimental setup.

A 4 mm square wire that spanned 630 mm (more than twice *PTFE* plate width) was used to perturb the flow with respect to the reference, empty wind tunnel without the wire case; see Figure C.2. The square wire was placed at 6 mm above the *PTFE* plate, resulting in a 1.5D gap. The attack angle was varied from 15 to 75° in 15° increments, while the wind speed was fixed at approximately 5 m/s. X, Y (into the paper) and Z in Figure C.2 represent the streamwise, widthwise, and vertical direction, respectively. The point of origin, x = 0, corresponds to the leading edge of the lower part of the square wire.

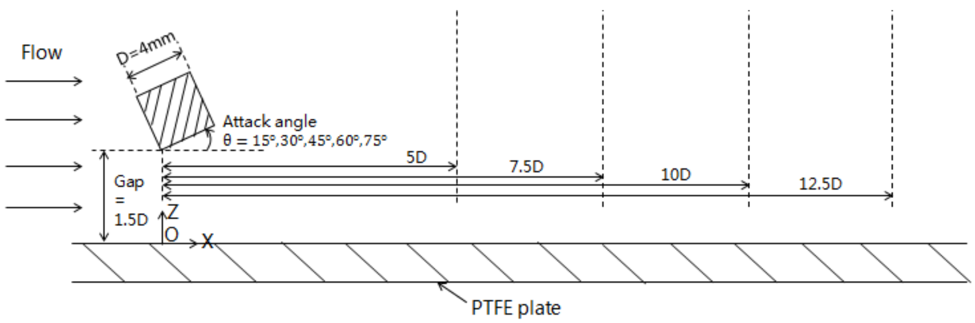

Figure C. 2. Square wire and flow measurement locations.

A triple sensor hotwire probe (type 55P95) with a constant temperature anemometer was employed to obtain the velocities at 5D, 7.5D, 10D and 12.5D downstream of the square wire; see Figure C.2. Each measured line was from 4 mm (1D) to 40 mm (10D) above the plate surface, with a spatial resolution of 1 mm. The velocity signals were low passed at 30 kHz, and 10^6 measurements were sampled at 80 kHz.

C.3 Data Processes

The total heat transferred away from the *PTFE* surface can be deduced from:

$$Q_{total} = K_{PTFE}A(\frac{T_{bottom} - T_{top}}{t_{PTFE}}) \quad \text{(C.1)}$$

Here, K_{PTFE} is the thermal conductivity of the *PTFE*, which is 0.25W $m^{-1}K^{-1}$, A is the area of the *PTFE* surface, t_{PTFE} is the thickness of the *PTFE* plate, T_{bottom} and T_{top} are the temperatures at the bottom and top surfaces of the *PTFE* plate, respectively. As the conduction to the rest of the wind tunnel fiberglass base is negligible, the total heat transfer consists of radiation and convection. The convective heat transfer, key parameter of this study, can be obtained from:

$$Q_{convection} = Q_{total} - Q_{radiation} \quad \text{(C.2)}$$

The radiation heat transfer can be estimated from:

$$Q_{radiation} = \varepsilon\sigma A(T_{top}^4 - T_{wall}^4) \quad \text{(C.3)}$$

where Boltzmann's constant,σ is 5.67x10^{-8}W$m^{-2}K^{-4}$ [20], emissivity ε is 0.92 and T_{wall} is the wall temperature of the wind tunnel.

The convective heat transfer coefficient can be calculated:

$$h = \frac{Q_{convection}}{A(T_{top} - T_{air})} \quad \text{(C.4)}$$

The corresponding non-dimensional Nusselt number, representing the ratio of convective heat transfer to conductive heat transfer, can be obtained from:

$$Nu = \frac{hL}{K_{air}} \quad \text{(C.5)}$$

where L is the characteristic length and K_{air} is the thermal conductivity of air. As the focus is on convective heat transfer enhancement, the normalized Nusselt number is introduced:

$$\frac{Nu}{Nu_0} = \frac{h}{h_0} \quad \text{(C.6)}$$

where Nu_0 and h_0 are the Nusselt number and the convective heat transfer coefficient for the un-perturbed (smooth) surface case without the square wire. It is worth noting the advantages of adopting this normalized Nusselt number. First, it does not depend on the characteristic length. Secondly, as long as the circulating wind tunnel air is at the same thermodynamic state, K_{air} is of no concern.

The electric efficiency of the *PV* panel is defined as:

$$\eta = \frac{P}{AG_T} \tag{C.7}$$

where P is electric power output, G_T is the solar irradiance. This efficiency is affected by cell temperature and solar irradiance, and can be simplified as [2]:

$$\eta = \eta_{ref}[1 - \beta(T_c - T_{ref})] \tag{C.8}$$

where η_{ref} is the efficiency at the reference temperature, β is the temperature coefficient, T_c is the cell temperature, and T_{ref} is the reference temperature (typically 25 ℃). Combining the two equations on efficiency, the power output can be expressed as:

$$P = AG_T\eta_{ref}[1 - \beta(T_c - T_{ref})] \tag{C.9}$$

In this study, we assume that the cell temperature, T_c, is equal to the temperature of the top surface of the *PTFE* plate, T_{top}. Thus, the power output increase compared with the un-wired case can be expressed as:

$$\frac{P}{P_0} \times 100\% = [\frac{1 - \beta(T_{top} - T_{ref})}{1 - \beta(T_{top,0} - T_{ref})}] \times 100\% \tag{C.10}$$

where we assume $\beta = 0.43\%$ in this study [21], and P_0 is power output of un-wired case.

With the 3D hotwire, the instantaneous velocities in the X, Y and Z directions were measured simultaneously. Each of these three components consists of the corresponding time-averaged velocity plus the fluctuating part, i.e.,

$$U = \bar{U} + u \ ; V = \bar{V} + v \ ; W = \bar{W} + w \tag{C.11}$$

where $\bar{U}, \bar{V}, \bar{W}$ are the respective time-averaged velocities, and u, v, w, the corresponding instantaneous fluctuating velocities. The time-averaged velocity can be calculated from:

$$\overline{U} = \frac{1}{N}\sum_{i=1}^{N} U_i \; ; \; \overline{V} = \frac{1}{N}\sum_{i=1}^{N} V_i \; ; \; \overline{W} = \frac{1}{N}\sum_{i=1}^{N} W_i \tag{C.12}$$

where N=10^6 is the sampling number.

The root-mean-square velocity,

$$u_{rms} = \sqrt{\sum_{i=1}^{N} \frac{{u_i}^2}{N-1}} \; ; \; v_{rms} = \sqrt{\sum_{i=1}^{N} \frac{{v_i}^2}{N-1}} \; ; \; w_{rms} = \sqrt{\sum_{i=1}^{N} \frac{{w_i}^2}{N-1}} \tag{C.13}$$

This fluctuating velocity can be normalized by the freestream velocity to give the relative turbulence intensity,

$$Tu = \frac{u_{rms}}{U_\infty} \; ; \; Tv = \frac{v_{rms}}{U_\infty} \; ; \; Tw = \frac{w_{rms}}{U_\infty} \tag{C.14}$$

Some form of vortex shedding is expected from the square wire under certain conditions. To describe the vortex shedding frequency, the normalized frequency, Strouhal number is introduced:

$$St = \frac{fD}{U_\infty} \tag{C.15}$$

Other than velocity fluctuation, turbulence length scale is another key parameter to describe the flow field turbulence [22]. The integral scale, representing the energy containing large eddies, can be derived from the autocorrelation function of turbulence fluctuating velocities. The autocorrelation function in the temporal distance is:

$$f(\tau) = \frac{\overline{u(t)u(t+\tau)}}{\overline{u^2(t)}} \tag{C.16}$$

This can be converted into the corresponding spatial autocorrelation function based on Taylor frozen hypothesis [23],

$$f(r) = f(\tau)\overline{U} \tag{C.17}$$

The integral time scale is defined as:

$$\tau_\Lambda = \int_0^\infty f(\tau)d\tau \tag{C.18}$$

The integration process was terminated at the first zero crossing point. From this, invoking the Taylor frozen hypothesis [10] gives

$$\Lambda = \overline{U}\tau_{\Lambda} \tag{C.19}$$

At the other end of the turbulence energy cascade, the Taylor microscale associated with the dissipation is

$$\lambda = \overline{U}\tau_{\lambda} \tag{C.20}$$

The Taylor timescale,

$$\tau_{\lambda} = \sqrt{\frac{\overline{2u^2}}{\overline{(\frac{du}{dt})^2}}} \tag{C.21}$$

C.4 Results and Discussion

In this section, the heat transfer results are discussed in the context of *PV* panel power output enhancement first. Subsequently, the physics behind the varying localized heat convection improvement up to 50D downstream is explained in terms of the detailed flow characteristics induced by the square wire.

C.4.1 Heat Transfer and Predicted Power Output Enhancement

The effect of the square wire attack angle on the convective heat transfer performance of the flat plate is depicted in Figure C.3. The results are portrayed in terms of the normalized Nusselt number, illustrating the convective heat transfer enhancement with respect to the un-wired case. It is clear from the figure that, the normalized Nusselt number increases with streamwise distance in the near-wire region, and it reaches a peak at around 5~8D downstream of the square wire. Farther downstream, the heat transfer augmentation slowly drops, indicating the flow is restored to a less perturbed condition. Moreover, the higher Nu/Nu_0 value can be observed behind the 60° attack angle wire, which indicates better convective heat transfer performance than that associated with the other attack angles.

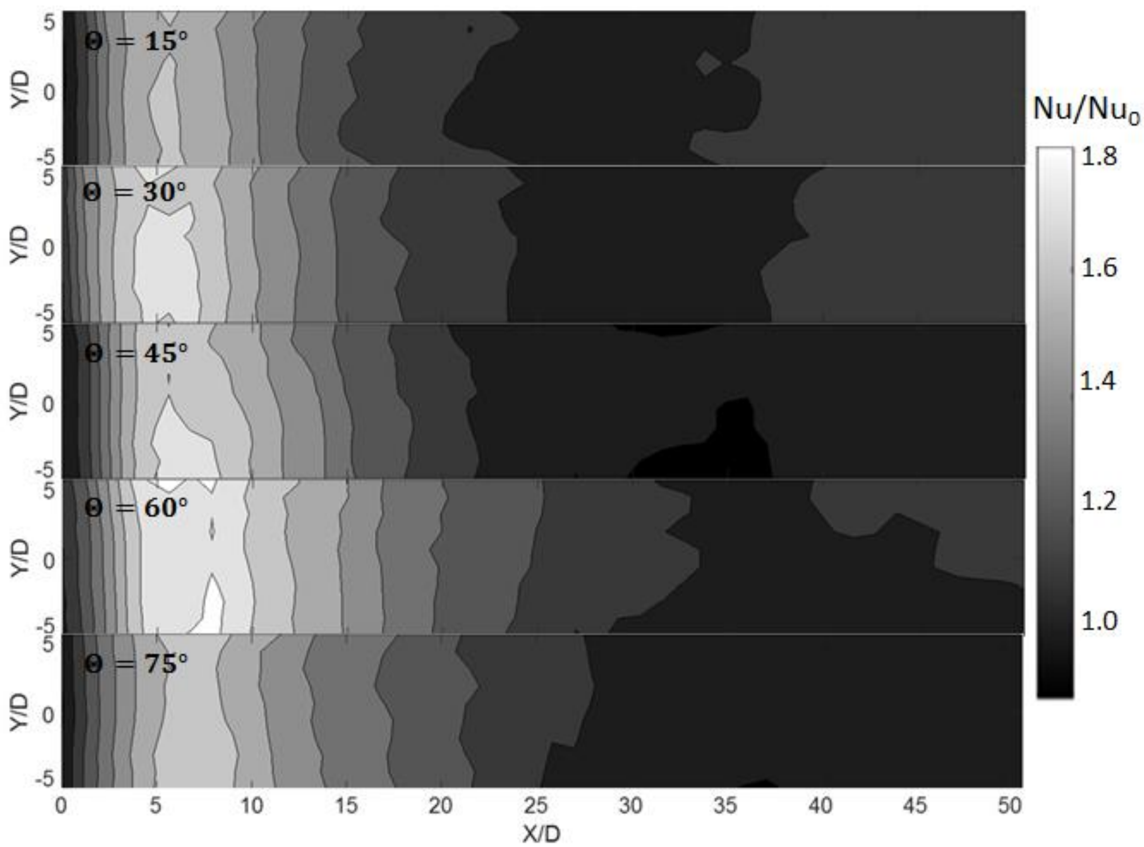

Figure C. 3. Contour of normalized Nusselt number (*Nu/Nu_0*) downstream of the square wire.

As the studied case is strictly two dimensional, with some unavoidable inhomogeneity in the Y direction, averaging the results across the ±5D in the Y direction can better delineate the variation in the convective heat transfer improvement in the streamwise direction. Figure C.4 shows this span-averaged normalized Nusselt number downstream of the square wire. The peak values can be clearly found at 5~8D downstream, varied with respect to the attack angle. The square wire with an attack angle of 60° gives the highest peak value of Nu/Nu_0, around 1.8, at about 8D downstream. The uncertainty of Nu/Nu_0 is around 0.066. This superior performance of the 60° attack angle wire continued all the way until roughly 26D downstream, before the 15° case out-performed it marginally. It is interesting to note that, over the studied surface area, this 15° turbulence generator promotes the least cooling. To better understand the heat transfer trend, the flow characteristics are examined next.

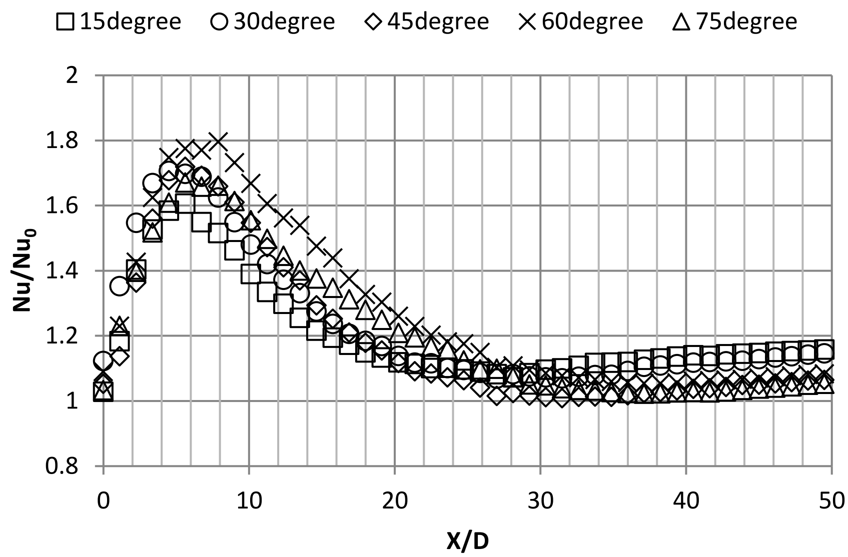

Figure C. 4. Span-averaged normalized Nusselt number downstream of the square wire.

Figure C.5 shows the area-averaged (area encompassed by Y= -5 to 5D, and Z = 0 to 20 or 50D) temperature and predicted power output increase of the surrogate *PV* panel, of which the temperature coefficient (β) is assumed to be 0.43% (Clear Power CS6P-230P, poly-crystalline [21]). It is clear from the figure that, over the entire studied area, the surrogate *PV* panel performs best when the attack angle is 60°, for the studied conditions. In this case, the area-averaged temperature from X/D = 0 to 50 decreases by 2.6℃ (from 80.09°C to 77.45°C), compared with the un-wired flat plate. This leads to a maximum of 1.5% power output increase for the 60° attack angle wire. If we focus on the near wake region, from X/D = 0 to 20, the area-averaged temperature of the *PV* panel behind the 60° square wire is approximately 5°C cooler than that without the wire. The practical effect is a significant power output boost of up to 2.8%. In order to explain the mechanism behind the difference of heat transfer improvement, the flow characteristics generated by the square wire will be detailed in the next section.

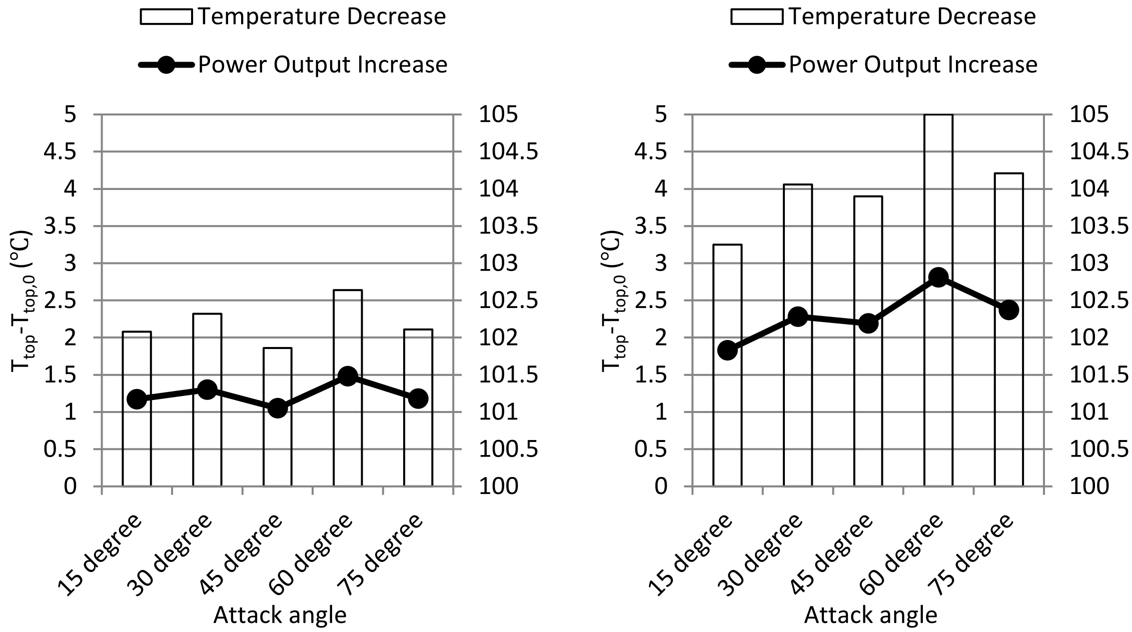

(a) X/D from 0 to 50 (b) X/D from 0 to 20

Figure C. 5. The area-averaged temperature and the predicted power output increase.

C.4.2 Flow Characteristics

C.4.2.1 Velocity Profile

Figure C.6 shows the time-averaged velocity profile in the X direction behind the square wire at different attack angle. It is clear from the figure that at 5D downstream of the square wire, velocity has a high value at a height of 1D from the plate, regardless of the attack angle. This is caused by the jet flow coming from the gap between the wire and the plate. Farther away from the plate, in the increasing Z direction, the velocity profile experiences a deficit at Z ≈ 2D. This signifies the wake region behind the wire. From the experimental study of Dutta et al. [24], the drag coefficient were affected by the orientation of the square cylinder, and the minimum drag coefficient was observed at the attack angle of 22.5°, (same as 67.5° due to the symmetry), as well as the minimum velocity deficit. On the other hand, Dayem and Bayomi [25] found that the minimum drag coefficient occurred at the square cylinder with attack angle of 30° (same as 60°). In the current study, the best performing 60° attack angle wire induced the least amount of velocity deficit; other than the un-wired reference case. The first runner-up, the 75° attack angle wire (see Figure C.5), seems to prevail on this farther downstream. It should be stressed that as far as the local heat transfer is concern, the near-plate (or wall) velocity is most important.

Namely, a larger local velocity would more effectively sweep the thermal energy out of the way. The overall velocity profile indicates, among other things, the amount of shearing (and thus, turbulence) and how the flow will further evolve. It is also clear that the jet emerging from the 1.5D gap between the wire and the plate does not persist far downstream.

Other than the streamwise velocity for this largely 2-dimensional case, the velocity in the Z direction is also of importance. As such, the velocity profile in the Z direction is plotted in Figure C.7. We can see from the graphs that, at 5D behind the wire, the W value starts from a large positive value (velocity vector pointing upward, away from the plate) at the closest-to-the-plate measurement points at Z/D ≈ 1; fear of hot-wire breakage prevented us from venturing closer). This upward, away from the plate, flow is good for convecting heat away. Notwithstanding, it is imperative to note that the magnitude of W is an order of magnitude small than that of U; compare Figure C.7 with Figure C.6. The uncertainty of U/U_∞ and W/U_∞ are around 0.030 and 0.022, respectively.

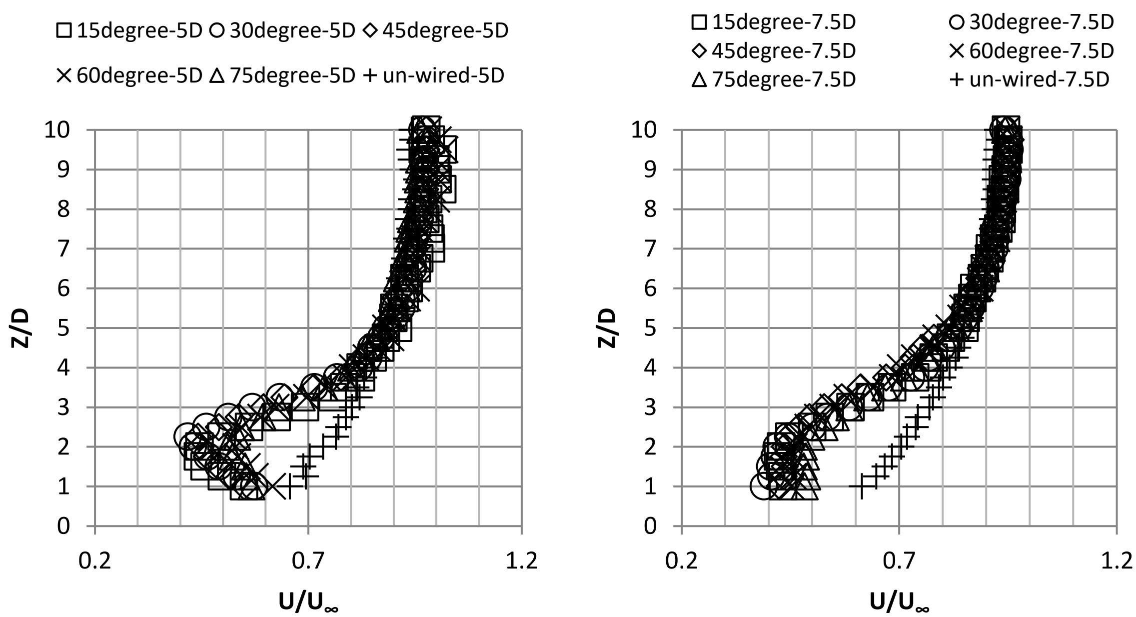

(a) X=5D (b) X=7.5D

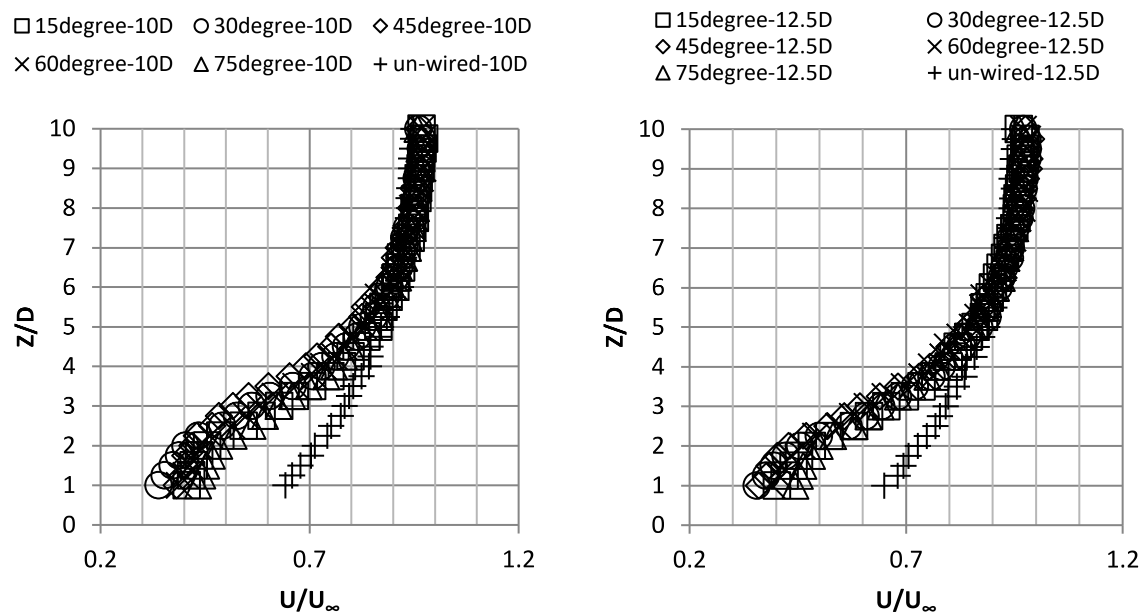

(c) X=10D (d) X=12.5D

Figure C. 6. U/U_∞ profile downstream of the square wire

The switching from a positive W to a negative one with increasing Z in Figure C.7 implies flow circulation, or, more correctly, it signifies a recirculation region. Physically, this is also beneficial as far as heat convection is concerned. The two most effective 'coolers' (θ = 60° and 75°) do not distinguish themselves with a stronger recirculation. This is most likely due to the aforementioned small W magnitude, limited by the omnipresent experimental uncertainties. While some negative, downward velocity persists beyond X ≈ 12.5D, the positive, upward W deteriorates rapidly, and is no longer seen shortly after X ≈ 5D. This appears to be another confirmation that the jet through the gap between the wire and the plate is weak.

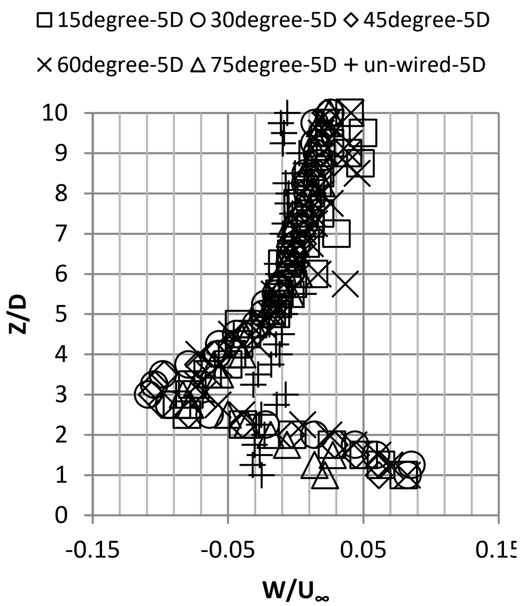

(a) X=5D

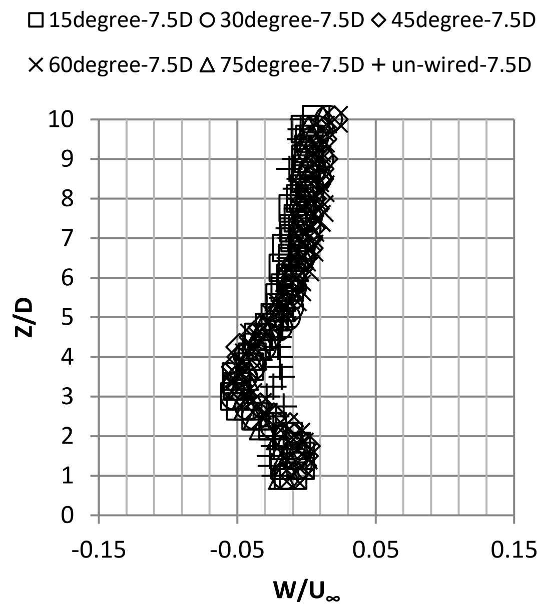

(b) X=7.5D

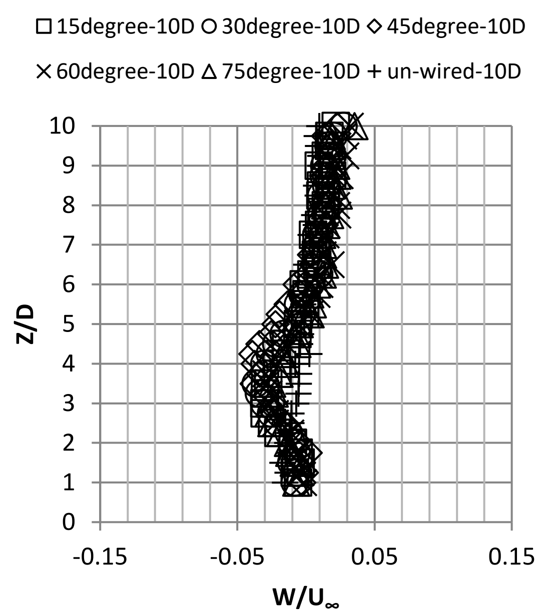

(c) X=10D

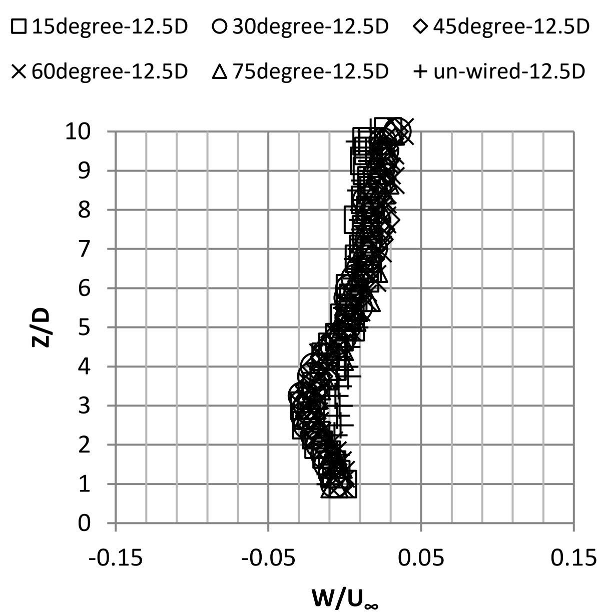

(d) X=12.5D

Figure C. 7. W/U_∞ profile downstream of the square wire.

C.4.2.2 Turbulence Intensity

In order to further understand the flow structure and its effect on heat transfer, turbulence intensity is detailed in this section. Figure C.8 shows the streamwise turbulence intensity profile, with uncertainty of around 0.012. The general trend of decreasing turbulence with distance downstream of the wire is obvious. The perturbed and significantly thickened boundary layer, on the other hand, persisted far downstream. Future study should aim at bringing the persisting high-*Tu* flow closer to the plate. At 5D downstream, two peaks corresponding to the two shear layers from the upper and bottom edges of the square wire. When the flow reaches 7.5D downstream, these *Tu* peaks are no longer obvious, due to the interaction between the shear layers from the bottom edge of the wire and the wall boundary layer. At 10D and 12.5D downstream, the turbulence intensity close to the wall (Z=1D) drops to approximately 0.1, (compared to around 0.8 in the un-wired case), which presumably indicates the decrease of the cooling effect. Figure C.8(a) shows the comparison of the *Tu* value at 5D downstream among the different studied attack angles. It is clear that, the turbulence intensity behind the square wire with an attack angle of 60° has a higher value than others, which translates to a better normalized Nusselt number, discussed earlier.

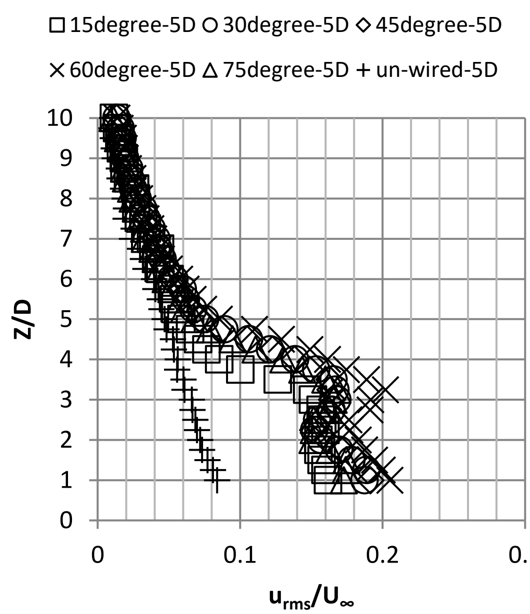

(a) X=5D

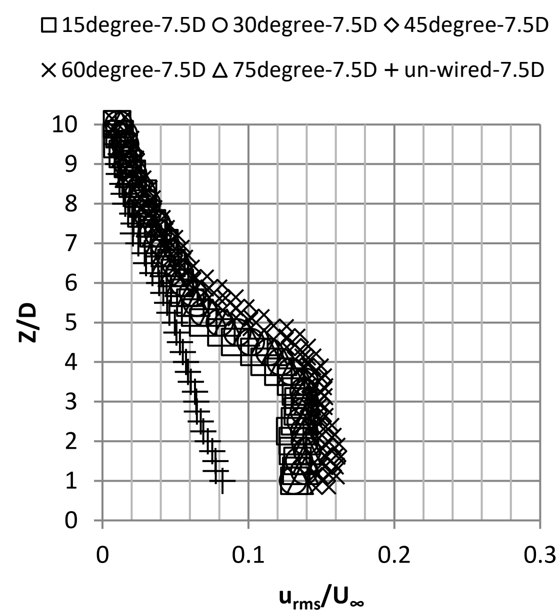

(b) X=7.5D

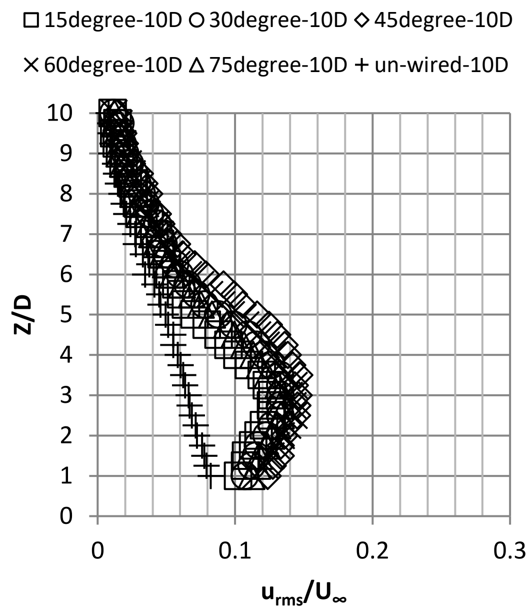

(c) X=10D

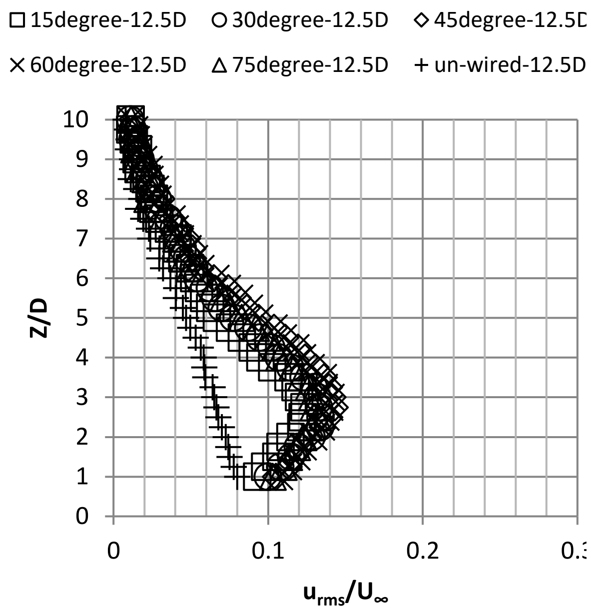

(d) X=12.5D

Figure C. 8. Tu profile downstream of the square wire.

Profiles of the vertical (Z component) turbulence intensity (*Tw*) are depicted in Figure C.9. The uncertainty is estimated to be around 0.01. A peak value can be observed clearly at 3D above the plate, presumably generated by the shear layer from the upper edge of the square wire. With increasing distance downstream, the *Tw* value decreases, indicating the decay of the wire-induced turbulence. Among others, the square wires with attack angles of 60° and 75° have the largest *Tw* values, while the 15° wire has the smallest one. These outcomes further support the respective largest and lowest heat transfer enhancement results.

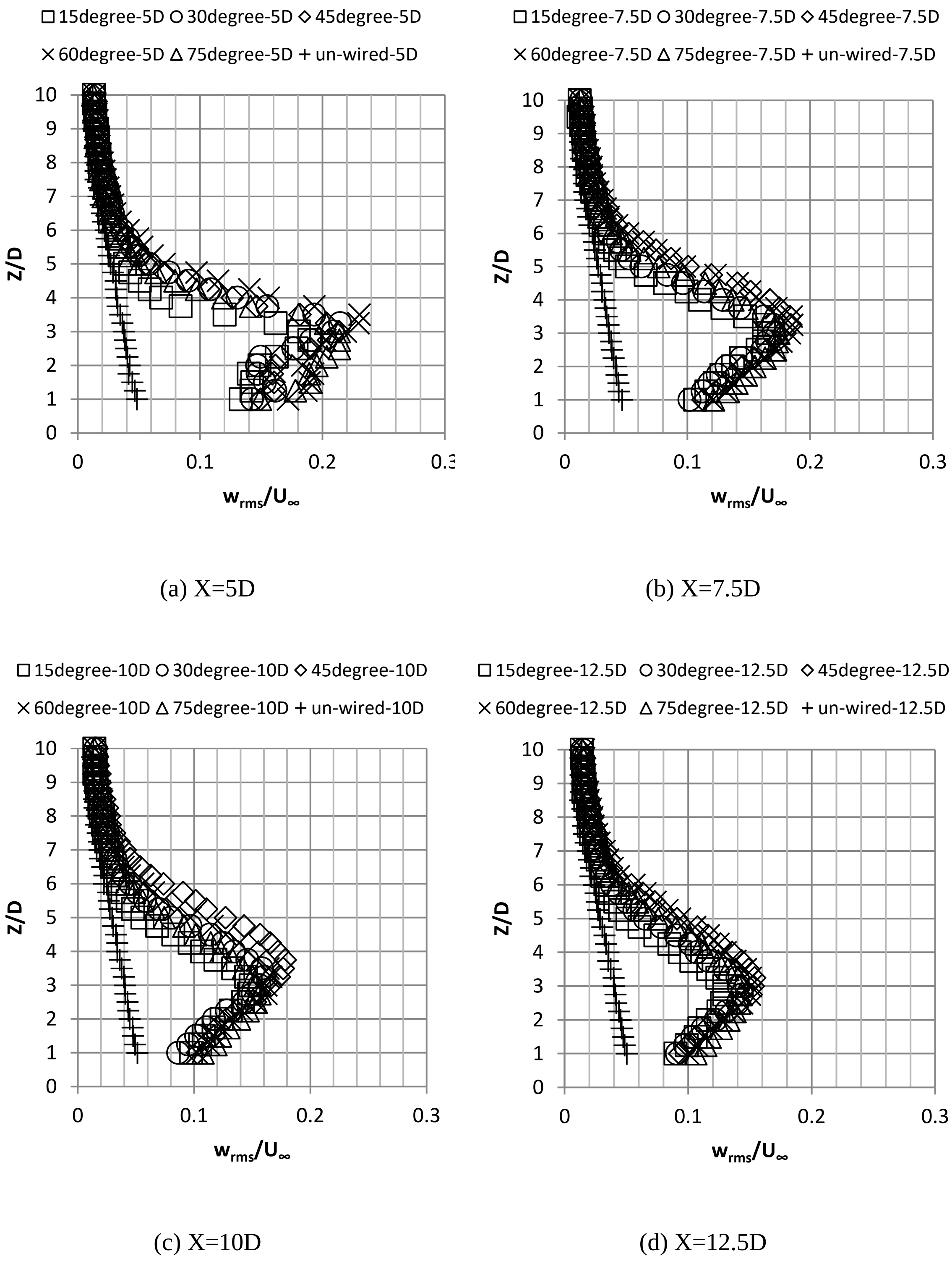

Figure C. 9. Vertical turbulence intensity, Tw, profile downstream of the square wire.

C.4.2.3 Power Spectrum

In addition to the turbulence intensity, the power spectrum of the fluctuating velocity is also of significance. As a bluff body is utilized, some regular vortex shedding is expected under certain conditions. The resulting vortices can play a significant role in convection heat transfer. The kinetic energy of the flow at 5D downstream of the square wire with an attack angle of 45°, as expressed in power spectrum is depicted in Figure C.10. The Y component power spectrum does not have an obvious peak, while the X and Z components supply a distinct a peak at a Strouhal number of approximately 0.08. This implies that the vortex generated by the square wire is primarily in the XZ-plane. Even with a significant attack angle and close to the plate, the obtained *St* = 0.08 is close to *St* = 0.12 a normal square cylinder [26], at the same Reynolds number, $Re = U_\infty D/\nu \approx 1270$). Note that the ground effect has been found to inhibit wake development, and thus, reduce the *St* value [27, 28]. Also notable is the occurrence of the most powerful X component vortex shedding at approximately 1D above the plate, while that of the Z component is at around 3D, at which the turbulence intensity reaches the highest value. A possible explanation for this phenomenon is that the flow volume at Z=1D is not only affected by the layer from the bottom edge of the wire, but also the wall boundary layer; see Figure C.11. The interaction of these two fluctuating turbulent shear layers tend to enhance the X fluctuating component while weakening the Z component.

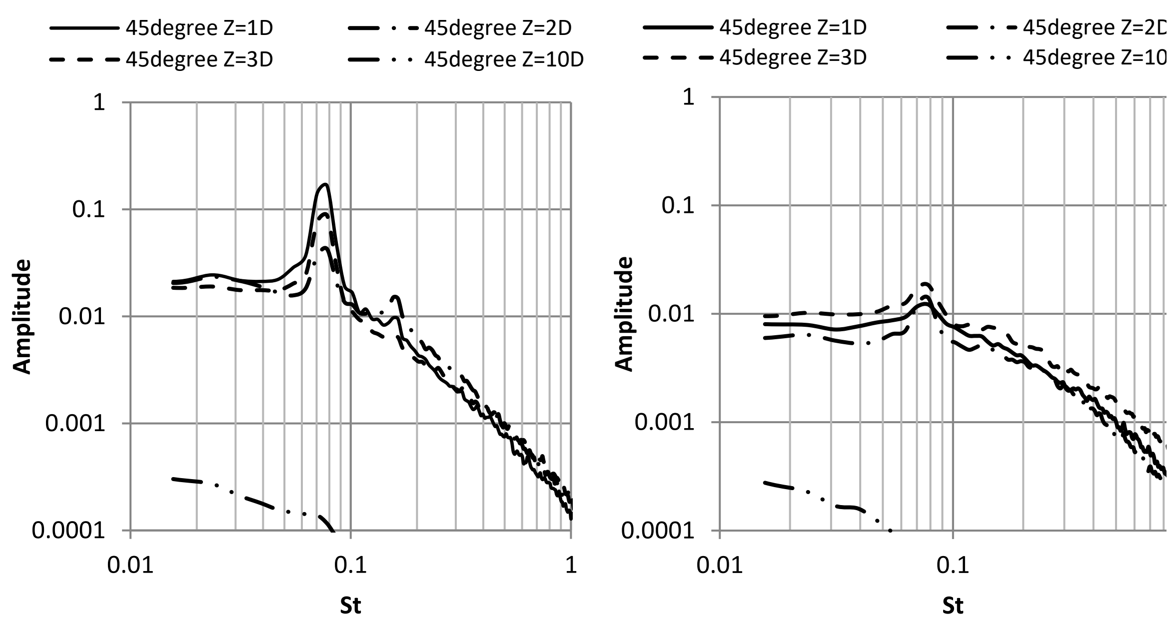

(a) X component (b) Y component

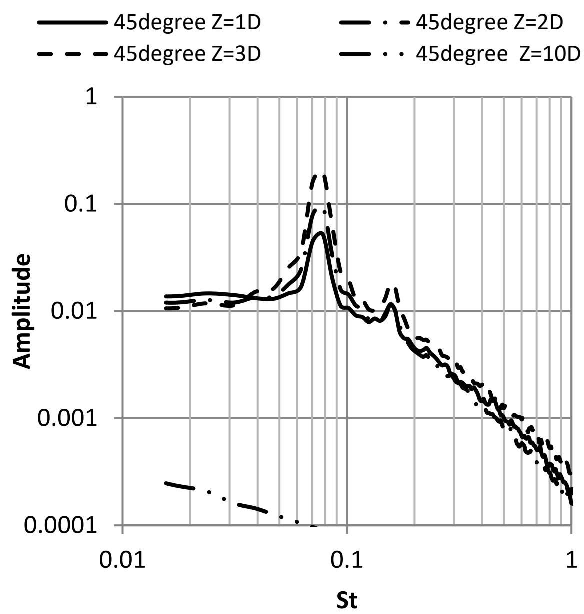

(c) Z component

Figure C. 10 Power spectrum at 5D behind the square wire with an attack angle of 45° (Z=1/2/3/10D)

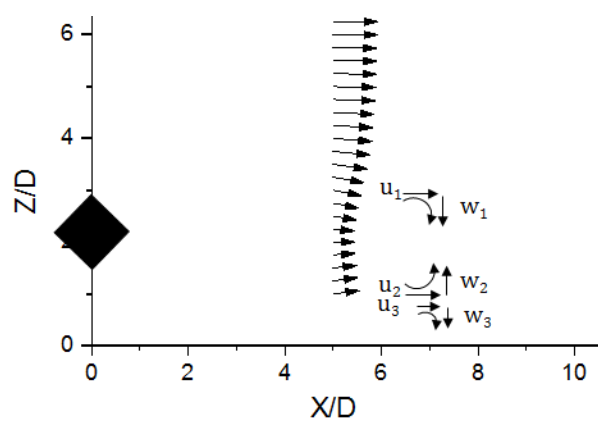

Figure C. 11. Velocity vector at 5D behind the square wire and the schematic diagram of the stress

Figure C.12 portrays the comparison of the power spectrum between the square wire with varying attack angles. The largest peak amplitude value occurs for the 60° case, while the 15° wire resulted in the smallest peak value. These results coincide with the results of the turbulence intensity, which indicates that the 60° wire produces a higher level of turbulence, or, more correctly, the strongest vortex shedding, leading to the most effective heat convection. It is worth emphasizing that the location of the vortex shedding is equally important. What is desirable is a street of vortices fluctuating up and down close enough to the heated surface, to shed the hot fluid near the surface into the freestream, and the cooler fluid unto the surface.

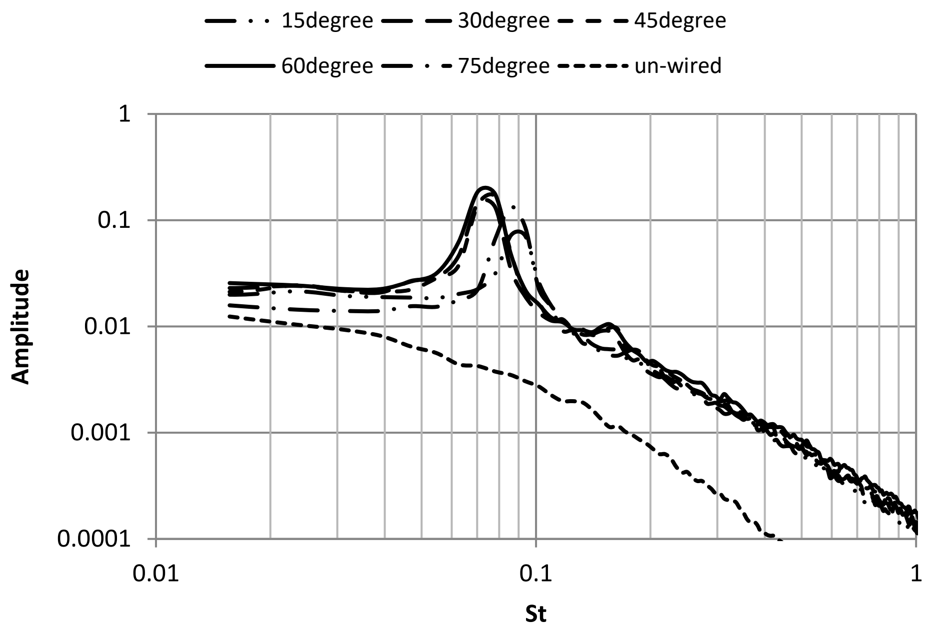

(a) X component (Z=1D)

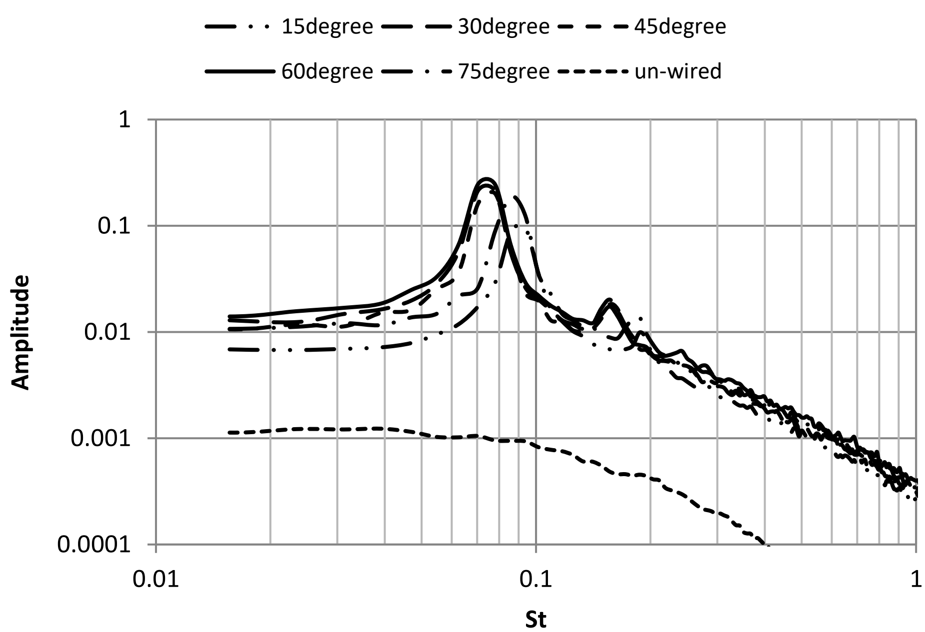

(b) Z component (Z=3D)

Figure C. 12. The effect of attack angle on the power spectra at 5D behind the square wire.

C.4.2.4 Reynolds Stress

Figure C.13 shows the Reynolds stress to complement the illustration of the flow structures such as regular vortices and bulk flow shears. The Reynolds stress is associated with the spatial gradients in time-averaged velocity, it connotes the wall friction and thus, convective heat transfer [29]. The maximum negative Reynolds stress occurs at Z ≈ 3D, where the peak values of turbulence intensity in the X and Z directions occur. Also, at 5D and 7.5D downstream of the wire, very large positive Reynolds stress can be observed near the plate, presumably due to the jet flow generated from the gap. Farther downstream, this jet generated $\overline{uw}$ decays and quickly approaches the un-wired case at Z=1D. From Figure C.13(a), it is also clear that, the absolute values of the Reynolds stress behind the 60° wire are higher than that associated with the other attack angles. The uncertainty of $\overline{uw}/U_\infty^2$ is around 0.001.

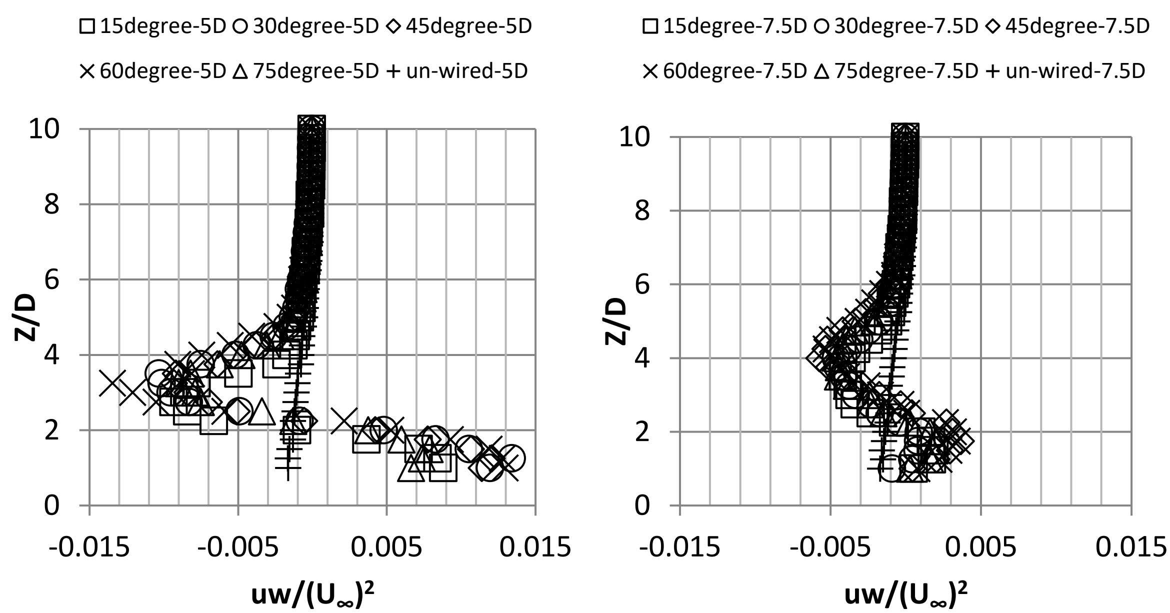

(a) X=5D (b) X=7.5D

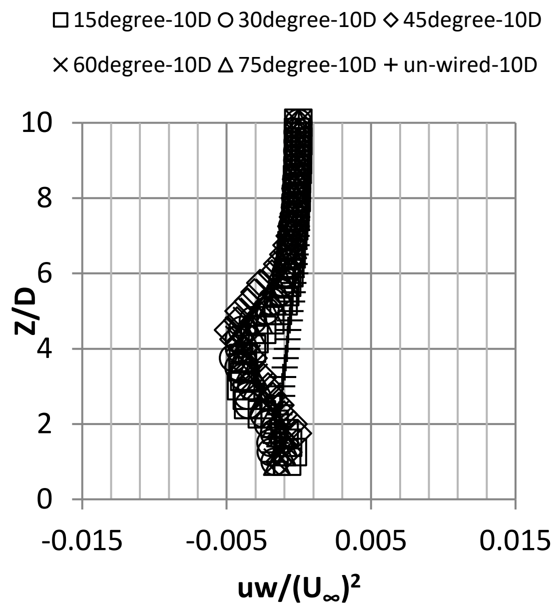

(c) X=10D

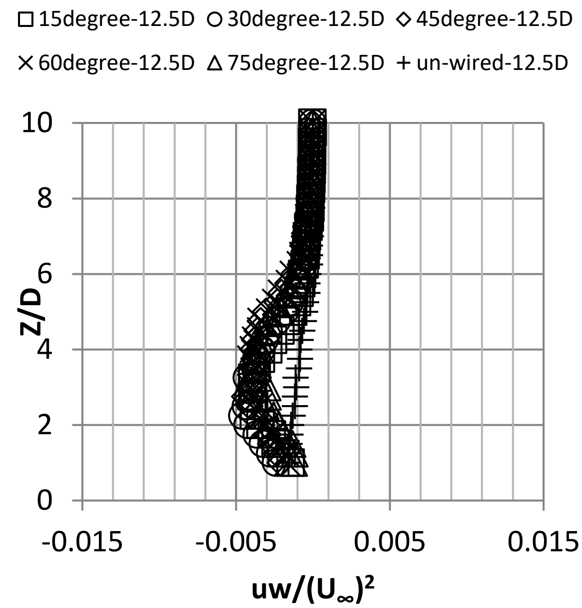

(d) X=12.5D

Figure C. 13. Normalized Reynolds stress profile in the XZ plane.

C.4.2.5 Integral Scale

The size of the eddying motion with respect to the thermal boundary layer, to a large extent, decides how effective the shoveling of the thermal energy from the heated panel is. As such, the streamwise integral scale for the region where the turbulence is of significant intensity ($Tu > 0.1$) is depicted in Figure C.14. The uncertainty is around 0.142. The enlarging integral scale above a height of approximately 2D is closely tied to the diminishing turbulence level, see Figure C.8. Shortly downstream of the wire, at X = 5D, the integral scale also increases below Y = 2D; see Figure C.14(a). This increase in the integral length probably has more to do with the jet ensuing from the gap between the wire and the plate. In other words, due to the shear layers generated by the upper and lower edges of square wire, the eddies at around 1D and 3D are somewhat larger). Presumably due to interference of the regular vortices shed from the cylinder, the integral scale results at some locations, especially farther downstream, are not very conclusive

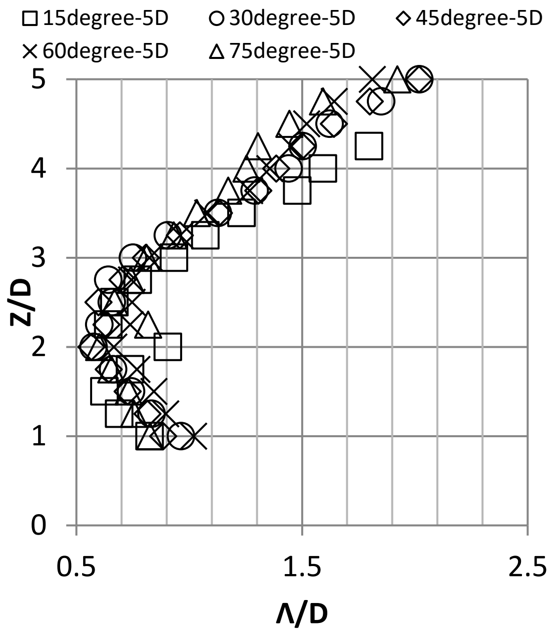

(a) X=5D

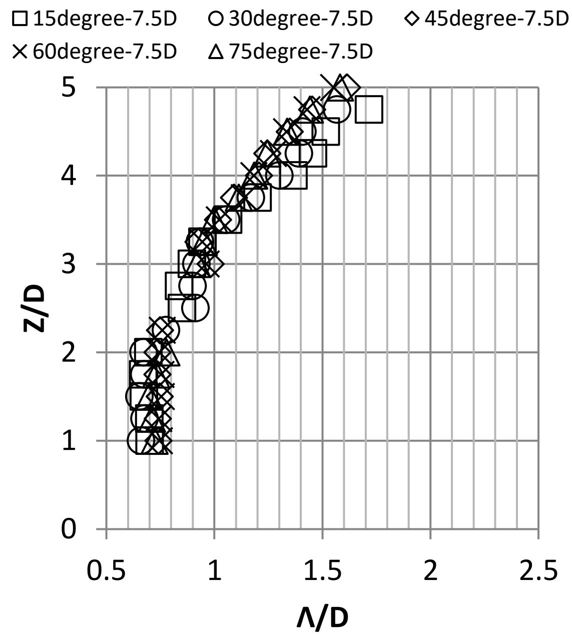

(b) X=7.5D

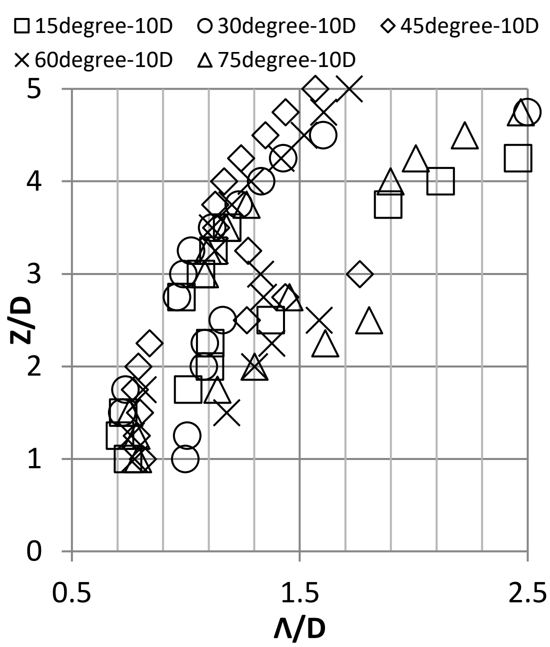

(c) X=10D

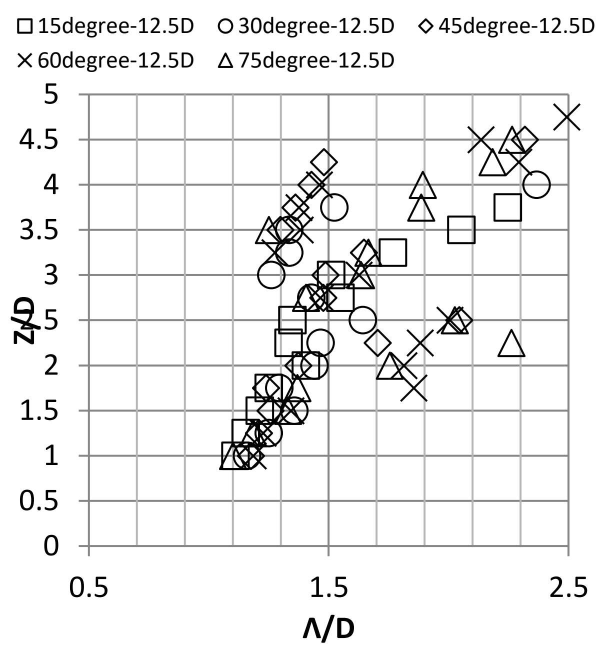

(d) X=12.5D

Figure C. 14. The streamwise integral scale profile

C.4.2.6 Taylor Microscale

Figure C.15 depicts the size of the dissipative Taylor microscale. It is clear from the figure that the smallest Taylor microscale values are detected Z ≈ 2D, which corresponds nicely to the more intense turbulence region. The general increase in the Taylor microscale with distance downstream is consistent with the turbulence decay. The uncertainty of normalized Taylor microscale is around 0.004.

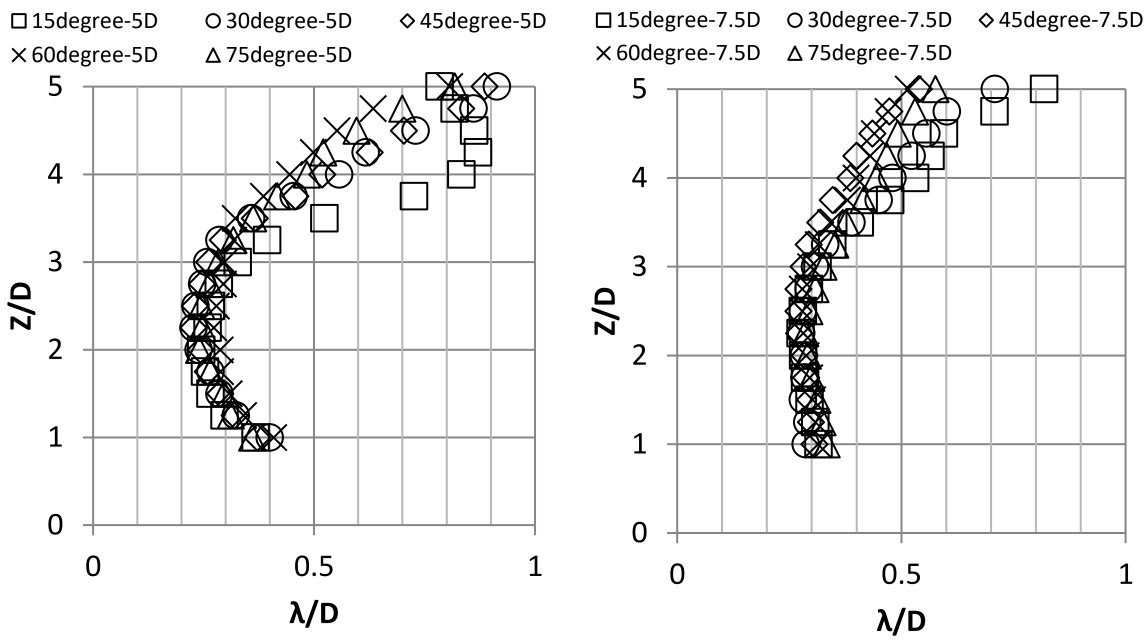

(a) X=5D (b) X=7.5D

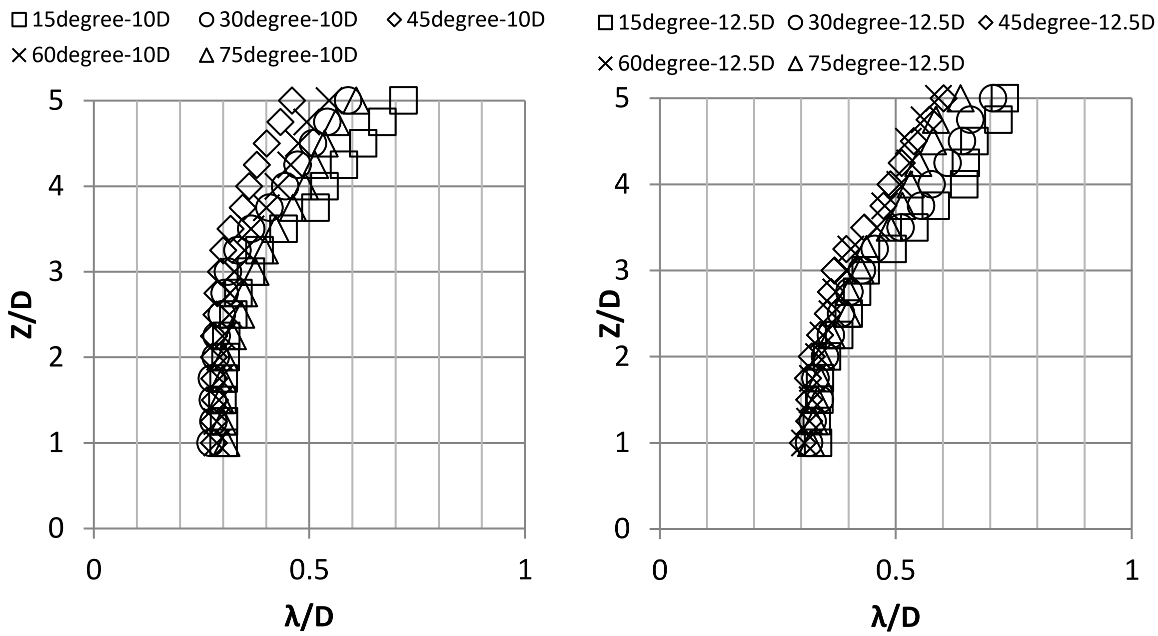

(c) X=10D (d) X=12.5D

Figure C. 15. The streamwise Taylor microscale profile.

C.5 Conclusions

A D = 4 mm square wire attack has been employed to scrutinize the effect of its attack angle on the effectiveness of convecting heat away from a surrogate *PV* panel at 5 m/s wind. A 1.5D gap between the wire and the plate allowed a jet to be emanated, in addition to generating a highly turbulent flow with vortex streets. The Nusselt number normalized by the base unperturbed (by the wire) Nusselt number, Nu/Nu_o, has a peak value at around 5 to 8D downstream. The square wire with an attack angle of 60° promoted the highest heat transfer enhancement, with a maximum Nu/Nu_o value of around 1.8. This corresponds to about 2.8% power output increase for the *PV* panel. Intense turbulence with large energy-containing eddies, and somewhat broad-banded vortex shedding, appear to furnish the best flow environment for convection heat transfer augmentation.

Acknowledgements

This work was made possible by Natural Sciences and Engineering Research Council of Canada and Ontario Centres of Excellence.

References

[1] International Energy Agency, 2017, “World Energy Outlook 2017 – Executive Summary”.

[2] D.L. Evans, 1981, “Simplified method for predicting photovoltaic array output,” Solar Energy, 27 (6), 555-560.

[3] A. A.B. Baloch, H. M.S. Bahaidarah, P. Gandhidasan, F. A. Al-Sulaiman, 2015, “Experimental and numerical performance analysis of a converging channel heat exchanger for PV cooling,” Energy Conversion and Management, 103, 14–27.

[4] S. Nizetic, D. Coko, A. Yadav and F. Grubisic-Cabo, 2016, “Water spray cooling technique applied on a photovoltaic panel: The performance response,” Energy Conversion and Management, 108, 287–296.

[5] S. Bhattacharjee, S. Acharya, A. Potar, A. Meena, D.S. Bairwa, D. Meena, M., Bhagora, P. Meena, P.K. Gautam, 2018, “An investigational back surface cooling approach with different designs of heat-absorbing pipe for PV/T system,” International Journal of Energy Research, 42 (5), 1921-1933.

[6] U. J. Rajput and J. Yang, 2018, “Comparison of heat sink and water type PV/T collector for polycrystalline photovoltaic panel cooling,” Renewable Energy, 116, 479-491.

[7] F. Fouladi, P. Henshaw and D. S-K. Ting, 2014, “Turbulent flow over a flat plate downstream of a finite height perforated plate,” Journal of Fluids Engineering, 137 (2), 021203-12.

[8] F. Fouladi, P. Henshaw and D. S-K. Ting, 2015, “Effect of a triangular rib on a flat plate boundary layer,” Journal of Fluids Engineering, 138 (1), 011101-11.

[9] F. Fouladi, P. Henshaw, D. S-K. Ting and S. Ray, 2013, “Flat plate convection heat transfer enhancement via a square rib,” International Journal of Heat and Mass Transfer, 104, 1202-1216.

[10] H. Wu, D. S-K. Ting, S. Ray, 2017, “An experimental study of turbulent flow behind a delta winglet,” Experimental Thermal and Fluid Science, 88, 46-54.

[11] H. Wu, D. S-K. Ting, S. Ray, 2018, “The effect of delta winglet attack angle on the heat transfer performance of a flat surface,” International Journal of Heat and Mass Transfer, 120, 117-126.

[12] E. Marumo, K. Suzuki, T. Sato, 1985, “Turbulent heat transfer in a flat plate boundary layer disturbed by a cylinder,” International Journal of Heat and Fluid Flow, 6 (4), 241-248.

[13] L. Wang and B. Sundén, 2005, “Experimental Investigation of Local Heat Transfer in a Square Duct With Continuous and Truncated Ribs,” Experimental Heat Transfer, 18: 179–197.

[14] R. Kamali, A.R. Binesh, 2008, “The importance of rib shape effects on the local heat transfer and flow friction characteristics of square ducts with ribbed internal surfaces,” International Communications in Heat and Mass Transfer, 35, 1032–1040.

[15] M. Ali, A. Tariq, B. Gandhi, 2013, “Flow and heat transfer investigation behind trapezoidal rib using PIV and LCT measurements,” Experiments in Fluids, 54: 1520.

[16] J. Liu, S. Hussain, J. Wang, L. Wang, G. Xie, B. Sundén, 2018, “Heat transfer enhancement and turbulent flow in a high aspect ratio channel (4:1) with ribs of various truncation types and arrangements,” International Journal of Thermal Sciences, 123: 99–116.

[17] B. V. Ravi, P. Singh and S. V. Ekkad, 2017, “Numerical investigation of turbulent flow and heat transfer in two-pass ribbed channels,” International Journal of Thermal Sciences, 112: 31–43.

[18] Thermal Conductivity of common Materials and Gases, https://www.engineeringtoolbox.com/thermal-conductivity-d_429.html, accessed on June 15, 2018.

[19] Emissivity Coefficients Materials, https://www.engineeringtoolbox.com/emissivity-coefficients-d_447.html, accessed on June 15, 2018.

[20] Radiation Heat Transfer, https://www.engineeringtoolbox.com/radiation-heat-transfer-d_431.html, accessed on June 15, 2018.

[21] F. Fouladi, P. Henshaw and D. S-K. Ting, 2013, "Enhancing Smart Grid realization with accurate prediction of photovoltaic performance based on weather forecast," International Journal of Environmental Studies, 70(5), 754-764

[22] D. S-K. Ting, 2016, "Basics of engineering turbulence," Academic Press, New York.

[23] G.I. Taylor, 1938, "The spectrum of turbulence," Proceedings of the Royal Society, London, 164(919): 476–490.

[24] S. Dutta, P. K. Panigrahi and K. Muralidhar, 2008, "Experimental investigation of flow past a square cylinder at an angle of incidence," Journal of Engineering Mechanics, 134(9): 788–803.

[25] A. M. A. Dayem and N. N. Bayomi, 2006 "Experimental and Numerical Flow Visualization of a Single Square Cylinder," International Journal for Computational Methods in Engineering Science and Mechanics, 7: 113–127.

[26] A. Okajima, 1982, "Strouhal Numbers of Rectangular Cylinders," Journal of Fluid Mechanics, 123: 379–398.

[27] R.R. Hwang, C-C Yao, 1997, "A numerical study of vortex shedding from a square cylinder with ground effect," Journal of Fluids Engineering, 119(3): 512–518.

[28] S. Bayraktar, S. Yayla, A. Oztekin, H. Ma, 2014, "Wall proximity effects on flow over cylinders with different cross sections," Canadian Journal of Physics, 92: 1141–1148.

[29] A. Tariq, P. K. Panigrahi and K. Muralidhar, 2004, "Flow and heat transfer in the wake of a surface-mounted rib with a slit," Experiments in Fluids, 37 (5): 701–719.

Appendix D DISTRIBUTION OF REFERENCE NUSSELT NUMBER IN THE ABSENCE OF STRIPS

Figure D.1 shows the distribution of reference Nusselt number in the absence of the strips at an incoming flow velocity of around 10 m/s. The averaged Nusselt number over the heated surface is estimated to be around $\overline{Nu}_0 = 638$. This is close to the value of theoretical calculation following the Equations (D.1) and (D.2).

$$Re = \frac{LU_\infty}{\nu} \tag{D.1}$$

where ν is kinematic viscosity, L is characteristic length of heated surface and U_∞ is freestream velocity. In the current calculation, Re is estimated to be around 2.1×10^6.

$$\overline{Nu}_0 = 0.037 * Re^{0.8} * Pr^{\frac{1}{3}} \tag{D.2}$$

Based on *Re* number and *Pr* number, the theoretical $\overline{Nu}_0$ is calculated to be approximately 612.

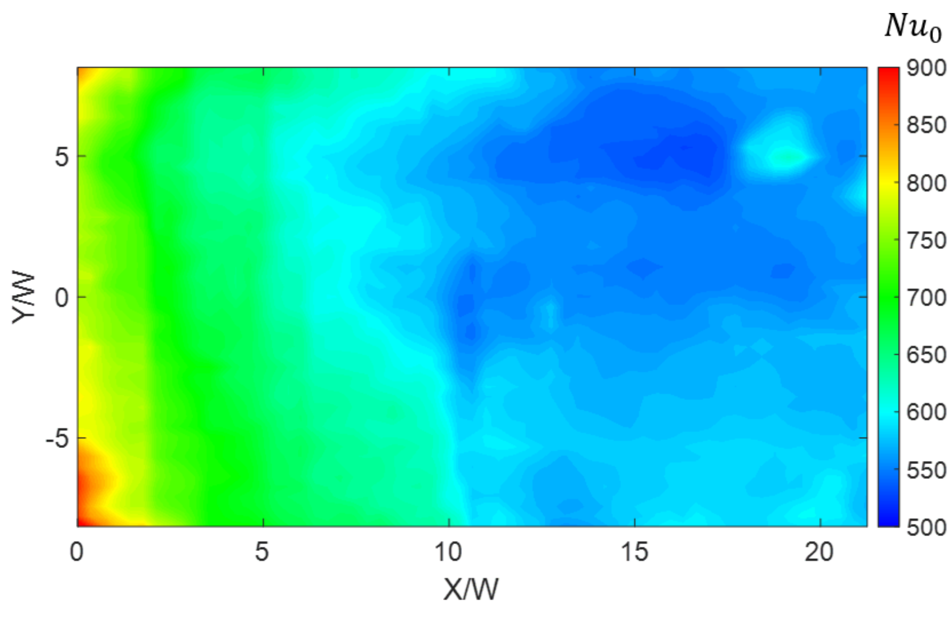

Figure D. 1 Distribution of reference Nusselt number in the absence of the strips at U_∞ = 10 m/s

VITA AUCTORIS

NAME:	Yang Yang
PLACE OF BIRTH:	Guangzhou, China
YEAR OF BIRTH:	1987
EDUCATION:	Middle School affiliated to Guangzhou University, Guangzhou, China, 2006 Jilin University, B.Sc., Changchun, China, 2010 Tongji University, M.Sc., Shanghai, China, 2013 University of Windsor, Windsor, ON, 2020